Summer 2013

Effects of carbon during Fe(II)-catalyzed Fe oxide recrystallization: implications for Fe and carbon cycling

Timothy Stephen Pasakarnis
University of Iowa

EFFECTS OF ORGANIC CARBON DURING FE(II)-CATALYZED FE OXIDE RECRYSTALLIZATION: IMPLICATIONS FOR FE AND CARBON CYCLING

by

Timothy Stephen Pasakarnis

A thesis submitted in partial fulfillment
of the requirements for the Doctor of
Philosophy degree in Civil and Environmental Engineering
in the Graduate College of
The University of Iowa

August 2013

Thesis Supervisors: Professor Michelle M. Scherer
Professor Gene F. Parkin

Graduate College
The University of Iowa
Iowa City, Iowa

CERTIFICATE OF APPROVAL

PH.D. THESIS

This is to certify that the Ph.D. thesis of

Timothy Stephen Pasakarnis

has been approved by the Examining Committee
for the thesis requirement for the Doctor of Philosophy
degree in Civil and Environmental Engineering at the August 2013
graduation.

Thesis Committee:

Michelle M. Scherer, Thesis Supervisor

Gene F. Parkin, Thesis Supervisor

David M. Cwiertny

Timothy E. Mattes

Michael L. McCormick

To my parents, to Ashley, and to Jackson, for giving me the support and perspective necessary to succeed

The engineer's dream is a model of perfect sphericity, the planet Earth with all irregularities removed, highways merely painted on a surface smooth as glass. Of course the engineers still have a long way to go but they are patient tireless little fellows; they keep hustling on, like termites in a termitorium. It's steady work, and their only natural enemies, they believe, are mechanical breakdown or "down time" for the equipment, and labor troubles, and bad weather, and sometimes faulty preparation by the geologists and surveyors.

Edward Abbey
The Monkey Wrench Gang

ACKNOWLEDGMENTS

There are numerous ways to describe the PhD experience, each of which is probably accurate to some point in the process. A journey, adventure, or odyssey might be an appropriate metaphor, but I think most recent graduates would agree that towards the end a PhD becomes a war. As in actual war, this war that is waged in the laboratory and electronic realms is not won by an individual, but rather a collection of individuals. Over the past four and a half years, I have relied on a long list of people to help in my battle against misbehaving experiments, equipment, instruments, weather, computers, vehicles, and parking meters.

First and foremost, this work would never have been possible without the constant support of my wife Ashley. From minor (baking snacks for group meeting) to major (holding down a three dog plus two year old household for over a month while I wrote my thesis) assistance, she kept our family functioning and my sanity intact, particularly during this critical final year. Adjusting our lives around my erratic lab schedule has certainly been trying, but ultimately something we survived due in large part to her many efforts. My son Jackson has been a blessing since the day he arrived, and while his tech support has been of debatable quality (particularly his help formatting my thesis late the night before it was due to committee), on many occasions I needed only to glance at his photos for a reminder of why to make efficient use of the time I was spending away from him. My parents have been behind me through all of my career decisions and non-decisions, and their decades of support and guidance have enabled me to remain confident and persevere through the tribulations that come as part of any research/graduate career.

I am also indebted to my co-advisors Michelle Scherer and Gene Parkin, who despite holding the same titles during my Master's work were happy to have me back for a PhD as well. They provided invaluable advice and guidance throughout the research

and writing processes, and weathered my sometimes fluctuating interest in the lab side of things with remarkable aplomb. Throughout my time in the lab, a host of other students have come and gone, all of whom made the drudgery of preparing and sacrificing individual reactors, the frustration of working in a glovebox, the swearing at the Mössbauer and ICP-MS, and the thousands of iron measurements a bit more tolerable. This non-inclusive list includes the folks responsible for the Pinball Challenge (Chris, Robert, Drew, Mike), the daily DJ sessions (Michelle, Jon S., Dan, Jessica, Luiza), and the various other lab diversions (experiments with the dry ice dinosaur, liquid nitrogen amended silly putty, etc.). I also had a number of people who directly helped me with data collection and other experimental tasks, including Jon S., Luiza, and Ian. Their contributions and tireless work on some of the most boring and monotonous tasks saved me countless hours, allowing me to publish a manuscript and complete much of my thesis in the span of just over two years.

Without the various forms of support and collaboration these people have provided, the thesis that follows would never have been possible, especially in the time frame that it was ultimately produced. I am extremely grateful to have had so many fantastic co-workers, family members, and friends to take part in this experience with me.

ABSTRACT

The reaction between aqueous Fe(II) and Fe(III) oxides is extremely complex, and can catalyze Fe(II)-Fe(III) electron transfer, exchange of Fe atoms between the aqueous and solid phases, mineral transformation, and contaminant reduction. Together, these processes represent a phenomenon referred to as Fe(II)-catalyzed Fe oxide recrystallization, which has been observed under controlled conditions in the laboratory for numerous Fe oxides. In the environment, Fe oxides are likely surrounded by organic carbon in various forms, but their potential to interfere with Fe(II)-catalyzed Fe oxide recrystallization, and its subsequent environmental relevance has not been well studied.

The Fe(II)-catalyzed recrystallization of stable Fe oxides goethite and magnetite was studied in the presence of several environmentally relevant types of organic carbon. For both goethite and magnetite, Fe(II)-catalyzed recrystallization continued relatively undeterred in the presence of electron shuttling compounds, natural organic matter, and extracellular polysaccharides. Slight inhibition was observed when spent media from dissimilatory iron-reducing cultures was present, but only by sorbing a long-chain phospholipid to the oxides was significant inhibition observed. The lack of interference by organic carbon indicates that Fe(II)-catalyzed Fe oxide recrystallization is likely to be relevant throughout a wide range of environments, and represents a significant process with regards to the geochemical cycling of Fe atoms, a claim supported by evidence of Fe(II) driven isotope mixing in real soils.

The movement of atoms during Fe(II)-catalyzed Fe oxide recrystallization is not limited to just Fe however. Multiple trace elements have been shown to exchange between the aqueous and solid phases along with Fe during the Fe(II)-catalyzed recrystallization of Fe oxides. The effect of organic carbon, both sorbed to the oxide surface and coprecipitated with the oxide, on Fe(II)-catalyzed atom exchange and transformation of ferrihydrite was studied. Again, the presence of organic carbon did not

appear to influence Fe atom exchange kinetics. It also did not appear to influence the rapid transformation of ferrihydrite to lepidocrocite. The presence of organic carbon does appear to ultimately have implications for mineral transformation, as over longer time periods it stabilized lepidocrocite, preventing its subsequent transformation to magnetite or goethite.

TABLE OF CONTENTS

LIST OF TABLES

LIST OF FIGURES

CHAPTER 1: INTRODUCTION

Iron Biogeochemistry

Iron (Fe) is the most abundant element in the Earth overall, and the fourth most abundant element in the lithosphere (1). The ability of Fe to exist in multiple oxidation states, the most common being ferrous (Fe(II)) and ferric (Fe(III)), makes it critical to both microbial respiration processes (2), and to the abiotic cycling of other elements on both a local and global scale. Cycling of Fe, particularly through the ocean, has been tied to the global carbon (3), nitrogen (4), and phosphorus (5) cycles. In subsurface environments with anaerobic conditions, Fe(III) can be biologically reduced to Fe(II) by dissimilatory iron reducing bacteria (DIRB), which couple that reduction with the oxidation of organic carbon (6). Fe(II) can also be produced abiotically in anaerobic environments by the weathering of Fe minerals (7), reduction by sulfide (8), or other indirect processes. The interaction of Fe(II) with mineral surfaces has been shown to catalyze the reduction of various groundwater contaminants (e.g., 9, 10), and extensive study of the mechanisms behind these transformations has followed.

Reactions at mineral interfaces have been studied for many decades due their ability to influence contaminant transport and transformation, nutrient cycling, local environment redox state, and many other geologic processes. Aqueous Fe(II) readily associates with various environmental surfaces, including metal oxides, silicate and clay minerals, and bacterial cell membranes; and the uptake process tends to be dependent on surface properties, solution chemistry, and adsorbate properties (11). Uptake measurements are typically collected in an indirect manner, by measuring the change in aqueous Fe(II) concentration after exposure to an oxide or other surface. By varying either the adsorbate concentration to create a sorption isotherm (e.g., 12), or pH to create a pH edge (e.g., 13), conclusions could be drawn regarding the surface charge and distribution / characteristics of sorption sites. These observations are often interpreted

using surface complexation models, which use an assumed surface in local equilibrium with the solution along with thermodynamic calculations to model sorption behavior.

Recent studies have revealed that the interaction between Fe(II) and Fe(III)-bearing minerals is significantly more complex than Fe(II) sorption at a static mineral surface. Under varying geochemical conditions, Fe(II) can induce transformation of ferrihydrite to lepidocrocite, goethite, or magnetite, via a proposed mechanism that includes electron transfer from sorbed Fe(II) to structural Fe(III) (14). Mössbauer spectroscopy has been used with isotopically labeled Fe to selectively examine "sorbed" Fe and bulk Fe oxides individually. Spectra of ^{56}Fe oxides, which are Mossbauer invisible, reacted with ^{57}Fe(II) demonstrate not only that the Fe(II) is oxidized to Fe(III), but also that the newly oxidized Fe(III) forms a surface layer characteristic of the underlying oxide (15-18). By switching the isotopes, a peak characteristic of Fe(II) appears in spectra of certain ^{57}Fe oxides (ferrihydrite, magnetite) following reaction with ^{56}Fe(II), indicating the reduction of structural Fe(III) to Fe(II). Similar observations have been made for magnetite and an Fe-bearing smectite clay in the presence of Fe(II) (19, 20).

Aqueous Fe(II) has also been shown, by use of radioactive ^{55}Fe, to catalyze the reductive dissolution of an Fe oxide, liberating Fe atoms originally bound in the oxide structure (21). Individually, Fe(II) has been shown to sorb to mineral surfaces, transfer an electron to structural Fe(III) in the mineral, and catalyze the release of structural Fe from that mineral. By using a stable Fe isotope tracer, Handler et al. (22) recently provided evidence for the coupling of these three processes in a single system containing aqueous Fe(II) and goethite. In this study, Fe(II) was enriched in ^{57}Fe and reacted with goethite containing natural isotope abundance. The changes in aqueous and solid isotope composition were tracked by multi-collector inductively coupled plasma mass spectrometry (MC-ICP-MS). As might be expected, bulk measurements of aqueous Fe(II) showed a rapid initial decrease in concentration due to some initial uptake of

Fe(II). After a steady state Fe(II) concentration was reached, the ^{57}Fe enrichment of the aqueous phase continued to decrease, whereas the ^{57}Fe enrichment of the solid phase increased. Most compelling however, was that the isotope composition of both the aqueous and solid phase asymptotically approached the equilibrium isotope composition predicted by a mass balance on the Fe isotopes, indicating that complete isotopic exchange had occurred between the aqueous and solid Fe. Despite undergoing complete isotopic mixing, there were no apparent particle size or morphology changes to the goethite solids observed by electron microscopy. The proposed mechanism for this reaction included sorption of Fe(II) to the goethite surface, interfacial electron transfer to structural Fe(III), conduction through the bulk Fe oxide, and reductive dissolution at a spatially separate site, termed a "redox-driven conveyor belt." Currently no direct evidence exists to confirm bulk conduction in goethite, although it has been shown to occur in single crystals of hematite as the result of potential gradients between distinct crystal faces (23).

While the exposure of numerous Fe oxides to aqueous Fe(II) has now been shown to cause extensive Fe atom mixing between the two phases, it is still not clear what mechanism(s) contribute to this behavior. It is important to note that the "redox-driven conveyor belt" was proposed for goethite because published Fe atom diffusion rates would require millions of years at ambient temperature for extensive atom exchange to occur (21 and references therein, 22). In magnetite however, Fe atom diffusion is thought to be faster than most Fe oxides due to significant structural vacancies in the inverse spinel structure. Diffusion rates vary widely throughout the literature (from 1.3 x 10^{-20} cm^2s^{-1} to 10^{-3} cm^2s^{-1}), but even a conservative range of diffusion values predicts that the 54-71% exchange observed within 10 days could be due to atom diffusion (24 and references therein). A number of studies have also suggested that diffusion through micropores can facilitate the movement of metal cations through Fe oxide structures (25-27), and indeed a recent study used electron tomography to map nanopores in hematite

nanocrystals (28), providing further evidence to support this possibility. Since there is currently little data that can be used to directly identify the individual mechanisms operating in a given system, the term "Fe(II)-catalyzed Fe oxide recrystallization" is used to refer to the mixing of Fe atoms between aqueous Fe(II) and Fe oxides which may occur by (*i*) dissolution / reprecipitation, (*ii*) bulk conduction, (*iii*) solid-state diffusion, (*iv*) pore diffusion, or some combination thereof.

Since natural Fe oxides form in complicated and heterogeneous environments, they frequently contain trace metal impurities. The mechanisms during which metal ions can be incorporated into Fe oxide crystal lattices were generally thought to include mineral formation, secondary mineralization, and weathering processes. Recently though, evidence has emerged to support the inclusion of Fe(II)-catalyzed recrystallization as an additional mechanism for the incorporation and release of metals from Fe oxides (29). During the transformation of unstable oxides (e.g., ferrihydrite, lepidocrocite) to more stable forms, a number of metals have been observed to possibly incorporate into the resulting goethite and magnetite structures, including Cu^{2+}, Zn^{2+}, As^{5+}, and U^{5+} / U^{6+} (30-33). It is easy to imagine how metals can be incorporated during secondary mineral transformation, as significant dissolution is followed by reprecipitation of Fe and (presumably) other cations present in solution. A more curious case exists for the stable oxides (e.g. hematite, goethite, magnetite) where Fe(II)-catalyzed recrystallization can result in substantial turnover of Fe atoms without any observable transformation to a secondary mineral phase. Recrystallization can be observed in hematite through growth and dissolution at distinct crystal faces, however magnetite and goethite both undergo significant turnover of Fe atoms with little visible change to mineral size, morphology, or structure. Regardless of visual evidence for recrystallization, trace metal incorporation / release has been observed following exposure to Fe(II) in hematite (nickel, cobalt, zinc (34, 35)), magnetite (cobalt (24)), and goethite (cobalt, copper, lead, nickel, zinc (35, 36)). There is still much to be learned

regarding the mechanism(s) by which trace metals can be incorporated in Fe oxides, what controls uptake / release, and whether these processes can lead to the incorporation or release of other elements as well.

Iron - Carbon Interactions in the Environment

The association of Fe and carbon has long been observed in soils, and the increase in organic carbon content observed with smaller grain sizes (37-39) was often attributed to the stabilization of organic matter by mineral surfaces. Organo-mineral associations have subsequently been studied in greater detail over time with a focus on this "sorptive preservation" (40). Organic matter fractions that are old in age tend to be chemically stable and resistant to oxidation (41), and the concentrations of these fractions often correlate with the content of Fe oxides, clays, and short-range order aluminosilicate minerals in the soil (42-44). Sorption onto Fe oxides can protect organic matter from decomposition by preventing access for hydrolytic enzymes, and by reducing the availability of organic functional groups through the formation of strong, multiple attachment surface complexes (45).

In addition to stabilizing organic matter, association of carbon and Fe may result in enhanced Fe stability. Studies have shown that the association of carbon and Fe can prevent the recrystallization of ferrihydrite to more crystalline forms (46), and although the presence of organic matter during mineral precipitation generally leads to less crystalline Fe minerals with decreased structural order (47), these phases may not necessarily be more reactive. At the same time, organic matter can inhibit the hydrolysis and precipitation of Fe(III) polymers (48), resulting in smaller Fe(III) oxides that can be biologically utilized at much faster rates than the oxides formed in the absence of organic matter (49). The behavior of Fe oxides associated with organic matter is both highly variable and extremely complex, and our understanding of the controls leading to this behavior is still very basic. Even having made that concession, an obvious question still

lingers for which there is little data from which to base hypotheses. Once these metastable organo-mineral complexes have formed, are these oxides still likely to undergo Fe(II) catalyzed recrystallization, and what happens to the organic carbon if recrystallization does occur? While numerous trace elements have been shown to incorporate into and release from Fe oxides that have been exposed to Fe(II), there is little data to suggest whether organic carbon compounds will behave similarly or not.

Objectives and Hypotheses

Objectives

The goal of this thesis is to further our understanding of Fe(II)-catalyzed Fe oxide recrystallization as it occurs in the natural environment. More specifically, this work investigates the complex interactions between sorbed and co-precipitated organic carbon and Fe oxides during the recrystallization process, along with the potential implications for soil carbon storage by Fe oxides.

Hypotheses

1. Structural and electronic characteristics intrinsic to individual Fe oxides influence their reactivity with respect to contaminants and other environmental constituents
2. The presence of sorbed and dissolved organic carbon will influence the rate / extent of Fe(II)-catalyzed recrystallization observed in Fe oxides
3. The influence of organic carbon compounds on Fe(II)-catalyzed recrystallization depends on the chemical and structural nature of the organic carbon involved
4. In cases where recrystallization is expected to include secondary mineral transformation, the interaction mode between carbon and iron (i.e. sorbed vs.

co-precipitated) influences Fe oxide recrystallization rate and mineral product distribution

5. Fe(II)-catalyzed recrystallization of Fe oxides occurs in real soils, and exerts a control on long term soil carbon storage

Thesis Overview

The thesis consists of three main chapters which address the overall study objectives and hypotheses as follows. Chapter 2 addresses hypothesis 1, examining how the ability of magnetite to reduce inorganic mercury depends on the Fe(II) content of the magnetite solids. Chapter 3 addresses hypotheses 2, 3, and 5 by examining the Fe(II)-catalyzed recrystallization of goethite and magnetite in the presence of four major types of environmentally relevant organic carbon compounds. Chapter 4 addresses hypotheses 4 and 5 by examining the Fe(II) induced transformation of ferrihydrite to secondary mineral phases in the presence of sorbed and coprecipitated organic carbon.

In Chapter 2, magnetite was synthesized with varying levels of Fe(II) in its lattice structure. Magnetites with different Fe(II) contents were then reacted with inorganic mercury, and the reduction of mercury / oxidation of structural Fe were tracked using wet chemical measurements, inductively coupled plasma – mass spectrometry (ICP-MS), as well as spectroscopic methods (X-ray near edge absorption spectroscopy, Mössbauer spectroscopy). This chapter has been published in the July 2, 2013 issue of *Environmental Science & Technology*.

Chapter 3 is a survey study which looked at Fe(II)-catalyzed recrystallization in the Fe oxides goethite and magnetite in the presence of organic carbon. A number of environmentally relevant organic carbon compounds were selected from four major types, which included natural organic matter, electron shuttling compounds, high molecular weight polysaccharides, and extracellular exudates from dissimilatory iron-reducing bacteria cultures. ^{57}Fe Mössbauer spectroscopy was used to assess the influence

of organic carbon on Fe(II)-Fe(III) interfacial electron transfer, while a ^{57}Fe enriched aqueous tracer and ICP-MS were used to measure migration of Fe atoms between the aqueous phase and mineral solids. This chapter is in preparation for submission to *Environmental Science & Technology*.

Chapter IV examines whether the mode of association between Fe and carbon influences the rate and extent of Fe oxide recrystallization, and whether the presence of carbon also changes the secondary mineral distribution when unstable Fe oxides are exposed to Fe(II). Ferrihydrite was synthesized in the presence of increasing levels of organic matter, and reacted with aqueous Fe(II) in the presence of either sorbed or coprecipitated organic matter. Fe atom exchange between ferrihydrite solids and the aqueous solution was tracked using an isotopically enriched tracer and measured by ICP-MS, and transformation of ferrihydrite to secondary mineral forms was examined over time using X-ray diffraction. This chapter is in preparation for submission to *Environmental Science & Technology*.

Appendix A contains a manuscript published in *Environmental Science & Technology* for which I conducted an experiment where magnetite with natural isotope abundance was repeatedly exposed to ^{56}Fe enriched Fe(II) to determine which sites in the magnetite structure are available for Fe atom exchange. Appendix B contains a manuscript in preparation for submission to *Environmental Science & Technology* for which I provided Mössbauer characterization of a soil sample reacted with ^{57}Fe(II) and comment / review during the preparation process. Appendix C contains data from aqueous Fe(III)-structural Fe(II) electron transfer and Fe atom exchange experiments that were included in my thesis proposal.

Analytical Background

X-ray Absorption Spectroscopy

X-ray absorption spectroscopy (XAS) is a high-energy technique that can be used to determine valence states and coordination environments of many elements. In XAS, a sample is bombarded with x-rays (typically from a synchrotron radiation source) that span a range of finely tuned energies. Atoms within a sample contain core electrons with well-defined binding energies, which can be ejected by the absorption of an x-ray at that particular energy level. The x-ray absorption and subsequent ejection of a photoelectron leads to an abrupt increase in the measured absorption coefficient, which is referred to as the "absorption edge" for a particular sample or element (50). X-ray absorption near edge spectroscopy (XANES) is the analysis of this absorption edge and the region immediately surrounding it (approximately 50 eV), which is typically used to determine the oxidation state of an element. An ejected photoelectron is then scattered by neighboring atoms, and the resulting scattering pattern can be observed in the extended x-ray absorption fine-structure (EXAFS) region, which extends to much higher energy levels, and can provide information about the neighboring structural environment of the absorber atom (51).

^{57}Fe Mössbauer Spectroscopy

The information provided by ^{57}Fe Mössbauer spectroscopy can provide insight into the oxidation state, magnetic behavior, and the overall nuclear environment of Fe atoms. It can also be used to identify and quantify multiple Fe phases, even in mixed environmental samples. As such, it has become a critical tool in the geosciences and Fe chemistry fields. The following review of the Mössbauer effect as it relates to the study of Fe minerals is adapted from a few rather comprehensive references (52-54).

Mössbauer spectroscopy relies on the principle of resonant absorption, where an excited source nucleus releases energy via γ-decay at a specific energy level, and the

sample nucleus absorbs γ-rays at that same specific energy. For ^{57}Fe Mössbauer, the ^{57}Co source decays to ^{57}Fe*, which is the excited state of Fe with nuclear spin I = 3/2. This Fe spontaneously decays to its ground state (I = ½) via the emission of a γ-ray at the characteristic 14.4 keV energy level. This 14.4 keV γ-ray serves as the radiation source for the Mössbauer apparatus, where it is aligned with the sample being analyzed, and a radiation detector. The interaction of this 14.4 keV γ-ray with ^{57}Fe atoms can be separated into two unique modes: 1) nuclei can recoil to conserve momentum, emitting or absorbing a γ-ray at an energy level equal to the initial γ-ray energy minus the energy lost to momentum, or 2) nuclei can emit and absorb in a recoilless manner, with the γ-ray energy maintained at 14.4 keV. It is only these recoilless absorption events that are measured, and the fraction of total γ-rays absorbed without recoil is referred to as the recoilless fraction. Analyzing samples in solid matrices and analyzing at low temperatures are two techniques routinely employed to increase the recoilless fraction and expedite data collection.

Resonant absorption requires that the ground energy state of the source and absorber nucleus be identical, which means that Fe atoms in a different coordination environment from the source will not absorb the emitted γ-ray. In order to account for this, the source is placed on a motor that oscillates back and forth, using the Doppler Effect to vary the energy of the γ-ray by adding or subtracting kinetic energy. This produces an energy spectrum, throughout which Fe nuclei with various ground state energy levels will absorb the γ-ray, appearing as a decrease in transmission as measured by the radiation detector. Shifts in nuclear ground state energy occur as the result of the local chemical environment, which can include oxidation state, coordination geometry, and bonding characteristics.

These variations in nuclear environment are typically described by three main parameters, the center shift (CS, δ), quadrupole splitting (QS, Δ), and hyperfine field interaction (H). A sample's CS measures the difference in s electron density between the

sample and a reference standard (α-Fe). Binding of elements with different electronegativity can change the density of electrons surrounding the nucleus, as can shielding from p, d, and f orbital electrons, leading to a shift in the nuclear ground state energy level. It is this electron shielding effect that allows for the distinction between Fe(III), where center shifts generally range from 0.3-0.5 mm/s, and Fe(II), where greater electron shielding contributes to lower electron density, and a larger shift of 0.8-1.4 mm/s.

The quadrupole shift / splitting is a measure of the local point symmetry (or lack thereof) of the nuclear electronic environment. In a cubic arrangement, which is perfectly symmetrical, the observed QS is equal to zero. When the quadrupole moment is not symmetric, it interacts with the electric field gradient generated by other charges in the crystal structure to split the +3/2 nuclear energy level into subsequent ±1/2 and ±3/2 levels. This splitting is observed as a peak doublet, where the separation between peak centers is equal to QS. Typical QS values range from 2.0-3.0 mm/s for Fe(II), and 0-0.7 mm/s for Fe(III).

The third parameter measured by Mössbauer spectroscopy is the hyperfine field interaction, which is the effective magnetic field observed at the nucleus. Due to its magnetic moment, the energy levels of the ^{57}Fe nucleus can be perturbed by a magnetic field, either applied externally, or internal as in magnetically ordered minerals. The effect of this perturbation is to completely remove the degeneracy of the nuclear energy levels, with the I=3/2 level splitting into four sublevels, and the I=1/2 level splitting into two sublevels. Splitting of energy levels appears as a sextet, with each peak corresponding to an allowed energy transition ($\Delta m \leq 1$), and peak intensities following Clebsch-Gordan coupling coefficients.

These three parameters form a powerful tool for the identification of Fe phases, with certain limitations. Currently, there is no precedent for calculating expected Mössbauer spectra from first principles. Consequently, interpretation of spectra is

performed empirically, an approach with some potential pitfalls. Due to the possible influence of sample variation (e.g., particle size, sample thickness, multiple electronic environments in a single phase), care should be taken to use complementary analytical methods to aid interpretation whenever possible.

Stable Isotope Analysis

Analysis of the abundance of stable isotopes in natural samples has taken place for over 50 years, with initial study focused on lighter elements such as hydrogen, carbon, nitrogen, oxygen, and sulfur. Recent advances in instrumental technology have greatly expanded the range of elements for which we can detect isotopic composition, allowing for high precision analysis of heavier elements (e.g., Fe) despite increasingly small relative mass differences between isotopes. The use of this technique allows us both to record variation in the isotope ratios of natural samples, and to examine the processes that contribute to these natural isotope fractionations experimentally (55).

Studies have shown the isotopic variation in Fe containing rocks and minerals of igneous origin to be quite small ($\delta^{56/54}Fe = 0.0 \pm 0.3‰$), while the variation in Fe-bearing phases from sedimentary origins may be significantly greater ($\delta^{56/54}Fe$ ranges from -1.6‰ to +0.9‰) (56). Natural variations in Fe isotope ratios may result from biological or chemical processes, due to inherent equilibrium isotope partitioning effects. These effects are based on thermodynamic modeling, which indicates that heavier atoms will tend to partition into bonding environments that minimize vibrational energy. Thus, complexes with strongly binding ligands in geometries with lower coordination numbers would be expected to accumulate heavier isotopes preferentially (57). Isotope fractionation was observed by Johnson et al. (58) as $\delta^{56/54}Fe = +2.7‰$ between Fe(III) and Fe(II) atoms in aqueous solution, which agrees with the thermodynamic predictions of Schauble et al. (57) due to the more rigid bonding environment associated with Fe(III) atoms.

Due to the level of precision required for isotope fractionation measurements, thermal ionization mass spectrometry (TIMS) and multi-collector inductively coupled mass spectrometry (MC-ICP-MS) are the most popular analytical methods employed. The necessity for measurements with accuracy in the sub per mille range can be avoided by using a tracer enriched in one of the isotopes, similar to the experimental setup described in (22). By enriching the aqueous Fe with ^{57}Fe to a level on the order of 80% (vs. 2.2% natural abundance), isotope exchange between the aqueous and solid phases can be tracked with the level of precision that can be achieved by single collector, quadrupole inductively coupled plasma mass spectrometry (ICP-MS). Isotopic enrichment at this level also has the effect of swamping out the relatively small natural isotope fractionation processes, allowing us to track the movement of atoms from the aqueous phase to the solid phase, and vice versa. Atom exchange manifests itself as a convergence of the fraction of ^{57}Fe (f^{57}Fe) for the aqueous phase (initial f^{57}Fe is highly positive due to enrichment) and the solid phase (initial f^{57}Fe near natural abundance), and in the case of complete exchange, both phases will come to equilibrium at the same f^{57}Fe value. Through careful setup of the experimental system, the equilibrium fractionation level can be predicted by performing an isotope balance on the entire system, weighting the initial enrichment of each phase by its mass.

CHAPTER 2: INFLUENCE OF CHLORIDE AND FE(II) CONTENT ON THE REDUCTION OF HG(II) BY MAGNETITE[1]

Abstract

Abiotic reduction of inorganic mercury by natural organic matter and native soils is well-known, and recently there is evidence that reduced iron (Fe) species, such as magnetite, green rust, and Fe sulfides can also reduce Hg(II). Here, we evaluated the reduction of Hg(II) by magnetites with varying Fe(II) content in both the absence and presence of chloride. Specifically, we evaluated whether magnetite stoichiometry (x = Fe(II)/Fe(III)) influences the rate of Hg(II) reduction and formation of products. In the absence of chloride, reduction of Hg(II) to Hg(0) is observed over a range of magnetite stoichiometries ($0.29 < x < 0.50$) in purged headspace reactors and unpurged low headspace reactors, as evidenced by Hg recovery in a volatile product trap solution and Hg L_{III}-edge X-ray absorption near edge spectroscopy (XANES). In the presence of chloride, however, XANES spectra indicate the formation of a metastable Hg(I) calomel species (Hg_2Cl_2) from the reduction of Hg(II). Interestingly, Hg(I) species are only observed for the more oxidized magnetite particles that contain lower Fe(II) content ($x < 0.42$). For the more reduced magnetite particles ($x \geq 0.42$), Hg(II) is reduced to Hg(0) even in the presence of high chloride concentrations. As previously observed for nitroaromatic compounds and uranium, magnetite stoichiometry appears to influence the rate of Hg(II) reduction (both in the presence and absence of chloride) confirming that it is important to consider magnetite stoichiometry when assessing the fate of contaminants in Fe-rich subsurface environments.

---

[1] Pasakarnis, T.S., et al., *Influence of Chloride and Fe(II) Content on the Reduction of Hg(II) by Magnetite*. Environmental Science & Technology, 2013. **47**(13): p. 6987-6994.

Introduction

Mercury (Hg) is a widespread surface and groundwater contaminant throughout the world (59). Although it is naturally occurring, anthropogenic activities such as fossil fuel burning, waste disposal, and mining have led to the mobilization of increased amounts of Hg into the environment (60). In anoxic environments, inorganic Hg can be converted to methylmercury, a potent neurotoxin, by sulfate- and iron-reducing bacteria (e.g., 61, 62). Bioaccumulation of methylmercury has led to fish consumption advisories in fifty states, one U.S. territory, and three tribal areas (63).

Processes governing the fate of inorganic Hg in the environment have been studied for decades, with early studies focused on the reduction of Hg(II) by organic acids (e.g., 64, 65, 66). Within the last ten years however, solid-bound and structural ferrous Fe (Fe(II)) has been implicated in abiotic reduction of Hg(II); as a surface species sorbed to non-ferruginous clay (67), as the ferrous sulfide mineral mackinawite (68), and as the mixed valence Fe (hydr)oxides green rust (69) and magnetite (70, 71). Reduction of Hg(II) can result in highly volatile Hg(0) (K_H = 729 Pa-m^3 mol^{-1}, 0.32 (unitless @ 25°C)) (72), which can volatilize into the atmosphere from the vadose zone, decreasing the pool of Hg available for methylation in anoxic environments (73).

Previous work by our group has shown that magnetite stoichiometry can dramatically influence reduction rates of substituted nitroaromatics (19, 74) and uranium (75), and others have shown that magnetite stoichiometry has a dramatic effect on conductivity (76, 77). Stoichiometric magnetite contains both Fe(II) and Fe(III) in a 1:2 ratio (Fe(II): Fe(III)). Removal of all Fe(II) from the structure of magnetite by oxidation or dissolution results in the formation of maghemite (γ-Fe_2O_3) which contains only Fe(III) (78). Partially oxidized magnetites can exist between the end-members of stoichiometric magnetite and maghemite, and can be referred to by their Fe(II) content (x) as shown in eq. 2-1.

$$x = \frac{{}^{Oct}Fe(II)}{{}^{Oct}Fe(III) + {}^{Tet}Fe(III)} \quad (2\text{-}1)$$

Reduction of Hg(II) to Hg(0) was recently observed for stoichiometric magnetite (Fe(II)/Fe(III) = 0.50) (70), however, it is unclear whether partially oxidized magnetite (x < 0.50) also reduces Hg(II), and whether magnetite stoichiometry will influence the rates of reduction and products formed.

To determine whether magnetite stoichiometry influenced the rate or extent of Hg(II) reduction, we reacted magnetite (with stoichiometries ranging from x = 0.50 to x = 0.29) with Hg(II) in deoxygenated water both with and without chloride present. We analyzed for volatile Hg products, as well as solid phase products with x-ray absorption spectroscopy (XAS) and found that Hg(II) was reduced by both near-stoichiometric and partially oxidized magnetite in the absence and presence of chloride. As we have previously observed for reduction of other compounds, we found that magnetite stoichiometry influences the rate of Hg(II) reduction in both the presence and absence of chloride.

Experimental Section

Magnetite Synthesis and Characterization

Magnetite was synthesized according to previously published methods (19, 74, 79). Briefly, the solids were prepared by precipitating magnetite with NaOH from a solution containing a 1 to 2 ratio of Fe(II) and Fe(III). Partially oxidized magnetite was made by adding hydrogen peroxide (approximately 30% H_2O_2) to oxidize Fe(II) to Fe(III). Maghemite was produced by oxidation of magnetite in air at 200°C. Magnetite stoichiometry was characterized by acidic dissolution (x_d) in 5 M HCl followed by measurement of aqueous Fe(II) colorimetrically by 1,10-phenanthroline complexation with Fe(III) masking by fluoride (79, 80). Total Fe was measured after reduction of

Fe(III) by hydroxylamine hydrochloride. The magnetite stoichiometry was also measured by Mössbauer spectroscopy (x_{MS})(79). The specific surface area was obtained via N_2 adsorption BET analysis and was found to be 68 ± 9 m^2 g^{-1}, which was consistent with the particle size measured by transmission electron microscopy (TEM) of 20 nm.

Mercury Uptake and Reduction Experiments

Mercury uptake and reduction by magnetite (1.5 g/L) of varying stoichiometries was measured in suspensions of deoxygenated de-ionized water, adjusted to an initial pH of 7.2. Experiments were done inside an anoxic glovebox (Thermo Scientific) with a 93% N_2/7% H_2 atmosphere. Mercury was added as Hg(II) in the form of $HgCl_2$ or $HgSO_4$ dissolved in 0.45 M HNO_3 and 0.5 M H_2SO_4 respectively, to a nominal concentration of 0.9 mM Hg(II). Hg trapping experiments were conducted in triplicate, in foil wrapped serum vials, with headspace continuously purged with N_2/H_2 into midget bubblers containing Hg(0) trapping solution as described in Zheng et al. (81), or in sealed reactors that were rotated end over end with headspace purged as previously described immediately prior to sampling. Samples were collected from the reaction vessel and trapping solution at the beginning (prior to addition of magnetite) and at the end of each experiment. Aqueous samples were diluted and preserved for analysis in 2% HNO_3 containing 1 mg/L gold (Au) added as $AuCl_3$ (82). Au acts as an oxidizing agent that converts or maintains Hg as soluble Hg(II). Magnetite solids were magnetically separated from the aqueous phase, dissolved in 5 M HCl, and diluted/preserved in HNO_3/Au as above to determine the fraction of Hg in the solid phase. Samples were analyzed by ICP-MS using a Thermo Fisher Scientific X Series 2 Quadrupole ICP-Mass Spectrometer, and quantified with standards prepared from NIST Standard Reference Material 1641d.

Synchrotron X-ray Spectroscopy Characterization

The speciation of Hg in the solid phase was determined by analysis of X-ray Absorption Near Edge Structure (XANES) spectra collected at the Hg L_{III}-edge (12,284 eV). Measurements were performed at the 10-ID beamline of the MRCAT/EnviroCAT sector at the Advanced Photon Source (83). The beamline undulator was tapered, and the energy of the incident X rays was scanned using a Si(111) cryogenically cooled double crystal monochromator in quick-scanning mode (approximately 2 min per scan for the extended region and 30 s per scan for the near-edge region). Harmonic content was removed by reflection from an Rh-coated harmonic rejection mirror. Absolute energy calibration was monitored by collecting a transmission XANES spectrum from a Hg/Sn amalgam sample (84) before and after the measurements of each Hg-magnetite sample.

The Hg-magnetite samples were prepared by filtration of the suspensions through an 0.22 μm nylon membrane filter and mounting of the resulting hydrated solid pastes in drilled Plexiglas slides with Kapton film windows. Filtration, sample transport, and the x-ray measurements were performed under strict anoxic conditions. Trace Hg remaining in the pore water of the samples does not have a significant contribution to the measured spectra. Data from the samples were collected in fluorescence mode using an Ar-filled ionization chamber. To avoid potential radiation–induced chemical changes to the Hg and to increase the amplitude of the x-ray absorption oscillation signal, the samples were kept at -180 ± 2 °C during the measurements using a liquid-nitrogen cooled spectroscopy stage (Linkam Scientific Instruments).

Several Hg standards were used in the analysis of Hg XANES: Hg/Sn amalgam used as the Hg(0) standard was prepared as described elsewhere (84), commercially available calomel (Hg_2Cl_2) obtained from Sigma Aldrich was used as the Hg(I) standard, and 2 mM $HgClO_4$ sorbed to 4 g/L maghemite at pH 6 was used as the Hg(II) standard.

X-ray diffraction

Powder x-ray diffraction patterns were collected with a Rigaku MiniFlex II system equipped with a Co source (Co$K\alpha$ = 1.78899 Å). Sample powders were mixed with a small amount of glycerol in an anaerobic glovebox to avoid oxidation during analysis (85).

Results and Discussion

Reduction of Hg(II) by Magnetite (in the *absence* of chloride)

To determine whether magnetite stoichiometry influences Hg(II) reduction, we reacted near-stoichiometric (x_{MS} = 0.50) and partially oxidized magnetite (x_{MS} = 0.29, 0.38) with aqueous Hg(II). We used a high concentration of Hg(II) (0.9 mM) in order to be able to determine speciation of Hg in the solid phase with XAS, which was added to the reactors as $HgSO_4$ to avoid introduction of chloride to the system. After three days Hg was found primarily in the aqueous phase and on the solids with negligible amounts recovered from the purged headspace (Figure 2.1a). Analysis of our aqueous and gas phase by ICP-MS requires first oxidizing the Hg to Hg(II) and therefore does not permit speciation of Hg in the aqueous or gas phase. We assume, however, that only Hg(0) enters the gas phase based on previous studies (e.g., 66, 70, 81), whereas the aqueous phase probably contains both Hg(II) and Hg(0). Negligible volatilization is consistent with the estimated value of 0.1% Hg volatilization based on Hg Henry's Law coefficient of 729 Pa m^3 mol^{-1} (72), our reactor geometry, and the conservative assumption of a saturated solution of Hg(0). Previous work looking at the reduction of Hg(II) by magnetite found significantly more volatilization of Hg (70%) presumably due to the much larger proportion of headspace in their reactor and much smaller concentration of Hg (70). Overall Hg recovery in our trapping experiments ranged from 55% to 90% with no clear pattern of Hg distribution among the three phases as a function of magnetite

stoichiometry. Note that some of the error bars on Hg recovery are quite large (up to 18%) due to challenges with sampling and preserving Hg in different phases for analysis by ICP-MS. Despite the low Hg recovery in some cases, it is clear that a significant portion of the recovered Hg is in the solid phase (35-73%).

To evaluate the speciation of Hg in the solid phase, XANES spectra were collected from samples reacted under similar conditions to our Hg recovery experiments (t = 3 days, [Hg(II)] = 0.9 mM, pH 7.2, no chloride present) and compared to those from Hg(0), Hg(I) (Hg_2Cl_2), and Hg(II) standards. XANES spectra of the Hg standards are shown in Figure 2.2a, and exhibit features that allow determination of the Hg valence state. The first derivative of the spectra accentuates the features and provides clear signatures of the different oxidation states of Hg (Figure 2.2b). All three Hg standards have a first-derivative peak near 12,283 eV. The Hg(0) data exhibit two additional small "shoulder" peaks at 12,292 eV and 12,298 eV, which become significantly smoothed in room temperature measurements of the same Hg(0) standard (Figure 2.3). The Hg(I) standard exhibits a characteristic peak at 12,291 eV, whereas the adsorbed Hg(II) standard has a dip at 12,287 eV and a broad peak at 12,297 eV (Figure 2.2b).

The spectra of magnetite solids containing higher Fe(II) contents (x_{MS} = 0.50 and 0.38) are near identical to the Hg(0) standard indicating complete reduction to Hg(0) has occurred (Figure 2.4a). Linear combination fitting of the first-derivative XANES confirms 100% reduction to Hg(0) by the high Fe(II) magnetite solids. Reaction of the more oxidized magnetite (x_{MS} = 0.29) with Hg(II), however, revealed some deviation from the Hg(0) standard. Linear combination fits of the first-derivative XANES indicate that whereas most of Hg on the solids was reduced to Hg(0) (80±5%), there was a fraction of the Hg present as Hg(II) (20±5%) (Figure 2.4a). After fifteen days reaction time, however, complete reduction to Hg(0) was observed indicating that the incomplete Hg(II) reduction observed after 3 days by x_{MS} = 0.29 magnetite was due to a kinetic limitation (Figure 2.5, Table 2.1).

Our findings of Hg(II) reduction to Hg(0) by stoichiometric magnetite are consistent with previous work where stoichiometric magnetite was shown to reduce Hg(II) (70). In that work, however, gaseous Hg(0) was observed as the primary reduction product and only Hg(II) was observed on the magnetite surface, in contrast to our observation of Hg(0) as the dominant species in the solid phase. Significant differences in the experimental design and Hg analysis are the most likely explanations. For example, we used much higher concentrations of Hg ($\approx$ 20,000 fold) to enable collection of XAS spectra. The high Hg loading required for XAS analysis exceeds the solubility of Hg(0)(*l*) (0.3 μM at 20°C) (86) even if only 0.03% is reduced which may have also led to Hg(0)(*l*) partitioning onto the solids. Indeed, when we ran a similar experiment at much lower Hg concentrations (250 nM), we observed almost half of the Hg(0) partition into the gas phase (data not shown). In addition, the previous study (70) used X-ray photoelectron spectroscopy (XPS) to analyze Hg on the solids. A high vacuum technique such as XPS may have volatilized any Hg(0) that might have accumulated on the surface.

Results showing the reduction of Hg(II) to Hg(0) by magnetite with varying stoichiometries are consistent with thermodynamic predictions. Reduction of Hg(II) to Hg(0) by magnetite is thermodynamically favorable based on a comparison of both the standard reduction potential (E^0) for stoichiometric magnetite, as well as previously measured open-circuit potentials (E_{OCP}) for magnetites of varying stoichiometries (78). As shown in the redox ladder in Figure 2.6, magnetite E_{OCP} values are still quite a bit more negative than the 0.851 V for the Hg(II) – Hg(0) couple, indicating that Hg reduction by the entire range of magnetite stoichiometries tested remains thermodynamically favorable.

To confirm that reduction of Hg(II) is coupled with oxidation of Fe(II) in magnetite, we used Mössbauer spectroscopy to monitor changes in magnetite stoichiometry before and after reaction with Hg(II). Prior to reaction with Hg(II), the

Mössbauer spectrum of nearly stoichiometric magnetite consists of two magnetically ordered sextets with the outer sextet corresponding to tetrahedrally and octahedrally coordinated Fe(III) (^{Oct,Tet}Fe(III)) in the magnetite lattice (Figure 2.7, top). The inner sextet corresponds to octahedrally coordinated Fe(II) and Fe(III) pairs that appear as an ^{Oct}Fe(2.5) sextet due to fast electron hopping between Fe(II) and Fe(III) (19, 79). After reaction with Hg(II), the Mössbauer spectrum indicates that the Fe remains as magnetite and that the ^{Oct}Fe(2.5) sextet area has decreased whereas the ^{Oct,Tet}Fe(III) sextet area has increased, both by about 17%, indicating that Fe(II) has been oxidized to Fe(III) within the magnetite (Figure 2.7, bottom). Negligible change in the Fe(II) content of the same magnetite suspended in deionized water was observed (i.e., x_{MS} went from 0.50 to 0.49).

We attempted to determine an electron balance on the Fe(II) oxidized and the Hg(II) reduced despite our incomplete Hg mass balance (51 to 90%) by assuming complete reduction of 0.9 mM Hg(II) to Hg(0) by stoichiometric magnetite. Complete reduction of Hg(II) to Hg(0) by Fe(II) in stoichiometric magnetite, based on the following reaction

$$\begin{aligned} Hg(II) + 2e^- &\rightarrow Hg(0) \\ Fe(III)_{mag} + e^- &\rightarrow Fe(II)_{mag} \end{aligned} \qquad (2\text{-}2)$$

results in a magnetite stoichiometry of $x = 0.32$ (detailed calculations are provided in the Supporting Information). A stoichiometry of $x = 0.32$ matches the measured magnetite stoichiometry (x_{MS}) after reaction with Hg(II) of 0.32(± 0.01) suggesting that all of the Hg(II) may have been reduced. Good agreement between the amount of Fe(II) in magnetite oxidized and the number of electrons required to reduce all of the Hg(II) to Hg(0) suggests that Fe(II) in magnetite is likely responsible for the Hg(II) reduction observed. Even at this high Hg loading, the availability of sufficient electron equivalents from the magnetite solids appears to facilitate reduction of Hg(II) to Hg(0) with the same result (Hg(0) as the dominant end product) as in experiments conducted at much lower Hg concentrations. Wiatrowski et al (70) also observed oxidation of 18% of Fe(II) in

magnetite after reaction with Hg(II), though it was unclear whether this corresponded to a stoichiometric amount of Hg reduction.

Reduction of Hg(II) by Magnetite (in the *presence* of chloride)

To investigate the effect of chloride on Hg reduction by magnetite, we reacted stoichiometric ($x_{MS} = 0.50$) and partially oxidized ($x_d = 0.46, 0.42$, $x_{MS} = 0.38, 0.29$) magnetite with high concentrations of Hg(II) (0.9 mM) added as $HgCl_2$. $HgCl_2$ is commonly used as a source of Hg in reduction experiments and chloride has been shown to slow the reduction rate of Hg(II) by magnetite (70). Chloride is well known to form strong complexes with Hg(II) ($\beta_1 = 6.7$, $\beta_2 = 13.2$, $\beta_3 = 14.2$, $\beta_4 = 15.2$) (87) which may influence the behavior of Hg(II). In the presence of chloride, distribution of Hg among the solids, aqueous, and gas phase after three days reaction changed only slightly from the distribution in the absence of chloride (Figure 2.1b). Hg again remained primarily in the solid phase (46-70%), although significantly less was present in the aqueous phase for the oxidized magnetites (4-6%) than for stoichiometric magnetite (25%) and for all stoichiometries in the absence of chloride (17-20%). Note, however, that in experiments conducted with a much shorter reaction time ($t = 1.0$ hr), chloride significantly influenced the distribution of Hg throughout the system (Figure 2.8). When chloride was absent, Hg distribution was nearly equal between the aqueous solution and magnetite solids, whereas when chloride was present the majority of Hg remained in solution (78-87%) with only a small amount in the solid phase (15-22%) and negligible volatilization (< 1%). We suspect that chloride complexation stabilized Hg(II) in solution and resulted in slower accumulation of Hg on the solids.

To evaluate the speciation of Hg in the solid phase, XANES spectra were collected from samples reacted under similar conditions to our Hg recovery experiments in the presence of chloride ($t = 3$ days, [Hg(II)] = 0.9 mM, pH 7.2, [Cl^-] = 1.8 mM). The

spectra of Hg associated with the stoichiometric magnetite solids ($x_{MS} = 0.50$) again closely resemble the Hg(0) standard, indicating complete reduction of Hg(II) to Hg(0) after 3 days, similar to the case with no chloride present (Figure 2.4b). Complete reduction to Hg(0) was also observed for magnetite with $x_d = 0.46$ and 0.42 (Table 2.1, Figure 2.3). Interestingly though, spectra for the more oxidized magnetite samples ($x_{MS} =$ 0.38, 0.29) reacted for 3 days deviate significantly from the Hg(0) standard, and are best fit using linear combinations of only the Hg(0) and Hg(I) standards (note the isobestic points in Figures 2.4b and 2.9). The presence of Hg(I) as Hg_2Cl_2 in reactors with oxidized magnetite was further confirmed by x-ray diffraction, which clearly shows peaks representative of Hg_2Cl_2 in addition to the characteristic peaks of magnetite (Figure 2.10). After three days, Hg in the solid phase exists as a mixture of Hg(0) and Hg(I), with the higher Hg(I) fractions corresponding with lower stoichiometry (70% observed for the more oxidized $x_{MS} = 0.29$ magnetite, 55% observed for $x_{MS} = 0.38$ magnetite, and no Hg(I) observed for $x \geq 0.42$) (Table 2.1). Formation of Hg(I) in the presence of chloride differs from the reduction of Hg(II) to Hg(0) without any detectable Hg(I) by the same magnetite particles ($x_{MS} = 0.38$ and 0.29) in the absence of chloride.

Detection of an Hg(I) species was surprising as most studies of Hg(II) reduction by environmentally relevant compounds, including fulvic acid (65), humic substances (66), podzolic sandy clay loam soil (88), tropical river humics (89), Fe(II) sorbed to phlogopite (67), green rust (69), and stoichiometric magnetite (70), have observed Hg(0) as the end product of reduction. While these studies tended to work at lower Hg concentrations, many had chloride present in the same 1:2 Hg:Cl ratio that we employed. One observation of Hg(II) reduction to Hg(I) and formation of calomel occurred during the sorption of Hg(II) on mackinawite (FeS) (68). At high Hg(II) to sulfur (in FeS) ratios, Hg uptake continued beyond that expected for stoichiometric precipitation of cinnabar (HgS). The additional uptake was attributed to reduction of Hg(II) and subsequent precipitation of Hg_2Cl_2 which was identified with XRD. The Hg and chloride

concentrations used in that study (200 mM and 5-15 mM respectively) greatly exceeded the solubility of calomel ($K_{sp} = 1.42x10^{-18}$) (86). While our Hg and chloride concentrations were substantially lower, the high Hg loading still likely exceeds the solubility limit for calomel, requiring as little as 0.08% of the initial Hg to exist as partially reduced Hg(I).

As noted earlier, chloride can form stable aqueous complexes with Hg(II) (e.g., $HgCl^+$, $HgCl_2$, $HgCl_3^-$, $HgCl_4^{2-}$) which have been used to explain the inhibition of Hg(II) reduction (66, 70) as well as Hg sorption (90) in the presence of chloride. Indeed, we saw a smaller proportion of Hg associated with the magnetite solids after one hour in purged systems containing chloride indicating slower Hg sorption in the presence of chloride (Figure 2.8). We also did not see any Hg(II) on the solids in the presence of chloride, even on the most oxidized magnetite, which contrasted with the chloride-free case. Whereas inhibition of Hg sorption by chloride seems reasonably straightforward based on a complexation argument, the mechanism for chloride to inhibit reduction of Hg by magnetite is more difficult to discern.

Based on previous work, we speculate that slower reduction observed in the presence of chloride may be due to a combination of stabilizing the disproportionation of Hg(I) and the lower standard reduction potential of Hg_2Cl_2. In the absence of chloride, reduction of Hg(II) to Hg(0) may proceed by reduction of Hg(II) to Hg(I) followed by disproportionation of Hg(I) to Hg(II) and Hg(0) (equations 2-3 and 2-4) (86).

$$Hg(II) + e^- = Hg(I) \quad (2\text{-}3)$$

$$2Hg(I) = Hg(II) + Hg(0) \quad (2\text{-}4)$$

In the presence of chloride, however, disproportionation of Hg(I) can be suppressed (as observed in (86)) and therefore, reduction of Hg might proceed via

equation 2-3 followed by complexation of Hg(I) with Cl^- to form calomel (equation 2-5) and subsequent reduction of calomel (equation 2-6).

$$2Hg(I) + 2Cl^- = Hg_2Cl_2 \quad (2\text{-}5)$$

$$Hg_2Cl_2 + 2e^- = 2Hg(0) + 2Cl^- \quad (2\text{-}6)$$

If the Hg is stabilized as Hg_2Cl_2, the lower redox potential of 0.27 V may then result in slower reduction to Hg(0). Observations that chloride can change the sorption mode of Hg onto goethite from a bidentate corner-sharing arrangement to a Type A ternary surface complex bonded monodentate with chloride may also provide some insight into the mechanism by which Cl^- stabilizes Hg(I) on iron oxide solids (91). In both cases (chloride and chloride-free) though, we speculate that the accumulation of Hg_2Cl_2 or Hg(0)(*l*) in the solid phase might slow the rate of Hg(II) reduction by blocking access to surface sites.

Effect of Magnetite Stoichiometry on Hg(II) Reduction

Both the limited number of samples characterized by synchrotron x-ray spectroscopy as well as the uncertainty in the Hg mass balance does not allow for rigorous quantification of rates of Hg(II) reduction. We can, however, evaluate the relative trends of solid phase Hg(II) reduction by magnetites with varying stoichiometry by comparing the relative fraction of Hg(II), Hg(I) and Hg(0) on the solids. As we noted earlier, in the absence of chloride, solid phase Hg(II) was completely reduced to Hg(0) within three days by both the near-stoichiometric magnetite with $x_{MS} = 0.50$ and partially oxidized magnetite with $x_{MS} = 0.38$ allowing us to estimate a minimum change in the fraction of solids Hg reduced to Hg(0) over time ($\Delta f / \Delta t$) of ≥ 0.33 d^{-1}. For the more oxidized magnetite, 80% of the Hg on the surface was reduced to Hg(0) within 3 days with complete reduction to Hg(0) observed after 15 days giving a $\Delta f / \Delta t$ of 0.067 d^{-1}.

When chloride was present, reduction of Hg(II) to Hg(0) by more stoichiometric ($x \geq 0.42$) magnetite still occurred within three days, however, reactors containing more oxidized magnetite ($x \leq 0.38$) contained a mixture of Hg(I) and Hg(0) after three days (Figure 2.4b).

To determine if surface-bound Hg(I) would continue to be reduced by the more oxidized magnetites, we collected XANES spectra at longer reaction times of 15 and 120 days (Figure 2.11 and Figure 2.12). A progression of decreasing Hg(I) and increasing Hg(0) over time can be seen in the XANES spectra, with no indication of Hg(II) at any time point. Examining the fraction of Hg(I) and Hg(0) over the 3 to 120 day time period, the decrease in Hg(I) is clearly coupled with a corresponding increase in Hg(0) on the surface of the oxidized magnetite (Table 2.1). Based on the change in fraction of Hg(0) from $t = 3$ days to $t = 120$ days, we estimate a $\Delta f / \Delta t$ of 0.0047 d^{-1} for $x_{MS} = 0.38$ magnetite, and 0.0026 d^{-1} for $x_{MS} = 0.29$ magnetite.

In the absence of chloride, the relative fraction of Hg reduced over time spans at least one order of magnitude (from $\Delta f / \Delta t > 0.33$ d^{-1} to 0.067 d^{-1}) when varying the magnetite Fe(II) content from near-stoichiometric (0.50) to oxidized (0.29). In the presence of chloride, however, the span is much larger, covering over 3 orders of magnitude, from $\Delta f / \Delta t = 0.0026$ (d^{-1}) for $x_{MS} = 0.29$ to $\Delta f / \Delta t > 0.33$ (d^{-1}) for $x = 0.42$ and higher (Table 2.1). This finding is consistent with previous work showing higher reaction rates for magnetite with greater Fe(II) content, as well as the possibility for reduction rates to vary over multiple orders of magnitude (19). Note that Wiatrowski et al. (70) saw decreased rates of Hg(II) reduction by stoichiometric magnetite as chloride levels increased, while we saw complete reduction of solids Hg occur within 3 days whether chloride was present or not. It is difficult to directly compare the two studies though as their reactor design, analytical approach (Hg loss from aqueous compared to our XAS solids analysis) and time scale (~16 minutes compared to days for our work) differed significantly from ours.

Our results clearly indicate that Fe(II) content (i.e., magnetite stoichiometry) has a significant effect on the reduction of Hg(II) similar to what we observed for both nitrobenzene (19, 74) and uranium (75). The influence of Fe(II) content on magnetite's reactivity will impact its ability to reduce contaminants in both natural environments (e.g., groundwater aquifers (92-94)) and water treatment technologies based on magnetite (e.g., 95, 96), which have become highly desirable due to the fact that even nanoscale particles can be efficiently removed or separated from solution magnetically (97). Methods for maintaining the reducing capacity of magnetite will be critical to the development of efficient and sustainable engineered and bio-engineered systems. Recent work has shown that Pd-functionalization of biomagnetite can enhance and maintain Cr(VI) reduction under varying environmental conditions, providing much better contaminant removal performance than unamended biomagnetite (96). Promotion of Fe reducing conditions may allow for similar performance enhancements by providing an ongoing supply of reduced Fe(II) to "recharge" the magnetite. We also suspect that Fe(II) content may play a role in heterogeneous Fe(II)-mediated Fenton-like reactions resulting in oxidation of contaminants, such as arsenic, under oxic conditions (e.g., 98).

Magnetite is an abundant Fe mineral in the subsurface, however, it is likely that there exists a wide range in stoichiometry based on the prevailing redox conditions. While stoichiometric magnetite appears to be an effective reductant for many contaminants, the presence of partially oxidized magnetite under oxic conditions may make its role less significant than laboratory studies indicate. Furthermore, environmental constituents, such as chloride (70, this study) or bacterial cell surfaces (71) may also slow or inhibit Hg reduction in natural environments. Previous work has shown, however, that oxidized magnetite can be reduced or recharged by aqueous Fe(II), resulting in more stoichiometric magnetite (19, 75). This opens the possibility for magnetite to serve as a reductant for Hg and other groundwater contaminants that can also be regenerated when Fe(II) is present in the aquifer, as magnetite is a common

product of sediment iron reduction by dissimilatory-iron reducing bacteria (DIRB) (e.g., 99). Magnetite has also been implicated in the transfer of electrons between diverse microbial species in sediments, a process that relies on mineral conductivity which also varies with Fe(II) content (100). Changes in magnetite Fe(II) content due to fluctuating redox conditions may have significant implications for the interaction and cooperation between subsurface microbial species.

Supporting Information

Calculation of Magnetite Stoichiometry

To calculate the change in magnetite stoichiometry based on reduction of 0.9 mM Hg(II), we use the formulas derived in our previous work to calculate the Fe(II) and Fe(III) content of the magnetite from the Fe(II)/Fe(III) ratio x (19). For 1.5 g/L stoichiometric magnetite:

$$1.5\,\frac{g}{L}Fe_3O_4 \times \frac{mol}{231.54g} \times \frac{3Fe}{mol\ Fe_3O_4} = 19.44\ mM\ Fe \qquad (2\text{-}7)$$

The magnetite used has a stoichiometry from Mossbauer of $x_{MS} = 0.50$, which corresponds to 6.48 mM Fe(II) and 12.96 mM Fe(III). Control experiments with magnetite suspended in DI water for 3 days resulted in $x_{MS} = 0.49$, which corresponds to the dissolution or oxidation of 0.09 mM Fe(II). For purposes of calculation, we assume based on our XANES results that the reaction with 0.9 mM Hg(II) results in complete reduction of all Hg in the reactor.

$$Hg(II) + 2e^- \rightarrow Hg(0) \qquad (2\text{-}8)$$

$$Fe(III)_{mag} + e^- \rightarrow Fe(II)_{mag} \qquad (2\text{-}9)$$

Since reduction of Hg(II) to Hg(0) requires two electrons, a concentration of 0.9 mM Hg(II) corresponds to 1.8 meq / L. The expected final stoichiometry is

$$x = \frac{Fe(II)}{Fe(III)} = \frac{6.48 - 1.80\ meq/L}{12.96 + 1.80\ meq/L} = 0.32 \qquad (2\text{-}10)$$

Mössbauer fitting of samples reacted with 0.9 mM $HgSO_4$ resulted in x_{MS}= 0.32, which matches our predicted value exactly. Since XANES only analyzes the speciation of solids associated Hg, we can also calculate the expected stoichiometry if only that fraction of the initial Hg was reduced. Solids associated Hg ranged from 35-73% of initial Hg, which corresponds to the transfer of 0.70-1.46 mM of e^- equivalents (respectively) to Hg from Fe(II), in addition to the Fe(II) lost or oxidized in controls. The predicted range of *x* is then:

$$\frac{Fe(II)}{Fe(III)} = \frac{6.48 - 0.70\ meq/L}{12.96 + 0.70\ meq/L} = 0.42 \text{ to } \frac{6.48 - 1.46\ meq/L}{12.96 + 1.46\ meq/L} = 0.35 \qquad (2\text{-}11)$$

Table 2.1. Speciation of solid phase Hg products from the reduction of Hg(II) by magnetite with varying stoichiometry.

Without chloride			*With chloride*		
	t = 3 d	t = 15 d	t = 3 d	t = 15 d	t = 120 d
$x = 0$[a]					
Hg(II) Hg(I) Hg(0)	100%[b] ND[c] ND	n/a[d]	100% ND ND	n/a	n/a
x = 0.29					
Hg(II) Hg(I) Hg(0)	20% ND 80%	ND ND 100%	ND 70% 30%	ND 60% 40%	ND 40% 60%
x = 0.38					
Hg(II) Hg(I) Hg(0)	ND ND 100%	n/a	ND 55% 45%	ND 45% 55%	ND ND 100%
x = 0.50					
Hg(II) Hg(I) Hg(0)	ND ND 100%	n/a	ND ND 100%[e]	n/a	n/a

[a] x = Fe(II)/Fe(III) measured by Mössbauer spectroscopy

[b] % determined by linear combination fitting of Hg-L_{III} edge XANES

[c] ND = non-detect

[d] n/a = not available (not measured)

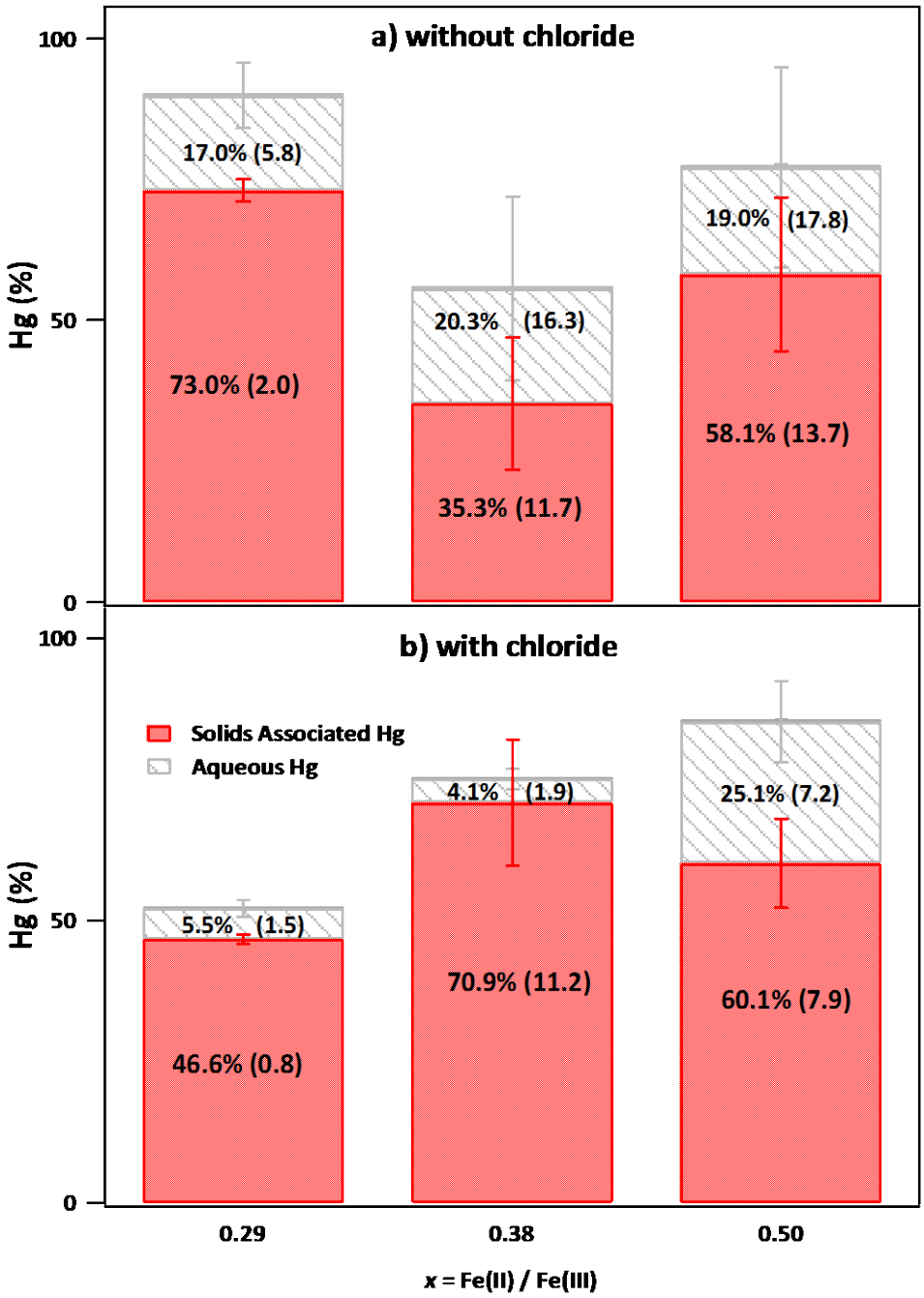

Figure 2.1. Partitioning of 0.9 mM (initial) Hg between the aqueous, solid, and gas phases in sealed magnetite reactors (pH 7.2, unbuffered) after 3 days. (a) shows the system with chloride absent, and (b) shows the system with chloride present. Volatile Hg was less than 1% in all reactors and is not shown. Graph bar labels represent average and one standard deviation [X% (1 S.D.)] of triplicate reactors.

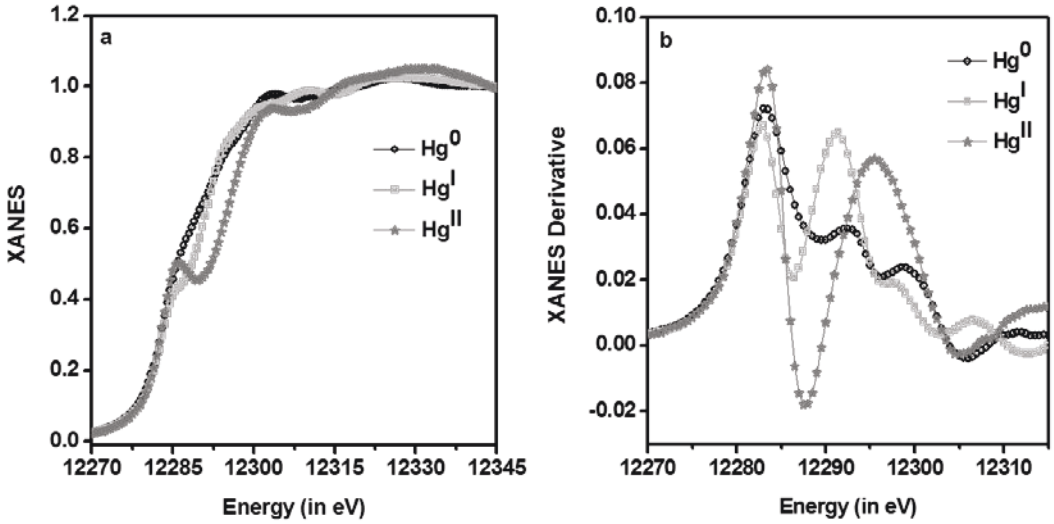

Figure 2.2. XANES spectra of Hg(0), Hg(I), and Hg(II) standards. a) Hg L_{III} edge XANES spectra and b) Hg L_{III} edge XANES first derivative spectra. All spectra were measured at -180˚C.

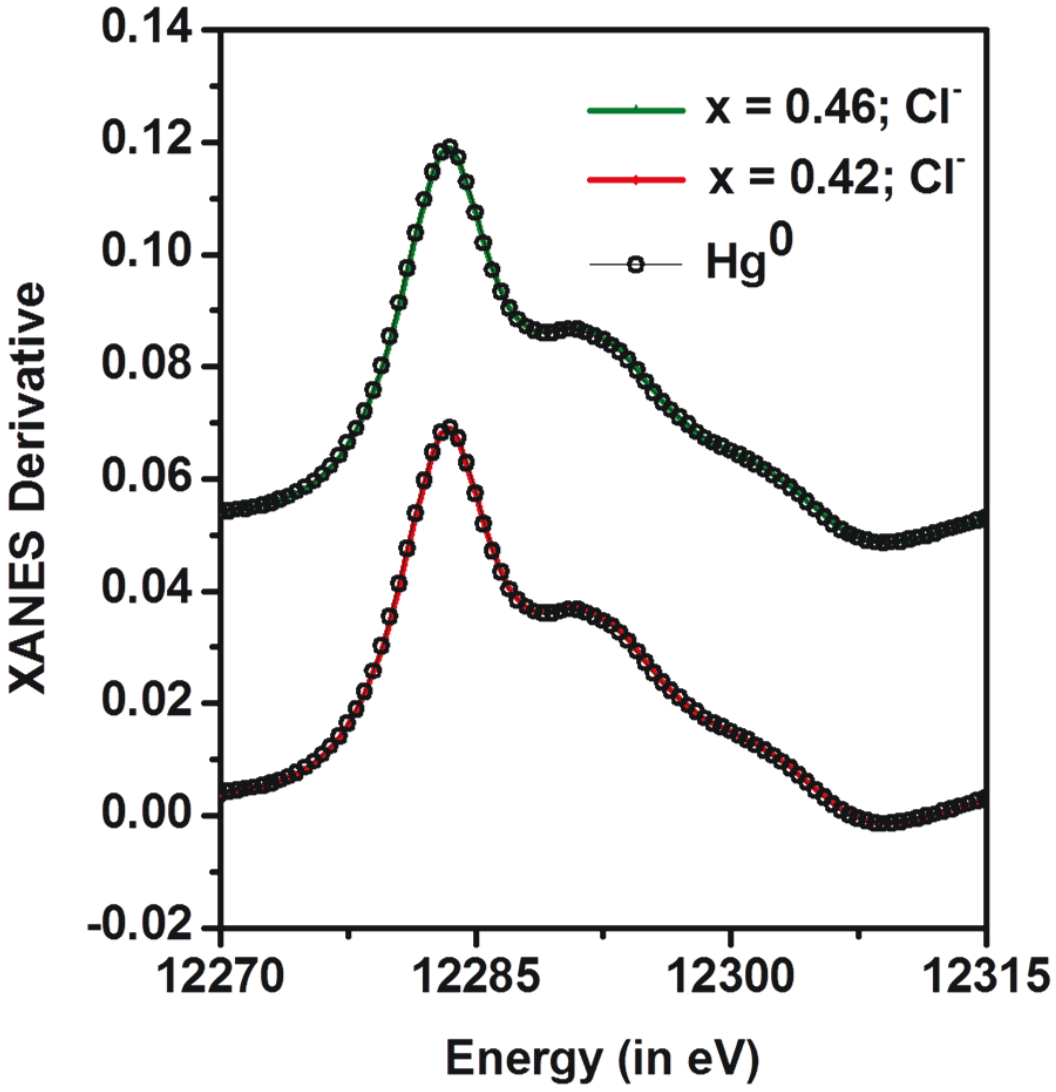

Figure 2.3. Room temperature Hg L_{III}-edge XANES derivative spectra for 0.9 mM Hg(II) reacted with $x = 0.46$ and $x = 0.42$ magnetite for 3 days in presence of 1.8 mM chloride, with Hg(0) standard XANES spectra for comparison.

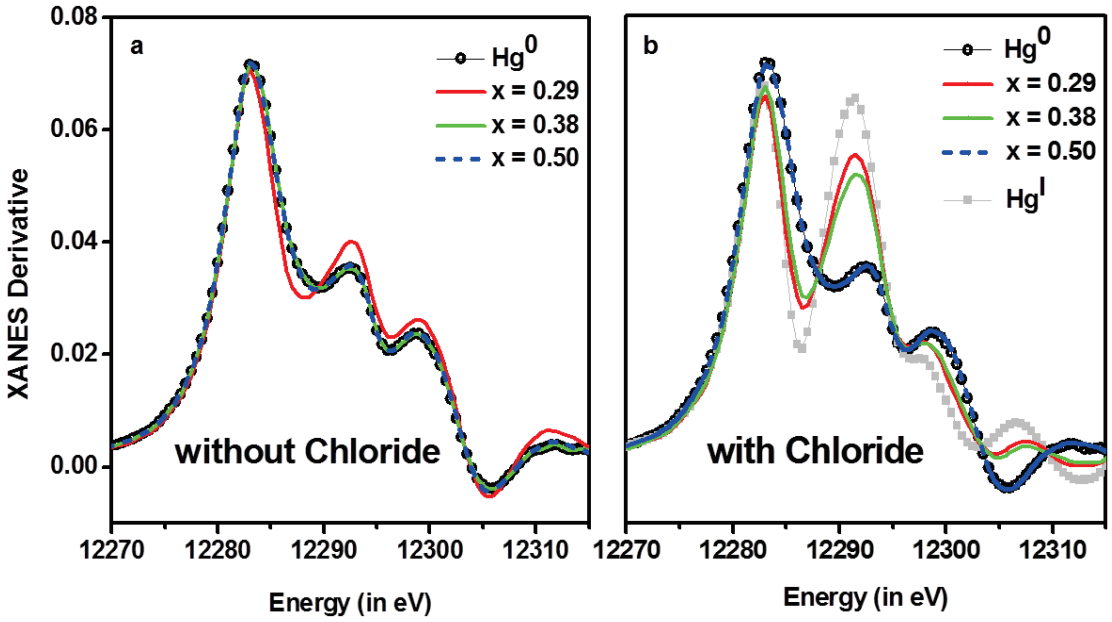

Figure 2.4. Hg L_{III} edge XANES first derivative spectra of standards and Hg(II) (0.9 mM) reacted for three days with stoichiometric (x_{MS} = 0.50) and partially oxidized (x_{MS} = 0.38, 0.29) magnetite at pH 7.2. (a) Hg(II) reacted in the absence of chloride and (b) Hg(II) reacted in the presence of chloride. Stoichiometric magnetite data (blue dash) overlapped with reduced Hg(0) (open symbol black) in both cases. Spectra were measured at -180°C.

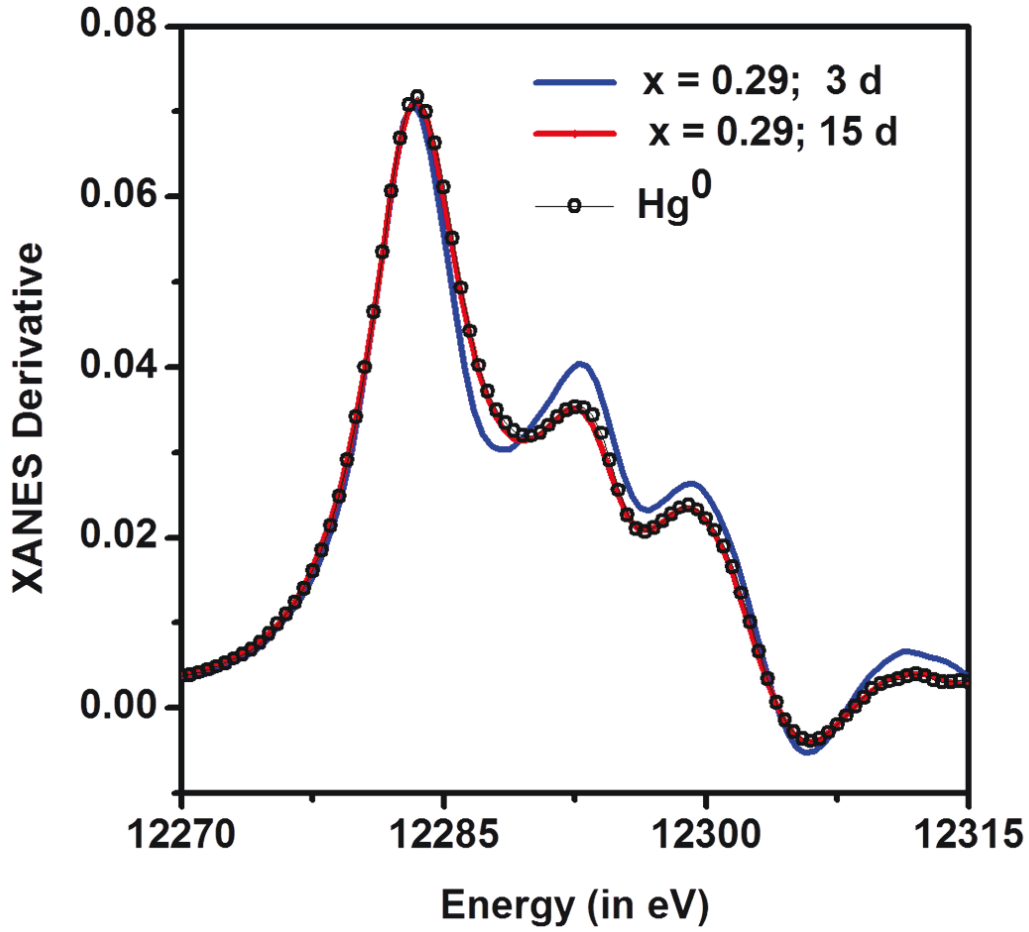

Figure 2.5. Hg L_{III}-edge XANES derivative data for 0.9 mM Hg(II) reacted with $x = 0.29$ magnetite for 3 and 15 days, compared to the Hg(0) standard spectrum. Spectra were collected at -180 °C.

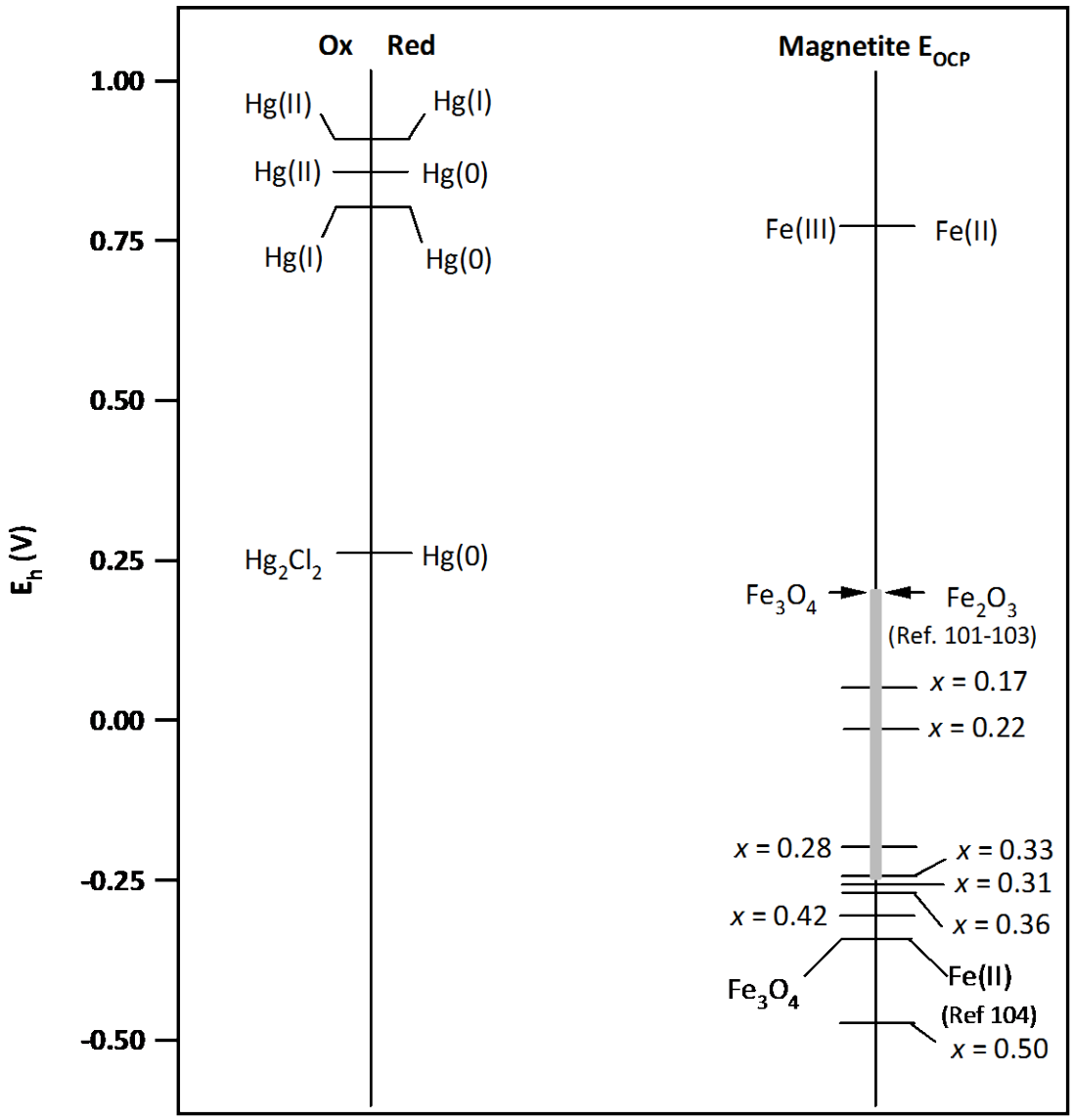

Figure 2.6. Redox ladder comparing standard reduction potentials (E_h^0) for pertinent Hg redox couples derived from thermodynamic data with measured open-circuit potential (E_{OCP}) of magnetite with varying stoichiometry (x) (74). E_h values for magnetite are reported from (101-104).

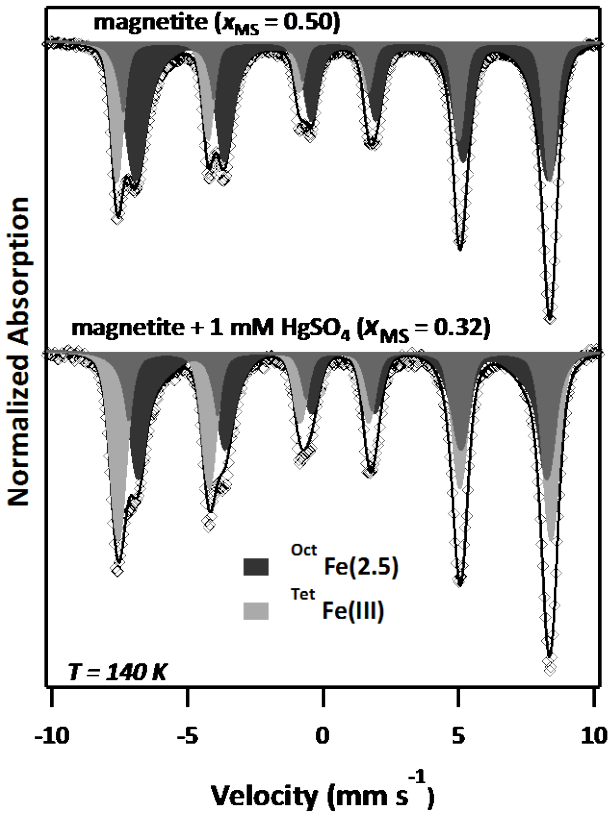

Figure 2.7. ^{57}Fe Mössbauer spectra of magnetite reacted with Hg(II) measured at 140 K. (Top) stoichiometric magnetite (x_{MS} = 0.50) and (bottom) stoichiometric magnetite reacted with 0.9 mM Hg(II) for three days in the absence of chloride. The change in stoichiometry from x_{MS} = 0.50 to 0.32 indicates oxidation of Fe(II) in the magnetite corresponding with reduction of Hg(II) in solution.

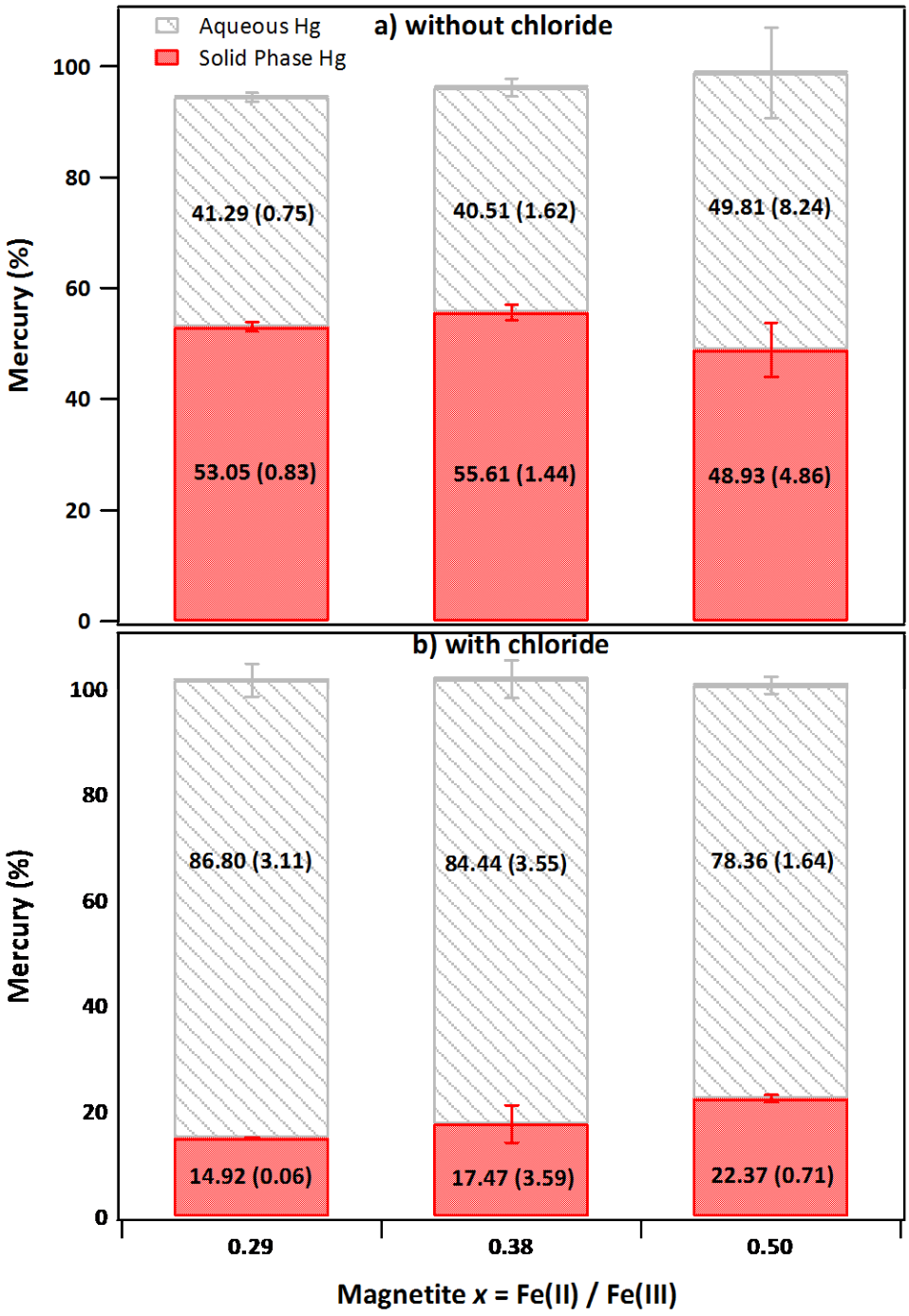

Figure 2.8. Partitioning of Hg between the aqueous, solid, and gas phases in constantly purged magnetite reactors after 1 hour. a) shows the system with chloride absent, while b) shows the system with chloride present. In all reactors, volatile Hg was less than 1% of total Hg, and is not shown.

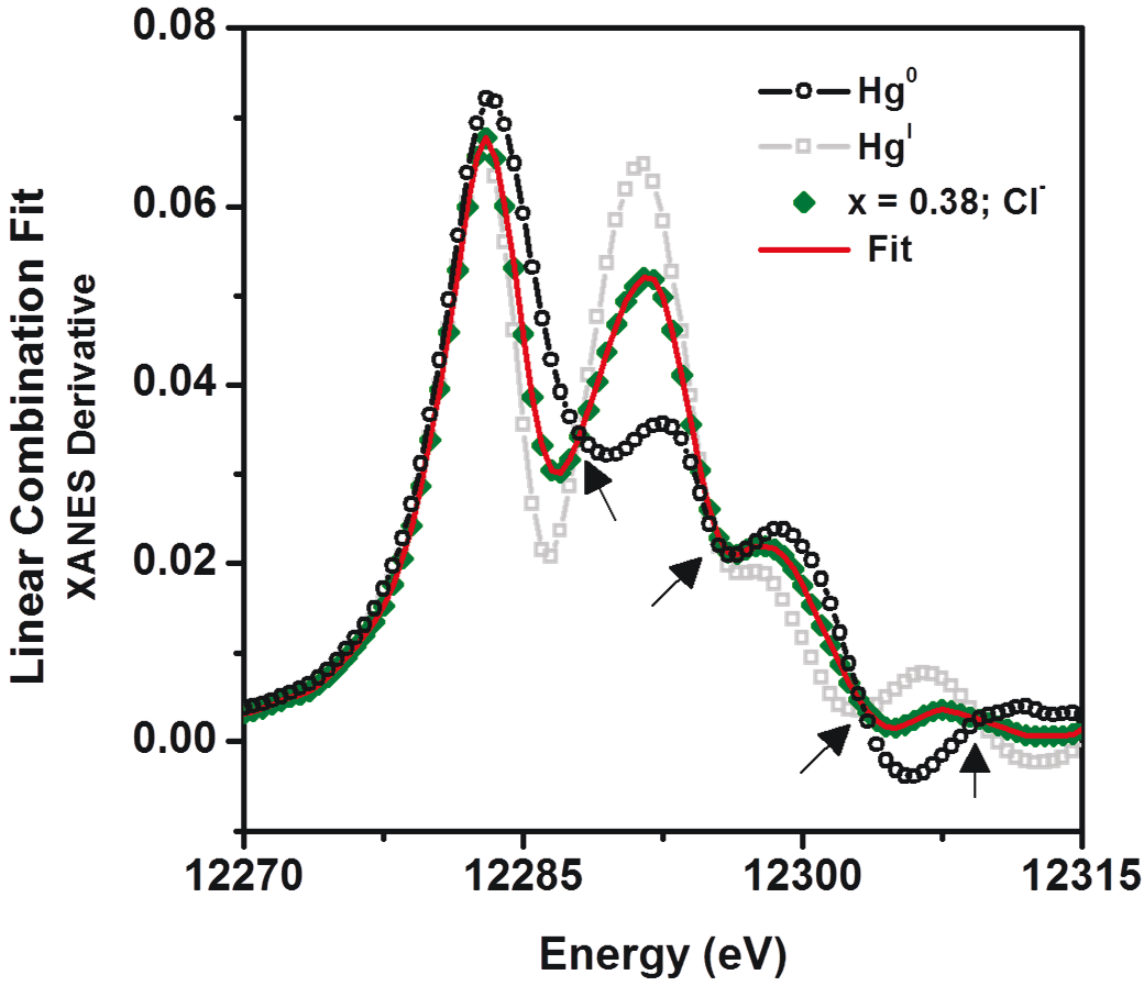

Figure 2.9. Hg L_{III} edge XANES derivative linear combination fit of partially oxidized (x_{MS} = 0.38) magnetite solids after 3 days reaction with 0.9 mM Hg(II) in the presence of chloride compared to data from the Hg(0) and Hg(I) standards. Isobestic points (noted by arrow heads) clearly indicate that the data is composed of Hg(I) (Hg_2Cl_2) and Hg(0) with zero contribution from Hg(II). Spectra were collected at -180°C.

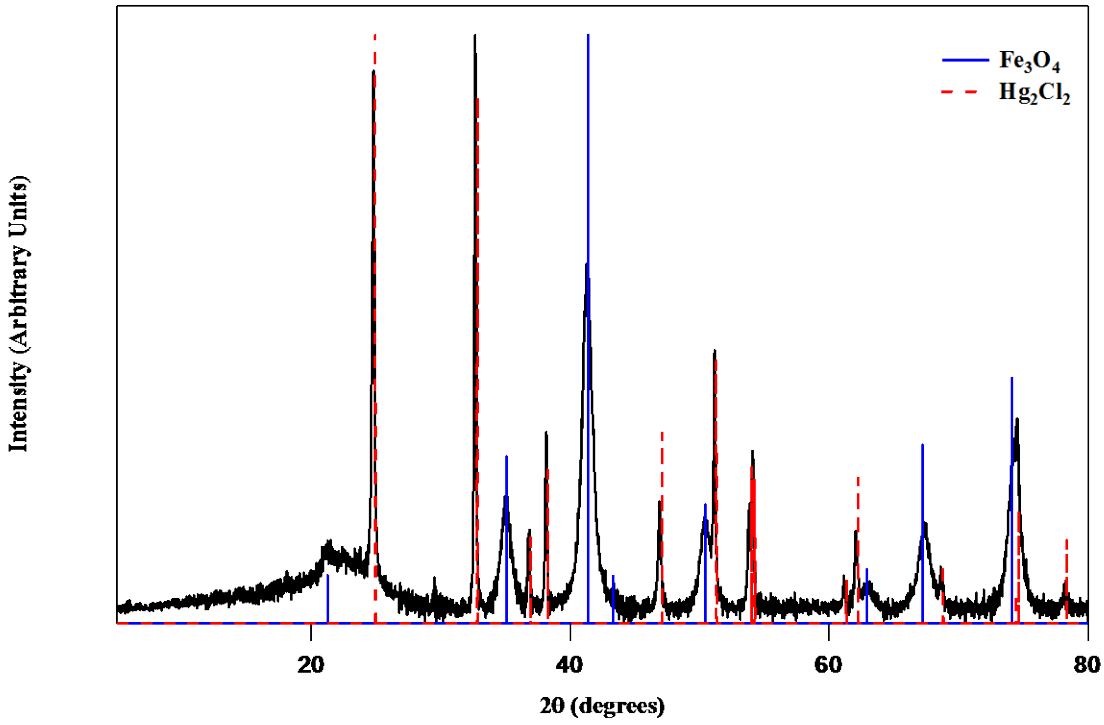

Figure 2.10. X-ray diffraction pattern for solids from reactors containing 0.9 mM $HgCl_2$ and 1.5 g/L magnetite ($x_{MS} = 0.29$). Peak locations for magnetite (solid blue lines) and calomel (dashed red lines) are overlaid on the sample spectrum.

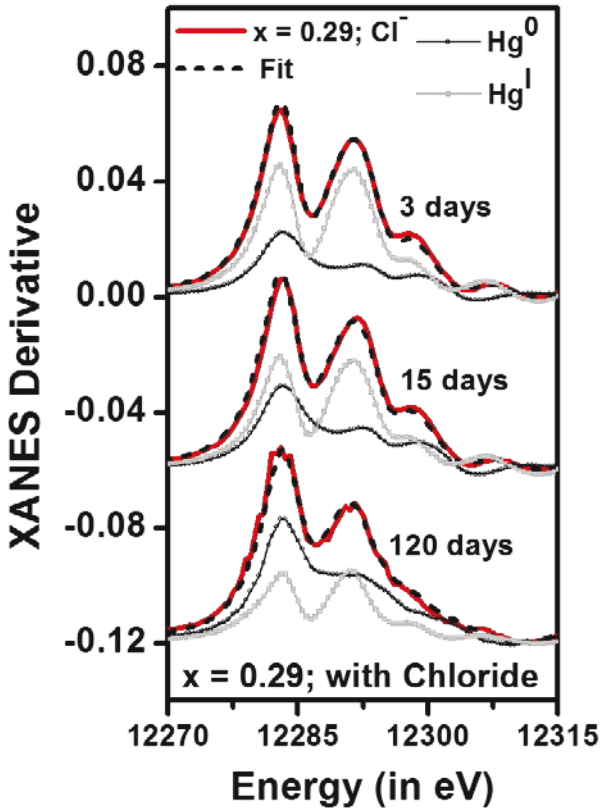

Figure 2.11. A time-series of Hg L_{III} edge XANES first derivative data and linear combination fits for partially oxidized $x_{MS} = 0.29$ magnetite reacted with Hg(II) in the presence of chloride. The dashed lines represent the linear combination fit to the data, with the weighted fit components for Hg(0) and Hg(I) plotted below each fit with symbols. The contribution of the Hg(I) fit component is gradually reduced with reaction time, from 70% after 3 days, to 60% after 15 days, and to 40% contribution after 120 days. Data for the standards and samples after 120 days reaction time were collected at room temperature, all other data were collected at -180 °C.

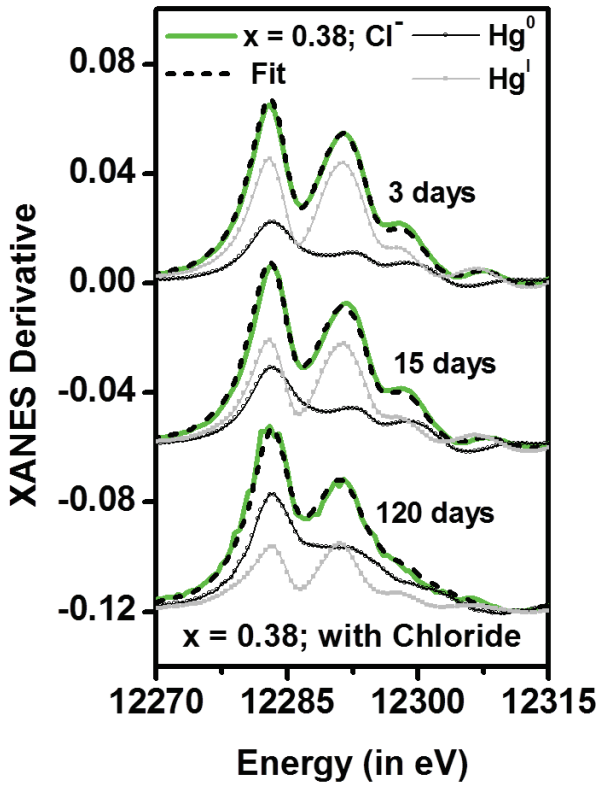

Figure 2.12. A time-series of Hg-L_{III} edge XANES first derivative data and linear combination fits for partially oxidized $x_{MS} = 0.38$ magnetite reacted with Hg(II) in the presence of chloride. The dashed lines represent the linear combination fit to the data, with the weighted fit components for Hg(0) and Hg(I) plotted below each fit with symbols. The contribution of the Hg(I) fit component is gradually reduced with reaction time, from 55% after 3 days, to 45% after 15 days, to no contribution after 120 days. Data for the standards and samples after 120 days reaction time were collected at room temperature, all other data were collected at -180 °C.

CHAPTER 3: EFFECT OF CARBON ON FE(II)-CATALYZED RECRYSTALLIZATION OF GOETHITE AND MAGNETITE

Abstract

Organic carbon exists throughout the subsurface environment in a variety of forms. Aqueous Fe(II) has been shown to induce interfacial electron transfer, Fe atom exchange, and recrystallization of otherwise stable Fe oxides. We observed rapid Fe(II)-catalyzed Fe oxide recrystallization of magnetite and goethite in the presence of electron shuttles, natural organic matter, and certain high molecular weight polysaccharides. In the presence of xanthan gum (goethite) and spent medium from dissimilatory iron reducing bacteria cultures (both goethite and magnetite), Fe(II)-catalyzed recrystallization was inhibited to a small extent, but still occurred rapidly. Only sorption of a long-chain phospholipid, which largely shuts down Fe(II)-Fe(III) electron transfer, substantially inhibited Fe atom exchange and Fe(II)-catalyzed recrystallization of goethite and magnetite, though limited exchange was still observed. Our findings identify Fe(II)-catalyzed Fe oxide recrystallization as a robust process that is likely to occur throughout a variety of organic carbon-rich biogeochemical environments.

Introduction

Reactions at mineral interfaces have been studied for many decades due their ability to influence contaminant transport and transformation, nutrient cycling, local environment redox state, and many other geologic processes. Aqueous Fe(II) readily associates with various environmental surfaces, including metal oxides, silicate and clay minerals, and bacterial cell membranes; and the uptake process tends to be dependent on surface properties, solution chemistry, and adsorbate properties (11). Recent studies involving aqueous Fe(II) and a variety of Fe minerals have demonstrated this association to be significantly more complex than simple sorption of a cation to a static mineral surface, instead encompassing numerous steps ultimately leading to isotopic mixing

between aqueous and solid phases. Substantial isotopic mixing has been observed in goethite, magnetite, ferrihydrite, and lepidocrocite upon exposure to aqueous Fe(II), although the exact mechanism for this extensive Fe atom turnover is still unclear (21, 22, 24).

Recrystallization of Fe oxides in the presence of Fe(II) can be readily observed by the transformation of unstable minerals to more stable mineral forms (e.g., ferrihydrite transforming to goethite, lepidocrocite transforming to magnetite), a process thought to occur via reductive dissolution and reprecipitation (14, 21, 105). In the case of more stable oxides, however, no visible changes to mineral phase or morphology occur despite substantial (and sometimes even complete) recrystallization following exposure to Fe(II) (22, 24). A number of potential mechanisms have been proposed to explain how extensive isotope mixing can occur without apparent changes to the oxide including (i) bulk conduction, (ii) solid-state diffusion, and (iii) pore diffusion (29). In the case of goethite, a mechanism linking mineral growth and dissolution at spatially separated sites by bulk conduction has been proposed as solid state diffusion rates are far too slow to explain the extent of atom exchange observed experimentally (22). For magnetite however, diffusion rate estimates vary widely in the literature, spanning some seventeen orders of magnitude. Even conservatively selected diffusion rates result in a calculated time of 4-19 days to reach the 55% exchange observed in one study indicating that solid state diffusion was also a viable mechanism in addition to bulk conduction for rapid Fe atom exchange in magnetite (24). In the absence of direct evidence for any of the three proposed mechanisms, it is difficult to conclusively determine whether one (or multiple) mechanisms are contributing to Fe oxide recrystallization.

While the body of literature regarding Fe(II)-catalyzed recrystallization of Fe oxides is growing, the majority of studies have been performed in simple solutions lacking many constituents likely to be present in subsurface environments. Fe oxides can act as sorbents for a variety of ligands in the environment including carbonate (106),

phosphate (107), silicates (108), and natural organic matter (ranging from low molecular mass acids (109) to high-molecular mass polysaccharides (110, 111) and humic substances (e.g., 112, 113). Fulvic acid and silica have been shown to inhibit Fe(II)-catalyzed release of ^{55}Fe from labeled ferrihydrite and lepidocrocite (114), whereas phosphate had little effect on isotopic exchange between Fe(II) and goethite (115).

While there is little data available on how organic carbon affects Fe(II)-catalyzed Fe oxide recrystallization, there is a significant body of work looking at how various forms of organic matter including humic acids (HA), fulvic acids (FA) and extracellular polysaccharides (EPS) affect Fe oxide dissolution. These observations, however, have often been conflicting. For example, EPS from *Shewanella putrefaciens* CN32 has been shown to slow reduction of lepidocrocite by *S. putrefaciens* CN32, whereas in similar systems organic matter either slowed bioreduction (L-HA Leonardite Humic Acid, ES-HA Elliott Soil Humic Acid, SR-FA Suwannee River Fulvic Acid, SR-HA Suwannee River Humic Acid) or had no effect (PL-FA Pony Lake Fulvic Acid) relative to unamended systems (116). HA has been shown to alternately inhibit or enhance microbial reduction of ferrihydrite depending on whether it is present solely as a surface sorbed species, or as dissolved HA which can act as an electron shuttling compound (117, 118). Further complicating matters is the fact that electron shuttling compounds not only include the redox active moieties in humic substances, but soluble electron transfer mediators directly generated by microorganisms. The DIRB *Shewanella* has been shown to produce flavin mononucleotide and riboflavin (RBF) both of which enhance the microbial reduction of ferrihydrite and lepidocrocite (119). It is likely in the reducing environments where we expect Fe(II)-catalyzed Fe oxide recrystallization to be relevant, some or all of these organic compounds will be present and associated with Fe oxides.

In this study, we examined the influence of various sorbed and dissolved organic compounds on the Fe(II)-catalyzed recrystallization of magnetite and goethite using an enriched Fe isotope approach. The goal of this work is two-fold; (*i*) to evaluate whether

Fe(II)-catalyzed recrystallization is likely to occur under the complex biogeochemical conditions encountered in natural environments, and (*ii*) to assess the influence of different organic compounds, including complex mixtures from real samples as well as individual reference and model compounds, on the Fe oxide recrystallization process. We chose goethite and magnetite because data already exists regarding the extent and rates of Fe(II)-catalyzed recrystallization in carbon free systems, and there is some indication that Fe atom exchange could occur via different mechanisms.

Experimental Section

Iron Oxide Synthesis

Magnetite was synthesized as previously described in Chapter 2. Goethite nanorods were synthesized as in our previous work (22), by adding 1 L of 0.48 M $NaHCO_3$ dropwise (~4.5 mL/min) to an equal volume of 0.4 M $Fe(NO_3)_3$ while stirring. The resulting suspension was microwaved to boiling, cooled immediately to 20° C in an ice bath, and purified by dialysis for 3 days. Conversion of the ferrihydrite particles to goethite was accomplished by raising the solution pH to 12 with 5 M KOH and heating the suspension to 90° C for 24 hours. Particles were purified by washing three times in deionized water and centrifuging prior to freeze-drying. Dried particles were ground with a mortar and pestle and passed through a 100-mesh sieve. Mössbauer invisible ^{56}Fe enriched goethite microrods were synthesized by dissolving $^{56}Fe(0)$ powder in HCl and deionized water such that the residual HCl concentration was 1 M following reductive dissolution of Fe(0). The resulting $^{56}Fe(II)$ solution was oxidized to Fe(III) with excess H_2O_2, and filtered (0.22 µm nylon). The solution pH was raised by adding 5 M KOH to a final concentration of 0.3 M, after which deionized water was added to bring the final volume to 100 mL. The solution and precipitate were transferred to an oven and aged at 70°C for 60 hours, after which the solids were washed four times by centrifugation and resuspension in deionized water. Solids were freeze dried and sieved as above.

Mössbauer invisible ^{56}Fe magnetite was synthesized from a ^{56}Fe(II) stock solution prepared from ^{56}Fe(0) as above. The stock solution was divided into two portions, and the Fe(III) portion was oxidized with a calculated amount of H_2O_2. The two portions were then re-combined and titrated to an alkaline pH to precipitate the magnetite solids. Solids were removed from solution by filtration, rinsed minimally with deionized water to prevent oxidation, and freeze dried under anoxic conditions. The ^{56}Fe magnetite stoichiometry (x = Fe(II) / Fe(III)) was 0.30±0.02 measured by acidic dissolution.

Sorbed and Dissolved Organic Carbon

To investigate the effect of sorbed and dissolved carbon on Fe(II)-catalyzed Fe oxide recrystallization, we obtained a variety of organic compounds organized in four general classes; (*i*) natural organic matter, (*ii*) electron shuttling compounds, (*iii*) high molecular weight polysaccharides, and (*iv*) extracellular exudates in spent medium from cultures of *S. oneidensis* (Table 3.1). Model natural organic matter (NOM) samples included soil organic carbon from the Critical Zone Observatory (CZO) site in Bisley, Puerto Rico, commercially produced humic acid (SA-HA, Sigma-Aldrich), as well as the environmentally isolated organic matter fractions Elliott Soil Humic Acid Standard (ES-HA) (International Humic Substances Society, IHSS), and Suwannee River Fulvic Acid Standard (SR-FA) (IHSS). We attempted to span a wide range of organic matter samples, including environmentally isolated and commercially produced humic acid, as well as samples with varying levels of aromaticity and functional group abundance (Table 3.2). Electron shuttling compounds included riboflavin (RBF, Acros Organics), which is secreted by species of the DIRB *Shewanella;* and 9,10-anthraquinone-2,6-disulfonic acid (AQDS, Sigma-Aldrich) which is commonly employed as a model for quinone moieties in humic substances (HS) (120). Model extracellular polysaccharides included alginic acid (AA, Sigma-Aldrich), a model for alginates exuded by *Pseudomonas* or *Azobacter* strains of bacteria (121); polygalacturonic acid (PGA,

Sigma-Aldrich), a model compound for the gelatinous mucilage covering the root apices of numerous plant species (122); and xanthan gum (XG, Sigma-Aldrich) from the bacterial strain *Xanthomonas campestris*. A phospholipid (1,2-dioleoyl-sn-glycero-3-phosphate or DOPA, Avanti Polar Lipids) was also used to simulate cell materials / biomass. Two types of spent media from *Shewanella oneidensis* MR-1, Luria-Bertani medium (LB) and defined *Shewanella* medium (DSM) were also used as a source of cellular exudates (Table 3.3).

Organic matter stock solutions were prepared by dissolving humic or fulvic solids in deionized water, mixing for one hour on a shaker table, and filtering the solution through an 0.22 μm nylon filter. Electron shuttle stock solutions were prepared by dissolution in deoxygenated, deionized water. Polysaccharide (500 mg / L) solids were added directly to reactors because homogeneous stock solutions could not be prepared. Soil extract was prepared from a sample of Luquillo, Puerto Rico CZO soil via room temperature extraction (four hours) in ultrapure water, followed by centrifugation and filtration (0.45 μm). Spent medium from cultures of *Shewanella oneidensis* MR-1 were prepared by centrifugation (defined mineral medium) or filter sterilization (0.22 μm) (LB medium) and ten-fold dilution in buffer solution. The phospholipid was prepared by suspension in buffer solution followed by sonication (2 hours).

Fe(II)-Fe(III) Electron Transfer in the Presence of Organic Carbon

We probed the effect of sorbed organic carbon on electron transfer between aqueous Fe(II) and Fe(III) in goethite and magnetite. Iron oxide solids synthesized from Mössbauer invisible ^{56}Fe (2 g/L) were allowed to equilibrate with the target organic compound in 10 mL of buffer solution (25 mM HEPES / KBr, pH 7.5) for 24 hours prior to addition of ^{57}Fe labeled Fe(II). For experiments with DOPA, the Fe oxide solids were

sonicated for 2 hours in buffer solution containing DOPA prior to adding ^{57}Fe(II). After 24 hours exposure to Fe(II), solids were collected on an 0.45 μm filter and analyzed by Mössbauer spectroscopy. Experimental conditions for electron transfer experiments are listed in Table 3.4.

Transmission Mössbauer spectroscopy was performed using a variable temperature helium cooled system with a 1024 channel detector. The ^{57}Co source (~50 mCi) was embedded in a Rh matrix and maintained at room temperature. Center shifts are reported relative to α-Fe foil at room temperature. Samples were prepared under anoxic conditions and sealed between two pieces of 5 mil Kapton Tape to prevent oxidation during sample transport and mounting.

Fitting of Mössbauer spectra was done with Recoil Software (University of Ottawa, Ottawa, Canada). Unless otherwise noted, Voigt-based fitting was used to model goethite spectra and extended-Voigt based fitting was used to model magnetite spectra.

Fe(II)-Catalyzed Recrystallization of Goethite and Magnetite in the Presence of Organic Carbon

To investigate the effect of sorbed and dissolved organic carbon on Fe(II)-catalyzed Fe oxide recrystallization in magnetite and goethite, we performed isotope exchange experiments using an isotopically enriched ^{57}Fe(II) tracer similar to those described in (115). Fe oxide solids were pre-equilibrated in buffer solution with organic carbon compounds and allowed to rotate for at least one hour before addition of the ^{57}Fe(II) tracer. For the experiments with DOPA, the phospholipid and iron solids were equilibrated by sonication for 2 hours prior to addition of the isotopically labeled iron tracer. Detailed experimental conditions are summarized in Table 3.5. Experiments involving goethite were performed in polypropylene centrifuge tubes sealed with Teflon tape, while those involving magnetite were performed in glass serum vials crimp sealed with Teflon coated butyl rubber septa. Reactors were covered in aluminum foil to

exclude light, and allowed to rotate end over end for periods up to 62 days. Following reaction, the aqueous and solid phases were separated by centrifugation at 8,500 rpm for 15 minutes (goethite) or magnetic field (magnetite). Residual solids were dissolved in 3 mL concentrated trace-metals grade HCl, and diluted to a final volume of 6 mL with deoxygenated, deionized water. Aqueous and residual solids samples were filtered (0.22 μm) and analyzed for Fe(II) and total iron colorimetrically with 1,10-phenanthroline using fluoride to mask Fe(III) as described in (80).

Fe isotope measurements were made using inductively coupled plasma - mass spectrometry (ICP-MS) with a Thermo Fisher Scientific X-series II Quadrupole ICP-MS. Aqueous and residual solids samples for isotope analysis were diluted to an approximate Fe concentration of 1 μM to maximize count rates while remaining on pulse count detector mode. All dilutions were performed in 2% trace metals grade HNO_3 to preserve the samples, and Fe isotopes were measured in collision cell mode, with 7% H_2 / 93% N_2 collision cell gas operating at a flow rate of approximately 4 mL / min. Variability in instrument sensitivity was monitored using an internal standard (10 ppb ^{59}Co). Results of isotope measurements are presented as isotope fractions, which are calculated as shown in equation 3-1.

$$f^{i}\mathrm{Fe} = \frac{^{i}counts}{^{54}counts + ^{56}counts + ^{57}counts + ^{58}counts} \quad (3\text{-}1)$$

Results and Discussion

Fe(II)-Fe(III) Electron Transfer in the Presence of Dissolved and Sorbed Carbon

Similar to our previous work (19, 115), we used isotopically labeled $^{57}Fe(II)$ and microgoethite or magnetite synthesized from ^{56}Fe to determine whether interfacial electron transfer occurs between aqueous Fe(II) and iron oxides in the presence of sorbed organic carbon. We reacted 1 mM aqueous $^{57}Fe(II)$ with Mössbauer invisible ^{56}Fe

microgoethite that was pre-equilibrated with natural organic matter, extracellular polysaccharides, spent DIRB growth medium, and a phospholipid (DOPA).

Since Mössbauer spectroscopy is specific to ^{57}Fe, microgoethite synthesized from ^{56}Fe initially produces a Mössbauer spectrum with no discernible features (Figure 3.1a). By adding aqueous Fe(II) enriched in ^{57}Fe, we are able to probe the oxidation state and local environment of the added ^{57}Fe(II) without any signal contribution from the iron oxide. Following exposure to ^{57}Fe(II), Mössbauer spectra of ^{56}Fe goethite consist of an Fe(III) sextet with overall parameters similar to naturally abundant goethite (Figure 3.1b, Table 3.6). This clearly indicates transfer of electrons from aqueous Fe(II) to the underlying goethite solid, resulting in oxidation of the aqueous Fe(II) to Fe(III) and formation of ^{57}Fe goethite on the solid surface, consistent with our previous work and others (15, 16, 115, 123). In samples where the ^{56}Fe goethite was pre-equilibrated with SR-FA and XG, the resulting spectra look similar to the carbon-free control, indicating that electron transfer continues to occur even when natural organic matter or polysaccharides are associated with the oxide surface (Figure 3.2b, c). Figures 3.3 and 3.4 show scanning electron microscope images of goethite and magnetite respectively, following equilibration with organic carbon. There is clear aggregation of the iron oxide nanoparticles resulting in the formation of larger particles, though the actual degree of oxide surface coverage by organic carbon is difficult to assess. The Mössbauer spectra collected from ^{56}Fe goethite equilibrated with spent DIRB medium (LB medium and DSM), however, look very different from the spectra discussed so far (Figure 3.2 d,e). While they clearly contain a sextet with goethite-like characteristics, there is significant contribution in the low-velocity range from additional spectral features. In control experiments where ^{56}Fe microgoethite was exposed to LB and DSM media without any Fe(II) present, the resultant Mössbauer spectra did not contain any peaks or visible features, ruling out the possibility that these low-velocity features are a result of some growth medium component.

The fitting results for our 77 K Mössbauer spectra are shown in Table 3.6. For the control experiment where ^{57}Fe(II) was reacted with ^{56}Fe goethite, the spectrum consists of an asymmetrical sextet and a broad collapsed feature which is only partially ordered. The sextet can be modeled as two sextets with center shift (CS) values of 0.49 and 0.48 mm/s, quadrupole splitting (QS) values of -0.12 and -0.11 mm/s, and hyperfine fields of 48.6 and 49.6 T respectively (Table 3.6b-1). Due to the extreme similarity in CS and QS values for sextet 1 and 2, the spectrum was also modeled with a single, two-component sextet, but this resulted in a slightly worse goodness of fit (χ^2, 69.5 for 1 sextet vs. 67.3 for 2 sextets) (Table 3.6b-2). While the CS values are very similar to the 0.47 mm/s typical of goethite, the QS values are significantly lower than the -0.24 mm/s usually observed. Previous work in our group under similar conditions also observed deviation in QS values relative to pure goethite (-0.24 mm/s), although they saw a lower QS for sextet 1 and higher QS for sextet 2 (-0.34 and 0.16 mm/s respectively), whereas we saw higher QS for both sextet 1 and 2 (-0.12 and -0.11 mm/s respectively) (115). Unlike their work, adding an Fe(II) doublet did not significantly improve the fit, despite similar Fe(II) and solids loading. We did find that our fits improved significantly by including a broad, magnetically collapsed sextet, which is consistent with previous findings. This collapsed feature represents approximately 10% of the sample area, but cannot be attributed to a specific iron oxide due to its broad hyperfine field distribution, and lack of discernible features resulting from its partial magnetic ordering. Work by collaborators examining Fe atom exchange in real soil has shown that in the presence of live DIRB, the pool of labile surface Fe that can be extracted with 0.5 M HCl appears to be preferentially re-solubilized relative to more crystalline Fe oxides, acting as a sort of exchange buffer between the aqueous and 7 M HCl extractable Fe (124)(Appendix B). The 0.5 M HCl extractable pool likely includes Fe(II) sorbed to mineral or soil surfaces, but may also include poorly crystalline Fe oxides that have formed during the recrystallization process. Performing a similar 0.5 M HCl extraction on our ^{56}Fe goethite

after exposure to ^{57}Fe(II) results in slight changes to the parameters for both goethite sextets and more noticeably the removal of the collapsed feature (Figure 3.1c, Table 3.6c). This may provide further evidence that the collapsed feature represents a low crystallinity / highly bioavailable Fe solid phase, which forms during the Fe(II)-catalyzed recrystallization of goethite.

Results of fitting for experiments with SR-FA and XG were similar to carbon-free controls. The spectrum from ^{56}Fe goethite reacted with spent LB medium contains a sextet indicative of goethite, but also a doublet with parameters indicative of octahedral Fe(II) similar to those previously reported for Fe(II) sorbed onto Fe oxide and clay minerals (15, 17, 125, 126). The presence of an Fe(II) doublet, which accounts for 5% of the area in the spectrum, indicates the possibility that interfacial electron transfer is being blocked between aqueous Fe(II) and goethite by some component of the spent medium. We also observed the presence of a larger Fe(II) doublet (25% spectral area) when ^{56}Fe goethite was equilibrated with spent DSM medium prior to reaction with ^{57}Fe(II), though the spectrum for this sample was particularly complicated and could not be adequately fit even with five model sites. These results indicate that a component present in spent DIRB medium appears to allow the sorption of Fe(II) without subsequent electron transfer to the underlying goethite, a phenomenon we did not observe with XG or SR-FA.

Previously, a long-chain phospholipid (DOPA) was used to block electron transfer in goethite, resulting in a spectrum that consists solely of an Fe(II) doublet (115). We attempted to reproduce those results as shown in Figure 3.2f. Interestingly, after 24 hours exposure to ^{57}Fe(II), the Mössbauer spectrum of our DOPA-equilibrated goethite consists not only of a large Fe(II) doublet (87% area) as previously observed, but also a small Fe(III) doublet (6% area), and a goethite sextet (6% area). Our experiment was carried out under similar conditions to previous work, the only difference being the exposure time to ^{57}Fe(II) (24 hours here vs. 4-8 hours in previous experiments), raising

the possibility that DOPA does not in fact block electron transfer, but instead slows it considerably. Similar to goethite, magnetite synthesized from ^{56}Fe produces negligible Mössbauer signal, as shown in Figure 3.5a. After exposure to ^{57}Fe(II), ^{56}Fe magnetite produces a signal consisting of two overlapping sextets (Figure 3.5b) corresponding to Fe(III) in octahedral and tetrahedral coordination (outer sextet), and Fe(II)-Fe(III) pairs in octahedral coordination (inner sextet) that appear as Fe(2.5) due to electron hopping between Fe(II) and Fe(III) at rates faster than the characteristic time of Mössbauer spectroscopy (approximately 10^{-8} s) (127). The resulting Mössbauer spectrum for ^{56}Fe magnetite with DOPA sorbed prior to ^{57}Fe(II) exposure is markedly different, consisting of a large doublet (62.5% of spectral area), a small magnetically ordered sextet (20% of spectral area) and a smaller doublet (16.5% of spectral area). Similar to what we observed for goethite, these components have parameters consistent with those of sorbed Fe(II) (large doublet), magnetite (sextet), and Fe(III) (small doublet) (Figure 3.5c, Table 3.7). For both goethite and magnetite, the presence of a large Fe(II) doublet with a minor contribution from Fe in a magnetic Fe oxide environment indicates that electron transfer from Fe(II) to structural Fe has been greatly inhibited, but not completely blocked. As phospholipids have been shown to form single and double bilayers as well as supported vesicles on oxide surfaces (128), we might expect sorption of DOPA onto magnetite to result in an electron donor-electron acceptor distance of up to 5 nm (129), which could block electron transfer as previously observed on ^{56}Fe goethite (115). Instead, we still observe some electron transfer after 24 hours reaction, albeit much less than in carbon free controls and reactors with SR-FA, XG, LB medium and DSM medium. While sorption of DOPA may result in electron donor-acceptor distances large enough to inhibit electron transfer, our results imply either that full coverage of the oxide surface has not been achieved, or that despite covering the oxide surface DOPA may allow for slow diffusion of Fe atoms or electrons, ultimately resulting in slow but continued electron transfer.

Fe(II)-Catalyzed Fe Oxide Recrystallization in the Presence of Organic Carbon

While electron transfer appears to occur readily between aqueous Fe(II) and goethite even in the presence of several forms of organic carbon, we sought to examine whether Fe(II) catalyzed Fe oxide recrystallization still occurs in the presence of these compounds. Previous work involving goethite with 10% aluminum substitution observed an approximately four-fold decrease in Fe(II) catalyzed recrystallization relative to unsubstituted goethite despite Fe(II)-Fe(III) electron transfer still occurring (115). In addition, natural organic matter has been shown to inhibit isotope exchange and transformation of several Fe(III) oxides including ferrihydrite, jarosite, and lepidocrocite (114). We tracked the exchange of Fe atoms between the aqueous and solid phases by exposing naturally abundant iron oxides (goethite and magnetite) that had been pre-equilibrated with organic carbon compounds to an isotopically labeled aqueous ^{57}Fe(II) solution, and measuring the Fe isotope composition of the aqueous and solid phases. To quantify the extent of isotopic exchange between aqueous Fe(II) and the goethite or magnetite solids, we calculated percent exchange as shown in equation 3-2.

$$\text{Percent exchange} = \frac{f_t - f_i}{f_e - f_i} \text{ x } 100 \qquad (3\text{-}2)$$

Here f_t represents the isotope composition at time t (given by $f^{57}\text{Fe} = {}^{57}\text{Fe} / \Sigma\text{Fe}$), f_i represents the initial isotope composition, and f_e is the equilibrium isotope composition for the system. Sorption of aqueous Fe(II) onto the iron oxide solids, a mass transfer process that does not necessarily represent Fe atom exchange between the aqueous and solid phases, biases the solid phase toward heavier composition. Consequently, percent exchange calculations are based on the f^{57}Fe in the aqueous phase, which represents migration of atoms from the aqueous phase into goethite or magnetite solids. We verified our percent exchange estimates by also tracking the release of Fe atoms from goethite or

magnetite solids into the solution with aqueous f^{54}Fe measurements, as the initial Fe(II) solution is highly depleted in ^{54}Fe (< 2%).

We measured the extent of Fe(II)-catalyzed recrystallization in nanoparticulate goethite and magnetite in control systems without any organic carbon present, and then in systems where the mineral had been pre-equilibrated with electron shuttling compounds (riboflavin, AQDS), natural organic matter (SA-HA, ES-HA, SR-FA, CZO soil extract), polysaccharides (AA, PGA, XG), spent medium from a DIRB culture (LB, DSM), or a phospholipid (DOPA).

Fe(II)-catalyzed recrystallization in goethite and magnetite

In control experiments involving goethite and aqueous Fe(II) without any organic carbon present, complete isotopic exchange was observed within 14 days, with as much as 90% of exchange occurring within the first 7 days. Fe(II) sorption occurs rapidly with approximately 50% of aqueous Fe(II) sorbed within 1 hour (Table 3.8). Following this initial sorption event, aqueous Fe(II) remained fairly constant until 7 days elapsed, after which there was a slight decrease between 7 and 14 days. Despite relatively little change in aqueous Fe(II) after 40 minutes of reaction, significant Fe atom exchange continued to occur throughout the experiment, increasing from 36.8% exchange after 40 minutes to 100.7% after 14 days (Table 3.8, Figure 3.6). This behavior was consistent with our previous observations of 99.3% exchange after 15.8 days (22) under similar conditions.

In the absence of any organic compounds, recrystallization of magnetite is also quite extensive and rapid in the presence of Fe(II). Under conditions similar to our goethite controls, (pH 7.5, HEPES buffer, 2 g/L solids loading), sorption of Fe(II) to the magnetite solids was slower overall, but followed a similar pattern. After 1 hour, only 15% of aqueous Fe(II) was sorbed, which increased to 22% after 6.7 days, and 50% after 62 days reaction (Table 3.8). Fe atom exchange between the aqueous phase and magnetite solids appeared to mimic the Fe(II) sorption behavior, with an initial rapid

exchange phase (35.7% after 1 hour) that gradually slowed over the course of the experiment to reach 75.0% exchange after 6.7 days, and 82.3% exchange after 63 days reaction (Table 3.9, Figure 3.7). These results differ somewhat from those observed in (24) (Appendix A), where approximately 50% exchange was observed in the first day, and very little further exchange occurred over 30 days (55.3% exchange). In that study, nearly all of the Fe(II) sorption occurred within the first 10 minutes of the experiment, after which aqueous Fe(II) remained relatively constant, though under slightly different conditions from ours (pH = 7.2, MOPS buffer, 1 g/L magnetite).

To investigate the observed differences in sorption behavior and extent of recrystallization, we performed an additional control experiment under the same conditions used in (24). At lower solids loading (1 g/L) and a lower pH (7.2), significantly less Fe(II) sorbed onto the solids (17%). Despite the dramatic difference in Fe(II) sorption, Fe atom exchange kinetics are remarkably similar in both experiments, with approximately 30% exchange after 1 hour, >50% exchange after 7 days, and approximately 80% exchange after 60 days (Figure 3.7).

Influence of electron shuttling compounds on
Fe oxide recrystallization

We saw little change in the Fe(II) sorption and isotope exchange behavior of goethite in the presence of riboflavin and AQDS. An initial rapid sorption event accounted for the majority of the aqueous Fe(II), though in both cases (RBF and AQDS) aqueous Fe(II) continued to decrease slowly over the course of the 60 day experiment (Table 3.8). Fe isotope exchange was as rapid, or slightly faster than goethite in the presence of Fe(II) alone, with nearly 90% exchange after 50 minutes (RBF) and 95% of Fe atoms exchanged after 7 and 9 days (RBF and AQDS respectively) (Figure 3.6).

With magnetite, we saw similarly little change in sorption and isotope exchange behavior when RBF or AQDS were present. Similar to the control, around 20% of Fe(II)

sorbed within 1 hour, after which sorbed Fe(II) continued to increase slowly over the 60 day experiment. After 7-9 days the fraction of Fe(II) sorbed to the solids was greater in the presence of RBF and AQDS (40% vs. 20%), but by the end of the 60 day experiment roughly 50% of aqueous Fe(II) had sorbed, which was very similar to the control (Table 3.9). The presence of RBF or AQDS did not noticeably change Fe atom exchange kinetics in magnetite, although the overall extent of exchange was higher with electron shuttling compounds present (91-96%) than in organic free controls (82%) (Table 3.9, Figure 3.8).

Influence of organic matter on Fe oxide recrystallization

In the presence of commercial and environmentally isolated OM samples, there was again little difference in the Fe(II) uptake behavior on goethite relative to the control experiment only containing Fe(II) and goethite (Table 3.8). Greater than 50% sorption occurred within 1 hour, and generally peaked at 60-80% sorption within 7 days remaining relatively constant for the remainder of the 60 day experiments. Fe isotope exchange data was also remarkably similar to the control when humic acids (SA-HA, ES-HA) were present, with approximately 90% exchange after 7 days and 100% exchange reached within 60 days of reaction. In reactors containing fulvic acid (SR-FA) or extracted soil carbon (CZO), initial atom exchange appeared to be somewhat inhibited, with exchange after 7 days ranging from 57.4% (40 mg/L SR-FA) to approximately 85% (8 mg/L SR-FA, CZO soil extract) vs. 95% in the control. Over longer periods of time however, goethite still reached 100% exchange within 60 days at high SR-FA loading, and was only slightly lower at low SR-FA loading (95%) and in the presence of CZO soil extract (90%) after 66 days (Figure 3.9).

The presence of organic matter seemed to exert little influence on Fe(II)-catalyzed recrystallization in magnetite as well. Sorbed organic matter led to slightly greater Fe(II) sorption over the course of the 60 day experiment, ranging from 52-60% vs. the 50%

observed with no organic matter present. Despite the increased Fe(II) sorption, Fe isotope exchange kinetics were largely unchanged by the presence of humic acids (SA-HA, ES-HA) and high concentration fulvic acid (SR-FA). Similar to our experiments with goethite though, the extent of exchange was slightly higher in the presence of these compounds than in the organic free control (Table 3.9, Figure 3.10). Interestingly, low fulvic acid loading (low SR-FA) and the presence of CZO soil extract resulted in some inhibition to Fe atom exchange, which appears to plateau around 70% at 7 days and remains relatively constant for >60 days of reaction.

Influence of high molecular weight polysaccharides on Fe oxide recrystallization

We used three model polysaccharides to investigate the potential effects of microbial extracellular polymeric substances (EPS) on Fe(II) catalyzed recrystallization in goethite. Following equilibration with the polysaccharides, aggregation behavior of nano-goethite changed dramatically, forming large aggregates that rapidly settle out of solution. Somewhat surprisingly then, there was little change in Fe(II) uptake relative to the control experiment (Table 3.8). While the presence of EPS did not appear to influence uptake of Fe(II) from solution, both the extent and kinetics of Fe isotope exchange were different in the presence of all three polysaccharides. After 7 days reaction, isotope exchange ranged from 70-80% in contrast to the >90% observed in the organic free control, experiments containing electron shuttles, and experiments containing natural organic matter. Even more interesting perhaps, is that little further exchange occurred between 7 and 60 days. While isotope exchange continued between 7 and 60 days in the other experimental systems eventually resulting in complete isotopic mixing, isotope exchange over that time scale in systems containing AA, PGA, and XG was relatively flat, reaching only 75.2%, 92.9%, and 70.3% exchange respectively after 60 days (Figure 3.11).

Similar experiments conducted with EPS and magnetite yielded much different results from those with goethite. Fe(II) sorption in the presence of EPS was highly variable, ranging from 2-30% after 1 hour (Table 3.9) and 40-60% after 7 days, with minimal uptake between 7 and 60 days. Despite dramatic aggregation of magnetite in the presence of polysaccharides, isotope exchange kinetics are nearly identical to the control experiment with Fe(II) and magnetite alone, which contrasts with the apparent inhibition observed with goethite (Table 3.9, Figure 3.12). In the presence of 500 mg/L alginic acid, polygalacturonic acid, and xanthan gum, approximately 40% of Fe atoms exchanged within 1 hour, 75% exchanged within 7 days, and 80% exchanged after 60 days.

Influence of extracellular exudates from DIRB on Fe oxide recrystallization

Experiments were also conducted with spent medium from cultures of a dissimilatory iron reducing bacterium (*Shewanella oneidensis* MR-1) to examine whether a combination of the bacterial exudates we previously examined, or else other exudates not yet considered can ultimately influence the Fe(II)-catalyzed Fe oxide recrystallization.

In reactors where goethite was equilibrated with ten-fold dilutions of spent LB medium and spent defined *Shewanella* medium (DSM), we saw substantially more uptake of Fe(II) from solution than in controls, with approximately 70-80% uptake within the first day and 90% overall uptake of Fe(II) from solution (Table 3.8). Despite increased sorption of Fe(II), Fe isotope exchange was inhibited in the presence of spent medium. Exchange initially occurs rapidly, reaching approximately 60% within 24 hours then increasing slowly for the duration of the experiment. The extent of exchange increased slowly to 80% in DSM after 30 days and remained flat through 65 days, while

a slow but constant increase in exchange from 54% after 7 days to 95% after 67 days was observed in LB medium (Figure 3.13).

Our experiments using magnetite and spent media produced similar results to our goethite experiments. Greater Fe(II) sorption was observed in the presence of spent media, with approximately 60% of Fe(II) sorbing rapidly (within 24 hours) after which aqueous Fe(II) remained constant (Table 3.9). Fe isotope exchange was inhibited when spent medium was present, though we again observed rapid Fe atom exchange over the first 24 hours of reaction (35-37%). Exchange continued to occur rapidly for DSM, reaching 61% after 7 days and remaining near 60% for the remainder of the 63 day experiment. In contrast, exchange slowed after 24 hours in LB medium increasing at a fairly constant rate from 35% to 69% after 69 days (Figure 3.14). This represents a 10-20% reduction in the extent of exchange compared to our control experiments.

We also examined Fe(II)-catalyzed recrystallization of goethite and magnetite in the presence of a phopholipid (DOPA). We discuss DOPA along with the extracellular exudates as it most closely resembles a bacterial cell membrane, and may be representative of situations with extremely high biomass loadings (e.g. biostimulation / enhanced bioremediation experiments). For our purposes however, DOPA is most significant because it is largely able to block interfacial electron transfer as described earlier. Experiments measuring Fe isotope exchange between ferrihydrite and ^{57}Fe labeled aqueous Fe(III) found that only Fe atoms in available surface sites participated, (130, 131). Based on these results and our observations of significant Fe atom exchange in several Fe oxides following exposure to Fe(II), we have hypothesized that the electron transfer step or the generation of a redox potential between Fe(II) and Fe(III) is critical for substantial recrystallization to occur. Blocking or inhibition of electron transfer could then be expected to inhibit Fe(II)-catalyzed recrystallization. In the presence of DOPA, Fe(II) sorption was very similar to that observed in the presence of spent media for both goethite and magnetite (87% and 68% respectively after 30 days). We also observed

significant inhibition of Fe atom exchange in both goethite and magnetite (20% and 25% respectively after 60 days) (Tables 3.8, 3.9, Figures 3.13, 3.14). The fact that atom exchange is not completely turned off is perhaps more surprising than the observation that it is inhibited by DOPA.

Discussion and Environmental Significance

As the physical and chemical properties of organic carbon compounds vary widely, so to do their effects on Fe(II)-catalyzed recrystallization of Fe oxides. We expected that the presence of certain forms of organic carbon, particularly those expected to sorb to Fe oxide surfaces (i.e., NOM, EPS) might inhibit Fe(II) sorption and Fe(II)-catalyzed Fe oxide recrystallization. Largely, however, this was not the case, and Fe electron transfer and atom exchange continued relatively unhindered in the presence of electron shuttles, NOM, EPS, and spent DIRB medium. Only the presence of a long-chain phospholipid resulted in significant inhibition of Fe atom exchange during our 60 day experiments. In addition, we observed no apparent changes to the mineral phases, i.e. goethite remained goethite after reaction and magnetite remained magnetite (Figures 3.15 and 3.16), which is consistent with previous studies performed in carbon free systems (22, 24).

We expect that both riboflavin and AQDS remain largely dissolved during reaction, where both compounds act as electron transfer mediators (ETMs) by diffusing to Fe oxide surfaces in their reduced form, where they can be oxidized via heterogeneous electron transfer. Their presence could potentially speed the transfer of electrons from aqueous Fe(II) to goethite or magnetite, assuming the Fe(II)-ETM and ETM-Fe oxide electron transfer rates are faster than the Fe(II)-Fe oxide electron transfer rate. In cases where electron transfer is expected to be the rate limiting step, electron shuttles can have a significant effect. Jiang and Kappler (118) observed electron transfer rates from *Geobacter sulfurreducens* to Fe(III) hydroxide up to 7 times faster when humic

substances (HS) were present to act as electron shuttles, resulting in accelerated Fe(III) mineral reduction and microbial metabolism. In the case of Fe(II)-catalyzed Fe oxide recrystallization however, electron transfer is thought to be extremely fast, and is unlikely to be the rate limiting step. The similarity we observed in atom exchange rate and extent in both the presence and absence of electron shuttling compounds with two Fe oxides corroborates this hypothesis, and points towards other steps (bulk conduction, reductive dissolution / detachment, or diffusion) as the potential rate limiter for Fe atom exchange.

In contrast, we hypothesized there was real potential for NOM to interfere with Fe(II) catalyzed recrystallization. While Latta et al. (115) have demonstrated that Fe(II)-goethite electron transfer happens readily in the presence of NOM (SA-HA), Jones and Waite (114) observed up to 40% less isotope exchange in ferrihydrite, and approximately 12% less exchange in lepidocrocite when 25 or 150 mg/L SR-FA was present. They claimed that sorption of NOM to the oxide surfaces resulted in blocking of dissolution sites, which could result in retardation of Fe atom exchange while electron transfer continues uninhibited. We have been able to reproduce this finding reasonably well using 150 mg/L SR-FA which was not filtered prior to addition to the reactor, and a similarly low ferrihydrite loading as in that study. In those reactors however, SR-FA represents up to 26% of the solids mass, and Fe(II) sorption is greatly diminished at pH 6.5, both of which may contribute to the slow rate of exchange observed in their study. In our experiments with goethite and magnetite however, we found that SR-FA and SA-HA, as well as ES-HA, had very little influence on the extent of Fe atom exchange in goethite and magnetite at pH 7.5. This was especially surprising given the complex nature of NOM-Fe oxide interactions. In particular, HA has been shown to inhibit microbial reduction of ferrihydrite at low concentrations where it is expected to mainly exist sorbed to the oxide (117). At higher concentrations however, where HA is also present as a dissolved species, reduction was stimulated, presumably due to the dissolved HA acting as an electron shuttle. To further complicate matters, HA can also influence

the aggregation behavior of Fe oxides. Sorption of HA to (positively charged) Fe oxides can lower the particle's point of zero charge (PZC) (132), and prevent aggregation due to increased repulsion between negatively charged particles and additional negatively charged HA molecules (133). Given our solids loading (2 g/L), and specific surface areas (115 and 66 m^2/g for nano-goethite and magnetite respectively), we would expect complete HA sorption based on the behavior observed in (117), though it is worth noting that they used a different NOM reference sample (Pahokee Peat Humic Acid) from the three used in this study. Even if dissolved OM is present, the minimal influence exerted by other electron shuttles (RBF, AQDS) makes it seem unlikely that any enhancement of Fe atom exchange would be observed. While we did not observe any isotope exchange inhibition, our experiments used two stable Fe oxides, which do not undergo secondary mineral transformation during Fe(II) catalyzed recrystallization. This is in contrast to the minerals used in (114), which readily transform to more stable minerals in the presence of Fe(II). It is possible that NOM prevents polymerization of Fe(III) during mineral transformation, though data in our own group indicate that Fe atom exchange and transformation of ferrihydrite may involve distinct mechanisms. Currently, the mechanism by which SR-FA can inhibit isotope exchange in ferrihydrite without a similar effect in magnetite or goethite remains a mystery, though studies using magnetite and goethite with unfiltered SR-FA and lower pH will provide a better basis for determining whether the differences are due to the minerals, or the experimental conditions.

Extracellular polymeric substances are known to be prevalent throughout the environment, but there is little information on how they may interact with Fe oxides, particularly crystalline Fe oxides like those used in our study, which have formed prior to exposure to EPS. Sorption of EPS from *Pseudomonas putida* onto goethite has been shown to lower its PZC from 7.6 to 3.2 by forming negatively charged inner-sphere complexes (110). While greater sorption of Fe(II) might be expected to result from the

increasingly negative surface charge, we did not observe any obvious trends in sorption behavior when EPS were sorbed to magnetite and goethite. We can speculate that binding of EPS to the oxide surface via ligand exchange may further stabilize surface Fe atoms, making them less likely to undergo electron transfer / reductive dissolution, although we have no direct observations in support of this hypothesis. EPS have also been shown to template the formation of nanocrystalline Fe oxides (134), and can provide suitable nucleation sites for dissolved Fe(III) species (47), factors which may be relevant for exchange processes involving dissolution / reprecipitation, or other forms of non-topotactic growth.

Having seen no clear inhibition of atom exchange from individual organic components, it came as a bit of a surprise that the combination of electron shuttles, EPS, and other cell materials likely to be present in spent *Shewanella* medium inhibited Fe atom exchange in both goethite and magnetite. While the complexity of the spent media precludes identification of the direct cause for inhibition, an obvious component of these solutions missing from our other experiments is cell materials, which may include lysed cell membranes and other structures either excreted during growth, or released following cell death. The fact that we saw some degree of electron transfer inhibition from spent media and DOPA may implicate cell wall and membrane materials in particular, which are similar in structure to the phospholipid we used. Binding of cell biomass has been shown to inhibit reduction of mercury (71) and bioreduction of lepidocrocite (116). While natural organic matter is known to cover mineral surfaces in a discontinuous manner, which is why the term "monolayer equivalent" is stressed in soils literature (40); DOPA and other phospholipids are capable of forming multiple bilayers on mineral surfaces (128, 135). Our observations that (*i*) electron transfer inhibition corresponds with atom exchange inhibition and (*ii*) atom exchange still proceeds despite electron transfer inhibition suggest that without complete blockage of Fe oxide surfaces, Fe(II)-catalyzed recrystallization is likely to occur in the presence of various organic sorbates.

Further study of electron transfer in DOPA sorbed Fe oxides may show that the extent of electron transfer is limited by the formation of a hydrophobic surface bilayer (i.e. there are finite surface sites available), or that the rate of electron transfer is simply slowed (the number of conductive "wires" in an oxide is limited by surface coverage). Further understanding of electron transfer in the presence of DOPA will provide critical information regarding connections between the rate / extent of electron transfer and Fe atom exchange in these minerals.

Despite the great variation in our results, we consistently see the same pattern of rapid isotope exchange usually followed by a long term phase of slower exchange, though that slow exchange phase can apparently be blocked by the presence of certain organic compounds. This behavior raises the possibility that two distinct mechanisms for Fe isotope exchange are occurring, a faster process which is dominant over short time scales (< 24 hours) and a slower long term mechanism which becomes dominant over long time scales. Further study of the factors impacting Fe(II)-catalyzed recrystallization may help to elucidate whether there are indeed two processes at work, and what the links between the electron transfer observed by Mössbauer spectroscopy and other aspects of Fe(II) catalyzed recrystallization (atom exchange, mineral growth / transformation) may be.

Table 3.1. Summary of organic carbon compounds used for electron transfer and Fe oxide recrystallization experiments.

Class	Compound	Abbreviation	Molecular Weight (g / mol)
Natural Organic Matter	Bisley CZO soil carbon	CZO	n/a
	Sigma-Aldrich Humic Acid	SA-HA	8000[a]
	Elliott Soil Humic Acid	ES-HA	n/a
	Suwannee River Fulvic Acid	SR-FA	1360[a]
Electron Shuttling Compounds	Riboflavin	RBF	376.36
	9,10-anthraquinone-2,6-disulfonic acid	AQDS	412.3
Extracellular Polysaccharides	Alginic Acid	AA	176.1
	(D-galacturonic acid) as Polygalacturonic Acid	PGA	194.1
	Xanthan um	XG	933.8
	1,2-dioleoyl-sn-glycero-3-phosphate	DOPA	722.9
S. oneidensis Spent Medium	Luria-Bertani Medium	LB	n/a
	Defined *Shewanella* Medium	DSM	n/a

Table 3.2. Selected physical and chemical characteristics of natural organic matter isolates used for electron transfer and Fe oxide recrystallization experiments.

	Elemental Composition (%)						avg MW	aromatic C	Carboxyl groups	Phenol Groups
	C	H	O	N	S	ash	(Da)	(% total C)	(meq (g C)$^{-1}$)	
Sigma-Aldrich Humic Acid[a]	55.23	4.48	37.64	0.32	2.33	n/a	8000	40	4.8	2.26
Elliott Soil Humic Acid[b,c]	58.13	3.68	34.08	4.14	0.44	0.88		50	8.28	1.87
Suwannee River Fulvic Acid[b,d]	54.2	3.92	38	0.72	0.35	0.19	1360	22.9	11.17	2.84

n/a = not available

[a] data from (136)

[b] data from (137)

[c] data from (138)

[d] data from (139)

Table 3.3. Growth medium recipes for *Shewanella oneidensis* MR-1 cultures used to generate spent medium for electron transfer and Fe oxide recrystallization experiments.

LB medium, Miller Composition	
Tryptone	10.0 g
Yeast extract	5.0 g
Sodium chloride	10 g

Defined *Shewanella* medium	
Dipotassium phosphate	0.225 g
Monopotassium phosphate	0.225 g
Ammonium sulfate	0.225 g
Sodium chloride	0.46 g
HEPES buffer	4.77 g
Vitamin mix	5 mL
Wolfe's mineral mix	5 mL
60% DL lactate syrup	9.37 g

Table 3.4. Experimental conditions for electron transfer experiments conducted in the presence of various organic carbon compounds.

Experiment ID	Solution Conditions	$pH_{initial}$	Organic Type	Organic loading	Solids Loading
Goethite					
^{56}Goethite	25 mM HEPES / KBr	7.5	Control	n/a	2 g/L
Gt-Low SR-FA	25 mM HEPES / KBr	7.5	NOM[a]	8 mg / L	2 g/L
Gt-XG	25 mM HEPES / KBr	7.5	EPS[b]	500 mg / L	2 g/L
Gt-LB	25 mM HEPES / KBr	7.5	DIRB exudates[c]	n/m[d]	2 g/L
Gt-DSM	25 mM HEPES / KBr	7.5	DIRB exudates	n/m[d]	2 g/L
Gt-DOPA	25 mM HEPES / KBr	7.5	Phospholipid	1 mM	2 g/L
Magnetite					
^{56}Magnetite	25 mM HEPES / KBr	7.5	Control	n/a	2 g/L
Mag-DOPA	25 mM HEPES / KBr	7.5	Phospholipid	1 mM	2 g/L

[a] NOM = natural organic matter

[b]EPS = extracellular polysaccharides

[c]DIRB = dissimilatory iron reducing bacteria

[d]n/m = not measured, spent media were diluted 1:10

Table 3.5. Experimental conditions for Fe atom exchange experiments conducted in the presence of organic carbon compounds.

Experiment ID	Solution Conditions	$pH_{initial}$	Organic Type	Organic loading	Fe oxide	Solids Loading
Fe(II) - 7.5	25 mM HEPES / KBr	7.5	Control	n/a	goethite / magnetite	2 g/L
Fe(II) - 7.2	50 mM MOPS	7.2	Control	n/a	magnetite	1 g/L
SA-HA	25 mM HEPES / KBr	7.5	NOM[a]	20 mg/L	goethite / magnetite	2 g/L
ES-HA	25 mM HEPES / KBr	7.5	NOM	40 mg/L	goethite / magnetite	2 g/L
SR-FA	25 mM HEPES / KBr	7.5	NOM	40 mg/L	goethite / magnetite	2 g/L
Low SR-FA	25 mM HEPES / KBr	7.5	NOM	8 mg/L	goethite / magnetite	2 g/L
CZO	25 mM HEPES / KBr	7.5	NOM	17 mg/L C	goethite / magnetite	2 g/L
RBF	25 mM HEPES / KBr	7.5	Electron shuttle	1 mM	goethite / magnetite	2 g/L
AQDS	25 mM HEPES / KBr	7.5	Electron shuttle	1 mM	goethite / magnetite	2 g/L
AA	25 mM HEPES / KBr	7.5	EPS[b]	500 mg/L	goethite / magnetite	2 g/L
PGA	25 mM HEPES / KBr	7.5	EPS	500 mg/L	goethite / magnetite	2 g/L
XG	25 mM HEPES / KBr	7.5	EPS	500 mg/L	goethite / magnetite	2 g/L
LB	25 mM HEPES / KBr	7.5	DIRB[c] exudates	1:10 dilution	goethite / magnetite	2 g/L
DSM	25 mM HEPES / KBr	7.5	DIRB exudates	1:10 dilution	goethite / magnetite	2 g/L
DOPA	25 mM HEPES / KBr	7.5	Phospholipid	1 mM	goethite / magnetite	2 g/L

[a] NOM = natural organic matter

[b]EPS = extracellular polysaccharides

[c]DIRB = dissimilatory iron reducing bacteria

Table 3.6. Fitting parameters for 77 K Mössbauer spectra of ^{56}Fe goethite reacted with ^{57}Fe(II) in the presence of various organic carbon compounds.

Component	CS (mm s^{-1})	QS (mm s^{-1})	H (Tesla)	std(H) (T) or std(QS) (mm s^{-1})	Area (%)	χ^2
a. *Goethite*[a]						
Sextet	0.48	-0.25	50.6			
b-1.*^{56}Gt + 1 mM ^{57}Fe(II) (2 sextet, 1 component)*						
Sextet 1	0.49	-0.12	48.6	1.11	59.3	67.3
Sextet 2	0.48	-0.11	49.6	0.40	28.7	
Collapsed Feature	0.59	0.05	35.3	10.97	12.0	
b-2.*^{56}Gt + 1 mM ^{57}Fe(II) (1 sextet, 2 component)*						
Sextet 1	0.49	-0.12	48.2	1.22	42.2	69.5
			49.5	0.60	45.8	
Collapsed Feature	0.59	0.05	35.3	10.97	12.0	
c. *^{56}Gt + 1 mM ^{57}Fe(II), 0.5 M HCl extracted*						
Sextet 1	0.46	-0.19	48.8	1.60	58.3	108.1
Sextet 2	0.50	-0.07	49.6	0.75	41.7	
d.*^{56}Gt + 500 mg/L xanthan gum + 1 mM ^{57}Fe(II)*						
Sextet 1	0.49	-0.12	48.5	1.10	80.7	16.8
Sextet 2	0.38	0.01	49.3	0.01	8.5	
Collapsed Feature	0.48	-0.01	28.7	11.8	10.8	
e.*^{56}Gt + 8 mg/L Suwannee River Fulvic Acid Standard + 1 mM ^{57}Fe(II)*						
Sextet 1	0.49	-0.11	48.7	1.14	85.3	52.3
Sextet 2	0.36	0.01	49.5	0.001	7.0	
Collapsed Feature	0.52	0.004	26.3	10.97	7.0	
f.*^{56}Gt + Spent Shewanella LB medium (1:10) + 1 mM ^{57}Fe(II)*						
Fe(II) doublet	1.32	2.59		0.54	4.9	29.1
Sextet 1	0.49	-0.07	48.4	1.44	64.3	
Collapsed Feature	0.42	-0.12	26.6	14.88	30.9	

Table 3.6 – continued

g. *^{56}Gt + Spent Shewanella DSM medium (1:10) + 1 mM ^{57}Fe(II)*						
Fe(II) doublet	1.40	2.80		0.54	21.0	66.0
Fe(III) doublet	0.64	0.38		0.21	5.6	
Sextet 1	0.63	-0.05	48.4	1.11	24.5	
Sextet 2	0.35	-0.10	48.2	0.92	24.6	
Collapsed Feature	0.42	-0.12	26.6	14.88	24.4	
h. *^{56}Gt + 1 mM DOPA + 1mM ^{57}Fe(II)*						
Fe(II) doublet	1.36	2.93		0.42	87.9	16.6
Fe(III) doublet	0.64	0.38		0.21	5.9	
Sextet 1	0.48	-0.06	47.3	1.85	1.9	
			49.8	0.89	4.3	

[a] Reference parameters from (140)

Table 3.7. Fitting parameters for 140 K Mössbauer spectra of ^{56}Fe magnetite reacted with ^{57}Fe(II) in the absence and presence of 1 mM phospholipid (1,2-dioleoyl-sn-glycero-3-phosphate, DOPA).

Component	CS (mm s^{-1})	QS (mm s^{-1})	H (Tesla)	std(H) (T) or std(QS) (mm s^{-1})	Area (%)	χ^2
a. *Magnetite*						5.4
Octahedral Sextet	0.72	-0.02	47.3	1.51	66.6	
			22.9	9.68		
			44.9	4.02		
Tetrahedral Sextet	0.38	0.003	49.4	0.55	33.4	
			49.6	0.01		
b. *^{56}Magnetite + 1 mM ^{57}Fe(II)*						4.7
Octahedral sextet	0.72	0.01	45.7	4.7	42.4	
Tetrahedral sextet	0.38	0.002	48.7	1.6	57.6	
c. *^{56}Magnetite + 1 mM DOPA + 1 mM ^{57}Fe(II)*						22.6
Fe(II) doublet	1.35	2.81		0.2	69.6	
Fe(III) doublet	0.74	0.25		0.2	10.8	
Octahedral sextet	0.73	-0.14	43.7	5.8	13.2	
Tetrahedral sextet	0.24	-0.03	49.0	2.0	6.4	

Table 3.8. Mass and Fe isotope data for Fe isotope tracer experiments between aqueous Fe(II) and goethite with various forms of organic carbon present.

	Aqueous Fe(II)					Solids				% Recovery		
Time (d)	Fe(II) (μmoles)	f^{57}Fe	% exchange	f^{54}Fe	% exchange	Fe(II) (μmoles)	Total Fe (μmoles)	f^{57}Fe	% exchange	Fe(II)	Fe(III)	Total Fe
Goethite (2 g/L) + 1 mM ^{57}Fe(II)												
0.00	18.9 (0.5)	0.368 (0.100)	0 (0)	0.0315 (0.005)	0	1.1 (0.2)	323.7 (13.6)	0.025 (0.0005)	0	100.0	100.0	100.0
0.03	9.6 (0.8)	0.248 (0.010)	36.8 (5.9)	0.0379 (0.0009)	38.2 (5.6)	49.1 (7.4)	592.9 (10.0)	0.030 (0.001)	34.3 (6.2)	294.3	168.5	175.9
0.35	8.7 (1.4)	0.151 (0.010)	66.5 (3.1)	0.0426 (0.0005)	66.3 (2.8)	233.3 (25.1)	379.3 (15.6)	0.034 (0.004)	53.7 (23.1)	1212.8	45.2	113.3
3.91	11.2 (2.6)	0.068 (0.018)	92.4 (5.5)	0.0479 (0.001)	97.6 (7.3)	87.8 (17.1)	312.0 (9.8)	0.034 (0.0008)	51.4 (4.5)	495.9	69.5	94.3
6.96	8.5 (1.1)	0.056 (0.019)	95.7 (3.7)	0.0482 (0.001)	99.6 (8.6)	18.6 (6.0)	317.5 (30.3)	0.036 (0.0004)	65.2 (2.2)	135.8	92.6	95.1
14.06	6.4 (0.2)	0.041 (0.013)	100.7 (4.1)	0.0479 (0.0004)	98.0 (2.5)	17.5 (3.5)	250.4 (6.8)	0.034 (0.002)	54.4 (10.4)	119.8	72.2	75.0
Goethite (2 g/L) + riboflavin + 1 mM Fe(II)												
0	14.8 (0.1)	0.774 (0.0043)	0	0.010 (0.0003)	0	1.1 (0.2)	323.7 (13.6)	0.024 (0.0002)	0	100.0	100.0	100.0
0.04	7.0 (3.1)	0.142 (0.011)	89.8 (1.4)	0.039 (0.0006)	78.7 (1.5)	8.5 (0.4)	299.0 (2.6)	0.049 (0.002)	68.1 (4.0)	97.5	90.0	90.4
6.99	5.3 (1.9)	0.086 (0.004)	95.9 (0.5)	0.044 (0.0006)	88.9 (1.5)	9.2 (2.3)	362.5 (117.7)	0.048 (0.0006)	72.2 (1.9)	90.9	109.5	108.6
60.91	4.3 (0.4)	0.0253 (0.002)	104.3 (0.3)	0.063 (0.0025)	143.3 (7.6)	6.6 (0.0)	317.9 (9.0)	0.040 (0.0009)	55.9 (3.2)	68.7	96.5	95.2
Goethite (2 g/L) + AQDS + 1 mM Fe(II)												
0	14.8 (0.1)	0.774 (0.0043)	0	0.010 (0.0003)	0	1.1 (0.2)	323.7 (13.6)	0.024 (0.0002)	0	100.0	100.0	100
9.18	4.4 (1.2)	0.121 (0.005)	91.1 (0.7)	0.046 (0.0002)	96.7 (0.5)	16.3 (0.8)	288.6 (5.5)	0.056 (0.0005)	98.8 (1.5)	130.1	84.5	86
60.92	2.7 (1.6)	0.024 (0.002)	104.6 (0.2)	0.052 (0.0005)	114.7 (2.8)	8.2 (0.8)	392.3 (46.6)	0.039 (0.0007)	51.4 (2.3)	68.5	119.2	11

Table 3.8 – continued

Goethite (2 g/L) + Sigma Aldrich Humic Acid (40 mg/L) + 1 mM Fe(II)												
0	14.8 (0.1)	0.774 (0.0043)	0	0.010 (0.0003)	0	1.1 (0.2)	323.7 (13.6)	0.024 (0.0002)	0	100.0	100.0	100.0
0.05	5.9 (0.8)	0.330 (0.033)	66.1 (4.2)	0.032 (0.002)	61.5 (4.5)	8.2 (1.7)	295.1 (5.9)	0.049 (0.0006)	69.1 (1.6)	88.7	88.8	88.8
6.58	5.9 (1.3)	0.113 (0.016)	92.1 (2.3)	0.044 (0.002)	87.6 (5.4)	15.4	313.2	0.048 (0.0005)	73.8 (1.5)	121.6	199.3	192.2
60.91	3.2 (0.6)	0.042 (0.032)	101.8 (4.9)	0.056 (0.007)	122.6 (20.4)	7.7 (1.7)	346.1 (35.5)	0.041 (0.0008)	58.3 (2.8)	68.4	105.0	103.3
Goethite (2 g/L) + Elliot Soil Humic Acid (40 mg/L) + 1 mM Fe(II)												
0	14.8 (0.1)	0.774 (0.0043)	0	0.010 (0.0003)	0	1.1 (0.2)	323.7 (13.6)	0.024 (0.0002)	0	100.0	100.0	100.0
6.81	6.0 (0.9)	0.118 (0.0008)	91.5 (0.1)	0.048 (0.0012)	103.4 (3.4)	32.4 (11.4)	506.8 (163.3)	0.053 (0.0004)	87.4 (1.1)	240.9	147.1	151.6
60.91	5.7 (3.0)	0.027 (0.004)	104.1 (0.6)	0.057 (0.0038)	130.3 (12.0)	7.8 (1.7)	256.2 (16.3)	0.038 (0.0011)	46.2 (3.8)	85.1	77.0	77.4
Goethite (2 g/L) + Suwanee River Fulvic Acid (8 mg/L) + 1 mM Fe(II)												
0.00	14.8 (0.1)	0.857 (0.028)	0	0.007 (0.001)	0	1.1 (0.2)	323.7 (13.6)	0.024 (0.0002)	0	100.0	100.0	100.0
1.05	7.4 (1.7)	0.278 (0.0066)	74.7 (0.8)	0.041 (0.0023)	86.0 (5.4)	8.8 (0.6)	324.1 (15.6)	0.059 (0.0052)	90.1 (12.1)	101.4	97.7	97.9
6.80	2.5 (0.3)	0.180 (0.0066)	85.0 (0.8)	0.046 (0.0007)	98.7 (1.8)	7.9 (1.4)	307.1 (1.1)	0.056 (0.0020)	88.0 (5.0)	65.6	92.8	91.5
31.00	4.5 (0.8)	0.096 (0.0148)	95.5 (1.9)	0.048 (0.0011)	103.8 (2.8)	9.0 (0.1)	414.8 (21.9)	0.065 (0.0015)	113.7 (3.7)	84.9	125.9	123.9
65.8	4.1 (1.1)	0.095 (0.0019)	95.6 (0.2)	0.051 (0.0004)	110.6 (1.1)	8.7 (1.0)	299.0 (14.1)	0.065 (0.0001)	111.7 (0.3)	80.7	90.2	89.7
Goethite (2 g/L) + Suwanee River Fulvic Acid (40 mg/L) + 1 mM Fe(II)												
0	14.8 (0.1)	0.774 (0.0043)	0	0.010 (0.0003)	0	1.1 (0.2)	323.7 (13.6)	0.024 (0.0002)	0	100.0	100.0	100.0
6.81	5.9 (2.1)	0.363 (0.038)	57.4 (5.3)	0.035 (0.002)	67.1 (4.2)	22.7 (1.1)	471.5 (26.0)	0.052 (0.001)	85.9 (10.0)	180.1	139.2	141.1
60.91	3.9 (2.2)	0.023 (0.001)	104.7 (0.2)	0.056 (0.004)	129.4 (12.1)	9.5 (1.7)	325.9 (7.9)	0.040 (0.0008)	54.8 (2.5)	83.8	98.1	97.5

Table 3.8 – continued

Goethite (2 g/L) + CZO Soil Extract (17 mg / L) + 1 mM Fe(II)												
0.00	14.8 (0.1)	0.857 (0.028)	0	0.007 (0.001)	0	1.2 (0.2)	318.1 (13.3)	0.024 (0.0002)	0	100.0	100.0	100.0
1.05	8.0 (1.6)	0.258 (0.013)	77.0 (1.5)	0.044 (0.0011)	94.8 (2.7)	9.6 (0.0)	291.7 (2.1)	0.059 (0.0026)	89.9 (5.9)	110.4	87.2	88.3
7.10	4.4 (1.1)	0.200 (0.060)	82.5 (7.6)	0.044 (0.0022)	92.0 (5.4)	9.6 (0.8)	315.6 (23.3)	0.056 (0.0001)	87.1 (0.2)	87.9	94.9	94.6
31.90	5.3 (0.4)	0.153 (0.012)	88.4 (1.5)	0.045 (0.0007)	96.4 (1.7)	9.1 (0.2)	299.4 (32.8)	0.064 (0.0006)	110.1 (1.5)	89.9	90.1	90.1
66.90	4.7 (1.1)	0.138 (0.0042)	90.2 (0.5)	0.049 (0.0004)	104.3 (0.8)	8.6 (0.5)	302.5 (7.9)	0.064 (0.001)	108.5 (0.5)	83.2	91.2	90.8
Goethite (2 g/L) + Alginic Acid (500 mg/L) + 1 mM Fe(II)												
0	14.8 (0.1)	0.774 (0.0043)	0	0.010 (0.0003)	0	1.1 (0.2)	323.7 (13.6)	0.024 (0.0002)	0	100.0	100.0	100.0
6.17	8.3 (3.0)	0.272 (0.079)	70.0 (10.9)	0.043 (0.005)	89.3 (14.2)	1.8 (1.2)	267.6 (9.5)	0.024 (0.0004)	0.2 (1.2)	63.2	82.5	81.5
67.11	3.4 (0.5)	0.258 (0.122)	75.2 (15.3)	0.035 (0.005)	70.0 (12.7)	8.6 (0.8)	309.8 (16.5)	0.062 (0.0002)	103.8 (0.5)	75.7	93.4	92.6
Goethite (2 g/L) + Polygalacturonic Acid (500 mg/L) + 1 mM Fe(II)												
0	14.8 (0.1)	0.774 (0.0043)	0	0.010 (0.0003)	0	1.1 (0.2)	323.7 (13.6)	0.024 (0.0002)	0	100.0	100.0	100.0
6.11	7.9 (1.0)	0.200 (0.043)	80.0 (5.9)	0.047 (0.001)	100.1 (2.7)	1.8 (0.0)	266.1 (3.2)	0.024 (0.0007)	-0.5 (2.2)	61.0	82.0	81.0
67.11	3.8 (0.6)	0.118 (0.007)	92.8 (0.9)	0.041 (0.0008)	85.1 (2.0)	8.8 (0.4)	304.9 (13.9)	0.064 (0.0008)	109.2 (2.1)	79.4	91.8	91.3
Goethite (2 g/L) + Xanthan Gum (500 mg/L) + 1 mM Fe(II)												
0	14.8 (0.1)	0.774 (0.0043)	0	0.010 (0.0003)	0	1.1 (0.2)	323.7 (13.6)	0.024 (0.0002)	0	100.0	100.0	100.0
6.10	6.9 (0.3)	0.228 (0.016)	76.1 (2.2)	0.043 (0.001)	89.4 (3.0)	3.1 (2.9)	249.7 (31.7)	0.023 (0.0003)	-2.7 (0.9)	62.7	76.5	75.8
67.11	4.4 (0.9)	0.297 (0.013)	70.3 (1.7)	0.033 (0.001)	64.6 (2.7)	8.9 (1.3)	312.0 (9.1)	0.063 (0.0005)	106.2 (1.4)	83.9	94.0	93.6

Table 3.8 – continued

Goethite (2 g/L) + LB Medium (1:10) + 1 mM Fe(II)												
0.00	14.8 (0.1)	0.857 (0.028)	0	0.007 (0.001)	0	1.1 (0.2)	323.7 (13.6)	0.024 (0.0002)	0	100.0	100.0	100.0
1.06	6.5 (1.9)	0.623 (0.083)	34.0 (9.8)	0.022 (0.0052)	42.3 (4.0)	10.9 (1.2)	289.5 (20.1)	0.055 (0.0017)	79.6 (4.0)	109.4	86.3	87.4
7.11	1.4 (0.1)	0.426 (0.043)	54.1 (5.4)	0.035 (0.0017)	69.9 (4.3)	12.9 (0.3)	316.8 (14.9)	0.053 (0.0019)	78.4 (4.7)	90.0	94.3	94.1
30.86	1.3 (0.5)	0.409 (0.067)	56.2 (8.4)	0.040 (0.0072)	82.7 (18.0)	10.2 (0.1)	291.7 (2.7)	0.065 (0.0005)	113.1 (1.2)	72.7	87.3	86.6
66.91	0.2 (0.0)	0.094 (0.065)	95.8 (8.1)	0.063 (0.0024)	139.0 (6.0)	6.9 (0.7)	352.7 (60.8)	0.066 (0.0007)	114.9 (1.7)	44.3	107.3	104.4
Goethite (2 g/L) + Defined mineral medium (1:10) + 1 mM Fe(II)												
0.00	14.8 (0.1)	0.857 (0.028)	0	0.007 (0.001)	0	1.1 (0.2)	323.7 (13.6)	0.024 (0.0002)	0	100.0	100.0	100.0
1.04	4.9 (1.8)	0.577 (0.114)	39.4 (13.4)	0.026 (0.007)	52.5 (16.2)	12.1 (0.6)	332.6 (76.6)	0.057 (0.0005)	84.8 (1.1)	106.6	99.3	99.6
6.83	3.3 (0.7)	0.423 (0.093)	54.5 (11.6)	0.033 (0.0047)	66.7 (11.8)	13.3 (0.4)	333.1 (56.4)	0.055 (0.0004)	85.7 (1.0)	104.8	99.2	99.4
30.73	1.6 (0.8)	0.220 (0.063)	80.0 (7.9)	0.050 (0.0035)	108.1 (8.8)	10.1 (0.5)	288.3 (5.3)	0.062 (0.0003)	104.9 (0.6)	77.3	86.3	85.7
64.77	1.3 (1.2)	0.217 (0.106)	80.3 (13.4)	0.049 (0.0086)	105.4 (21.3)	10.2 (0.5)	333.4 (17.1)	0.065 (0.0009)	112.0 (2.3)	72.0	100.2	98.9
Goethite (2 g/L) + DOPA (1 mM) + 1 mM Fe(II)												
0	14.8 (0.1)	0.911 (0.0013)	0	0.0037 (0.0001)	0	1.1 (0.2)	323.7 (13.6)	0.024 (0.0002)	0	100.0	100.0	100.0
29.89	1.9 (0.2)	0.791 (0.022)	14.2 (2.6)	0.0113 (0.0005)	17.8 (3.1)	15.1 (0.9)	304.1 (2.1)	0.073 (0.0005)	160.4 (1.2)	106.9	89.6	90.5
61.77	1.0 (0.0)	0.744 (0.009)	19.7 (1.1)	0.0140 (0.0008)	23.9 (1.8)	14.7 (1.1)	455.3 (25.2)	0.074 (0.0003)	164.0 (0.7)	98.2	136.7	134.9

Table 3.9. Mass and Fe isotope data for Fe isotope tracer experiments between aqueous Fe(II) and magnetite with various forms of organic carbon present.

	Aqueous Fe(II)					Solids				% Recovery		
Time (d)	Fe (mmoles)	f^{57}Fe	% exchange	f^{54}Fe	% exchange	Fe(II) (mmoles)	Total Fe (mmoles)	f^{57}Fe	% exchange	Fe(II)	Fe(III)	Total Fe
Magnetite (2 g/L) + 1 mM Fe(II) (pH 7.5 HEPES)												
0.00	14.8 (0.1)	0.774 (0.044)	0	0.010 (0.003)	0	124.5 (19.9)	357.2 (1.7)	0.021 (3E-5)	0	100.0	100.0	100.0
0.05	14.7 (0.4)	0.570 (0.046)	35.7 (5.8)	0.022 (0.002)	37.6 (5.9)	158.2 (28.9)	407.5 (32.3)	0.039 (0.0004)	53.7 (1.3)	124.0	107.1	113.5
6.67	11.3 (0.2)	0.232 (0.020)	75.0 (2.8)	0.038 (0.001)	75.5 (3.8)	128.8 (10.2)	363.2 (34.7)	0.045 (0.001)	77.4 (3.6)	100.6	100.7	100.7
62.95	7.5 (0.5)	0.196 (0.032)	82.3 (4.0)	0.037 (0.002)	74.6 (3.9)	175.7 (32.1)	428.8 (119.3)	0.052 (0.002)	92.2 (6.4)	131.5	108.8	117.3
Magnetite (1 g/L) + 1 mM Fe(II) (pH 7.2 MOPS)												
0.00	14.8 (0.1)	0.774 (0.044)	0	0.010 (0.003)	0	46.4 (5.5)	184.2 (24.0)	0.021 (3E-5)	0	100.0	100.0	100.0
0.05	17.1 (1.0)	0.625 (0.059)	30.9 (7.8)	0.016 (0.003)	25.6 (6.7)	55.5 (4.0)	149.3 (13.3)	0.037 (0.001)	18.4 (0.7)	118.4	66.9	82.8
0.97	15.3 (1.0)	0.468 (0.031)	51.9 (4.1)	0.024 (0.002)	45.7 (4.1)	56 (1.7)	151.3 (8.9)	0.053 (0.001)	36.6 (1.3)	116.4	69.3	83.8
6.85	12.6 (0.5)	0.433 (0.023)	56.5 (3.1)	0.026 (0.001)	50.1 (2.8)	37.8 (0.9)	97.5 (9.8)	0.059 (0.001)	43.8 (1.0)	82.3	43.4	55.4
34.82	12.3 (0.3)	0.286 (0.056)	76.1 (7.5)	0.036 (0.003)	78.9 (7.9)	137.7 (18.4)	496.3 (103.0)	0.049 (0.005)	32.0 (5.5)	244.8	260.9	255.9
57.95	13.6 (2.0)	0.259 (0.049)	79.8 (6.5)	0.038 (0.003)	82.8 (6.8)	293.8 (50.4)	251.5 (11.6)	0.054 (0.001)	38.0 (1.4)	501.7	-30.8	133.9
Magnetite (2 g/L) + riboflavin (1 mM) + 1 mM Fe(II)												
0.00	14.8 (0.1)	0.774 (0.044)	0	0.010 (0.003)	0	124.5 (19.9)	357.2 (1.7)	0.021 (3E-5)	0	100.0	100.0	100.0
0.07	14.0 (1.1)	0.519 (0.028)	42.1 (3.5)	0.021 (0.002)	36.6 (3.8)	160.1 (0.8)	406.4 (25.6)	0.039 (0.0008)	53.4 (2.3)	124.9	105.9	
7.00	8.9 (2.7)	0.249 (0.009)	72.7 (1.2)	0.035 (0.0004)	67.4 (1.1)	213.5 (32.6)	526.8 (115.6)	0.044 (0.0008)	76.5 (2.7)	159.6	134.6	
62.68	6.4 (1.6)	0.107 (0.017)	91.1 (2.6)	0.042 (0.001)	82.8 (2.7)	113.4 (9.2)	345.3 (17.6)	0.037 (0.0005)	56.1 (1.7)	86.0	99.7	

Table 3.9 – continued

Magnetite (2 g/L) + AQDS (1 mM) + 1 mM Fe(II)												
0	14.8 (0.1)	0.774 (0.044)	0	0.010 (0.003)	0	124.5 (19.9)	357.2 (1.7)	0.021 (3E-5)	0	100.0	100.0	100.0
0.08	10.2 (1.5)	0.548 (0.095)	38.5 (11.9)	0.020 (0.005)	34.0 (12.5)	139.6 (33.3)	333.1 (41.8)	0.043 (0.0004)	65.9 (1.3)	107.5	83.2	92.3
9.18	9.6 (0.7)	0.260 (0.028)	71.1 (3.9)	0.036 (0.004)	69.0 (9.4)	146.8 (23.8)	393.7 (20.3)	0.046 (0.001)	82.7 (4.7)	112.3	106.1	108.4
62.68	5.6 (1.6)	0.071 (0.010)	96.6 (1.5)	0.048 (0.002)	102.1 (5.8)	100.3 (6.4)	314.5 (21.1)	0.037 (0.0007)	56.1 (2.7)	76.0	92.0	86.0
Magnetite (2 g/L) + Sigma Aldrich Humic Acid (20 mg/L) + 1 mM Fe(II)												
0.00	14.8 (0.1)	0.774 (0.044)	0	0.010 (0.003)	0	124.5 (19.9)	357.2 (1.7)	0.021 (3E-5)	0	100.0	100.0	100.0
0.05	14.0 (1.1)	0.552 (0.046)	38.1 (5.8)	0.023 (0.003)	40.2 (6.1)	145.8 (8.6)	395.2 (8.7)	0.038 (0.001)	49.1 (3.1)	114.6	107.2	110.0
6.67	11.7 (1.2)	0.257 (0.009)	71.5 (1.2)	0.037 (0.0003)	71.6 (0.9)	143.8 (11.3)	303.2 (30.0)	0.045 (0.0004)	78.9 (1.2)	111.6	68.5	84.6
62.68	6.8 (1.6)	0.071 (0.031)	96.6 (4.7)	0.052 (0.003)	113.6 (10.4)	135.7 (31.6)	479.2 (110.5)	0.036 (0.001)	53.1 (3.7)	102.3	147.6	130.6
Magnetite (2 g/L) + Elliot Soil Humic Acid (40 mg/L) + 1 mM Fe(II)												
0.00	14.8 (0.1)	0.774 (0.044)	0	0.010 (0.003)	0	124.5 (19.9)	357.2 (1.7)	0.021 (3E-5)	0	100.0	100.0	100.0
0.05	13.8 (1.3)	0.479 (0.102)	47.1 (12.8)	0.027 (0.005)	50.4 (12.2)	112.7 (20.4)	306.4 (46.6)	0.037 (0.001)	47.4 (3.5)	90.8	83.2	86.1
6.92	9.6 (1.5)	0.236 (0.007)	74.4 (1.0)	0.043 (0.0007)	87.3 (1.8)	222.9 (0.6)	485.2 (1.5)	0.045 (0.002)	78.7 (6.7)	166.9	112.7	133.0
62.68	7.2 (1.2)	0.108 (0.008)	91.0 (1.2)	0.050 (0.001)	107.6 (3.1)	95.9 (9.8)	258.5 (3.9)	0.038 (0.0007)	60.2 (2.5)	74.0	69.9	71.4
Magnetite (2 g/L) + Suwanee River Fulvic Acid (8 mg/L) + 1 mM Fe(II)												
0.00	14.8 (0.1)	0.774 (0.044)	0	0.010 (0.003)	0	124.5 (19.9)	357.2 (1.7)	0.021 (3E-5)	0	100.0	100.0	100.0
1.18	10.0 (0.5)	0.429 (0.033)	56.5 (3.8)	0.030 (0.003)	60.7 (7.1)	137.6 (18.2)	384.2 (63.1)	0.049 (0.0016)	77.5 (4.6)	105.9	106	105.9
7.00	5.9 (0.2)	0.309 (0.015)	68.3 (1.9)	0.037 (0.001)	74.2 (1.5)	134.4 (1.5)	415.5 (111.4)	0.048 (0.0002)	80.1 (0.5)	100.7	120.8	1
30.94	7.0 (0.5)	0.279 (0.028)	72.0 (3.4)	0.038 (0.002)	77.7 (4.0)	112.4 (4.2)	332.8 (4.3)	0.051 (0.0002)	89.1 (0.6)	85.7	94.7	
65.03	6.9 (0.3)	0.292 (0.019)	70.3 (2.4)	0.040 (0.001)	81.8 (2.5)	138.5 (11.0)	368.3 (12.9)	0.055 (0.0003)	101.5 (0.8)	104.3	98.8	1

Table 3.9 – continued

Magnetite (2 g/L) + Suwanee River Fulvic Acid (40 mg/L) + 1 mM Fe(II)												
0	14.8 (0.1)	0.774 (0.044)	0	0.010 (0.003)	0	124.5 (19.9)	357.2 (1.7)	0.021 (3E-5)	0	100.0	100.0	100.0
0.06	16.3 (2.3)	0.624 (0.005)	29.0 (0.6)	0.020 (0.0002)	32.2 (0.5)	157.3 (20.0)	373.5 (24.6)	0.036 (0.0007)	44.9 (2.1)	124.6	92.9	104.8
6.92	8.8 (0.6)	0.251 (0.007)	72.4 (1.0)	0.042 (0.0006)	85.2 (1.6)	211.2 (28.5)	479.8 (25.4)	0.043 (0.001)	72.9 (3.6)	157.9	115.4	131.3
62.68	4.8 (0.0)	0.121 (0.006)	89.0 (0.9)	0.050 (0.0004)	108.2 (1.2)	120.7 (6.2)	443.8 (79.4)	0.036 (0.001)	52.3 (4.2)	90.1	138.9	120.6
Magnetite (2 g/L) + CZO Soil Extract (17 mg / L) + 1 mM Fe(II)												
0.00	14.8 (0.1)	0.774 (0.044)	0	0.010 (0.003)	0	124.5 (19.9)	357.2 (1.7)	0.021 (3E-5)	0	100.0	100.0	100.0
1.17	9.6 (0.5)	0.342 (0.004)	66.6 (0.5)	0.038 (0.004)	78.5 (8.4)	136.0 (13.6)	392.3 (93.3)	0.050 (0.0019)	80.0 (5.4)	104.5	110.2	108.0
6.98	6.1 (0.2)	0.318 (0.007)	67.1 (0.9)	0.036 (0.001)	72.8 (1.6)	151.2 (16.9)	412.0 (41.6)	0.048 (0.0007)	80.0 (2.2)	112.9	112.1	112.4
31.15	7.9 (0.5)	0.280 (0.028)	71.9 (3.4)	0.038 (0.002)	77.2 (3.7)	130.3 (0.6)	389.0 (9.1)	0.048 (0.0006)	80.3 (1.8)	99.2	111.2	106.7
69.98	7.8 (0.6)	0.285 (0.033)	71.3 (4.1)	0.039 (0.0017)	80.7 (4.1)	150.8 (20.7)	405.7 (48.4)	0.053 (0.0027)	94.5 (8.1)	113.9	109.5	111.2
Magnetite (2 g/L) + Alginic Acid (500 mg/L) + 1 mM Fe(II)												
0	14.8 (0.1)	0.774 (0.044)	0	0.010 (0.003)	0	124.5 (19.9)	357.2 (1.7)	0.021 (3E-5)	0	100.0	100.0	100.0
0.06	16.9 (2.4)	0.516 (0.020)	42.5 (2.5)	0.022 (0.001)	38.8 (2.2)	104.8 (5.0)	325.6 (10.3)	0.031 (0.0009)	27.5 (2.7)	87.3	94.9	92.1
7.32	11.2 (1.3)	0.240 (0.031)	73.9 (4.3)	0.036 (0.002)	69.3 (4.1)	111.9 (15.9)	322.9 (39.1)	0.042 (0.002)	69.5 (6.4)	88.3	90.7	89.8
64.1	10.2 (1.2)	0.206 (0.016)	76.1 (2.4)	0.0362 (0.001)	64.6 (3.4)	126.5 (2.3)	340.8 (6.7)	0.046 (0.0002)	89.5 (0.6)	98.1	92.1	94.3
Magnetite (2 g/L) + Polygalacturonic Acid (500 mg/L) + 1 mM Fe(II)												
0	14.8 (0.1)	0.774 (0.044)	0	0.010 (0.003)	0	124.5 (19.9)	357.2 (1.7)	0.021 (3E-5)	0	100.0	100.0	100.0
0.07	10.4 (0.9)	0.430 (0.001)	53.2 (0.2)	0.027 (0.0003)	51.2 (0.7)	98.5 (7.6)	305.3 (26.0)	0.032 (0.0006)	31.4 (1.8)	78.2	88.8	84
7.31	6.7 (0.5)	0.217 (0.005)	77.1 (0.6)	0.038 (0.0006)	73.6 (1.5)	114.4 (2.9)	324.1 (14.3)	0.044 (0.004)	74.4 (11.6)	86.9	90.1	88
64.13	6.4 (0.4)	0.173 (0.029)	81.2 (4.3)	0.038 (0.001)	70.9 (4.3)	103.2 (30.7)	283.6 (85.5)	0.047 (0.002)	95.4 (8.8)	78.7	77.5	78

Table 3.9 – continued

Magnetite (2 g/L) + Xanthan Gum (500 mg/L) + 1 mM Fe(II)												
0	14.8 (0.1)	0.774 (0.044)	0	0.010 (0.003)	0	124.5 (19.9)	357.2 (1.7)	0.021 (3E-5)	0	100.0	100.0	100.0
0.09	13.2 (2.7)	0.498 (0.079)	44.8 (9.9)	0.023 (0.004)	41.6 (9.8)	107.7 (3.4)	320.9 (11.3)	0.032 (0.0004)	30.4 (1.2)	86.8	91.6	89.8
7.30	9.3 (0.7)	0.249 (0.084)	72.7 (11.7)	0.037 (0.004)	70.9 (10.6)	102.8 (12.3)	289.3 (27.5)	0.046 (0.002)	81.0 (6.2)	80.5	80.2	80.3
64.13	7.8 (0.7)	0.198 (0.017)	77.3 (2.5)	0.037 (0.001)	66.4 (2.2)	109.2 (5.1)	296.4 (3.1)	0.046 (0.0006)	89.8 (2.2)	84.0	80.4	81.8
Magnetite (2 g/L) + Spent LB Medium (1:10) + 1 mM Fe(II)												
0.00	14.8 (0.1)	0.774 (0.044)	0	0.010 (0.003)	0	124.5 (19.9)	357.2 (1.7)	0.021 (3E-5)	0	100.0	100.0	100.0
1.16	7.3 (0.8)	0.610 (0.021)	35.3 (2.4)	0.022 (0.001)	42.8 (2.4)	121.1 (1.7)	349.6 (4.7)	0.050 (0.0003)	81.9 (0.9)	92.1	98.2	95.9
6.99	5.7 (0.2)	0.501 (0.015)	44.3 (1.8)	0.027 (0.002)	50.2 (4.0)	151.2 (27.1)	443.6 (5.3)	0.046 (0.0003)	73.9 (0.8)	112.6	125.7	120.8
29.99	4.3 (1.4)	0.374 (0.027)	60.2 (3.4)	0.035 (0.003)	69.9 (7.4)	207.1 (27.1)	580.5 (32.3)	0.048 (0.0034)	81.4 (10.2)	151.7	160.5	157.2
69.84	2.8 (2.1)	0.304 (0.073)	68.9 (9.2)	0.041 (0.006)	85.3 (14.7)	168.0 (28.9)	549.1 (123.6)	0.054 (0.0041)	97.9 (12.3)	122.6	163.8	148.3
Magnetite (2 g/L) + Spent Defined Mineral Medium (1:10) + 1 mM Fe(II)												
0.00	14.8 (0.1)	0.774 (0.044)	0	0.010 (0.003)	0	124.5 (19.9)	357.2 (1.7)	0.021 (3E-5)	0	100.0	100.0	100.0
1.18	8.2 (0.3)	0.593 (0.026)	37.2 (3.0)	0.024 (0.002)	46.0 (3.9)	152.1 (10.2)	413.1 (34.4)	0.048 (0.0014)	74.4 (4.0)	115.1	112.3	113.3
7.00	4.9 (0.4)	0.365 (0.011)	61.3 (1.3)	0.034 (0.0002)	68.1 (0.6)	151.8 (6.1)	401.6 (22.8)	0.047 (0.0009)	76.6 (2.8)	112.4	107.4	109.3
29.76	4.6 (0.1)	0.372 (0.054)	60.3 (6.7)	0.034 (0.003)	67.3 (7.0)	125.1 (4.0)	318.2 (29.2)	0.049 (0.0004)	82.5 (1.3)	93.1	83.0	86.8
62.92	5.0 (0.7)	0.420 (0.032)	54.5 (4.0)	0.033 (0.002)	64.6 (5.8)	140.5 (7.5)	378.1 (33.5)	0.056 (0.0005)	103.7 (1.6)	104.4	102.1	103.0
Magnetite (2 g/L) + DOPA (1 mM) + 1 mM Fe(II)												
0.00	14.8 (0.1)	0.774 (0.044)	0	0.010 (0.003)	0	124.5 (19.9)	357.2 (1.7)	0.021 (3E-5)	0	100.0	100.0	10(
29.98	5.3 (0.5)	0.709 (0.007)	23.7 (0.8)	0.016 (0.0006)	29.1 (1.5)	127.3 (9.6)	387.5 (4.8)	0.054 (0.0005)	90.6 (1.3)	95.2	111.8	10:
61.84	4.9 (0.1)	0.698 (0.016)	25.0 (1.9)	0.017 (0.0006)	30.6 (1.5)	166.7 (62.6)	479.5 (31.0)	0.058 (0.0006)	104.3 (1.7)	123.1	134.4	13(

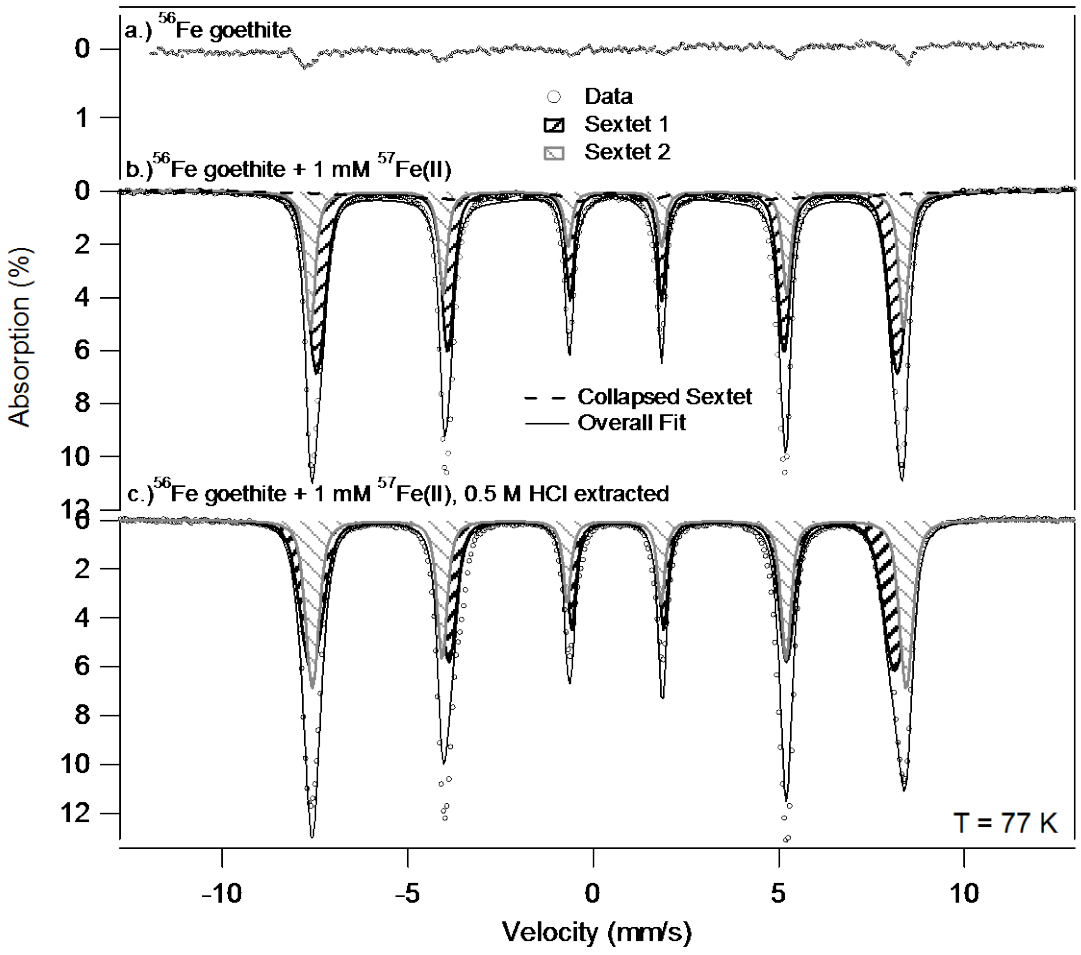

Figure 3.1. 77 K Mössbauer spectra of ^{56}Fe goethite reacted with ^{57}Fe(II). (a) shows ^{56}Fe goethite prior to reaction, (b) shows ^{56}Fe goethite reacted with ^{57}Fe(II), and (c) shows ^{56}Fe goethite reacted with ^{57}Fe(II) and extracted with 0.5 M HCl. Fit parameters are reported in Table 3.6.

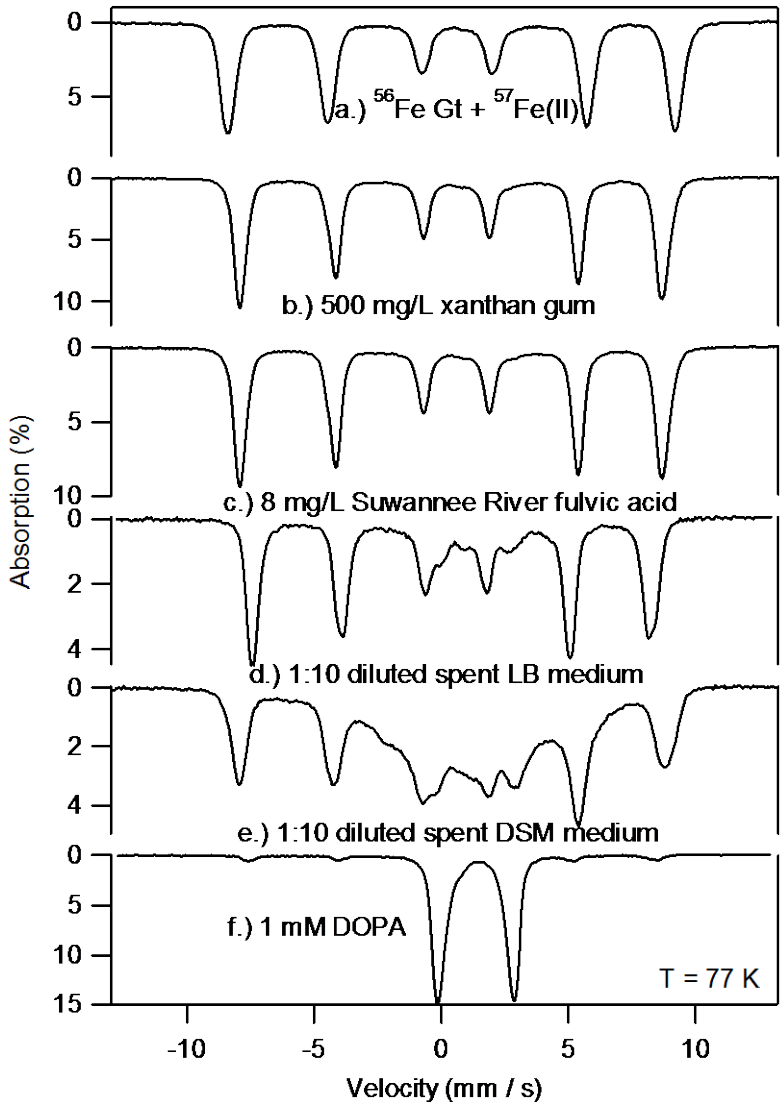

Figure 3.2. 77 K Mössbauer spectra of ^{57}Fe(II) reacted with ^{56}Fe goethite in the presence of organic carbon. (a) control with no organic carbon present, (b) 500 mg/L xanthan gum, (c) 8 mg/L Suwannee River Fulvic Acid, (d) a tenfold dilution of spent luria broth (LB) medium from a culture of *Shewanella oneidensis* MR-1, (e) a tenfold dilution of spent defined mineral medium (DSM) from *S. oneidensis* MR-1, and (f) 1 mM DOPA. Fitting parameters are reported in Table 3.6.

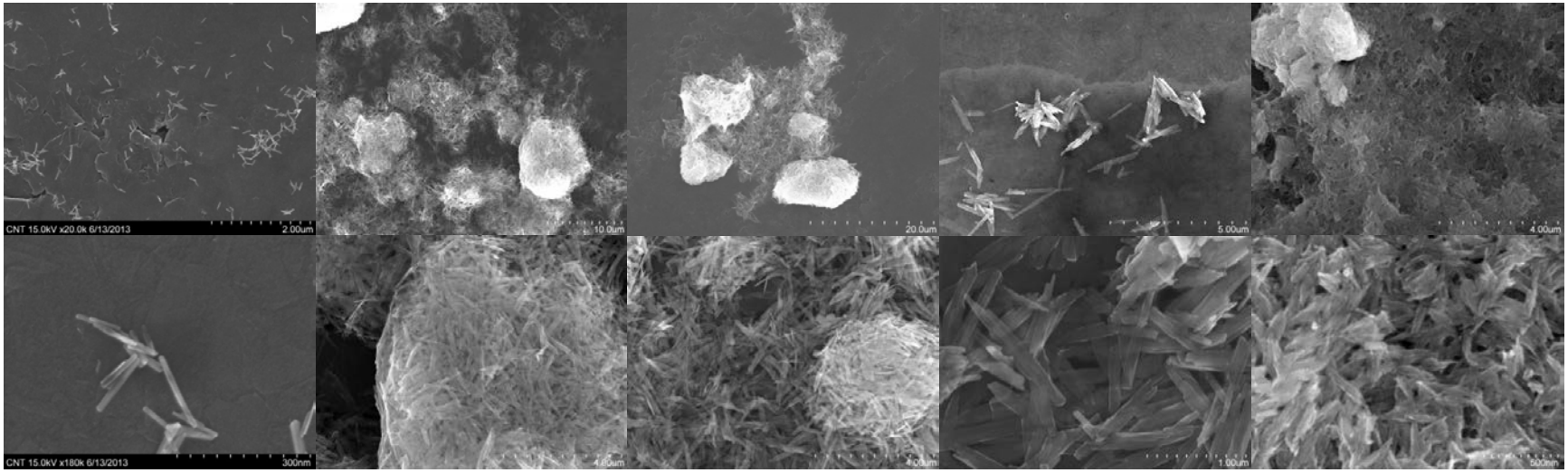

a) Untreated goethite b) AA c) PGA d) XG e) DOPA

Figure 3.3. Scanning electron microscope images of goethite reacted with organic carbon compounds. Images include goethite with no organic carbon (a), and goethite following equilibration with alginic acid (b), polygalacturonic acid (c), xanthan gum (d), and DOPA phospholipid (e) at lower (upper panel) and higher magnification (lower panel).

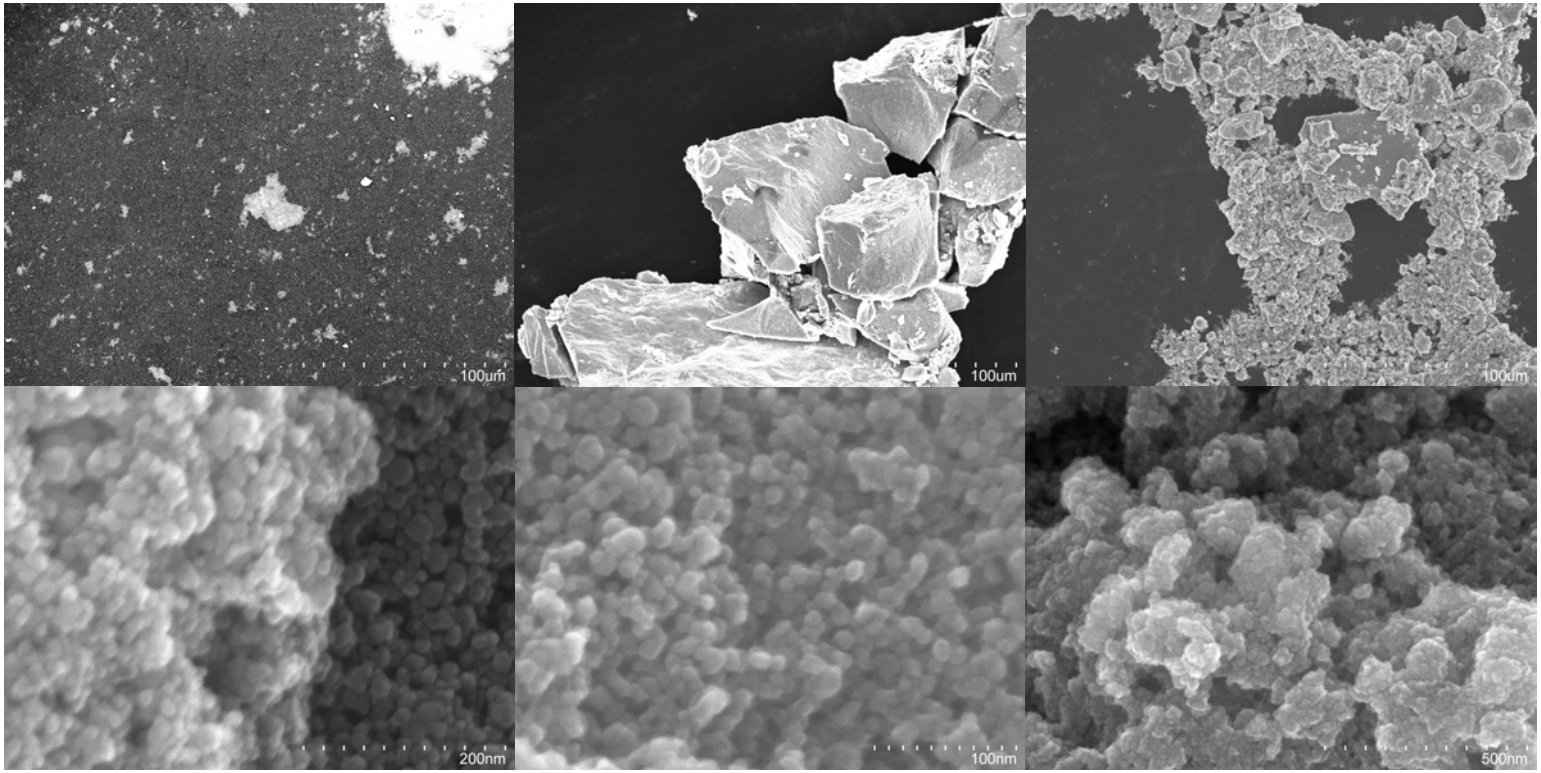

Figure 3.4. Scanning electron microscope images of magnetite reacted with organic carbon. Images include untreated magnetite (a) and magnetite following equilibration with xanthan gum (b) and DOPA phospholipid (c) at lower (upper panel) and higher magnification (lower panel).

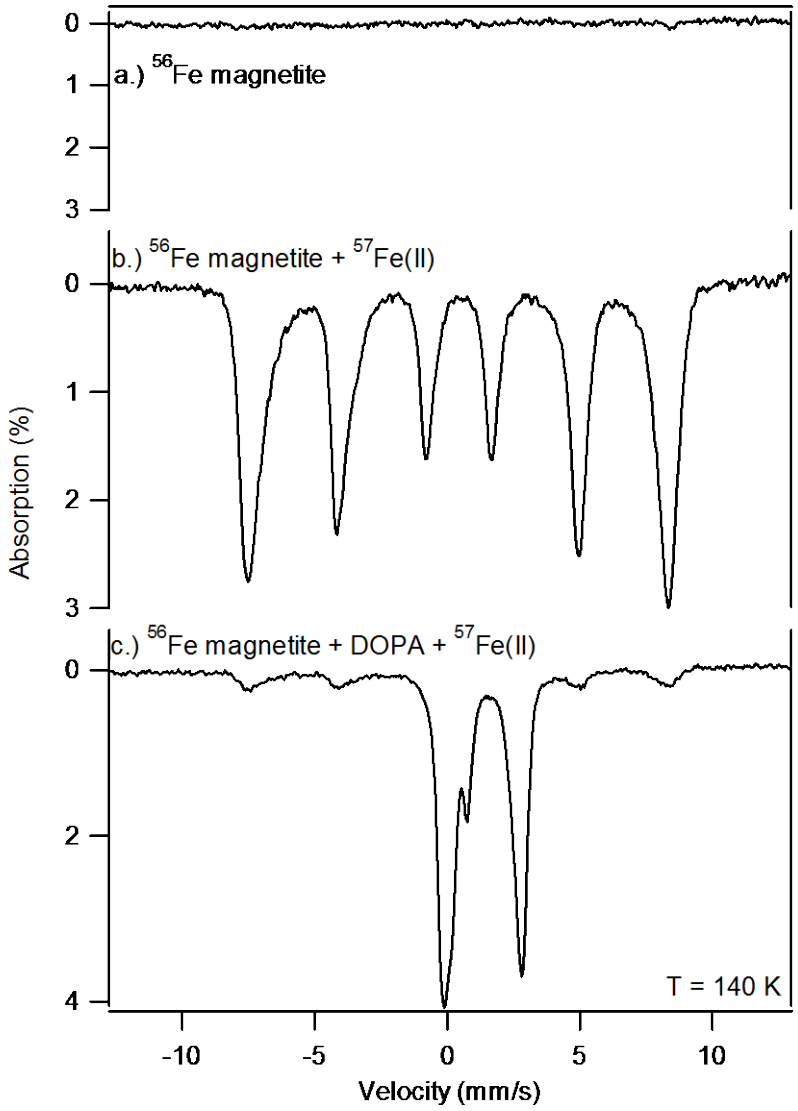

Figure 3.5. Mössbauer spectra of ^{57}Fe(II) reacted with ^{56}Fe magnetite in the absence and presence of 1 mM phospholipid (DOPA). (a) unreacted ^{56}Fe magnetite, (b) ^{56}Fe magnetite reacted with ^{57}Fe(II), (c) ^{56}Fe magnetite reacted with ^{57}Fe(II) after exposure to DOPA. Fitting parameters are reported in Table 3.7.

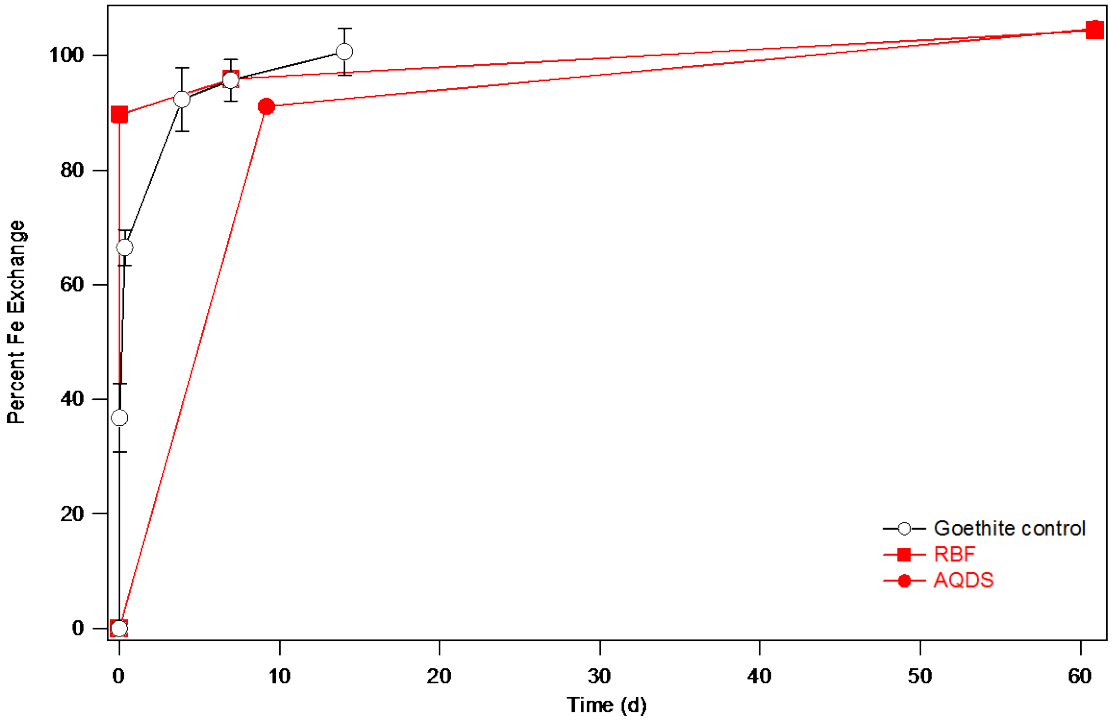

Figure 3.6. Extent of Fe(II)-catalyzed recrystallization of 2 g/L goethite in control experiments and in the presence of electron shuttling compounds. Recrystallization experiments were performed with 1 mM initial aqueous ^{57}Fe(II) at pH 7.5.

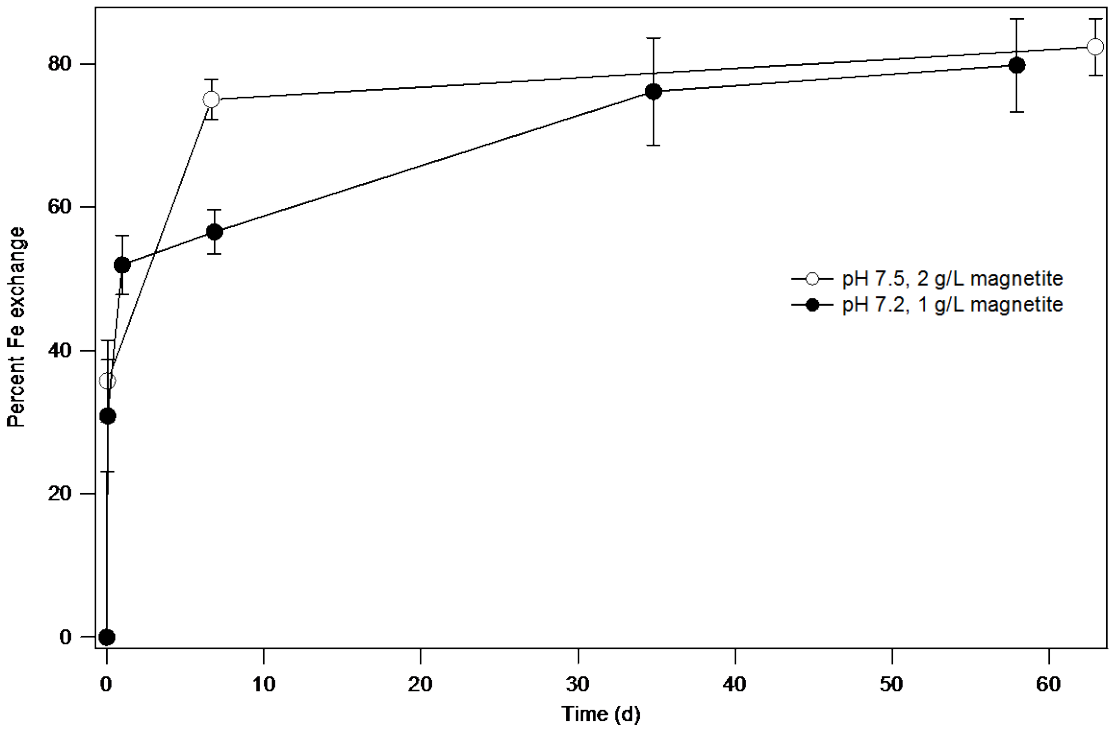

Figure 3.7. Effect of pH and solids loading on Fe(II)-catalyzed recrystallization of magnetite.

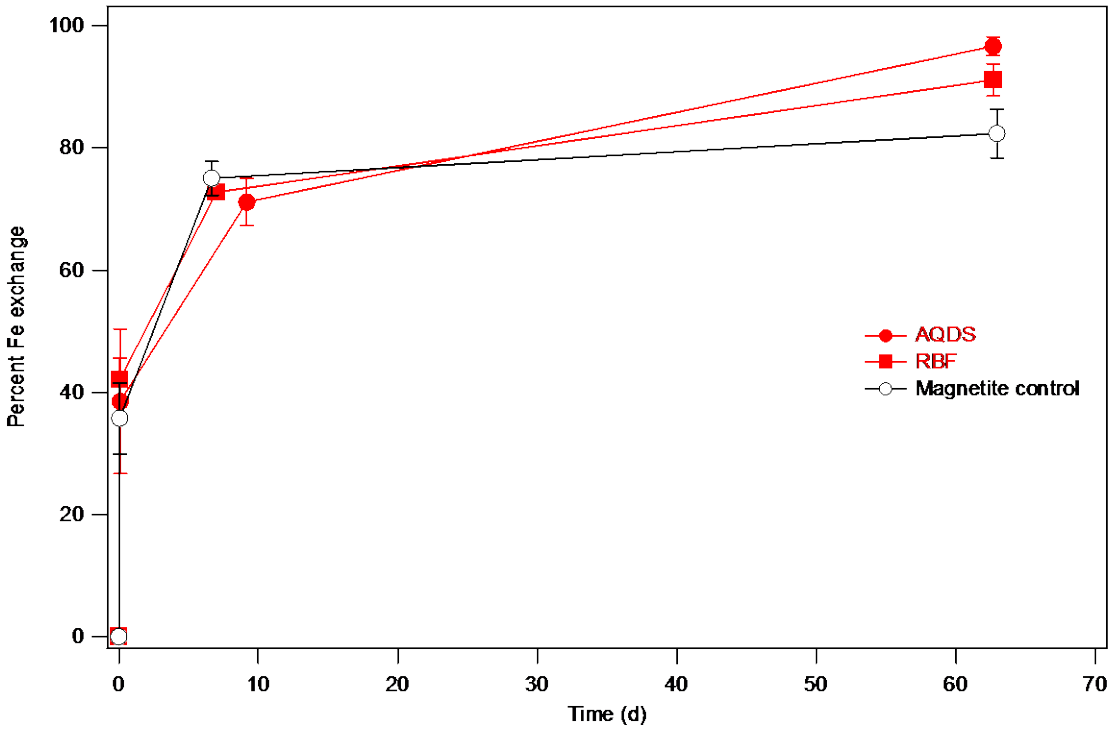

Figure 3.8. Extent of Fe(II)-catalyzed recrystallization of 2 g/L magnetite in control experiments and in the presence of electron shuttling compounds. Recrystallization experiments were performed with 1 mM initial aqueous ^{57}Fe(II) at pH 7.5.

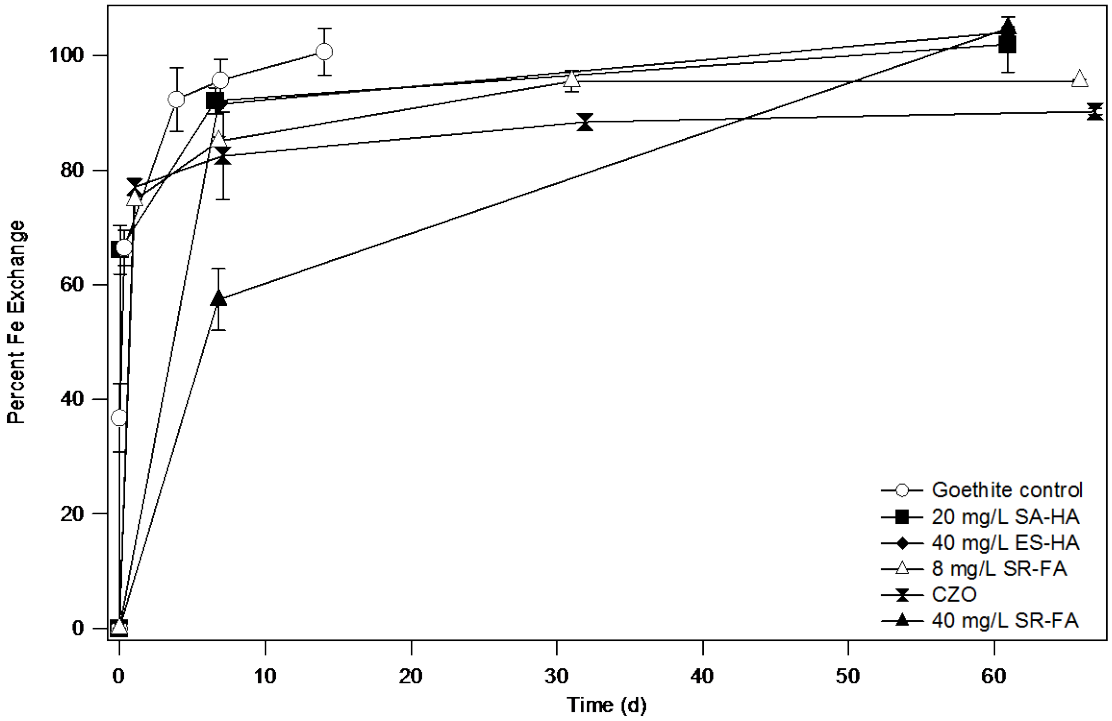

Figure 3.9. Effect of sorbed and dissolved natural organic matter isolates on Fe(II)-catalyzed recrystallization of 2 g/L goethite. Recrystallization experiments were performed with 1 mM initial aqueous ^{57}Fe(II) at pH 7.5.

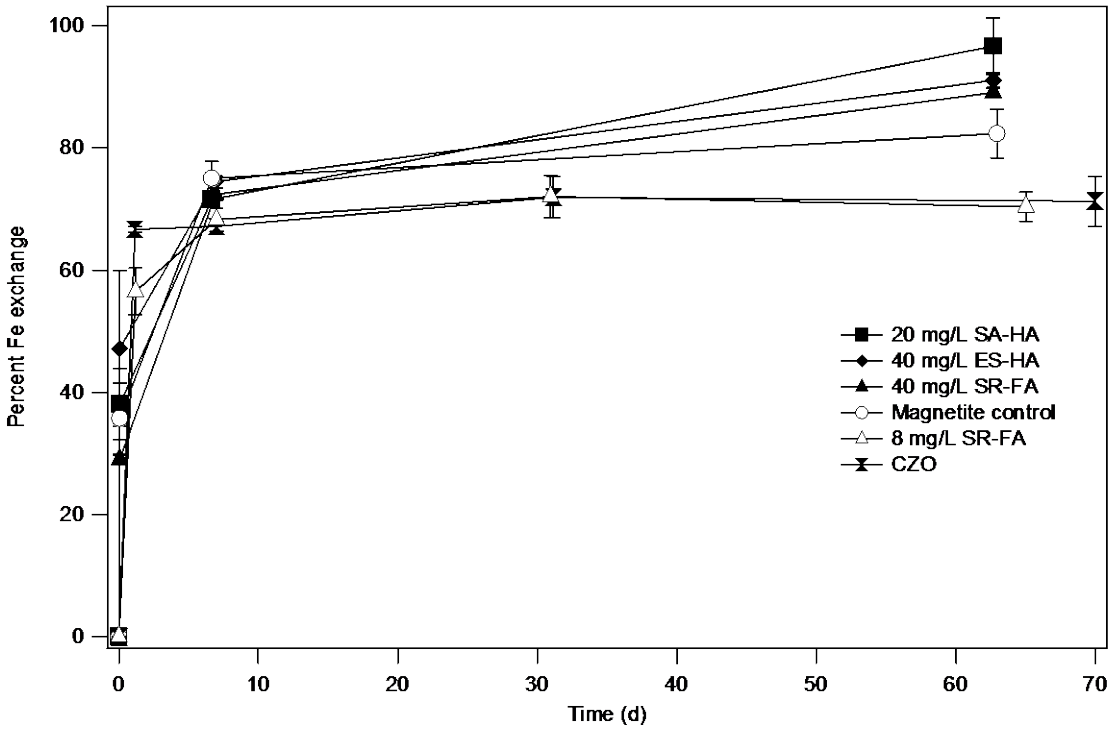

Figure 3.10. Effect of sorbed and dissolved natural organic matter isolates on Fe(II)-catalyzed recrystallization of 2 g/L magnetite. Recrystallization experiments were performed with 1 mM initial aqueous ^{57}Fe(II) at pH 7.5.

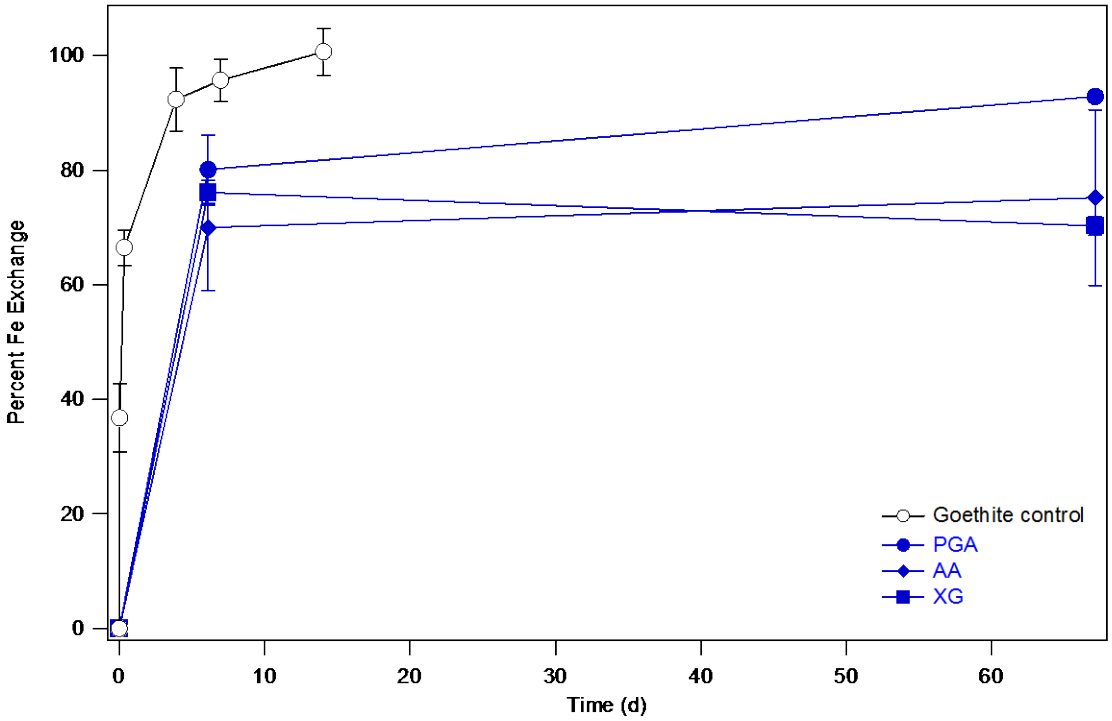

Figure 3.11. Influence of extracellular polysaccharides on Fe(II)-catalyzed recrystallization of 2 g/L goethite. Recrystallization experiments were performed with 1 mM initial aqueous ^{57}Fe(II) at pH 7.5.

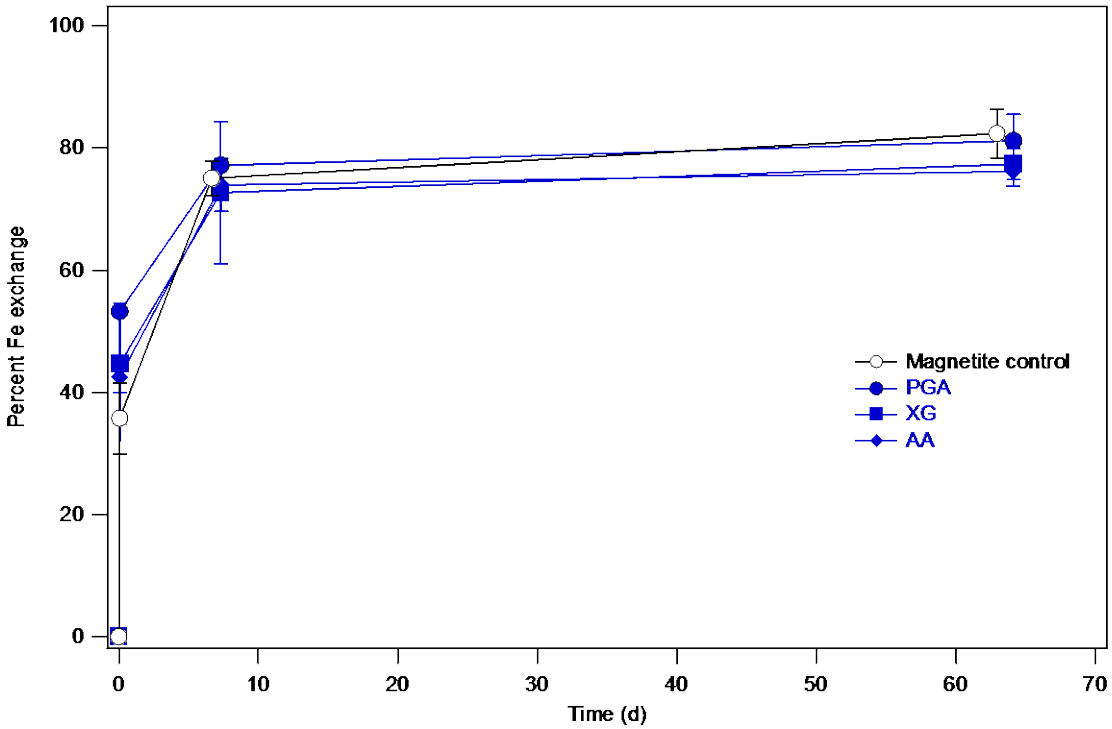

Figure 3.12. Influence of extracellular polysaccharides on Fe(II)-catalyzed recrystallization of 2 g/L magnetite. Recrystallization experiments were performed with 1 mM initial aqueous ^{57}Fe(II) at pH 7.5.

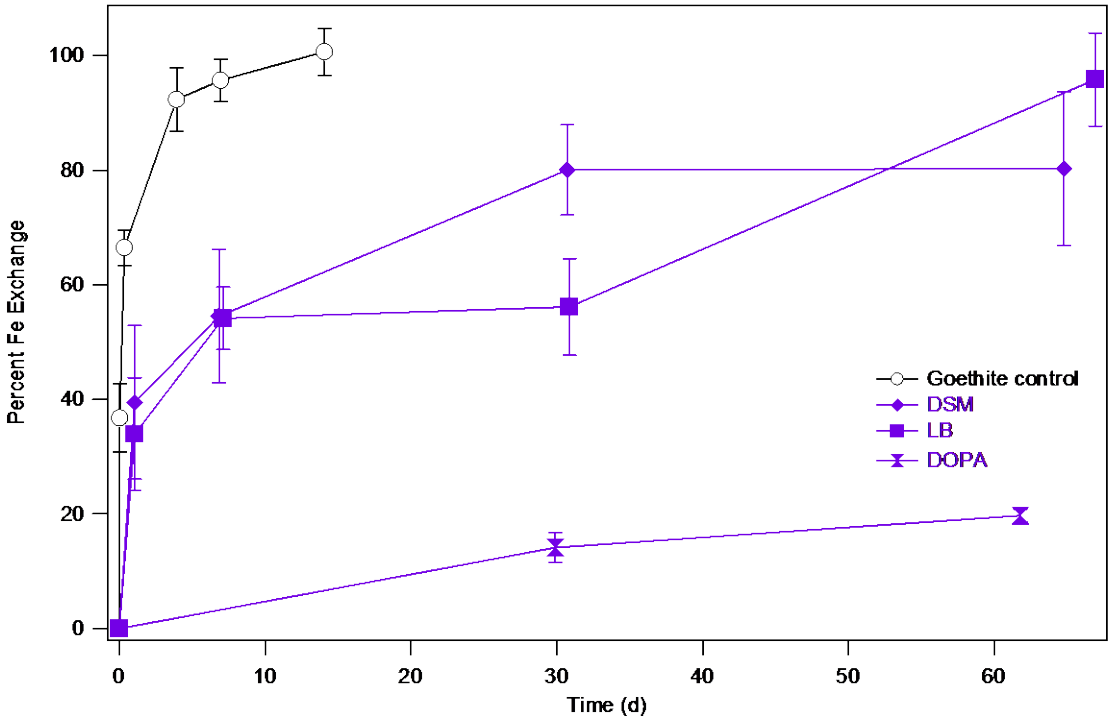

Figure 3.13. Influence of bacterial exudates from dissimilatory iron reducing cultures and phospholipids on Fe(II)-catalyzed recrystallization of 2 g/L goethite. Recrystallization experiments were performed with 1 mM initial aqueous ^{57}Fe(II) at pH 7.5.

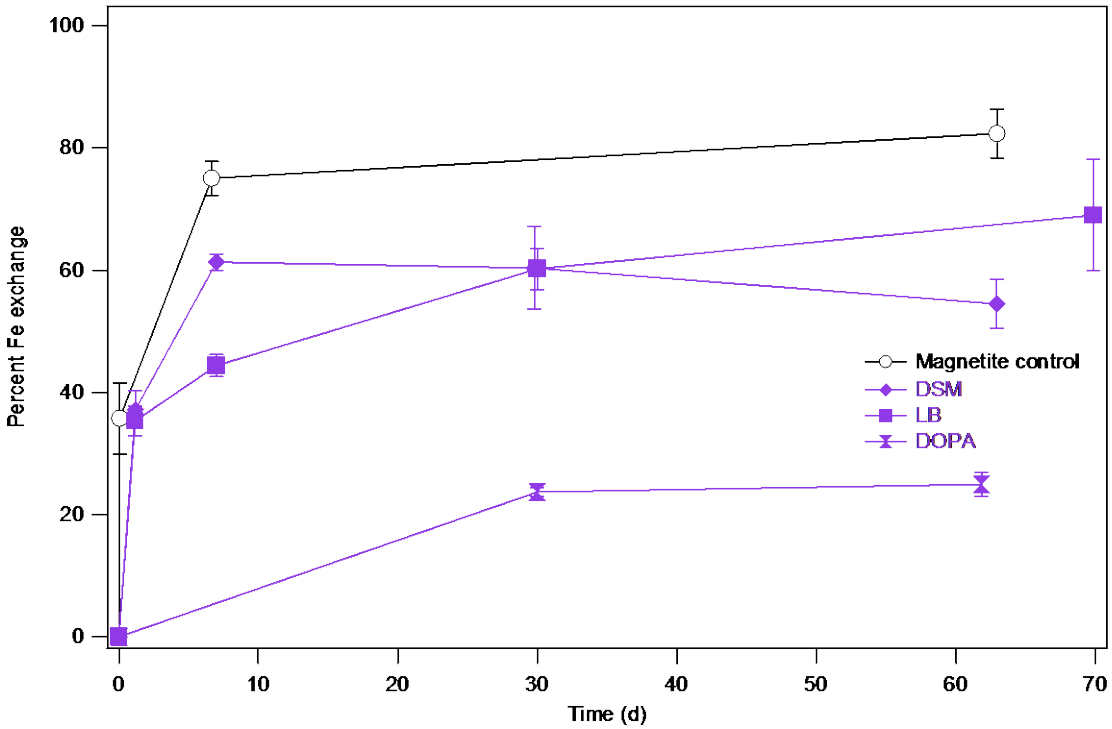

Figure 3.14. Influence of bacterial exudates from dissimilatory iron reducing cultures and phospholipids on Fe(II)-catalyzed recrystallization of 2 g/L magnetite. Recrystallization experiments were performed with 1 mM initial aqueous ^{57}Fe(II) at pH 7.5.

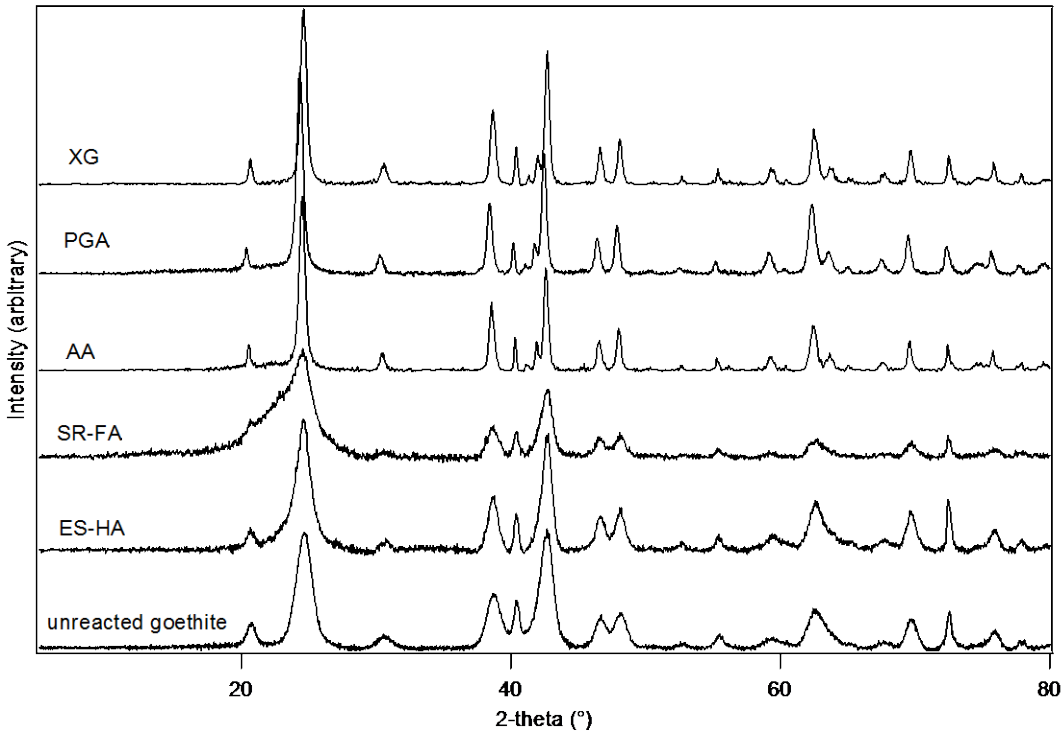

Figure 3.15. X-ray diffraction spectra of goethite before and after reaction with $^{57}Fe(II)$ in the presence of organic carbon compounds.

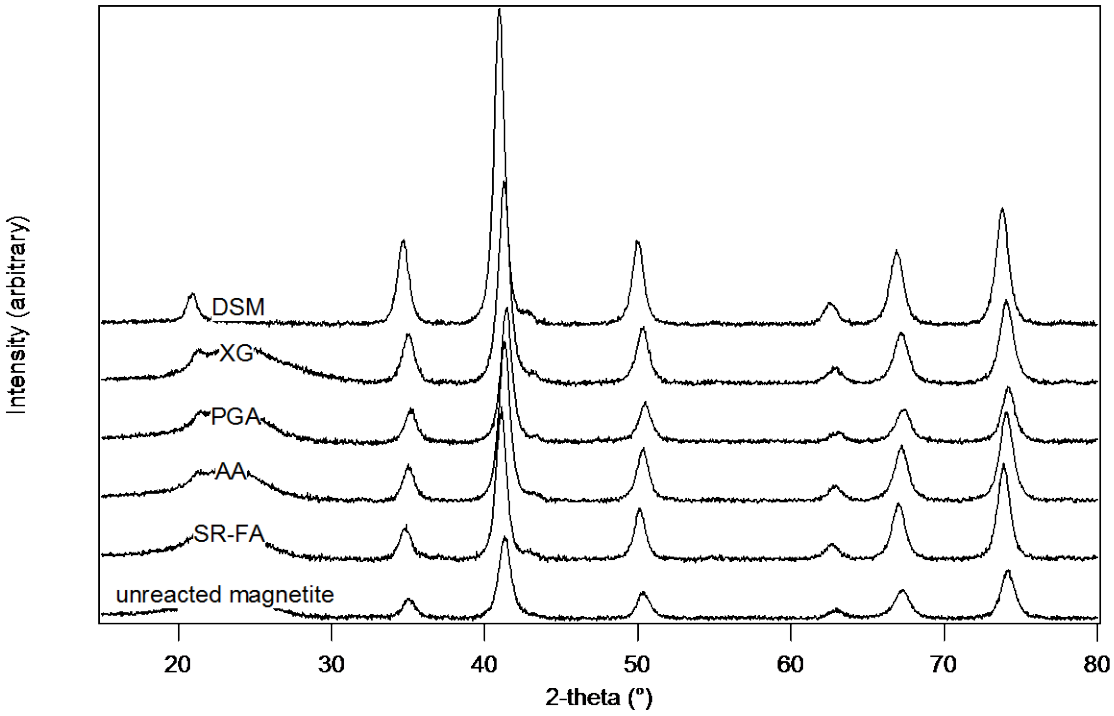

Figure 3.16. X-ray diffraction spectra of magnetite before and after reaction with $^{57}Fe(II)$ in the presence of organic carbon compounds.

CHAPTER 4: EFFECT OF ORGANIC CARBON ON FE(II) TRANSFORMATION OF FERRIHYDRITE

Abstract

The association of iron (Fe) and organic carbon has been well documented in soils and sediments throughout the environment, and often results in long-term stabilization of both iron and carbon. Aqueous Fe(II) has been shown to catalyze secondary mineral transformation of unstable Fe oxides such as ferrihydrite and lepidocrocite, resulting in significant Fe atom mixing between the aqueous and solid phases and the formation of new phases. Here we examine how the presence of sorbed and coprecipitated organic carbon influences the Fe(II)-catalyzed transformation of ferrihydrite. We observed minor influence of carbon on the dissolution of ferrihydrite-humic acid coprecipitates with higher C:Fe ratios corresponding to slower dissolution. Using a ^{57}Fe labeled tracer and stable isotope measurements, we found that Fe atom exchange still occurs with increasing levels of organic carbon, which had little effect on the rate of atom exchange regardless of whether it was sorbed or coprecipitated. Interestingly though, exchange was slightly faster for the coprecipitates with higher C:Fe ratios. The presence of organic carbon did influence secondary mineral transformation over longer time periods (15-29 days) by preventing transformation of lepidocrocite to magnetite or goethite as identified by x-ray diffraction.

Introduction

Soils represent the second largest global reservoir of carbon (C), storing as much as three times the amount present in either the atmosphere or terrestrial vegetation in the form of soil organic matter (SOM) (141). Extensive research into the mechanisms of SOM stabilization and degradation has uncovered a dynamic interplay of biological, physical, and chemical processes that ultimately lead to residence times that range from years to hundreds of years (142). As atmospheric carbon dioxide levels continue to rise,

a detailed understanding of the factors controlling C storage and release in soils will be critical for predicting feedback between soils and the atmosphere, and establishing best management practices to promote / maintain C storage in soils.

The association between organic carbon (OC) and Fe minerals throughout the environment is a phenomenon that has been observed for decades (e.g., 143, 144), though it was initially unclear whether this association was simply due to a common affinity for solid surfaces, or due to an actual stabilization mechanism. In subsequent research, it has become apparent that close association between organic matter and reactive mineral phases, particularly the poorly crystalline Fe and Al mineral surfaces with high surface areas found in soils, imparts a protective effect on OM from biotic and abiotic degradation (145) and ultimately represents the dominant control on organic matter stabilization in subsoil environments (44). It has been suggested that Fe(III) oxyhydroxides are the most important sorbents for OM leading to long-term sequestration (40, 146, 147). Similar observations have been made in freshwater and marine sediments, where up to 21% of organic C was found to be stabilized by direct chelation and/or co-precipitation with poorly crystalline reactive Fe phases (Figure 4.1), a finding that corresponds to an estimate of 19 to 45 x 10^{15} grams of organic C stabilized by Fe globally (148). In both soils and sediments, enhanced preservation of organic matter ultimately results in its accumulation in areas rich in Fe oxides highlighting the important role Fe plays in the long term stabilization of C on a global scale.

The behavior of Fe oxides in redox active subsurface environments is highly complex, and our understanding of this behavior has changed substantially in the past decade. At near-neutral pH, Fe(III) is sparingly soluble and tends to precipitate initially as ferrihydrite, a poorly crystalline and metastable Fe-oxide. Ferrihydrite has been observed in a variety of redox-active surface environments, including soils, sediments, and both freshwater and marine environments (149). As a result of its poor crystallinity and high reactivity, ferrihydrite is considered the most bioavailable Fe oxide, and thus

has a large influence on the global cycling of carbon through dissimilatory iron reduction (150). In addition to being highly bioavailable, ferrihydrite is thermodynamically unstable with respect to various more crystalline Fe oxides (goethite, lepidocrocite, magnetite) and readily transforms to these mineral phases in the presence of a strong reductant or other catalyst (109).

The structure and composition of Fe oxides in the environment is known to differ from their laboratory synthesized counterparts (49, 117, 151). Despite having similar overall short- and intermediate-range ordering to that of synthetic ferrihydrite, natural ferrihydrite can contain significant amounts of Al, Si, and OC, which are intimately associated with the ferrihydrite aggregates, and generally result in smaller particle sizes, lower crystallinity, and increased structural disorder. These changes to Fe mineral structure have been shown to influence the rates and products of microbial Fe(III) reduction (117), yet it remains to be seen whether similar effects may be observed on the exchange of Fe atoms and subsequent mineral transformation of ferrihydrite-carbon coprecipitates.

Here, we examine the influence of OC on the Fe(II) catalyzed transformation of ferrihydrite. Our goals were to determine how the presence of coprecipitated C in Fe-C minerals affects the kinetics of Fe atom exchange with aqueous Fe(II), and how it influences the kinetics and products of secondary mineral transformation. We also sought to determine the fate of the OC during Fe(II) catalyzed transformation in order to assess whether coprecipitation with Fe can act as a mechanism of long term stabilization, or whether carbon can be liberated during processes with significant Fe atom turnover.

Experimental Section

Iron Oxide and Coprecipitate Synthesis

Two-line ferrihydrite was prepared by the neutralization of a 50 mM $FeCl_3 \cdot 6H_2O$ solution with 0.4 M NaOH to a pH of 7.5 followed by repeated (5 times)

washing/centrifugation steps with deionized water to remove excess ions. Ferrihydrite-humic acid (Fh-HA) co-precipitates were synthesized by adding Elliott Soil Humic Acid solids to the $FeCl_3 \cdot 6H_2O$ solution without filtration at various C/Fe ratios, raising the solution pH to 7.5 by the addition of NaOH while mixing and washing as above. Minerals containing coprecipitated Elliott Soil Humic Acid are referred to as Fh-HA-1 and Fh-HA-2 for initial C:Fe ratios of 1 and 2 respectively. Solids were freeze-dried, ground with a mortar and pestle, and sieved (100 mesh).

Sorbed Organic Carbon

Organic carbon stock solutions for experiments with sorbed OC were prepared by dissolving Elliott Soil Humic Acid solids in deionized water, mixing for one hour on a shaker table, and filtering the solution through a 0.22 μm nylon filter. Ferrihydrite solids were pre-equilibrated in buffer solution with dissolved OC for at least 1 hour prior to addition of ^{57}Fe labeled Fe(II).

Mineral Characterization

Powder x-ray diffraction (pXRD) patterns of ferrihydrite and Fh-HA coprecipitates were obtained using a Rigaku Miniflex II system with Co source (CoK_α = 1.78899 Å). Unreacted samples were mounted as dry powders, whereas samples reacted with Fe(II) were mixed with a small amount of glycerol in an anaerobic glovebox to avoid oxidation of the sample during analysis (85). Samples were analyzed from 20-80° 2θ with a 0.02° step size and 2.0 second dwell time. Patterns were fit and analyzed using Jade 6 Software (Materials Data Inc., USA). In samples containing glycerol, a broad peak was observed at approximately 24° 2θ. Coprecipitates were also analyzed using ^{57}Fe Mössbauer spectroscopy as described in Chapter 3.

Reactivity of Fe-C coprecipitates was measured by dissolution in ascorbic acid, using methods adapted from (152). Ferrihydrite and FH-HA solids (10 mg) were suspended in 500 mL of 10 mM ascorbic acid (pH 3.0) and mixed rapidly. At designated

time intervals, 1.5 mL aliquots were removed from the suspension, filtered, and analyzed for aqueous Fe(II) by 1,10-phenanthroline. Fe(II) fluxes were calculated as described in (153).

Images of the minerals were obtained via scanning electron microscope (Hitachi S-4800 EM) and transmission electron microscope (JEOL JEM 1230) to evaluate particle sizes, morphology, and aggregation behavior.

Fe Atom Exchange with Aqueous Fe(II)

We examined the influence of varying levels of coprecipitated OC on the Fe atom exchange between ferrihydrite and aqueous Fe(II) using an isotopically enriched ^{57}Fe(II) tracer, similar to the experiments detailed in Chapter 3, and our previous work (22, 24, 115). Batch reactors were prepared by adding 15 mL of pH 7.0 MOPS buffer (50 mM) to a glass serum vial, and adding an aliquot of concentrated ^{57}Fe(II) stock to yield a final Fe(II) concentration of ~1 mM. A counter-spike of 0.5 M KOH was also added to the vials to maintain pH at 7.0 following Fe addition. After 1 hour of equilibration, the Fe(II)-buffer solution was filtered through a 0.2 μm nylon filter into 15 mL polypropylene centrifuge tubes, and initial Fe(II) was measured. Pre-weighed 30 mg portions of ferrihydrite or Fh-HA solids were then added to vials, which were capped and allowed to rotate end-over-end for times up to 25 days. Three vials were sacrificed at each time point, and sampled by centrifugation at 8,500 rpm for 15 minutes to separate the aqueous and residual solids phases. Aqueous and residual solids samples were analyzed for Fe(II), total Fe, and Fe isotopes as previously described in Chapter 3. Experiments were conducted at a lower pH than our previous work due to the low PZC of our co-precipitates (~5.5 or lower), which resulted in near complete sorption (>95%) of aqueous Fe(II) at pH 7.5.

Results and Discussion

Characterization of Fh-HA coprecipitates

Fh-HA coprecipitates were synthesized with different C:Fe ratios by varying the mass of OC present during precipitation of Fe(III), resulting in minerals with nominal C:Fe ratios ranging from 0 (ferrihydrite) to 2; which are referred to as Fh when no carbon is present, Fh-HA-1 for C:Fe = 1, and Fh-HA-2 for C:Fe = 2. Scanning electron micrographs (SEMs) of all three Fh-HA coprecipitates show poorly crystalline particles in amorphous aggregates ranging in size from sub-micron to tens of microns (Figure 4.2). In all cases, individual particles can be observed on the surface of larger aggregates. For ferrihydrite (without carbon) (Figure 4.2, top) the aggregates have relatively sharp edges despite having no clear or consistent morphology, while individual particles are generally amorphous. As the proportion of OC increases, both the aggregates and the smaller component particles display edges and surfaces with increasingly poor definition relative to pure ferrihydrite (Figure 4.2 middle, and bottom), qualitative evidence of the lower crystallinity typically observed in the presence of carbon (144).

Due to analytical constraints, we are not currently able to measure the C content of the coprecipitates directly, however we are working to be able to make those measurements with a total organic carbon analyzer in the future. In the absence of direct measurements, we can qualitatively verify the presence of OC in the Fh-HA-1 and Fh-HA-2 coprecipitates by visual examination before and after dissolution in concentrated acid. Figure 4.3 shows pure ferrihydrite, Fh-HA-1, and Fh-HA-2 solids after freeze-drying. Pure ferrihydrite has a reddish-brown coloring, which becomes increasingly brownish-black as higher levels of organic C are present during precipitation. To synthesize the coprecipitates, we used a purified humic acid isolate as a source of organic C, which is by definition acid insoluble. Upon dissolution of the coprecipitates in concentrated HCl, the coprecipitated humic acid remains in solid form, and precipitates

out of solution as shown in Figure 4.4. With increasing amounts of initial C present during precipitation, there is a corresponding increase in the insoluble fraction remaining after acid dissolution. X-ray diffraction (XRD) patterns for the synthesized Fh-HA coprecipitates are shown in Figure 4.5. Both naturally occurring and synthetic ferrihydrite have low levels of crystal ordering, which can vary between the two end-members, two-line and six-line ferrihydrite, which refer to the XRD patterns produced by its poorly crystalline and more crystalline forms respectively (109). Poorly crystalline two-line ferrihydrite produces an XRD pattern that consists of two broad peaks at approximately 40° and 74° 2θ, which is consistent with our observations for ferrihydrite precipitated in the absence of OC. Asymmetry or peak shoulders like those visible in both peaks of Figure 4.5 (bottom) have previously been modeled by the addition of smaller peaks at d-spacings corresponding to ferrihydrites with greater than two-line crystallinity. As C:Fe ratio increases, the pattern still consists of two broad peaks at 2θ values similar to synthetic 2-line Fh, but broadening of both peaks, and the disappearance of subtle peak shoulders is observed (Figure 4.5 middle and top), which can indicate a decrease in the size of coherent scattering domains, or an increase of stacking disorder in the anionic crystal layers (154). The second peak also shifts to slightly higher d-spacing (lower 2θ) similar to what was observed in ferrihydrite with increasing soil organic matter content (154), although they observed that shift in both peaks. One process for ferrihydrite precipitation, suggested by (155), proceeds via formation of Fe octahedra chains, followed by edge-linking to plate-like polyoctahedral chains, and finally cross-linking of those chains. Eusterhues et al. (154) hypothesized that interactions between Fe octahedra and organic molecules interfere with that final cross linking step, resulting in plate-like coherent scattering domains that only have two XRD peaks. In transmission electron micrographs (TEMs), Fh-HA-1 and Fh-HA-2 show a preponderance of small plate-like crystals, ranging in diameter from approximately 0.10-0.25 μm, dispersed around the larger more well defined aggregates, which may provide further evidence to

support these hypotheses regarding how organic matter can influence ferrihydrite precipitation (arrows in Figure 4.6). TEM images in (154) focus on individual ferrihydrite particles on the edges of large aggregates, making it impossible to tell whether they observed similar plate like particles in coprecipitates containing OC.

^{57}Fe Mössbauer spectra were collected at 13 K for each of our Fh-HA coprecipitates (Fh, Fh-HA-1, Fh-HA-2) (Figure 4.7). Each spectrum consists of a broadened sextet, which indicates that the Fe in the sample has magnetically ordered at the measurement temperature of 13 K. For the sample precipitated without humic acid, the quadrupole splitting (QS) and mean hyperfine field values of -0.009 mm/s and 48.0 T agree nicely with reported values for 2-line ferrihydrite (Table 4.1) (109). The center shift (CS) value of 0.47 mm/s is much higher than the reported value of 0.24 mm/s (109), but still falls within the range of 0.24-0.54 mm/s observed for Fe(III) (156). Other studies examining ferrihydrite coprecipitates have found CS values in the range of 0.35-0.36 mm/s for pure ferrihydrite, also higher than 0.24 mm/s (though not as high as those observed in our study). CS and QS values remain relatively constant as the ratio of C:Fe is increased, but the mean hyperfine field decreases systematically, from 48.0 T (Fh) to 47.1 T (Fh-HA-1) and 46.1 T (Fh-HA-2). This trend agrees nicely with characterization results in similar experiments involving ferrihydrite with coprecipitated SOM (144, 154), and polysaccharides (47). A decrease in mean hyperfine field can be indicative of decreased particle size / crystallinity (157) or diminished interparticle interactions (158). As C:Fe increased in our coprecipitates, XRD data indicated a decrease in crystallinity, and TEM images show greater numbers of small un-aggregated particles, though it was not clear whether the organic matter influenced individual particle sizes. If organic matter can act as a matrix into which ferrihydrite aggregates are embedded, as suggested in (151), the reduction in hyperfine field could be due to a combination of all three of the aforementioned characteristics.

As the transformation of ferrihydrite to more crystalline mineral phases is thought to occur via dissolution and reprecipitation (e.g., 14, 109), we used ascorbic acid to probe the possible influence of coprecipitated C on the reductive dissolution of ferrihydrite. Results of reductive dissolution experiments are shown in Figure 4.8. We determined Fe(II) fluxes in (moles Fe g^{-1} ferrihydrite) by calculating the amount of Fe(II) dissolved per unit time, given by the slope of the lines in Figure 4.8 between 50 and 200 minutes reaction, and dividing by the solids loading (2 g/L) . Similar to our isotope exchange experiments, there appeared to be little difference in the dissolution kinetics between ferrihydrite and Fh-HA-1, with calculated Fe(II) fluxes of 1.86×10^{-3} and 1.88×10^{-3} mol g^{-1} s^{-1}. We found the coprecipitates with the highest level of carbon (Fh-HA-2 and Fh-sorbed HA) had the slowest reductive dissolution kinetics, with calculated Fe(II) fluxes of 1.74×10^{-3} mol g^{-1} s^{-1} and 8.76×10^{-4} mol g^{-1} s^{-1} respectively. This was rather unexpected based on isotope exchange data where we saw faster exchange in Fh-HA-2 and Fh-sorbed HA than Fh or Fh-HA-1, and based on bioreduction studies where mineral dissolution tends to be faster in the presence of high levels of coprecipitated or dissolved organic matter (117, 159). Detachment of Fe(II) during reductive dissolution is often thought to be rate-limiting in Fe atom exchange processes, but our results point towards some other mechanism being responsible for the rate of Fe atom exchange observed in ferrihydrite. It is worth noting that even in experiments with the highest levels of carbon, our dissolution fluxes were higher than those observed for wüstite (153) when surface area-normalized, which should represent the upper bound for dissolution of Fe(III) hydroxides. To follow the methods of (152) we stirred our reactors continuously, while reactors were agitated hourly in (153). If reductive dissolution of wüstite was limited by mass transfer, the continuous stirring in our reactors likely prevented mass transfer limitation and resulted in higher rates of reductive dissolution.

Influence of Coprecipitated and Sorbed Organic Carbon on Atom Exchange and Fe(II) Transformation in Ferrihydrite

We examined the influence of coprecipitated carbon on Fe(II) catalyzed transformation of ferrihydrite by exposing our Fh-HA coprecipitates to ^{57}Fe labeled Fe(II). During the reaction, we monitored isotope exchange by ICP-MS, and transformation of the Fe solids by collecting pXRD patterns over time. The various experimental conditions tested are summarized in Table 4.2.

Fe atom exchange in Fh-HA coprecipitates

Fe atom exchange was rapid for all of our solids with significant exchange (>50%) occurring within the first hour (Table 4.3, Figure 4.9). After ~1 hour reaction time, increasing the ratio of coprecipitated C to Fe from 0 to 1 appeared to have no effect (62.5% vs 61.0%), but increasing further to a 2:1 ratio resulted in a greater extent of isotope exchange (78.0%). We also tracked isotope exchange in ferrihydrite with 40 mg/L sorbed Elliott Soil Humic Acid, which corresponds to C:Fe = 2, and observed similar exchange compared to the same ratio of coprecipitated C (Figure 4.9). Within 24 hours, complete exchange was reached in reactors containing Fh (with and without dissolved HA), Fh-HA-1, and Fh-HA-2, indicating that the presence of coprecipitated C has little to no inhibitory effect on Fe atom exchange in ferrihydrite. These results are rather surprising given that organic matter has been observed to stabilize Fe(III) and prevent oxide crystallization. Aquatic organic matter can form stable complexes with aqueous Fe(III), suppressing hydrolysis and polymerization at low Fe concentrations (< 11,953 μg / g organic matter) and resulting in small ferrihydrite-like particles with high surface areas at high Fe concentrations (>23,000 μg / g organic matter) (48); and can also inhibit transformation of a non-crystalline Fe(III) floc to goethite by either Fe(II) or S(-II) when coprecipitated with the Fe(III) (46). During Fe(II) oxidation, SOM can form

complexes with Fe(III), resulting in 4-line ferrihydrite rather than the six-line ferrihydrite / lepidocrocite mixture formed in SOM free experiments (144).

Overall results in the literature however appear to be mixed regarding how the presence of organic matter can influence the behavior of Fe oxides. Inhibition of lepidocrocite bio-reduction has been shown to vary by the type of dissolved organic matter present (116), and whereas sorbed humic substances can lead to inhibition of ferrihydrite bioreduction, dissolved humic substances can have an enhancing effect (117). Similarly, coprecipitated organic matter can impart a stabilizing effect on Fe subject to reductive dissolution (46), or can enhance the dissolution of Fe-C coprecipitates by siderophores and low molecular weight acid anions (160). The general lack of agreement on how organic matter affects the stability of Fe minerals relative to chemical or biological dissolution makes interpretation of our data rather challenging. Our results are particularly puzzling as previous work saw release of Fe from ^{55}Fe labeled ferrihydrite was significantly inhibited by sorbed/dissolved fulvic acid (114). A lower solids loading and pH were used in that work, and it is unclear whether the Suwannee River Fulvic Acid (SR-FA) standard was filtered before addition to the reactors. Based on their experimental conditions, the C:Fe ratios in their systems appear to be 4.18 and 0.70 for 150 mg/L and 25 mg/L SR-FA, which bracket our C:Fe ratio of 2.0. In an experiment under conditions similar to that study (MES buffer, pH 6.5, 150 mg/L unfiltered SR-FA, 0.42 g/L ferrihydrite, 1 mM Fe(II), designated as Fh-sorbed HA (Jones)) we also observed significant inhibition of atom exchange, with only 18% exchange occurring after 1 day. At pH 6.5, Fe(II) sorption diminishes greatly, to approximately 9% vs. the 70-90% we observed at pH 7.0. Perhaps more importantly, the use of unfiltered organic matter in reactors introduces solids to the reactor in addition to the Fe oxide being studied. At 150 mg/L SR-FA and 0.42 g/L ferrihydrite, SR-FA represents 26% of the solids mass in each reactor, where in our studies at pH 7.0 those solids have been filtered out, leaving only the dissolved humic or fulvic fraction in the reactors. If SR-FA solids

are acting as a competitive sorbent for Fe(II), there may simply be little interaction between Fe(II) and ferrihydrite under these conditions, leading to the reduced rate of exchange observed over 1 day.

Recent work by some of our collaborators has observed a non-linear effect of co-precipitated carbon, where bioreduction is slower for low C:Fe ratios (i.e., C:Fe<1) than for ferrihydrite, but faster for high ratios (i.e. C:Fe > 2) (159). Since the results of Jones et al. (114) encompassed C:Fe ratios both higher and lower than what we used, this probably does not explain why we failed to see an inhibitory effect at our C:Fe ratio of 2.0. The most likely explanation for this apparent discrepancy is confusion in reporting organic matter concentrations. In (117) and this study, organic matter concentrations are reported in nominal terms prior to filtration, which removes significant organic solids mass from the solution. In (114) the SR-FA concentrations were also reported nominally, but it does not appear that any filtration step occurred. With negligible humic solids mass, it is likely that the actual loading of organic matter to Fe solids in our study is much lower compared to that work than the 0.4- to 2-fold range we calculated earlier. Without direct measurement of organic carbon or some other surrogate following reactor preparation, comparing results between these various studies remains quite difficult. The non-linear trend now observed in multiple studies is curious though, but may be explained by the changes to physical and chemical properties induced by coprecipitation with organic matter. Even small amounts of co-precipitated C result in changes to crystal structure typically associated with lower stability (i.e., smaller particle size, lower crystallinity, increased disorder) (151), but increasing levels of C also lead to decreased specific surface area (SSA) and porosity, as well as a lowering of the PZC (151). At low levels of coprecipitated C, changes to particle size and crystallinity may act as the dominant influence on stability, but are overcome by the reductions in SSA and increasingly negative surface charge due to PZC lowering. We did see a modest increase

in Fe(II) sorption as C:Fe increased, which would be consistent with a lower PZC for Fh-HA-1 and Fh-HA-2.

Both organic matter and silica can bond to similar sites on Fe oxide surfaces via oxygen donor atoms (161, 162), and both have been observed to retard Fe oxide transformation (163, 164). This behavior was generally attributed to the ability of both silica and organic matter to block dissolution sites on mineral surfaces, or to inhibit nucleation of more stable Fe oxides (165). Blocking of dissolution sites would be expected to slow the rate and possibly extent of Fe atom exchange, and multiple studies have found that to be true for silica (114, 166). While our group has found that sorbed silica does not inhibit Fe(II)-Fe oxide electron transfer, we have not examined how it can influence Fe atom exchange in ferrihydrite (or other Fe oxides), nor how it effects the transformation of ferrihydrite to other mineral phases. A comparison of its effects on ferrihydrite transformation with those of natural organic matter would be valuable to our interpretation of both how transformation may occur, and how these anions can inhibit these processes.

Our results clearly demonstrate though that the Fe(II)-catalyzed recrystallization of ferrihydrite is likely to occur in the presence of organic matter. At pH 7.0, all of our coprecipitates approached 100% isotopic exchange within 1 day regardless of the presence of sorbed or coprecipitated organic matter, which is much faster and to a much greater extent than observed for plain ferrihydrite previously (though under different conditions) (114). At lower pH (6.5) and in the presence of fulvic acid solids however, atom exchange was significantly slower, highlighting the importance of being able to directly quantify and report aqueous and solids OC concentrations. Further study of Fe(II)-induced recrystallization in low C:Fe ratio coprecipitates (i.e. $0.1 < C:Fe < 0.5$) is certainly warranted, as is further characterization of natural ferrihydrites to determine what levels of coprecipitated C are environmentally relevant.

Influence of coprecipitated C on ferrihydrite transformation

We collected pXRD patterns for each of our minerals after 1, 5, 15, and 29 days reaction with ^{57}Fe(II) (Figure 4.10). By 24 hours reaction, at which point complete isotopic exchange had been reached for all of our Fh-HA coprecipitates, significant mineral transformation had occurred as observed by pXRD. The poorly defined peaks characteristic of 2-line ferrihydrite disappeared, and were replaced by five characteristic peaks of lepidocrocite. There are no apparent differences in the crystalline structure of the three Fh-HA coprecipitates as C:Fe increases from 0 to 2.0, indicating that in the timescale of Fe isotope exchange, the presence of coprecipitated C does not appear to influence secondary mineral transformation. No significant changes appear in the patterns from 1 to 5 days reaction, and only after 15 days reaction do two new peaks emerge in the Fh pattern. These peaks are characteristic of magnetite, and are also absent from the patterns for Fh-HA-1 and Fh-HA-2. The magnetite peaks in the Fh pattern become further resolved after 29 days reaction and are joined by two peaks characteristic of goethite, whereas patterns for Fh-HA-1 and Fh-HA-2 still indicate lepidocrocite as the dominant mineral form (Figure 4.10). A schematic of the mineral transformation observed in these experiments is shown in Figure 4.11. In systems with pure ferrihydrite, transformation to lepidocrocite has been observed almost immediately following exposure to 2 mM Fe(II) (6.7 mmol Fe(II) / g ferrihydrite), with a gradual transition to magnetite as the dominant mineral form occurring from roughly 1 to 9 days of reaction. In experiments performed at a lower Fe(II) concentration (0.2 mM, 0.67 mmol Fe(II) / g ferrihydrite), there was still rapid transformation to lepidocrocite, only without any subsequent formation of goethite or magnetite (14). Our experiments were conducted at an intermediate Fe(II) concentration (1 mM) but a low Fe(II) : oxide ratio (0.50 mmol Fe(II) / g ferrihydrite), making our observation of rapid transformation to lepidocrocite followed by a slow evolution of magnetite as a minor phase seem consistent with the previous study.

The presence of organic matter, which appeared to have little influence on rapid Fe atom exchange in ferrihydrite, does influence the slower process of secondary mineral transformation where it appears to prevent the transformation of lepidocrocite to magnetite. This raises a question regarding the fate of the coprecipitated carbon. Fe(II) has been shown to catalyze the release of several incorporated trace elements from Fe oxides (35). Since complete Fe atom turnover has occurred within 1 day, it is possible that coprecipitated carbon has been liberated to solution, which would render our Fh-HA-2 sample similar to our Fh-sorbed HA sample. Unfortunately, we do not yet have mineral transformation data for the Fh-sorbed HA case, which would provide some potential insight into this question. We may also be able to speculate further as to the fate of the coprecipitated carbon by tracking aqueous total organic carbon during and after complete isotope exchange has occurred.

It is rather surprising however that the presence of organic carbon appears to inhibit transformation to magnetite, but seems to have no effect on lepidocrocite formation. As mentioned in Chapter 3, there are at least four mechanisms by which Fe(II)-catalyzed recrystallization can occur (dissolution / reprecipitation, bulk conduction, solid state diffusion, pore diffusion). Transformation of ferrihydrite to lepidocrocite is thought to occur via dissolution / reprecipitation (109), and there are several examples of organic matter inhibiting or poisoning the precipitation and crystal growth of Fe oxides (e.g., amorphous ferric hydroxide (167), ferrihydrite(48, 114), jarosite, schwertmannite (114)). Subsequent formation of magnetite is then thought to occur through lepidocrocite dissolution and crystal growth via surface nucleation on ferrihydrite (14) or precipitation on lepidocrocite (168). The fact that (initially) coprecipitated humic acids can inhibit magnetite formation suggests they either prevent dissolution of lepidocrocite, or somehow limit access to nucleation sites on the ferrihydrite surface. Since O'Loughlin et al. (116) saw slower reduction/dissolution of lepidocrocite by *S. putrefaciens* CN32 when Elliott Soil Humic Acid was present, it does

seem possible that the dissolution and reprecipitation of ferrihydrite to lepidocrocite releases C to solution, which can sorb to the resulting lepidocrocite, stabilizing it from further transformation.

Environmental Significance

The association between organic matter and Fe oxides is common throughout the environment, particularly in situations where the oxides precipitate in the presence of bacterial cells or exudates (134, 169). Sorption of organic matter to Fe oxides (especially poorly crystalline oxides) can inhibit chemical and biological oxidation of the organic matter (e.g., 43, 147, 170, 171) while affecting the crystallinity, particle size, aggregation behavior, and surface chemistry of the oxide, potentially preventing secondary mineral transformation (144, 172). Co-precipitation of organic matter and Fe oxides may result in C incorporation into the mineral structure, but the small particle size and disordered nature of ferrihydrite make it difficult to distinguish between actual incorporation versus the formation of separate but intimately mixed nano-scale carbon and Fe phases (151). Our results demonstrate that coprecipitation of ferrihydrite with natural organic matter leads to some differences in mineral structure and reactivity, but has little effect on Fe isotope exchange kinetics or rapid transformation of ferrihydrite to lepidocrocite. At longer reaction times however, the presence of organic matter ultimately stabilizes lepidocrocite and inhibit its transformation to magnetite or goethite. The fate of the organic matter during this process remains to be determined, and our understanding of the role of Fe oxides as a preservative for SOM hinges heavily on being able to determine whether coprecipitated C remains mineral associated following secondary oxide transformation. It is not clear whether the process of transformation to a more crystalline structure requires the expulsion of impurities, similar to the expulsion of ions from seawater during freezing, resulting in a crystalline product that is relatively impurity free (173). Additional insight into this question may be gained by adding organic matter

during different phases of mineral synthesis (e.g., during the titration / baking steps of goethite synthesis, where ferrihydrite is converted to goethite; or during the Fe(II) catalyzed transformation of lepidocrocite to magnetite during synthesis).

Recommendations for Future Work

The work in this chapter has highlighted a number of potential avenues for additional exploration which are detailed below.

Quantification of organic matter in both the solid and aqueous phases is critical to understanding the amount of organic matter that can coprecipitate with ferrihydrite, whether that organic matter remains associated with the Fe mineral during Fe atom exchange and lepidocrocite transformation over short time scales, and what role the organic matter plays during longer term transformation to goethite or magnetite. We are currently refining total organic carbon measurement capabilities, which will allow us to directly measure the concentration of organic carbon in the Fh-HA coprecipitates, and in the aqueous solution at various stages during reaction with Fe(II).

We have shown that coprecipitated organic matter can inhibit the transformation of lepidocrocite to goethite and magnetite, but have not examined the role of sorbed organic matter in this transformation process. Similar transformation experiments will be performed by equilibrating pure ferrihydrite with Elliott Soil Humic Acid prior to exposure to Fe(II), and collecting pXRD spectra over time.

So far, we have only explored the effect of a single type of organic matter on Fe atom exchange and transformation in ferrihydrite. Numerous organic matter reference samples are available with varying aromatic content, functional group distributions, and molecular weights. The sorption behavior of organic matter not only can vary from one mineral to another, but also can depend on the source and properties of the organic matter. Preferential sorption of high molecular weight fractions has been observed for aquatic and lacustrine natural organic matter on metallic oxides (174, 175), whereas

preferential sorption of low molecular weight fractions was observed for Sigma Aldrich humic acid (176). We might expect organic matter with such variation in physical and chemical properties to have different effects on the transformation of ferrihydrite by Fe(II).

Table 4.1. Fitting parameters derived from 13 K Mössbauer spectra collected for ferrihydrite-humic acid (Fh-HA) coprecipitates.

Component	CS (mm s^{-1})	QS (mm s^{-1})	H (T)	std(H) (T) or std(QS) (mm s^{-1})	Area (%)	mean H (T)	χ^2
2-line ferrihydrite[a]							
Sextet	0.24	-0.01	47				
Ferrihydrite							
Sextet 1	0.47	-0.009	46.2	2.4	46.3	48.0	5.4
			49.5	1.4	53.7		
Fh-HA-1 (1 site, 2 component)							
Sextet 1	0.47	-0.01	46.0	3.0	68.9	47.1	7.2
			48.7	0.8	21.1		
Fh-HA-1 (2 site, 1 component)							
Sextet 1	0.45	-0.01	45.5	3.1	66.4	45.5	5.8
Sextet 2	0.5	-0.02	48.4	1.3	33.6	48.4	
Fh-HA-2 (1 site, 2 component)							
Sextet 1	0.47	-0.01	43.9	3.0	45.0	46.1	3.7
			47.9	1.7	55.1		
Fh-HA-2 (2 site, 1 component)							
Sextet 1	0.45	-0.01	45.4	3.3	71.7	45.4	3.8
Sextet 2	0.5	-0.01	48.2	1.1	28.3	48.2	

[a]Reference parameters from (109)

Table 4.2. Experimental conditions for Fe atom exchange experiments conducted with ferrihydrite and ferrihydrite-humic acid coprecipitates. ES-HA is coprecipitated in samples Fh-HA-1 and Fh-HA-2, while ES-HA and SR-FA are present in suspension for Fh-sorb HA and Fh-sorb HA (Jones).

Experiment ID	Solution Conditions	$pH_{initial}$	Solids Loading	Carbon loading	Organic matter used
Fh	50 mM MOPS	7.0	2 g/L	0 mg/L, filtered	ES-HA
Fh-HA-1	50 mM MOPS	7.0	2 g/L	10 mg/L, filtered	ES-HA
Fh-HA-2	50 mM MOPS	7.0	2 g/L	20 mg/L, filtered	ES-HA
Fh-sorb HA	50 mM MOPS	7.0	2 g/L	20 mg/L, filtered	ES-HA
Fh-sorb FA (Jones)[a]	50 mM MES	6.5	0.4 g/L	150 mg/L, unfiltered	SR-FA

[a]experimental conditions from (114)

Table 4.3. Chemical and isotopic data during enriched Fe(II) tracer isotope exchange experiments with Fe-C coprecipitates.

		Aqueous Fe(II)				Residual Solids			Fe Recovery		
Time (d)	Fe (μmoles)	f^{57}Fe	% exchange	f^{54}Fe	% exchange	Fe (μmoles)	f^{57}Fe	% exchange	Fe(II)	Fe(III)	Total Fe
Fh (C : Fe = 0)											
0.00	15.7 (0.5)	0.862 (0.024)	0	0.0063 (0.0013)	0	429.8 (44.2)	0.024 (0.0002)	0	100	100	100
0.05	6.0 (0.7)	0.355 (0.020)	62.5 (2.5)	0.0355 (0.0014)	69.4 (3.5)	424.5 (65.1)	0.063 (0.007)	135.8 (23.0)	96.9	95.6	95.6
0.90	5.6 (1.2)	0.042 (0.003)	101.3 (0.4)	0.0513 (0.0008)	107.1 (1.8)	314.9 (1.6)	0.070 (0.0008)	152.7 (2.8)	108.4	69.5	70.9
Fh-HA-1 (C:Fe = 1)											
0.00	15.7 (0.5)	0.862 (0.024)	0	0.0063 (0.0013)	0	241.3 (29.1)	0.024 (0.0002)	0	100	100	100
0.04	6.7 (0.5)	0.379 (0.027)	61.2 (3.4)	0.0342 (0.0011)	67.4 (2.7)	285.0 (57.9)	0.078 (0.0054)	173.8 (10.7)	90.4	113.1	111.6
0.90	2.4 (0.2)	0.072 (0.005)	100.3 (0.6)	0.0500 (0.0003)	105.8 (0.7)	228.3 (22.9)	0.091 (0.0015)	204.7 (2.9)	88.8	89.5	89.4
Fh-HA-2 (C : Fe = 2)											
0.00	15.7 (0.5)	0.862 (0.024)	0	0.0063 (0.0013)	0	257.8 (23.0)	0.024 (0.0003)	0	100	100	100
0.04	3.8 (0.7)	0.241 (0.079)	78.4 (10.0)	0.0429 (0.0032)	87.1 (7.8)	190.3 (9.7)	0.086 (0.0014)	191.3 (3.0)	82.7	69.1	70.0
0.90	2.8 (1.4)	0.065 (0.006)	100.8 (0.8)	0.0506 (0.0010)	105.6 (2.5)	208.1 (20.3)	0.088 (0.0002)	195.8 (0.4)	116.0	73.9	76.5
Fh-sorbed HA											
0.00	15.7 (0.5)	0.862 (0.024)	0	0.0063 (0.0013)	0	429.8 (44.2)	0.024 (0.0002)	0	100	100	100
0.04	4.5 (0.8)	0.245 (0.030)	76.2 (3.7)	0.0352 (0.0014)	68.7 (3.3)	270.3 (4.0)	0.059 (0.0002)	124.6 (0.6)	31.4	63.0	61.8
1.00	2.1 (0.2)	0.064 (0.018)	98.9 (2.1)	0.0531 (0.0007)	111.0 (1.6)	313.1 (1.0)	0.081 (0.0003)	173.4 (1.0)	81.1	70.6	71.0

Table 4.3 – continued

Fh-sorbed HA (Jones)											
0.00	20.5 (0.2)	0.862 (0.024)	0	0.0063 (0.0013)	0	62.9 (11.1)	0.024 (0.0002)	0	100	100	100
0.06	18.9 (0.2)	0.875 (0.015)	5.4 (2.3)	0.0059 (0.0009)	6.3 (2.7)	133.7(28.3)	0.047 (0.0035)	125.4(1.6)	91.2	219.0	186.0
0.98	18.8 (0.6)	0.793 (0.008)	17.7 (1.3)	0.0102 (0.0005)	18.7 (1.5)	100.8 (12.9)	0.076 (0.0004)	208.0 (0.2)	94.3	163.2	145.4

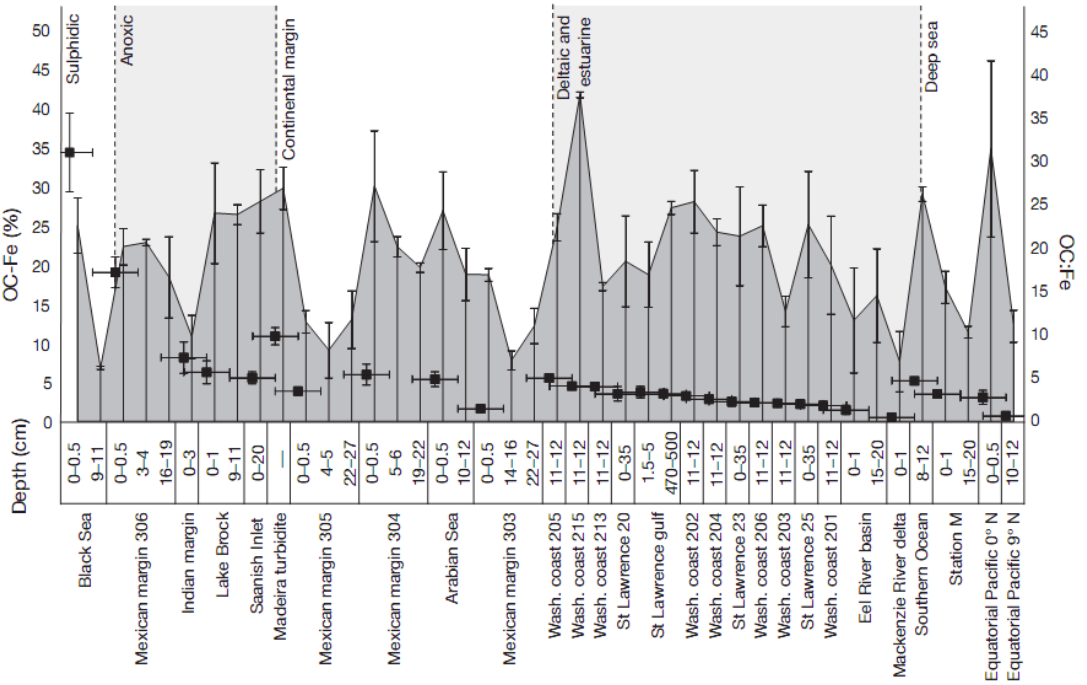

Figure 4.1. Control corrected percentage of total sediment organic carbon bound to reactive Fe phases in samples collected from a wide range of marine and freshwater environments from (148). Black squares indicate molar organic carbon : Fe ratios in the uppermost surface sediment layer from each sample.

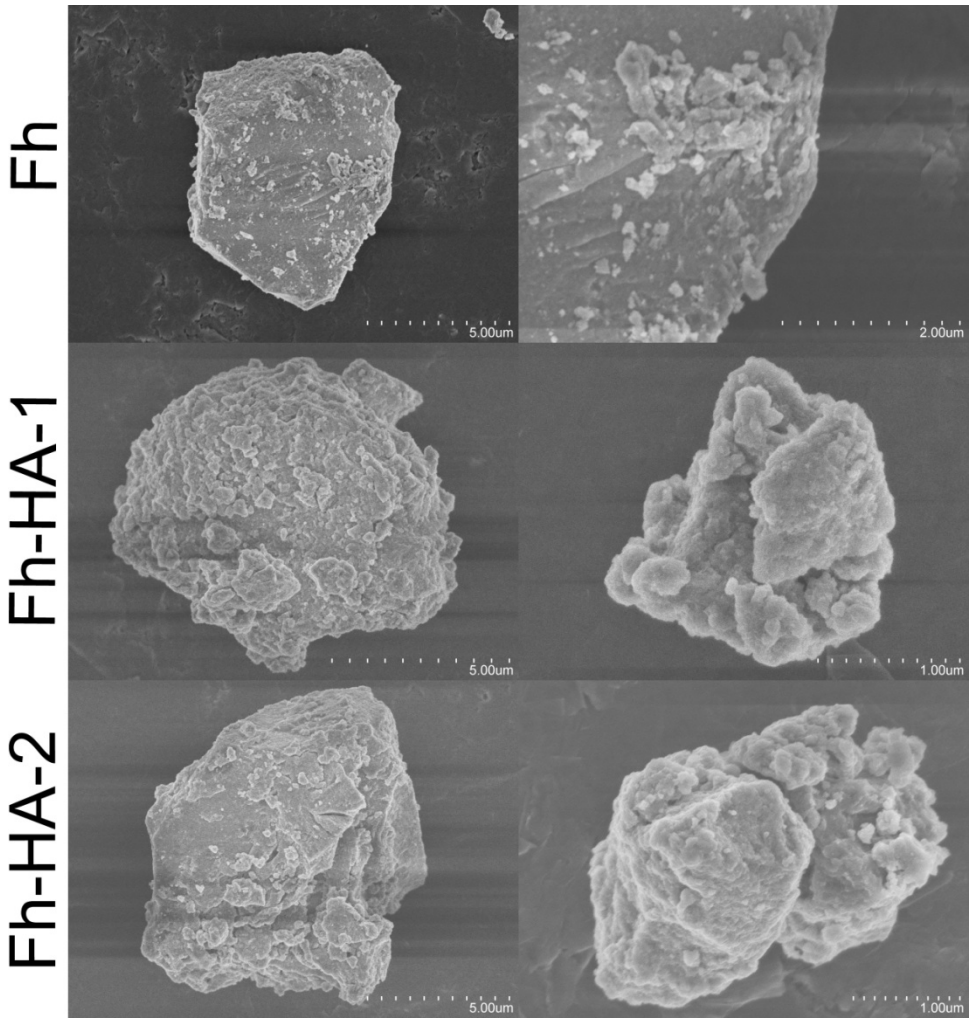

Figure 4.2. Scanning electron micrographs (SEM) of ferrihydrite-humic acid coprecipitates. Images show the variable morphology and changes in particle aggregation behavior with increasing amounts of coprecipitated carbon from carbon free ferrihydrite (top), to Fh-HA-1 (middle), and Fh-HA-2 (bottom).

Figure 4.3. Photograph of washed and freeze dried ferrihydrite and Fh-HA coprecipitates. As the ratio of initial C:Fe increases from left to right, the reddish brown coloration of ferrihydrite is gradually replaced by the darker brownish-black color of humic acid.

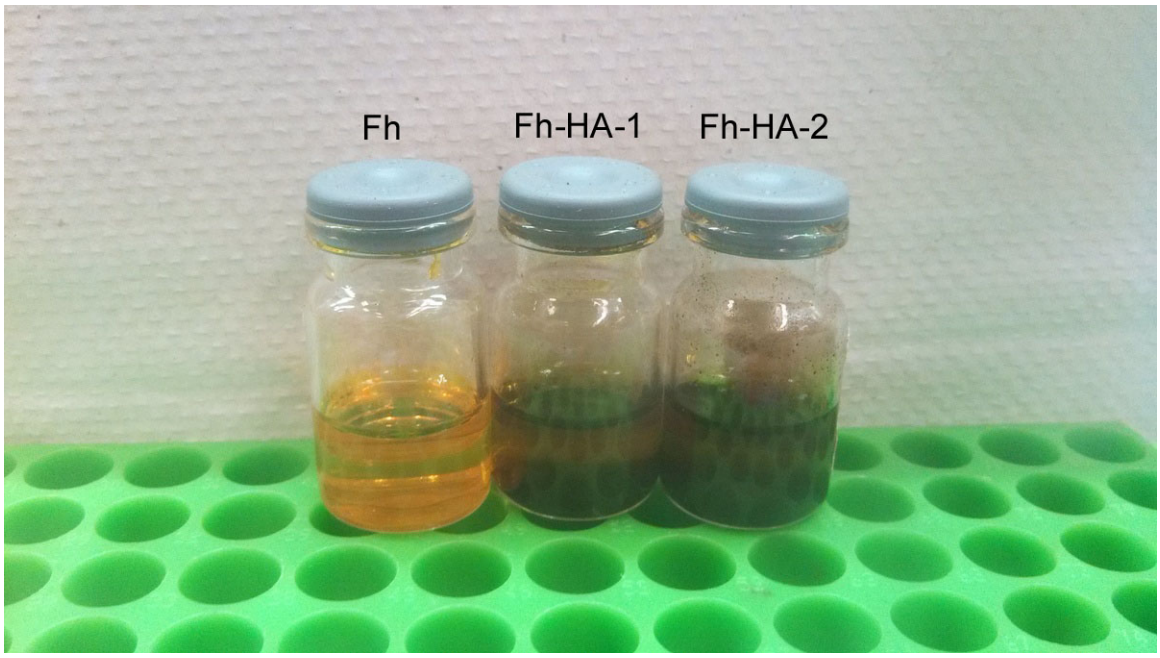

Figure 4.4. Photograph of ferrihydrite and Fh-HA coprecipitates after dissolution in concentrated HCl. Pure ferrihydrite contains no carbon, and dissolves completely in acid, while the humic acid in coprecipitates remains insoluble even at low pH.

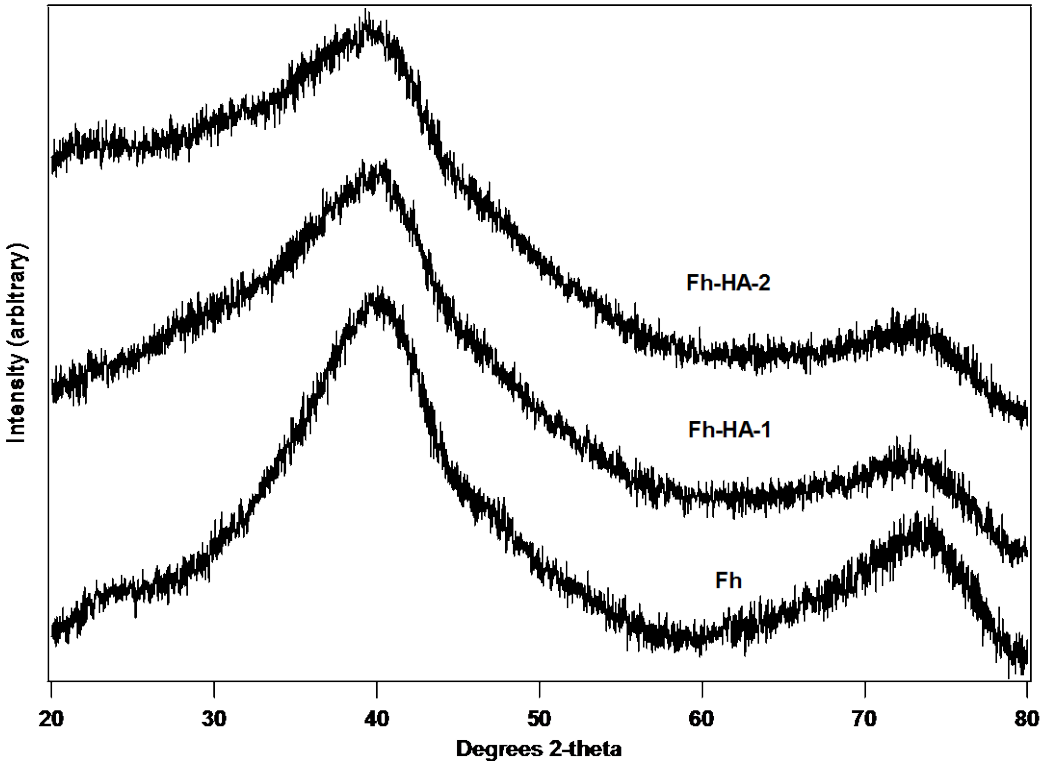

Figure 4.5. Initial powder X-ray diffraction (pXRD) patterns for Fh-HA coprecipitates synthesized by Fe(III) hydrolysis in the presence of Elliott Soil Humic Acid Standard.

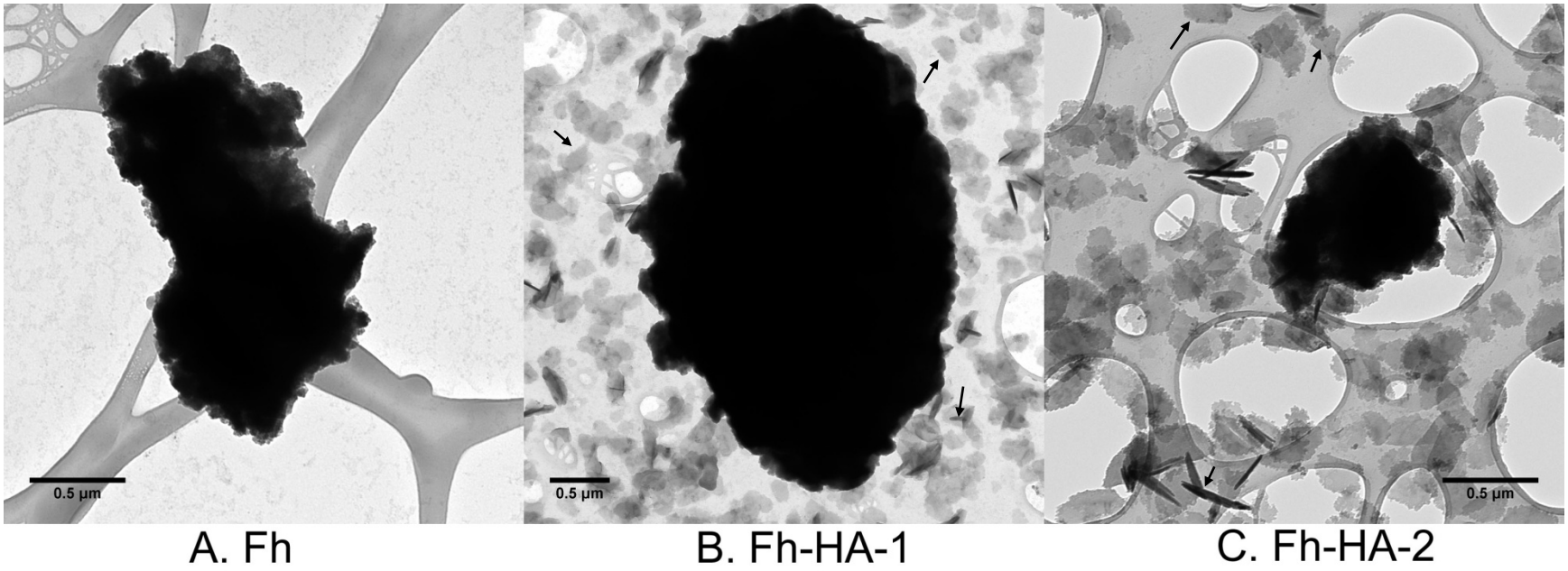

Figure 4.6. Transmission electron micrographs (TEM) of ferrihydrite–humic acid coprecipitates. Images of ferrihydrite (A), Fh-HA-1 (B), and Fh-HA-2 (C) all show the formation of large aggregates from individual ferrihydrite particles. As the C:Fe ratio increases from left to right, organic matter may inhibit cross linking of ferrihydrite octahedral chains during precipitation, resulting in higher density of the larger plate-like particles visible surrounding the aggregates. Arrows indicate the plate-like scattering domains oriented both parallel and perpendicular to the field of view.

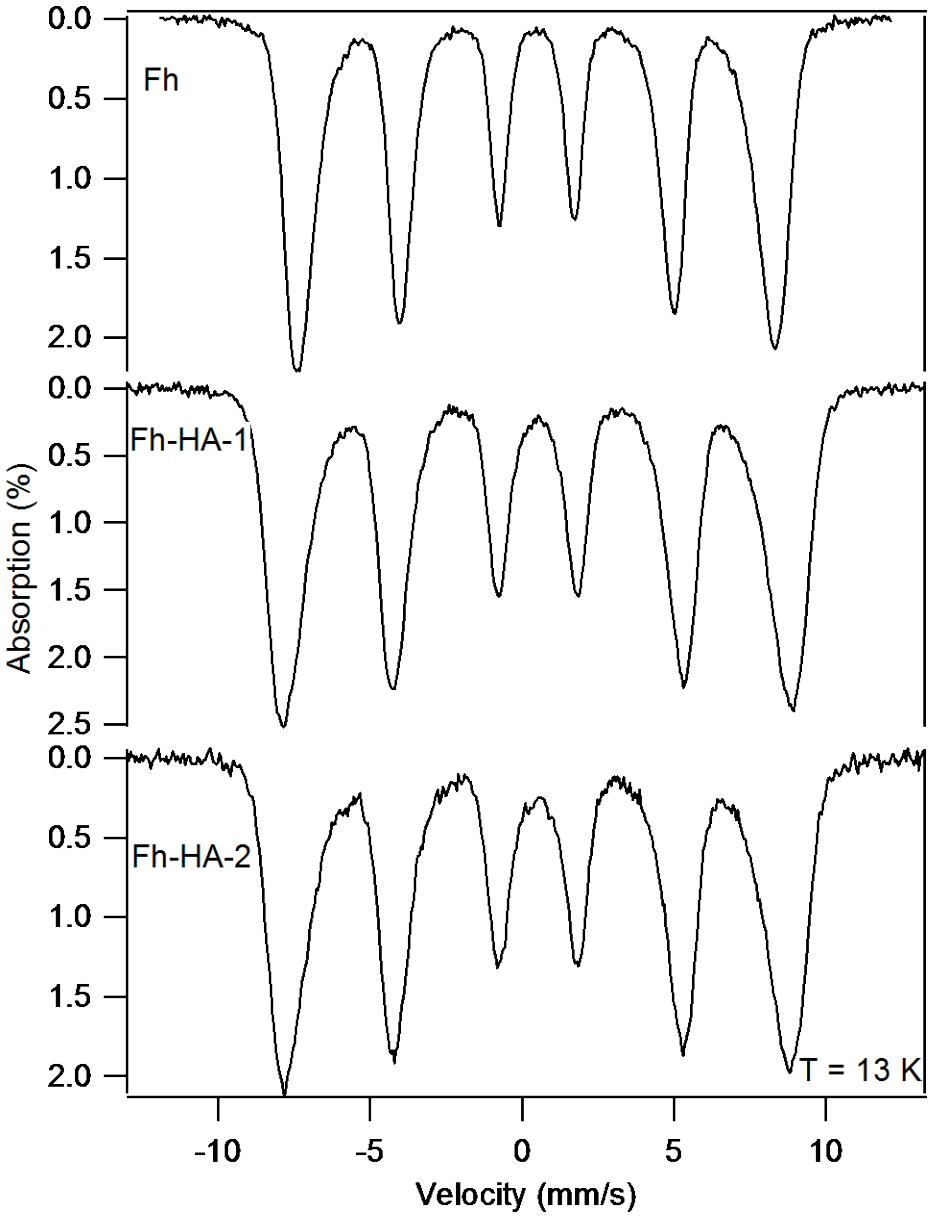

Figure 4.7. ^{57}Fe Mössbauer spectra of Fh-HA coprecipitates synthesized by Fe(III) hydrolysis in the presence of increasing amounts of Elliott Soil Humic Acid standard.

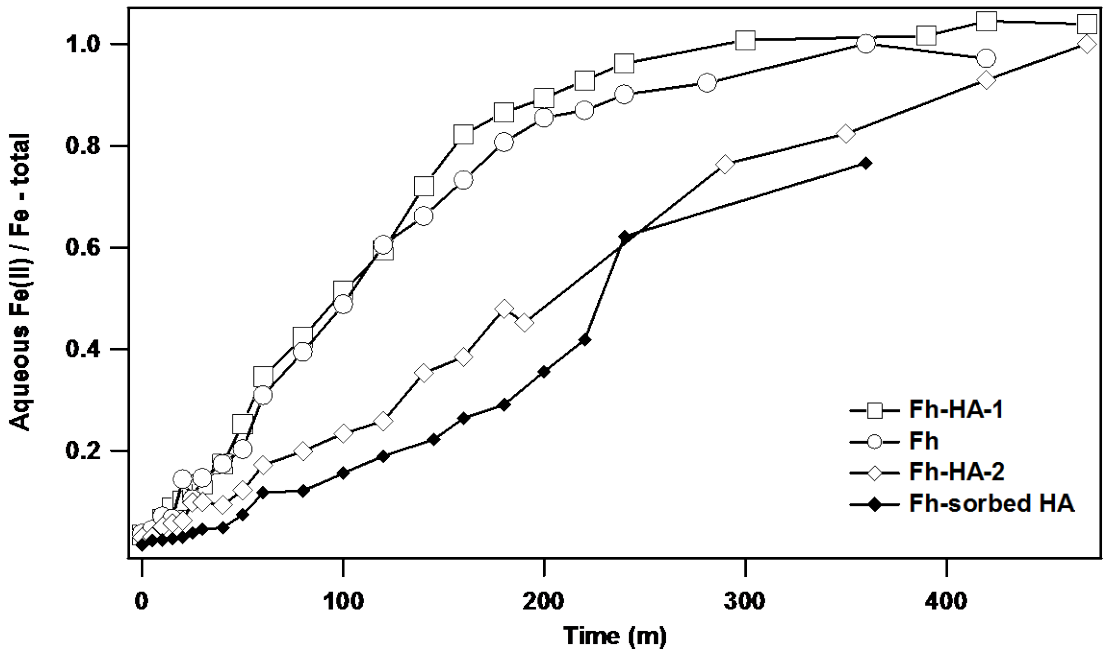

Figure 4.8. Reductive dissolution kinetics of Fh-HA coprecipitates in 10 mM ascorbic acid at pH 3.0. Dissolution was fastest for ferrihydrite (C:Fe = 0) and Fh-HA-1 (C:Fe = 1) with corresponding Fe(II) dissolution fluxes of 1.88×10^{-3} and 1.86×10^{-3} mol $g^{-1}s^{-1}$, while Fh-HA-2 and Fh-sorbed HA dissolution was substantially slower with 1.74×10^{-5} mol $g^{-1}s^{-1}$ and 8.76×10^{-4} mol $g^{-1}s^{-1}$ Fe dissolution flux respectively.

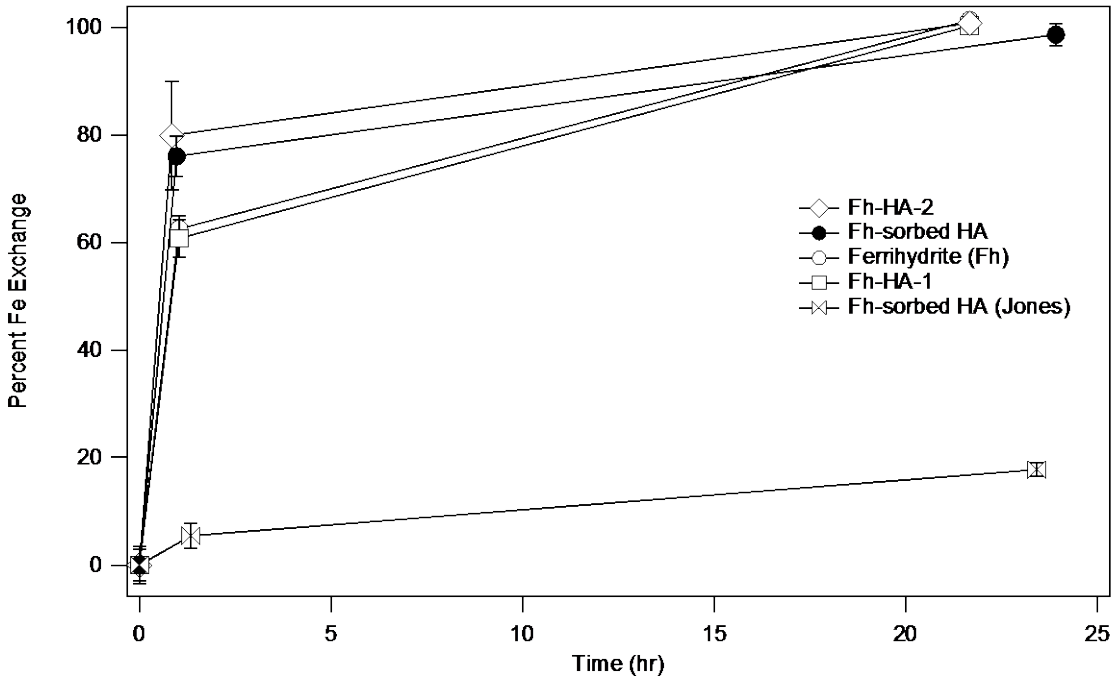

Figure 4.9. Percent Fe exchange measurements for Fh-HA coprecipitates during reaction with aqueous $^{57}Fe(II)$. Percent exchange was calculated from equation 3-2 in the text, error bars represent 1-standard deviation of duplicate or triplicate reactors. Experimental conditions are summarized in Table 4.2.

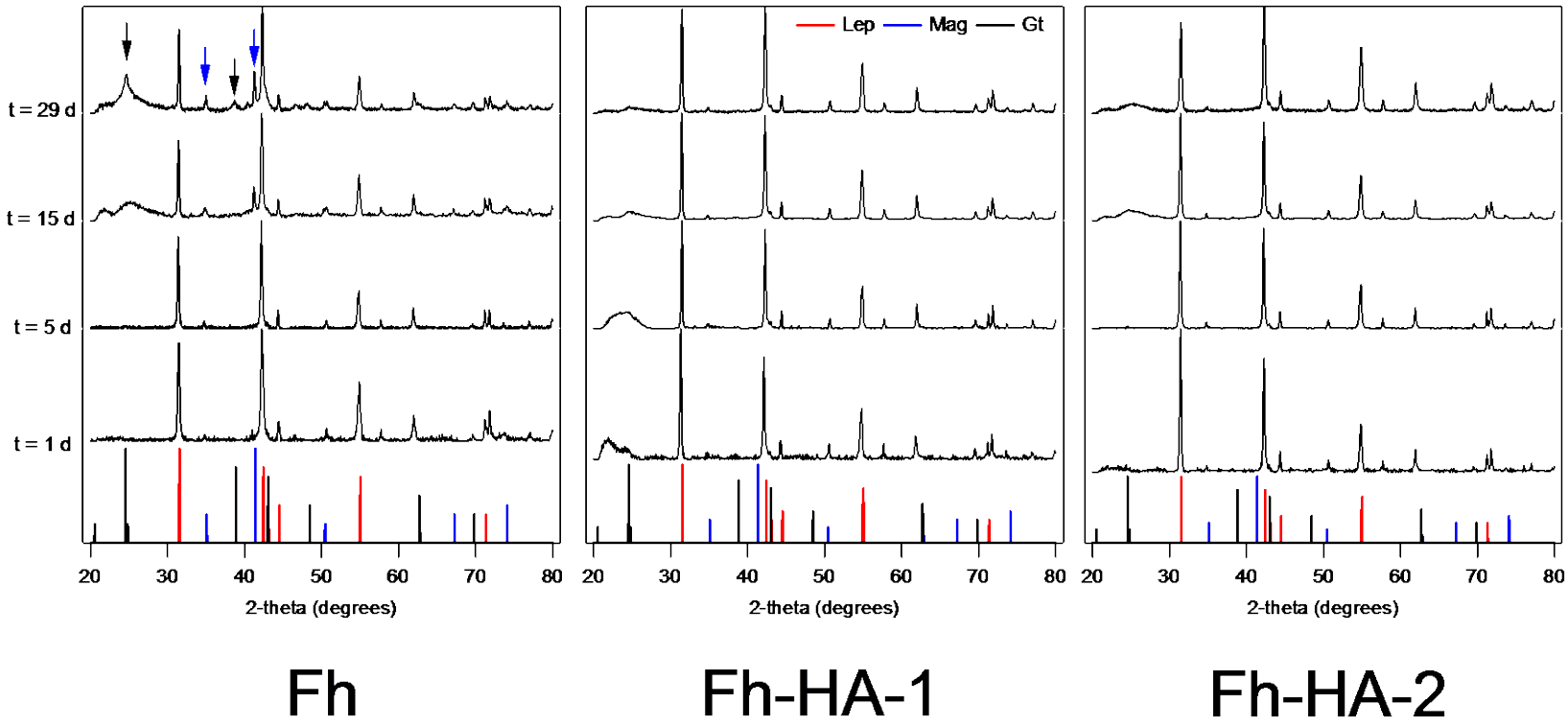

Figure 4.10. Powder X-ray diffraction (pXRD) patterns for Fh-HA coprecipitates after reaction with aqueous Fe(II) for periods ranging from 1 to 29 days. Reference patterns for lepidocrocite (red lines), magnetite (blue lines), and goethite (black lines) are displayed below experimental patterns. Characteristic peaks for goethite (black arrows) and magnetite (blue arrows) appear after 29 days in reactors with Fh, but are absent for Fh-HA-1 and Fh-HA-2.

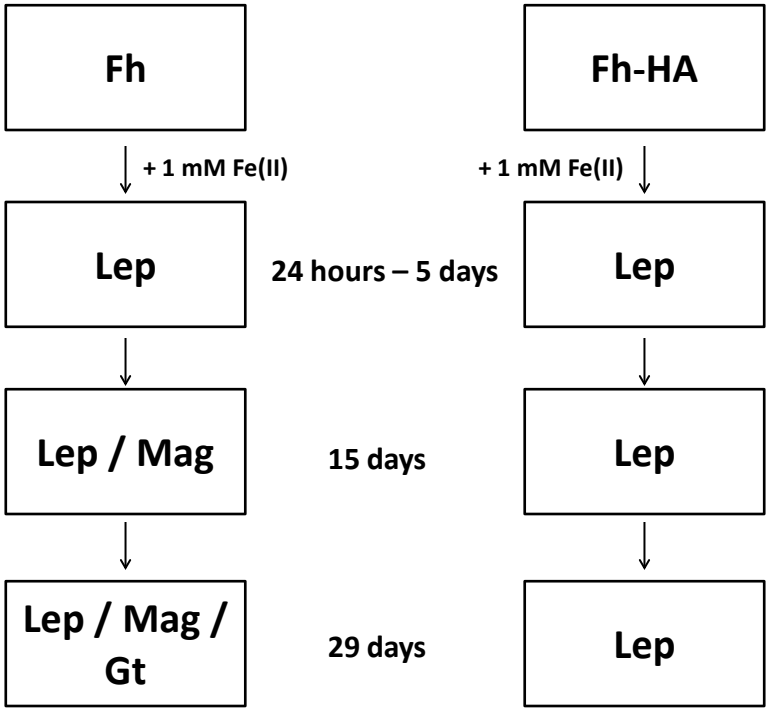

Figure 4.11. Conceptual model depicting the Fe(II)-catalyzed transformation pattern of ferrihydrite (Fh) and ferrihydrite-humic acid coprecipitates (Fh-HA) to lepidocrocite (Lep), magnetite (Mag), and goethite (Gt).

CHAPTER 5: ENVIRONMENTAL SIGNIFICANCE

Summary

The studies detailed in this thesis provide us with a further understanding of just how complex the interaction between Fe(II) and Fe oxides is throughout the environment. Dissimilatory iron reduction is common throughout reducing environments, resulting in widespread subsurface areas where both Fe(III) (precipitated in mineral form) and Fe(II) are simultaneously present. Aqueous Fe(II) has been shown to "recharge" magnetite, changing its sorption capacity for Fe(II), conductivity, and reactivity towards contaminants. In Chapter 2, we demonstrated that the Fe(II) content of magnetite can significantly influence its ability to reduce inorganic mercury. Recharging of magnetite by Fe(II) makes it a better reductant, which can be observed by its enhanced ability to reduce nitroaromatic compounds, radionuclides, and now heavy metals.

While the Fe(II)-Fe oxide interaction has been explored extensively through the lens of contaminant reduction, only recently has our focus shifted to directly examine (in contaminant free systems) the recrystallization process that can occur in Fe oxides exposed to aqueous Fe(II). Research from our group has now demonstrated that the reaction of Fe(II) with several Fe oxides can result in significant and often rapid Fe isotope exchange between the aqueous and solid phases (Table 5.1, Figure 5.1), which may be accompanied by secondary mineral transformation (ferrihydrite), preferential growth and dissolution at distinct crystal faces (hematite), or no apparent changes at all (goethite, magnetite). As a whole, we refer to these processes as Fe(II)-catalyzed Fe oxide recrystallization, which in experimental systems appears to be relevant to nearly every oxide tested so far.

Having observed the seeming ubiquity of this process, we are only beginning a systematic investigation of the factors that may influence the kinetics of Fe(II)-catalyzed Fe atom exchange and Fe oxide recrystallization. This study will ultimately include an

examination of fundamental oxide properties (band gap, particle size, surface area, conductivity, etc.), solution conditions (level of ^{57}Fe enrichment, ratio of aqueous Fe to solids, presence of environmentally relevant anions and other constituents), and experimental complexity (pure oxides vs. real soil samples). While great strides have been made toward understanding the mechanisms behind Fe(II)-catalyzed recrystallization, the relevant mechanism(s) may vary from mineral to mineral, and we still lack direct evidence to differentiate between dissolution/reprecipitation, bulk conduction, solid-state diffusion, and pore diffusion. Our initial work with goethite led to a hypothesized mechanism relying on bulk conduction, a property that can vary widely among Fe oxides, which range from conductors to insulators. While a very good correlation can be drawn between decreasing mineral band gap (increasing conductivity) and contaminant reduction in the presence of Fe(II) (Figure 5.2), we do not see the same trend for Fe atom exchange, where we would expect magnetite (a conductor) to undergo exchange faster than our other semi-conducting oxides. Whether this is due to different mechanisms, a rate limiting step other than bulk conduction, or other physical properties of the oxides is not yet clear.

What is clear from the work in Chapters 3 and 4, is that Fe(II)-catalyzed Fe oxide recrystallization is a robust process, which likely happens in a wide variety of geochemical environments. Despite the presence of many different types of environmentally relevant forms of organic carbon, we observed significant Fe atom exchange in goethite and magnetite. Even after sorbing a phospholipid to magnetite and goethite, which was shown to largely shut down interfacial electron transfer between aqueous Fe(II) and the underlying oxide, we still observed isotope mixing between the two phases (albeit to a much lesser extent). In ferrihydrite systems, we still observed rapid and complete isotopic exchange when organic carbon was present either as a sorbed or coprecipitated species. This implies that in environmental systems, the extent of Fe atom exchange observed may very well depend on the Fe oxide content of the soil, as

those oxides will undergo significant or even complete recrystallization despite the complex nature of the surrounding environment. There are likely to be exceptions to this broad statement of course, as research in our own group has shown that aluminum substitution can inhibit Fe atom exchange in goethite, but that so far appears to be an isolated case. Indeed, in Fe(II)-catalyzed recrystallization experiments performed by collaborators using real soil samples, they observed limited Fe atom exchange (~4% after 30 days) (Figure 5.3), but found that the mass of Fe exchanged in the residual soil solids agreed well with the mass of Fe recovered by acid ammonium oxalate extraction, which targets nano-crystalline Fe oxides (124) (Appendix B). This perhaps indicates that the observed exchange was due to the complete turnover of Fe oxides which made up only a fraction (15%) of the overall solids mass. Similar evidence was provided by Mössbauer spectroscopy, where the increase in spectral area attributed to the addition of ^{57}Fe labeled Fe(II) could be entirely accounted for by the increased area of the Fe(III)-hydroxide sextet, implicating those oxides as the dominant sink for electrons from aqueous Fe(II) (Figure 5.4). Further data indicates that goethite can undergo this process continuously, as long as an isotope enrichment gradient exists between the aqueous phase and the oxide solids. In experiments with goethite where the isotopically enriched aqueous Fe(II) was removed and replaced with fresh Fe(II) solution at 7 and 14 days, we continued to see substantial Fe atom exchange even after the removal / replacement steps (Figure 5.5).

Thus, Fe(II)-catalyzed Fe oxide recrystallization has proven to be a nearly impossible process to shut down, and remains difficult to inhibit even partially. For these reasons, its environmental relevance should remain high, and the possibility for continued cycling of trace elements and other compounds in concert with Fe lead to significant implications for pollutant dynamics and carbon storage. Because there is still so much uncertainty regarding the mechanisms and factors influencing Fe(II)-catalyzed Fe oxide recrystallization, the potential for future study is rich.

Recommendations for Future Work

Despite the insights gained into the environmental relevance of Fe oxide recrystallization, a number of questions still remain unanswered.

What is the fate of carbon following Fe oxide recrystallization?

While we showed that sorbed and coprecipitated carbon generally exert little influence on rates of Fe atom exchange, the ultimate fate of the carbon is unclear, particularly in the coprecipitated case. Determining the answer to this question will be of increasing importance due to concerns regarding long term soil carbon storage and potential feedbacks between soil and atmospheric carbon. Carbon measurements in the solid and aqueous phase will provide some initial insight into the stability of carbon in Fe-carbon coprecipitates during reaction with Fe(II). Elemental mapping techniques (EDX, STXM) may also be beneficial in determining how the spatial distribution of carbon changes following reaction with Fe(II). Most studies have so far focused on ferrihydrite-organic matter coprecipitates, presumably because ferrihydrite is the first Fe oxide to precipitate. To truly assess the possibility of long term carbon storage by coprecipitation, organic matter can be added during different phases of mineral synthesis to determine whether it can be incorporated into stable minerals (e.g., goethite, magnetite) more likely to facilitate long term storage.

How does Fe(II) catalyze Fe atom exchange and oxide recrystallization?

We are still very much in the dark as to the mechanism responsible for Fe atom exchange in stable Fe oxides, and the driving force behind this group of processes. The results of Chapter 3, where we saw atom exchange in systems where electron transfer was largely inhibited, were somewhat counterintuitive and beg further study. While electron transfer is assumed to be extremely fast, we have only speculated about the

effect of donor-acceptor distance on the possibility of electron transfer. The use of a hydrophobic, bilayer forming compound (similar to semi-permeable cell membranes) may introduce another step (and rate) in the recrystallization process, diffusion or migration of the Fe(II) or electron to the oxide surface through this layer. One could envision how an additional step of this nature could result in slower electron transfer and Fe atom exchange, both of which were observed when DOPA was present. We also observed an apparent decrease in the extent of exchange over long periods of time, a phenomenon which is not adequately described by the addition of this so-called "diffusion" step. Instead, it is possible that we observed limited electron transfer and Fe atom exchange because DOPA does effectively block Fe(II) from transferring an electron to the underlying oxide, but does not form perfect vesicles around goethite and magnetite particles, leaving some fraction of the oxide surface accessible to Fe(II). In our electron transfer experiments using DOPA, Mössbauer spectra indicated greater electron transfer occurs over 24 hours in magnetite than goethite (20% in magnetite vs. 6% in goethite), yet we observed very similar Fe atom exchange in magnetite (25%) and goethite (20%) after 60 days reaction. Perhaps both atom exchange and electron transfer occur at different rates in magnetite and goethite, and we simply failed to see that difference by having our first atom exchange sample at 30 days. A combination of long term experiments that examine both electron transfer and Fe atom exchange at similar time points may help us to further decipher how the two processes are connected, and how exactly DOPA perturbs these reactions. Additional study of the Fe oxide-DOPA system, perhaps using an electrochemical approach might further illuminate how Fe(II) catalyzes Fe oxide recrystallization, even in the presence of anions capable of forming surface coatings thick enough to theoretically block electron transfer.

Table 5.1. Experimental conditions for Fe atom exchange experiments with different Fe oxide minerals.

Fe oxide	Solution conditions	$pH_{initial}$	Solids loading	$[Fe(II)]_{initial}$	$f^{57}Fe_{initial}$
ferrihydrite	50 mM MOPS	7.0	2 g/L	1 mM	85.9%
goethite	25 mM HEPES / KBr	7.5	2 g/L	1 mM	36.8%
hematite	10 mM oxalate / KCl	7.1	1 g/L	1 mM	92.6%
magnetite	50 mM MOPS	7.2	1 g/L	1 mM	85.7%

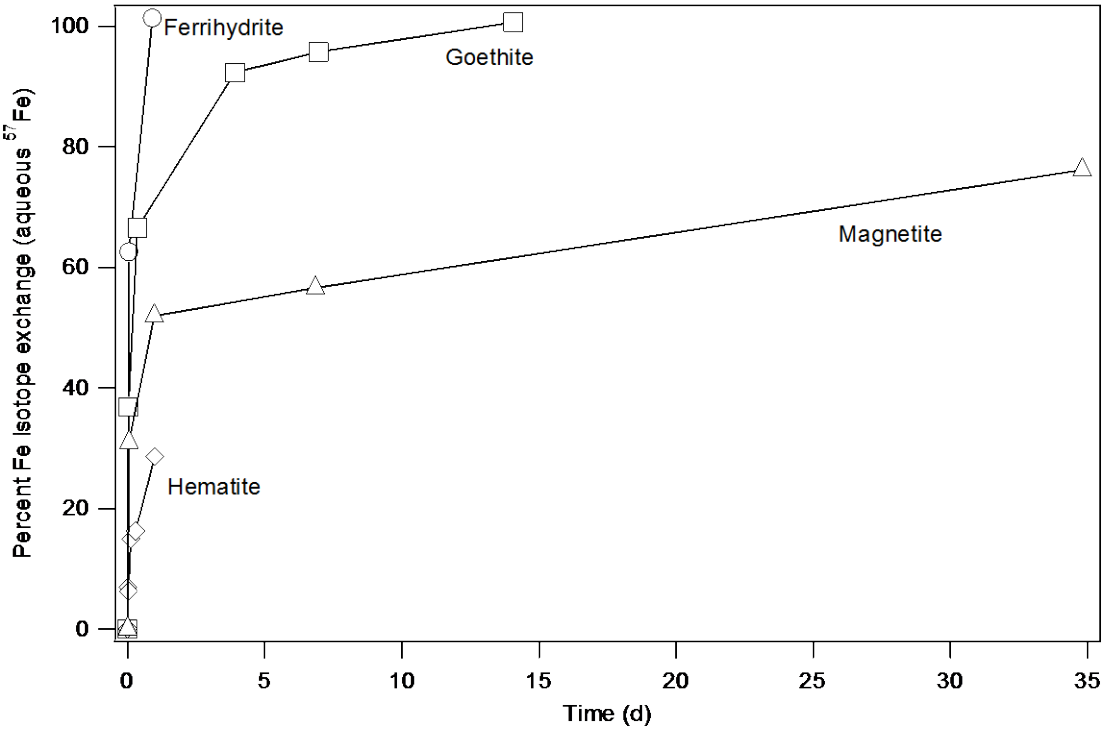

Figure 5.1. Fe(II)-catalyzed atom exchange and recrystallization in various Fe oxide minerals. Experiment conditions are shown Table 5.1.

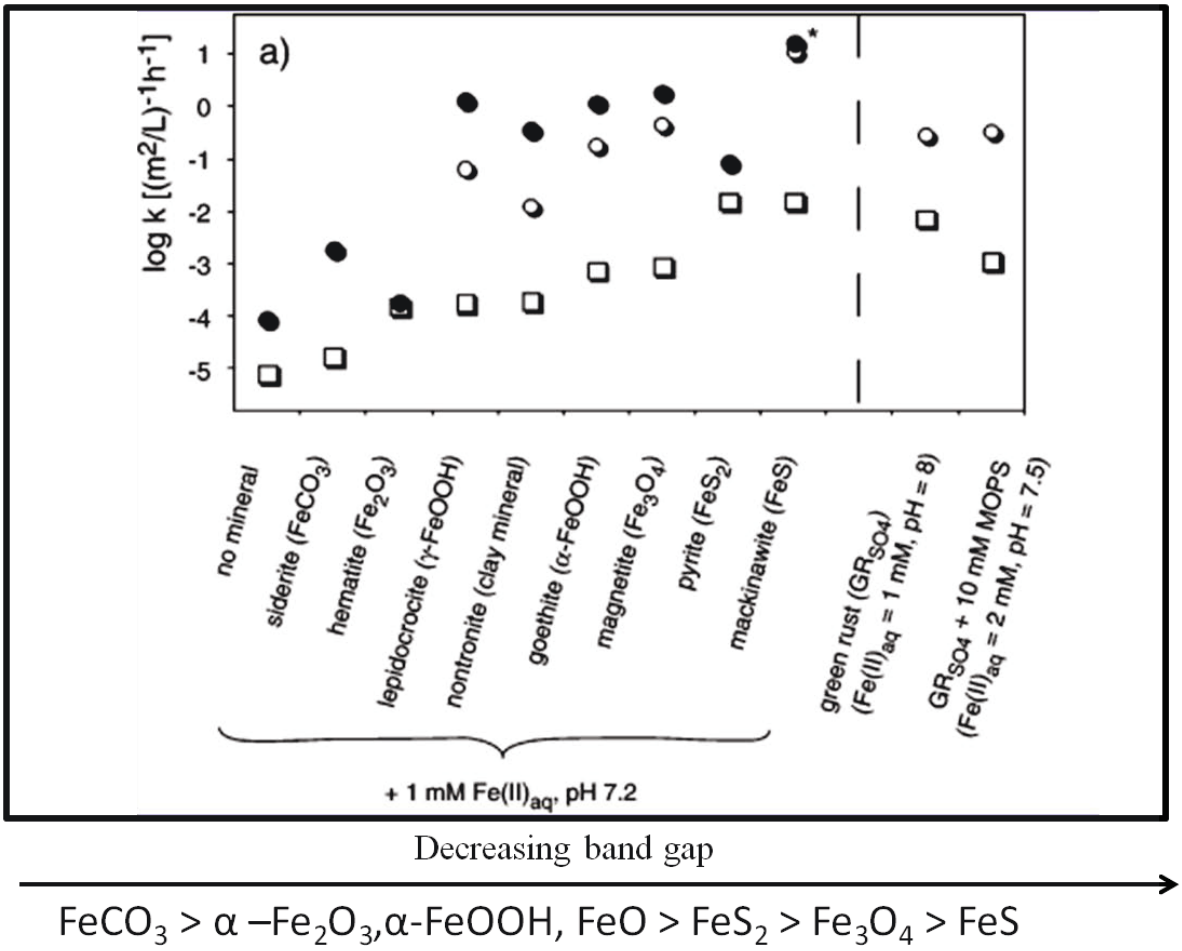

Figure 5.2. Logarithmic pseudo-first-order rate constants for the reduction of hexachloroethane (squares), 4-chloronitrobenzene (filled circles), and 4-chlorophenyl hydroxylamine (open circles) by aqueous Fe(II) with various Fe(II) containing minerals. Adapted from (177).

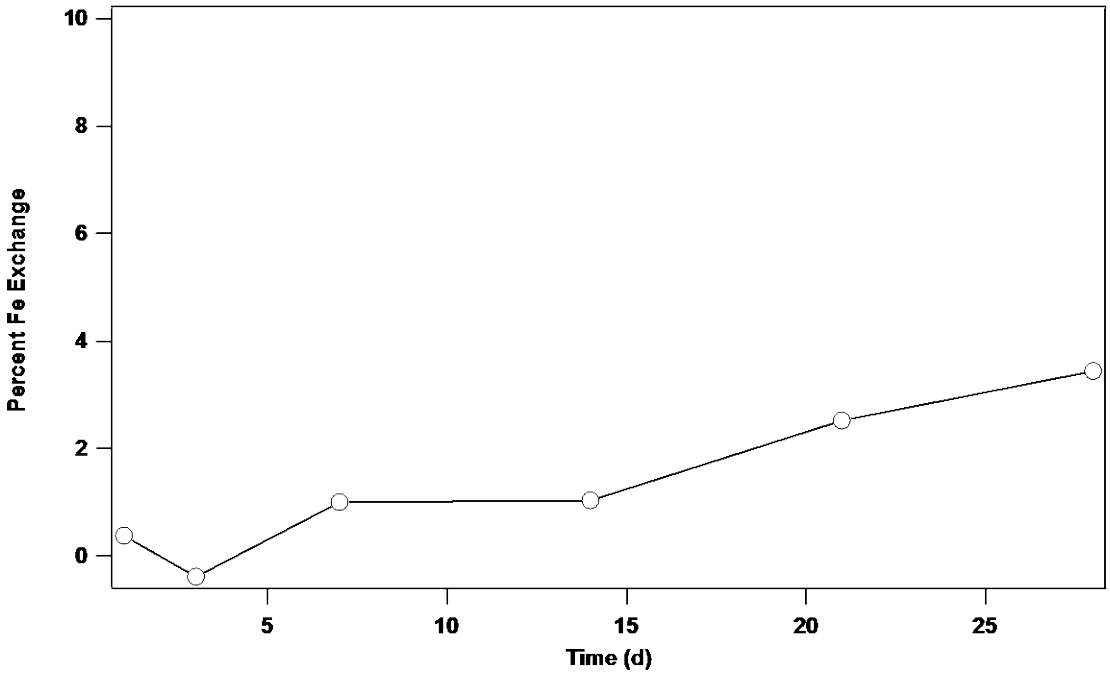

Figure 5.3. Fe isotope exchange measured in ^{57}Fe tracer experiments with soil samples from the Bisley, Puerto Rico Critical Zone Observatory site.

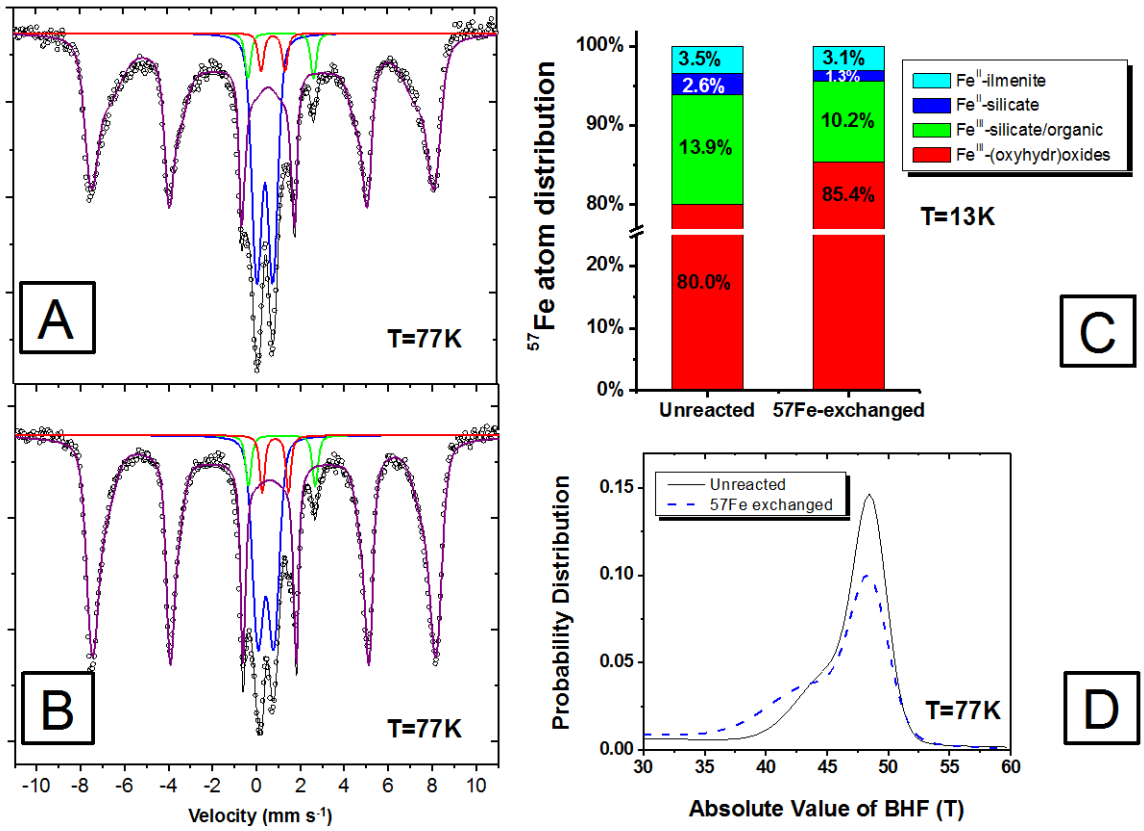

Figure 5.4. ^{57}Fe Mössbauer spectra of Bisley, PR soil samples. Spectra show the soil sample before (B) and after (A) reaction with ^{57}Fe enriched Fe(II). The increase in total Fe resulting from addition of the ^{57}Fe labeled tracer is almost entirely accounted for by the area increase of the Fe(III)-(oxyhydr)oxide sextet (shown in (C)), indicating that it is the dominant phase acting as a sink for electrons in the soil sample.

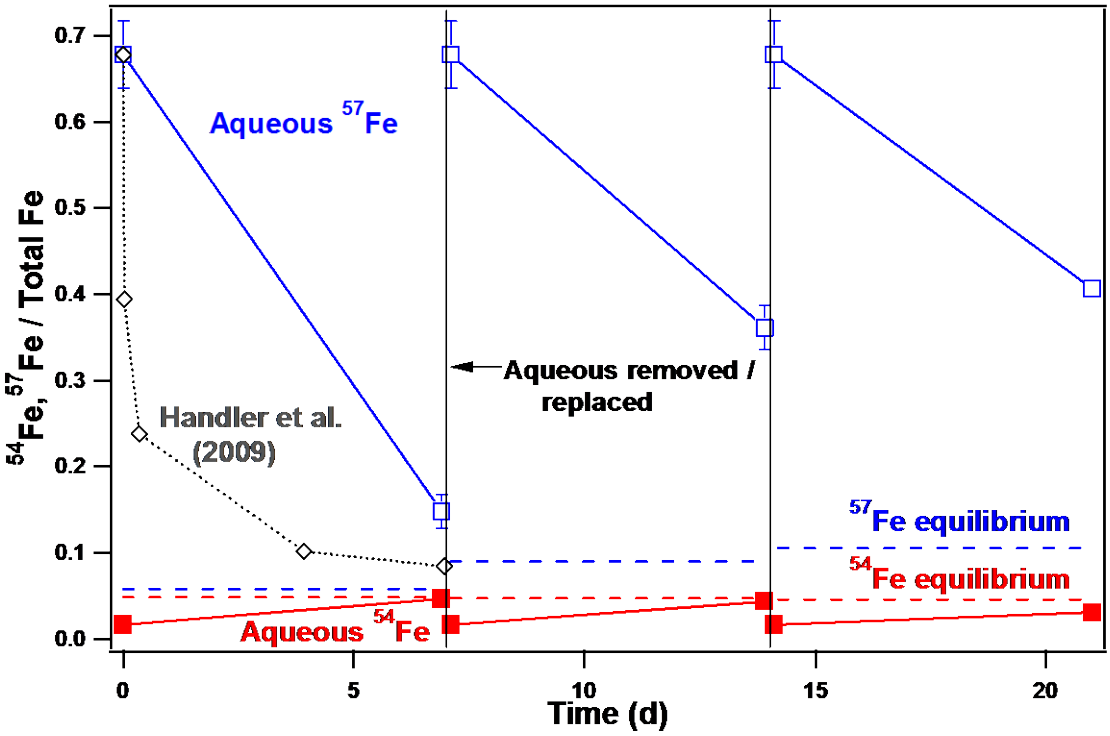

Figure 5.5. Measured fraction of ^{57}Fe and ^{54}Fe in aqueous goethite suspension after sequential additions of enriched ^{57}Fe(II). Sequential additions of 1 mM ^{57}Fe-enriched Fe(II) were performed at 7 and 14 days as shown by the vertical lines.

APPENDIX A: FE ATOM EXCHANGE BETWEEN AQUEOUS FE^{2+} AND MAGNETITE[2]

[2]Gorski, C.A., Handler, R.M., Beard, B.L., Pasakarnis, T., Johnson, C.M., Scherer, M.M., Fe Atom Exchange between Aqueous Fe^{2+} and Magnetite. *Environmental Science & Technology*, 2012. **46**(20): p. 12399-407.

ENVIRONMENTAL Science & Technology

Article

pubs.acs.org/est

Fe Atom Exchange between Aqueous Fe^{2+} and Magnetite[#]

Christopher A. Gorski,[†,⊥] Robert M. Handler,[‡,⊥] Brian L. Beard,[§] Timothy Pasakarnis,[∥] Clark M. Johnson,[§] and Michelle M. Scherer*[,∥]

[†]Environmental Chemistry, Swiss Federal Institute of Aquatic Science and Technology, Eawag, Ueberlandstrasse 133, 8600 Duebendorf, Switzerland

[‡]Sustainable Futures Institute, Michigan Technological University, 1400 Townsend Drive, Houghton, Michigan 49931, United States

[§]Department of Geoscience, University of Wisconsin, Madison, 1215 West Dayton Street, Madison, Wisconsin 53706, United States

[∥]Civil and Environmental Engineering, University of Iowa, Iowa City, Iowa 52242, United States

Supporting Information

ABSTRACT: The reaction between magnetite and aqueous Fe^{2+} has been extensively studied due to its role in contaminant reduction, trace-metal sequestration, and microbial respiration. Previous work has demonstrated that the reaction of Fe^{2+} with magnetite (Fe_3O_4) results in the structural incorporation of Fe^{2+} and an increase in the bulk Fe^{2+} content of magnetite. It is unclear, however, whether significant Fe atom exchange occurs between magnetite and aqueous Fe^{2+}, as has been observed for other Fe oxides. Here, we measured the extent of Fe atom exchange between aqueous Fe^{2+} and magnetite by reacting isotopically "normal" magnetite with ^{57}Fe-enriched aqueous Fe^{2+}. The extent of Fe atom exchange between magnetite and aqueous Fe^{2+} was significant (54−71%), and went well beyond the amount of Fe atoms found at the near surface. Mössbauer spectroscopy of magnetite reacted with $^{56}Fe^{2+}$ indicate that no preferential exchange of octahedral or tetrahedral sites occurred. Exchange experiments conducted with Co-ferrite ($Co^{2+}Fe_2^{3+}O_4$) showed little impact of Co substitution on the rate or extent of atom exchange. Bulk electron conduction, as previously invoked to explain Fe atom exchange in goethite, is a possible mechanism, but if it is occurring, conduction does not appear to be the rate-limiting step. The lack of significant impact of Co substitution on the kinetics of Fe atom exchange, and the relatively high diffusion coefficients reported for magnetite suggest that for magnetite, unlike goethite, Fe atom diffusion is a plausible mechanism to explain the rapid rates of Fe atom exchange in magnetite.

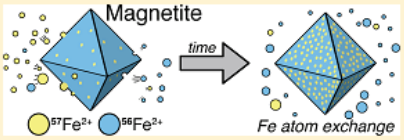

INTRODUCTION

Iron (Fe) redox cycling has been shown to impact several important biogeochemical reactions, including macro- and trace-nutrient availability for microorganisms[1,2], the solubility and accessibility of heavy and radioactive elements (e.g., uranium) present in groundwater[3−7], and the degradation and sorption of organic environmental contaminants.[8−11] The reaction between aqueous Fe^{2+} and Fe oxides, however, remains poorly understood due to the multitude of possible reaction pathways and the complexity of evaluating heterogeneous reaction mechanisms.[12−15]

Several Fe oxides (e.g., ferrihydrite and lepidocrocite) are known to undergo secondary mineralization reactions when reacted with aqueous Fe^{2+}[16−19] or Fe-reducing bacteria.[20−23] Secondary mineralization is thought to involve either topotactic reformation or nucleation and recrystallization.[16−18,20] For several more stable Fe oxides, including goethite and hematite, aqueous Fe^{2+} and reduction by Fe-reducing bacteria do not appear to result in any significant secondary mineralization products.[13,24−27] Only recently have studies shown that aqueous Fe^{2+} reacted with this latter class of Fe oxides results in extensive recrystallization and atomic exchange of Fe between the solid mineral and the aqueous phase.[17,28−35] The mechanism and thermodynamic driving force of recrystallization remains a topic of debate in the literature,[12,18,36,37] but it is has been proposed that this process involves electron conduction rather than Fe diffusion, especially at low temperatures.[12,13,31,38]

Like goethite and hematite, magnetite (ideal formula: Fe_3O_4) does not undergo a secondary mineralization reaction when exposed to aqueous Fe^{2+}.[39,40] Whether or not magnetite undergoes significant Fe atom exchange when exposed to aqueous Fe^{2+}, however, remains unknown. To what extent magnetite participates in Fe atom exchange is of particular importance to ongoing work investigating the long-term fate of radionuclides that are structurally incorporated into the magnetite lattice.[41,42]

Magnetite is also a compelling mineral to study from a mineralogical standpoint because our knowledge of what

[#]This article was intended for the Transformations of Nanoparticles in the Environment Focus Issue (July 3, 2012; Volume 46, Issue 13)

Received: December 23, 2011
Revised: March 28, 2012
Accepted: April 26, 2012
Published: May 11, 2012

Table 1. Specific Surface Area (SSA) and Particle Size Measurements for Magnetite and Co-Ferrite Particles Determined Using pXRD and TEM[a]

sample	pXRD crystallite diameter (Scherrer eq) (nm)[b]	TEM particle diameter (nm)[c]	pXRD SSA (m^2g^{-1})[b]	TEM SSA (m^2g^{-1})
stoich. mag.	11.0 ± 0.1[d]	14.9 ± 3.5	105 ± 1[d]	77 ± 15
stoich. mag. + Fe^{2+}	11.0 ± 0.2	15.1 ± 4.7	105 ± 2	76 ± 18
nonstoich. mag.	9.1 ± 0.3	10.5 ± 2.4	128 ± 4	110 ± 20
nonstoich. mag. + Fe^{2+}	9.9 ± 0.3	10.8 ± 3.4	117 ± 3	109 ± 26
Co-ferrite	33.8 ± 1.5	29.6 ± 12.9	34 ± 1	39 ± 12
Co-ferrite + Fe^{2+}	27.8 ± 1.0	37.8 ± 15.5	41 ± 1	30 ± 9

[a]Conversions between SSA and particle diameter were made by assuming a density of 5.2 $g\,cm^{-3}$ and a spherical geometry. Note pXRD measures the primary crystallite size, not the particle size, which explains the larger values for SSA. [b]pXRD provides a primary crystallite size that can be smaller than the particle size. [c]Average particle diameter; n = 50 particles. [d]($\pm\sigma$).

controls the extent of Fe^{2+} uptake is relatively well understood compared to the other Fe oxides.[13] Magnetite can contain varying fractions of structural Fe^{2+} (x, eq 1):

$$x = \frac{Fe^{2+}}{Fe^{3+}} \quad (1)$$

where x can range between 0 (completely oxidized) and 0.5 (stoichiometric); intermediate phases are referred to as partially oxidized or nonstoichiometric. Magnetite stoichiometry (x) has been shown to control the extent of Fe^{2+} uptake at neutral pH values, where the maximum extent of Fe^{2+} uptake appears to be limited by the bulk solid stoichiometry reaching x = 0.50.[40,43,44] Using Mössbauer spectroscopy, we have previously shown that this process occurs by reduction of structural octahedral Fe^{3+} atoms.[40]

To (*i*) gain further insights into the mechanism(s) responsible for aqueous Fe^{2+}−magnetite exchange reactions and (*ii*) examine their implications for the fate of structurally incorporated heavy metals and radionuclides, we measured the kinetics and extent of Fe exchange between magnetite and ^{57}Fe-enriched aqueous Fe^{2+}. This approach allowed us to calculate what fraction of structural Fe in magnetite exchanged with aqueous Fe^{2+} in solution at a circumneutral pH over the period of one month. Additional experiments were done utilizing the isotopic specificity of ^{57}Fe Mössbauer spectroscopy to determine if exchanged Fe in magnetite occurred preferentially at octahedral or tetrahedral Fe sites. We also examined Fe atom exchange between Co-ferrite (ideal structure: $CoFe_2O_4$) and aqueous Fe^{2+} in an attempt to discriminate between electron conduction and atomic diffusion as the rate-limiting steps controlling interfacial Fe atom exchange between magnetite and aqueous Fe^{2+}.

■ MATERIALS AND METHODS

All experiments and syntheses were conducted in a 93:7 N_2:H_2 anaerobic glovebox (O_2 < 1 ppm) unless otherwise noted. All solutions were purged with N_2 for at least 1 h prior to introduction into the glovebox, where they were allowed to equilibrate with the glovebox atmosphere several days prior to use. Glassware, plastic, and Co-ferrite were allowed to equilibrate in the glovebox atmosphere several days before use to minimize the presence of sorbed O_2. All reactors were covered in aluminum foil to avoid photochemical reactions.

Magnetite Synthesis and Solids Characterization. Magnetite batches were synthesized in the anaerobic chamber as previously described.[40] Briefly, isotopically normal Fe^{2+} and Fe^{3+} were combined at a 1:2 ratio in deionized water (added as $FeCl_2$ and $FeCl_3{\cdot}6H_2O$, respectively) before raising solution pH to 10 with NaOH. Magnetite precipitates were aged in anoxic suspension for 24 h. To produce a magnetite sample with a nonstoichiometric Fe^{2+}:Fe^{3+} ratio (i.e., Fe^{2+}:Fe^{3+} < 0.5), one magnetite suspension was allowed to mix for an additional day after spiking with 30% H_2O_2 to partially oxidize the sample. Solids were collected by filtration and freeze-dried, with great care taken to prevent oxygen intrusion into the anaerobic container during the brief (~4 h) removal from the glovebox atmosphere for freeze-drying. Previous work with this magnetite synthesis method has reliably produced magnetite batches of relatively uniform particle morphology, with no observable secondary Fe phases in X-ray diffraction (XRD) patterns.[40,45] Co-ferrite was purchased (NanoAmor, Houston, TX, USA) and used as received.

The stoichiometry of each batch was determined by dissolving preweighed samples in 5 M HCl in the anaerobic glovebox, with reactors covered in Al foil to prevent photoreactions. Fe^{2+} and total Fe measurements were measured colorimetrically using the phenanthroline method, as previously described.[40,45] Cobalt concentrations were determined colorimetrically using 1-nitroso-2-naphthol-3,6-disulfonic acid disodium salt hydrate (NRS) as a complexing agent, adapting the method of Zahir and Keshtkar.[46] Samples were buffered at pH 6.0, heated for 1 h at 60 °C, and acidified with HCl prior to analysis at 520 nm. NRS is not selective for Co^{2+}, but Co^{3+} is not expected to be present in solution at circumneutral pH due to solubility constraints. Fe^{2+}:Fe^{3+} analyses of magnetite in which Fe^{2+}:Fe^{3+} was added in the stoichiometric 1:2 ratio and not oxidized with H_2O_2 indicated an initial magnetite stoichiometry very close to the predicted value of x = 0.50 (x = 0.51 ± 0.01). The magnetite solids exposed to H_2O_2 during aging had an initial Fe^{2+} content well below stoichiometry (x = 0.29 ± 0.01). Acidic dissolution indicated that the Co-ferrite was Co deficient, with a Co:Fe ratio of 0.41 ± 0.003 (ideal = 0.50). The adjusted unit formula can be written as $Co_{0.86}Fe_{2.09}O_4$.

To access changes in the magnetite and Co-ferrite samples before and after exposure to $^{57}Fe^{2+}_{aq}$, we used several techniques to track the stoichiometry (Mössbauer spectroscopy, powder X-ray diffraction (pXRD)) and particle size (BET, transmission electron microscopy (TEM), and pXRD). TEM imaging (Jeol 1230) was performed on samples equilibrated in buffer (described below) for 30 days with and without the presence of Fe^{2+}_{aq} to determine if the particle sizes significantly changed. Samples were filtered through a 0.45-μm filter, rinsed with deionized water to remove traces of buffer salt or Fe^{2+}_{aq}, and suspended in methanol prior to placement on Cu-grids for

TEM imaging. The average particle size was measured for 50 particles using ImageJ software, as larger sample sizes did not affect the variation in sizes observed (Table 1).

pXRD patterns were collected for magnetite before and after equilibration with Fe^{2+}_{aq} over 30 days (Figure S1). Samples were prepared by mixing solids with a small amount of glycerol to prevent inadvertent oxidation during the measurement.[45] Patterns were collected with a Co-source between 15° and 90° 2θ with a 0.02° step size and a 1.5 s dwell time. Patterns were fit to determine the primary crystallite size (Scherrer equation),[47] the unit cell dimensions to extract the stoichiometry, and the relative peak intensities to calculate relative Fe site abundances (Jade 6 software; Materials Data, Inc., Livermore, CA).[45] The stoichiometry could not be measured reliably from the fitted *d*-spacing for these samples, which was likely due to differences in the sample heights. The relative peak intensities did not provide meaningful data, consistent with our previous analyses.[45]

^{57}Fe Mössbauer spectra were collected at 140 K for the magnetite and Co-ferrite before and after exposure to $^{57}Fe^{2+}_{aq}$ (Figure S2, Table S1). The sample preparation, details of the Mössbauer spectrometer, and fitting methods have been previously described.[45] The stoichiometry measured by Mössbauer spectroscopy was lower than that of acidic dissolution for stoichiometric ($x_{Mössbauer}$ = 0.45, $x_{dissolution}$ = 0.51) magnetite and higher for nonstoichiometric ($x_{Mössbauer}$ = 0.29, $x_{dissolution}$ = 0.34) (Table S2). In our previous work, we have shown that the dissolution and Mössbauer stoichiometry values are in good agreement with one another.[45] In the text, we refer to the dissolution stoichiometry values, although the interpretation would not change if the stoichiometry values determined by Mössbauer spectroscopy were used.

Fe Atom Exchange Studies Using Stable Isotopes. Experiments using an enriched ^{57}Fe isotope tracer were performed in a similar fashion as reported in earlier work with goethite solids.[31] An aqueous Fe^{2+} stock was created by combining different amounts of dissolved ^{57}Fe and ^{56}Fe (Chemgas, 96% and 99%, respectively, 300 mM Fe^{2+} dissolved in 1 M HCl) to achieve ∼70% enrichment in ^{57}Fe ($\delta^{57/56}$Fe = 715.91‰; $\delta^{57/56}$Fe defined below), as compared to isotopically "normal" Fe (i.e., $\delta^{57/56}$Fe ≈ 0‰). Small amounts of enriched $^{57}Fe^{2+}$ stock were added to 15 mL of 50 mM 3-(*N*-morpholino)-propanesulfonic acid (MOPS), buffered at pH 7.2, to create a ∼1 mM Fe^{2+} solution. After sitting for 1 h, Fe^{2+}−MOPS solutions were filtered with 0.2-μm nylon syringe-tip filters into a new glass vial. Initial Fe^{2+} concentration was measured, and experiments were initiated by adding 15.0 ± 0.1 mg of magnetite solid to produce a solution with 1 ± 0.007 g/L magnetite. Batch reactors were crimp-sealed and mixed on an end-over-end rotator in the dark. After time periods ranging from 10 min to 30 days, reactors were sacrificed in triplicate for chemical and isotope analysis. Control reactors were also used that contained magnetite solids without Fe^{2+}_{aq}, and Fe^{2+}_{aq} in the absence of magnetite solids.

Sequential extractions were performed on individual reactors. The aqueous phases of batch reactors were separated by magnetically attracting the solids and decanting the solution into a syringe with a 0.2-μm nylon filter. After filtering, the solution was acidified to stabilize Fe^{2+} and Co in solution. Magnetite solids were resuspended in 5 mL of a new buffer solution, with the goal of removing roughly as much Fe^{2+} as was lost due to net Fe^{2+} uptake during reaction. The extent of Fe^{2+} uptake varied considerably for each type of magnetite solid; as a result, different extract solutions and times were used for each type of solid (Table S3). After extraction, the solids were magnetically separated. Magnetite solids remaining after extraction were completely dissolved in 5 M HCl. Complete dissolution occurred in a matter of minutes at room temperature for magnetite, while heating at 60 °C for multiple hours was required to dissolve Co-ferrite. In addition to colorimetric Fe^{2+}, Fe^{3+}, and Co analyses, each sample was analyzed for stable Fe isotope ratios using multicollector inductively coupled plasma mass spectrometry (MC-ICP-MS) (Micromass IsoProbe), following previously established methods.[31]

Stable isotope measurements of ^{57}Fe and ^{56}Fe are expressed in the δ (delta) notation, which reports the relative proportions of two isotopes in comparison to an accepted reference standard:

$$\delta^{57/56}\mathrm{Fe}(‰) = \left(\frac{\frac{^{57}\mathrm{Fe}}{^{56}\mathrm{Fe}_{sample}} - \frac{^{57}\mathrm{Fe}}{^{56}\mathrm{Fe}_{std}}}{\frac{^{57}\mathrm{Fe}}{^{56}\mathrm{Fe}_{std}}} \right) \times 1000 \quad (2)$$

In this study, $^{57}Fe/^{56}Fe_{std}$ is the average isotopic ratio for terrestrial igneous rocks.[48] Tracking the changes in isotopic composition of the two reservoirs of Fe in this system (aqueous and solid Fe) allowed us to determine if ^{57}Fe-enriched Fe from the aqueous phase became incorporated into the solid phase. For reference, previous studies have reported a very minor preference for heavy Fe to be associated with the solid, where $\delta^{57/56}$Fe values are ∼0.1 to 0.7‰ higher in the solid than Fe^{2+}_{aq};[49−51] these differences are approximately two orders of smaller than the differences discussed here, and hence do not affect the extent and rates of exchange as measured in the ^{57}Fe-enriched tracer experiments.

The repeated exchange experiment with magnetite and $^{56}Fe^{2+}_{aq}$ was done by exposing 1 g/L isotopically "normal" magnetite to 4.5 mM $^{56}Fe^{2+}_{aq}$ at pH 7.2 for five 24 h cycles. Every cycle, the solids were magnetically separated from the solution, then fresh buffer containing 4.5 mM $^{56}Fe^{2+}_{aq}$ was added back to the reactor. After five cycles, the solids were collected for Mössbauer analysis. No net $^{56}Fe^{2+}$ uptake was observed after the first exposure to $^{56}Fe^{2+}_{aq}$.

■ RESULTS AND DISCUSSION

Fe Atom Exchange between Magnetite and Aqueous Fe^{2+}. To assess the extent and rate of Fe atom exchange between aqueous Fe^{2+} (Fe^{2+}_{aq}) and magnetite, we conducted a ^{57}Fe-enriched isotope tracer experiment adapting an approach similar to that used in our previous work.[31,33] We reacted isotopically "normal" magnetite ($\delta^{57/56}$Fe of +0.07‰) with Fe^{2+}_{aq} enriched with ^{57}Fe ($\delta^{57/56}$Fe of +715.91‰) and tracked the relative abundance of the ^{57}Fe and ^{56}Fe isotopes in both phases over time. We observed a rapid decrease in the $\delta^{57/56}$Fe of the Fe^{2+}_{aq} accompanied by a similarly rapid increase in the $\delta^{57/56}$Fe for the residual magnetite (Figure 1, top; Table 2). Residual magnetite was the magnetite remaining after a mild chemical extraction in which we tried to remove the Fe^{2+} transferred to the solid due to net Fe^{2+} uptake (Tables S3 and S4). The rapid rates of exchange after one day were followed by a much slower, but measurable, exchange rate.

The change in $\delta^{57/56}$Fe values in both phases indicates that Fe atom exchange has occurred, resulting in a more uniform distribution of ^{57}Fe atoms between both phases. Unlike our previous work with goethite,[31] neither the Fe^{2+}_{aq} nor magnetite

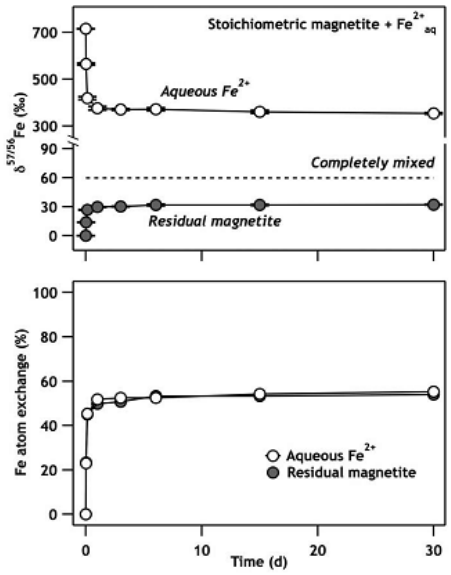

Figure 1. (Top) Measured $\delta^{57/56}$ values of stoichiometric magnetite equilibrated with aqueous Fe^{2+} for the aqueous and residual magnetite over 30 days. The dashed line represents the predicted $\delta^{57/56}$ of the system assuming complete equilibration. All data points are the average of three triplicate reactors. (Bottom) Calculated Fe atom exchange values for the data points in the top panel using eq 3.

reached the equilibrium isotope composition (δ_e) of 59.63‰ calculated from a mass balance on the reactor (dashed line in Figure 1), indicating that only a portion of the structural Fe in magnetite exchanged with Fe^{2+}_{aq}. The percent of Fe atom exchange can be calculated from

$$\text{percent exchange} = \frac{\delta_t - \delta_i}{\delta_e - \delta_i} \times 100 \quad (3)$$

where δ_t is the isotopic composition at time t and δ_i is the initial isotopic composition of the phase. There is strong agreement between the percent exchanged calculated using the Fe^{2+}_{aq} and residual magnetite phases (55.3% and 54.1%, respectively), with slightly more than half of the Fe exchanged within one day (Figure 1, bottom). The extent of exchange goes well beyond the Fe atoms available on the magnetite surface based on a simple spherical model (radius = 6.5 nm, Calc. S1). Exchange of 55% of the Fe represents almost 12 times the number of all surface Fe^{2+} and Fe^{3+} atoms present, or a depth of exchange of 2.5 nm into the 6.5 nm particle (assuming a magnetite unit cell dimension of 0.84 nm).[45]

We conducted a similar ^{57}Fe-enriched Fe^{2+}_{aq} tracer experiment with nonstoichiometric magnetite ($x = Fe^{2+}/Fe^{3+} = 0.29$) to evaluate if stoichiometry would influence the rate or extent of exchange. Previous work has shown that magnetite stoichiometry (x) strongly influences the extent of Fe^{2+} uptake, kinetics of contaminant reduction, particle conductivity, and redox properties.[39,40,52−54] Nonstoichiometric magnetite exhibited similar rates and extent of exchange as stoichiometric magnetite (Figure S3, Table 2). There is reasonable agreement between the percent exchange calculated using the Fe^{2+}_{aq} and residual magnetite phases (63.1% and 71.3%, respectively). Changes in isotope composition for nonstoichiometric magnetite indicate that slightly more exchange occurred with the nonstoichiometric magnetite (63.1−71.3%) as compared to the 55% observed for stoichiometric magnetite after 30 days (Table 2). Similar to stoichiometric magnetite, the rate of exchange was rapid with more than half of the Fe exchanged within one day. Note that, consistent with our earlier work,[40] significant mass transfer of Fe^{2+} from the aqueous phase to magnetite occurred for the nonstoichiometric magnetite (979 μM of 1000 μM Fe^{2+}_{aq} was taken up), and this is the likely explanation for the moderate disagreement in the percent exchange calculated for aqueous and solid phases. Using the percent exchange values without correcting for the mass transfer of Fe^{2+} to the magnetite phase would have resulted in erroneously high estimates of Fe exchanged. To minimize this potential bias, we used the residual magnetite (after extraction) values in our exchange calculations.

Despite the substantial exchange of Fe between the aqueous phase and magnetite (54−71% for stoichiometric and nonstoichiometric magnetite, respectively), we observed little change in the magnetite particle size or morphology over time and found no evidence for formation of any secondary phases. TEM images, pXRD patterns, and Mössbauer spectra were collected on magnetite samples before and after 30 days exposure to $^{57}Fe^{2+}_{aq}$, as well as control samples in buffer with no Fe^{2+}_{aq}. TEM images of the particles showed no significant change in particle size or morphology (Table 1, Figure S4). pXRD patterns (Figure S1), and Mössbauer spectra were consistent with magnetite as the only Fe-bearing phase present in the sample (Figure S2, Table S1). Mössbauer spectral analysis showed that the Fe^{2+} content in the magnetite samples increased upon exposure to Fe^{2+}_{aq} (nonstoichiometric: x_{init} = 0.34, x_{final} = 0.39, stoichiometric: x_{init} = 0.45, x_{final} = 0.50; Figure S2, Table S1), consistent with our previous work that showed Fe^{2+} taken up by magnetite becomes structurally incorporated.[40] The lack of a secondary transformation of magnetite when reacted with Fe^{2+}_{aq} is consistent with previous work.[40,44]

Is Only Octahedral Fe Exchanging? The abrupt decrease in the rate of Fe isotope exchange between magnetite and Fe^{2+}_{aq} after one day suggests that only a fraction of the structural Fe in magnetite is participating in rapid Fe atom exchange. The extent of Fe exchange (54−71%) is close to the 2/3 fraction (67%) of octahedral Fe present in stoichiometric magnetite (ideal formula: $^{Tet}Fe^{3+}[^{Oct}Fe^{2+}Fe^{3+}]O_4$), which raises the interesting possibility that only the octahedral Fe is exchanging. Tronc, Jolivet, and co-workers have compiled several compelling lines of evidence based on aqueous Fe^{2+} and Fe^{3+} concentrations, Mössbauer spectra, and pXRD patterns to argue that Fe dissolution in magnetite occurs preferentially at ^{Oct}Fe sites in mildly acidic conditions (pH = 2−2.5).[39,43,44,55] Electron transfer in magnetite is also thought to occur predominantly between $^{Oct}Fe^{2+}$ and $^{Oct}Fe^{3+}$ sites.[56]

To test whether octahedral Fe in magnetite was preferentially exchanging with Fe^{2+}_{aq}, we exchanged isotopically "normal" stoichiometric magnetite (2.2% ^{57}Fe) with aqueous $^{56}Fe^{2+}$ five times for 24-h equilibration periods. As expected, the total measured absorbance of the ^{56}Fe-cycled magnetite decreased significantly (77%) because of the decreased concentration of ^{57}Fe in the magnetite structure (Figure 2). If octahedral Fe

Table 2. Mass and Isotope Data for Fe Isotope Tracer Experiments between Fe^{2+}_{aq} and Stoichiometric Magnetite, Non-Stoichiometric Magnetite, and Co-Ferrite

		Aqueous Fe^{2+}			Residual magnetite		
	Time (d)	Fe (μmol)	$\delta^{57/56}$Fe (‰)	% Ex[a]	Fe (μmol)	$\delta^{57/56}$Fe (‰)	% Ex.
Stoichiometric magnetite	0	15.17 (0.24)[b]	715.91 (0.24)		167.16	0.07 (0.02)	
	0.007	13.97 (4.40)	564.79 (4.40)	*23.0*	172.99 (6.07)	13.94 (0.11)	*23.3*
	0.130	13.21 (6.29)	417.98 (6.29)	*45.4*	167.70 (6.17)	26.88 (0.27)	*45.0*
	1.000	13.44 (7.20)	375.79 (7.20)	*51.8*	170.44 (3.26)	29.80 (0.24)	*50.0*
	3.000	13.68 (3.85)	370.43 (3.85)	*52.6*	169.94 (2.32)	30.35 (0.16)	*50.9*
	6.040	13.15 (6.71)	371.36 (6.71)	*52.5*	163.94 (3.19)	31.83 (0.83)	*53.3*
	15.000	13.91 (6.52)	359.66 (6.52)	*54.3*	166.77 (5.31)	31.83 (0.51)	*53.3*
	30.000	13.90 (2.81)	352.89 (2.81)	*55.3*	170.63 (2.05)	32.26 (0.23)	*54.1*
Non-stoichiometric magnetite	0	15.04 (0.09)	715.91 (0.24)		170.85	0.08 (0.06)	
	0.007	8.03 (0.05)	653.34 (1.71)	*9.5*	157.89 (2.94)	16.11 (0.48)	*27.7*
	0.500	4.00 (0.14)	484.94 (12.83)	*35.1*	165.69 (3.18)	26.66 (0.00)	*45.9*
	1.000	1.69 (0.08)	349.05 (4.92)	*55.8*	166.76 (2.93)	35.19 (0.21)	*60.6*
	3.000	0.90 (0.11)	315.43 (3.76)	*60.9*	171.23 (2.66)	37.91 (0.47)	*65.3*
	6.000	0.55 (0.02)	310.90 (7.56)	*61.6*	173.31 (6.16)	38.53 (0.63)	*66.4*
	14.960	0.45 (0.02)	312.54 (1.64)	*61.3*	167.03 (1.42)	40.81 (0.14)	*70.3*
	29.880	0.32 (0.00)	300.70 (8.90)	*63.1*	165.64 (7.85)	41.40 (0.72)	*71.3*
Co-ferrite	0	15.21 (0.14)	715.91 (0.24)		119.31	0.05 (0.04)	
	0.007	11.81 (0.03)	698.01 (0.08)	*2.8*	121.27 (4.03)	11.70 (0.08)	*14.4*
	0.170	10.03 (0.31)	661.46 (5.81)	*8.6*	119.44 (0.48)	18.62 (1.74)	*22.9*
	1.000	7.61 (0.18)	625.16 (2.92)	*14.3*	124.51 (0.83)	31.28 (0.93)	*38.6*
	3.000	7.69 (0.17)	626.15 (2.63)	*14.1*	122.67 (1.64)	30.51 (0.54)	*37.6*
	6.130	7.06 (0.19)	617.41 (3.88)	*15.5*	124.46 (1.10)	33.80 (0.92)	*41.7*
	15.080	7.17 (0.15)	606.15 (15.08)	*17.3*	121.41 (2.65)	32.90 (0.37)	*40.6*
	30.040	6.61 (0.32)	607.85 (4.14)	*17.0*	124.44 (3.58)	34.95 (0.34)	*43.1*

[a] % Ex. = percent exchange calculated using eq 3 in the text.
[b] Standard deviation measured from triplicate reactors.

were preferentially exchanging with Fe^{2+}_{aq}, we would also expect to see a preferential decrease in the octahedral ^{57}Fe signal in the ^{57}Fe Mössbauer spectra because ^{56}Fe is transparent. The ^{57}Fe Mössbauer spectrum of the magnetite exchanged with aqueous ^{56}Fe does not show any decrease in the relative fraction of the octahedral Fe (Figure 2). Instead, the spectrum of the ^{56}Fe-cycled magnetite appears nearly identical to that of unreacted magnetite demonstrating that the ^{57}Fe present in the magnetite retained its relative abundance in octahedral and tetrahedral sites and no preferential exchange of octahedral (or tetrahedral) Fe occurred (Table S1).

We were surprised to see no indication that octahedral Fe is preferentially exchanged with Fe^{2+}_{aq}. Based on earlier work,[39,43,44,55,56] we anticipated that preferential exchange of octahedral Fe was the most plausible explanation for the 54−71% exchange observed in Figures 1 and S3. The lack of preferential exchange requires some other explanation for the abrupt slow down in Fe exchange after about 60%. At this point, we can only speculate that perhaps some type of surface passivation occurred[34,35,57,58] or that there is a thermodynamic equilibrium between Fe^{2+}_{aq} and magnetite that limits how long Fe atom exchange occurs.[12] Further work is underway to investigate what might be limiting the extent of exchange in magnetite.

Mechanism of Exchange between Magnetite and Aqueous Fe^{2+}. How more than half of Fe in magnetite exchanged without any apparent structural or morphological changes remains, as it was for goethite, a fascinating question. In our previous work with goethite, we observed complete exchange with Fe^{2+}_{aq} and we proposed a conceptual model involving oxidative Fe^{2+} sorption, $Fe^{2+} - Fe^{3+}$ oxide electron transfer, bulk electron conduction, and reductive dissolution.[31] Through these steps, we proposed a "redox-driven conveyor belt" model, where all of the Fe atoms in the goethite would be eventually exposed and exchanged with the aqueous phase. Our conceptual model was derived from the previous finding that a potential gradient between two hematite crystal faces could drive bulk electron conduction through the mineral and result in hematite growth at one face and reductive dissolution and surface pitting at the other.[34]

For the case of goethite, we ruled out Fe atom diffusion within the crystal lattice as a potential exchange mechanism because diffusion rates for Fe in goethite are much too slow to explain the observed rate of exchange (nearly complete exchange was observed in 10 days and diffusion rates would require time scales on the order of millions of years) (refs 17, 31 and refs therein). For magnetite, however, diffusion rates are thought to be significantly faster,[59−63] suggesting that Fe atom diffusion might be a plausible explanation for the rapid atom

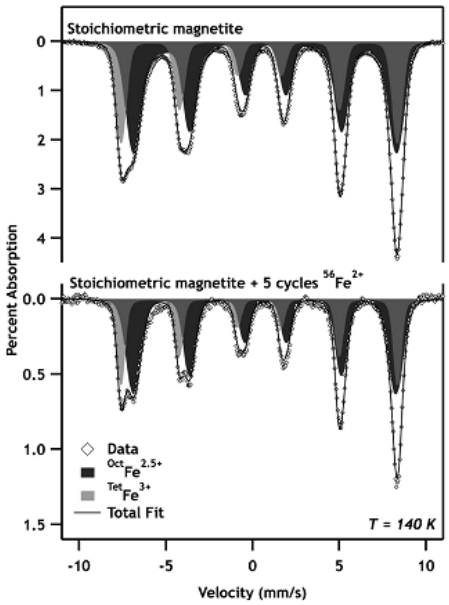

Figure 2. (Top) ^{57}Fe Mössbauer spectrum of isotopically normal stoichiometric magnetite at 140 K. (Bottom) The Mössbauer spectrum of the same stoichiometric magnetite (1 g/L) equilibrated with 4.5 mM $^{56}Fe^{2+}$ in a series of five batch reactors for 24 h each. The magnetite was collected by magnetic separation, then resuspended in a fresh buffer solution. Note that the *y*-axis scales differ significantly between the two spectra, with the bottom spectrum having only 23% of the spectral area of the top. This loss of spectral area is attributed to $^{56}Fe^{2+}$ exchanging with structural ^{57}Fe.

exchange observed in magnetite. With only half of the octahedral sites and one-eighth of tetrahedral sites occupied in the stoichiometric (i.e., inverse spinel) structure, magnetite contains significant structural vacancies that may facilitate Fe diffusion, and several studies have invoked fast Fe diffusion rates to explain rapid rates of magnetite oxidation[59−62] and dissolution.[43] Additional works have argued for both O and Fe atomic diffusion in magnetite, but these studies were carried out at high temperatures and with large single crystals, and their applicability to environmentally relevant, nanoparticulate samples remains unclear.[64−66]

Although rates of Fe atom diffusion are thought to be faster in magnetite than most Fe oxides, room temperature diffusion coefficients (D) reported for magnetite vary widely, ranging from values as low as 1.3×10^{-20} cm^2 s^{-1} to as high as 10^{-3} cm^2 s^{-1},[59,60] with other studies reporting values in the 10^{-12}−10^{-16} range.[61,62] It is important to note that these diffusion coefficients are not from direct measurements of Fe atom diffusion, but instead from the rate of magnetite oxidation, which may involve a different rate limiting step than diffusion of structural Fe.[53] Using a conservative range of D values (10^{-18} to 10^{-20} cm^2 s^{-1}), we estimate the time to reach 55% exchange in stoichiometric magnetite based on the Fe diffusion model used in these studies is 4.5 h to 19 days (Calc S2). Clearly, in addition to the electron conduction mechanism we proposed for goethite, Fe diffusion is a possible mechanism for rapid Fe atom exchange in magnetite.

To further probe whether the Fe atom exchange was controlled by an electron conduction mechanism or by Fe atomic diffusion, we conducted a ^{57}Fe-enriched isotope tracer experiment using Co-ferrite (ideal structure: $^{Tet}Fe^{3+}[^{Oct}Co^{2+}Fe^{3+}]O_4$). Co-ferrite is structurally similar to magnetite, but $^{Oct}Fe^{2+}$ is replaced with $^{Oct}Co^{2+}$. Substituting $^{Oct}Fe^{2+}$ with $^{Oct}Co^{2+}$ dramatically changes the electronic properties of the solid, where the electron conductivity (σ) drops by approximately 6 orders of magnitude (magnetite:[54] σ = 30 S^{1-} cm^{-1} (298 K); Co-ferrite:[67] $\sigma = 2 \times 10^{-5}$ S^{1-} cm^{-1} (323 K)). The large difference in conductivity, yet similar atomic radii of Co (1.52 Å) and Fe (1.56 Å), provide a convenient mineral to probe whether diffusion or conduction might be the rate limiting step since the small size difference of Fe^{2+} and Co^{2+} would not be expected to strongly influence diffusion rates.[68]

Using our ^{57}Fe-enriched Fe^{2+}_{aq} tracer experiment with isotopically normal Co-ferrite, we observed a rapid decrease in the $\delta^{57/56}$ of the Fe^{2+}_{aq} accompanied by a similarly rapid increase in the $\delta^{57/56}$ for the Co-ferrite over a period of several days (Figure 3), indicating atom exchange is occurring on time scales similar to what we observed for magnetite (Figure 1). Estimating extents of exchange for Co-ferrite is complicated by

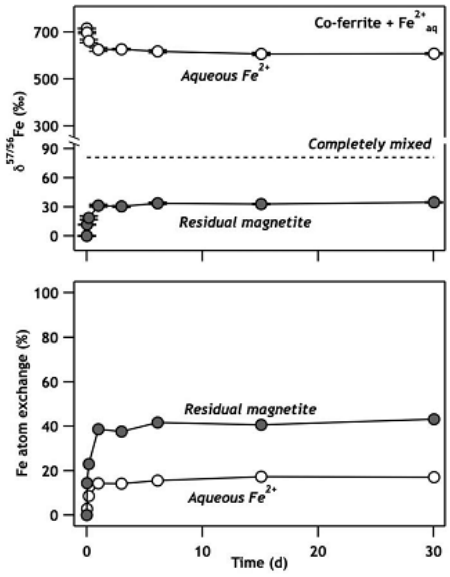

Figure 3. (Top) Measured $\delta^{57/56}$ values of Co-ferrite (ideal formula: $CoFe_2O_4$) equilibrated with aqueous Fe^{2+} for the aqueous and residual magnetite over 30 days. The dashed line represents the predicted $\delta^{57/56}$ of the system assuming complete equilibration. All data points are the average of three triplicate reactors. (Bottom) Calculated Fe atom exchange values for the data points in the top panel using eq 3.

the dissolution of structural Co^{2+} (10%) (Figure S5). Loss of Co^{2+} from the Co-ferrite means that $\delta^{57/56}$ values for aqueous Fe^{2+} will underestimate the extent of exchange (17.0%) since Co is not included in the exchange calculation (eq 3). Changes in solid phase Fe isotope composition provide a more reliable measurement of percent Fe exchange and indicate slightly less exchange for Co-ferrite (43%) relative to magnetite (Table 2). As observed with the magnetite samples, no significant change in the particle size (TEM) or crystallite size (pXRD) was observed for the Co-ferrite before and after reaction with Fe^{2+}_{aq} (Table 1).

The 43% Fe atom exchange observed between Co-ferrite and aqueous Fe^{2+}_{aq} was slightly smaller than the exchange observed for magnetite (54−71%) over 30 days. The smaller extent of exchange may be attributed to the Co substitution in the crystalline lattice or to the larger particle size of the Co-ferrite used in this study (Table 1). In either case, the lack of significant impact of Co substitution on the rate and extent of atom exchange between Fe^{2+}_{aq} and magnetite suggests that for magnetite, unlike goethite, Fe atom diffusion is a plausible mechanism to explain the rapid rates of Fe atom exchange we observe. Bulk electron conduction, however, is also possible, but if it is occurring, conduction does not appear to be the rate-limiting step. This may be specific to magnetite, as the structural octahedral vacancies provide a likely means for atomic rearrangement and mobility.

Our results suggest that Fe cycling between the aqueous phase and magnetite is much more dynamic than we previously thought. Similar to our previous findings with goethite, it is now clear that Fe atoms in the bulk structure of magnetite are able to exchange with the aqueous phase, despite the lack of significant dissolution or observable change in particle size or morphology. These findings raise interesting questions regarding trace metal sequestration and release from magnetite. For example, when ferrihydrite is reduced in the presence of trace metals, some metals, including chromium, arsenic, and uranium, have been shown to become structurally incorporated in the newly formed magnetite.[42,69−75] On the other hand, reduction-induced release of structurally incorporated metals has also been observed.[71,76,77] Whereas magnetite appears to be able to structurally incorporate trace metals as a result of an initial secondary mineralization process, subsequent exposure to Fe^{2+}_{aq} or Fe^{3+}-reducing bacteria may lead to remobilization of these metals due to the substantial Fe atom exchange that can occur. These two distinct mechanisms may offer insights into the long-term fate of structurally incorporated trace metals in Fe oxides.

■ ASSOCIATED CONTENT

Supporting Information

Additional figures, tables, and calculations as mentioned in the text. This material is available free of charge via the Internet at http://pubs.acs.org.

■ AUTHOR INFORMATION

Corresponding Author

*E-mail: michelle-scherer@uiowa.edu; phone: (319) 335-5654; fax: (319) 335- 5660.

Author Contributions

⊥Equal first-authorship.

Notes

The authors declare no competing financial interest.

■ ACKNOWLEDGMENTS

We thank Lingling Wu and Andy Czaja for help with the isotopic analyses. We also gratefully acknowledge funding for this work from the National Science Foundation grant NSF-EAR 1123978.

■ REFERENCES

(1) Jenne, E. A. Controls on Mn, Fe, Co, Ni, Cu, and Zn concentration in soils and water - Significant role of hydrous Mn and Fe oxides. *Adv. Chem. Ser.* **1968**, *73*, 337−387.

(2) Coughlin, B. R.; Stone, A. T. Nonreversible adsorption of divalent metal-ions (Mn^{II}, Co^{II} Ni^{II} Cu^{II} and Pb^{II}) onto goethite - Effects of acidification, Fe^{II} addition, and picolinic-acid addition. *Environ. Sci. Technol.* **1995**, *29* (9), 2445−2455.

(3) Hsi, C. D.; Langmuir, D. Adsorption of uranyl onto ferric oxyhydroxides: Application of the surface complexation site-binding model. *Geochim. Cosmochim. Acta* **1985**, *49*, 1931−1941.

(4) Murphy, R. J.; Lenhart, J. J.; Honeyman, B. D. The sorption of thorium (IV) and uranium (VI) to hematite in the presence of natural organic matter. *Colloids Surf., A* **1999**, *157* (1−3), 47−62.

(5) Moyes, L. N.; Parkman, R. H.; Charnock, J. M.; Vaughan, D. J.; Livens, F. R.; Hughes, C. R.; Braithwaite, A. Uranium uptake from aqueous solution by interaction with goethite, lepidocrocite, muscovite, and mackinawite: An X-ray absorption spectroscopy study. *Environ. Sci. Technol.* **2000**, *34* (6), 1062−1068.

(6) Duff, M. C.; Coughlin, J. U.; Hunter, D. B. Uranium co-precipitation with iron oxide minerals. *Geochim. Cosmochim. Acta* **2002**, *66* (20), 3533−3547.

(7) Frierdich, A. J.; Hasenmueller, E. A.; Catalano, J. G. Composition and structure of nanocrystalline Fe and Mn oxide cave deposits: Implications for trace element mobility in karst systems. *Chem. Geol.* **2011**, *284* (1−2), 82−96.

(8) Klausen, J.; Trober, S. P.; Haderlein, S. B.; Schwarzenbach, R. P. Reduction of substituted nitrobenzenes by Fe(II) in aqueous mineral suspensions. *Environ. Sci. Technol.* **1995**, *29* (9), 2396−2404.

(9) Sorensen, J.; Thorling, L. Stimulation by lepidocrocite (γ-FeOOH) of Fe(II)-dependent nitrite reduction. *Geochim. Cosmochim. Acta* **1991**, *55* (5), 1289−1294.

(10) Chun, C. L.; Hozalski, R. M.; Arnold, T. A. Degradation of drinking water disinfection byproducts by synthetic goethite and magnetite. *Environ. Sci. Technol.* **2005**, *39* (21), 8525−8532.

(11) Elsner, M.; Schwarzenbach, R. P.; Haderlein, S. Reactivity of Fe(II)-bearing minerals toward reductive transformation of organic contaminants. *Environ. Sci. Technol.* **2004**, *38*, 799−807.

(12) Felmy, A. R.; Ilton, E. S.; Rosso, K. M.; Zachara, J. M. Interfacial reactivity of radionuclides: Emerging paradigms from molecular-level observations. *Mineral. Mag.* **2011**, *75* (4), 2379−2391.

(13) Gorski, C. A.; Scherer, M. M. Fe^{2+} Sorption at the Fe Oxide-Water Interface: A Revised Conceptual Framework. In *Aquatic Redox Chemistry*; Tratnyek, P. G., Grundl, T., Haderlein, S., Eds.; 2011; Vol. *1071*, pp 477−517; ISBN 13: 9780841226524.

(14) Borch, T.; Campbell, K.; Kretzschmar, R. How electron flow controls contaminant dynamics. *Environ. Sci. Technol.* **2009**, *44* (1), 3−6.

(15) Borch, T.; Kretzschmar, R.; Kappler, A.; Van Cappellen, P.; Ginder-Vogel, M.; Voegelin, A.; Campbell, K. Biogeochemical redox processes and their impact on contaminant dynamics. *Environ. Sci. Technol.* **2010**, *44* (1), 15−23.

(16) Hansel, C. M.; Benner, S. G.; Fendorf, S. Competing Fe(II)-induced mineralization pathways of ferrihydrite. *Environ. Sci. Technol.* **2005**, *39*, 7147−7153.

(17) Pedersen, H. D.; Postma, D.; Jakobsen, R.; Larsen, O. Fast transformation of iron oxyhydroxides by the catalytic action of aqueous Fe(II). *Geochim. Cosmochim. Acta* **2005**, *69* (16), 3967−3977.

(18) Yang, L.; Steefel, C. I.; Marcus, M. A.; Bargar, J. R. Kinetics of Fe(II)-catalyzed transformation of 6-line ferrihydrite under anaerobic flow conditions. *Environ. Sci. Technol.* **2010**, *44* (14), 5469−5475.

(19) Tamaura, Y.; Ito, K.; Katsura, T. Transformation of γ-FeO(OH) to Fe_3O_4 by adsorption of iron(II) ion on γ-FeO(OH). *J. Chem. Soc., Dalton Trans.: Inorg. Chem.* **1983**, *2*, 189−194.
(20) Hansel, C. M.; Benner, S. G.; Neiss, J.; Dohnalkova, A.; Kukkadapu, R.; Fendorf, S. Secondary mineralization pathways induced by dissmilatory iron reduction of ferrihydrate under advective flow. *Geochim. Cosmochim. Acta* **2003**, *67* (16), 2977−2992.
(21) Roden, E. E.; Urrutia, M. M. Influence of biogenic Fe(II) on bacterial crystalline Fe(III) oxide reduction. *Geomicrobiol. J.* **2002**, *19* (209), 209−251.
(22) Roden, E. E.; Zachara, J. M. Microbial reduction of crystalline iron(II) oxides: Influence of oxide surface area and potential for cell growth. *Environ. Sci. Technol.* **1996**, *30* (5), 1618−1628.
(23) Cutting, R. S.; Coker, V. S.; Fellowes, J. W.; Lloyd, J. R.; Vaughan, D. J. Mineralogical and morphological constraints on the reduction of Fe(III) minerals by Geobacter sulfurreducens. *Geochim. Cosmochim. Acta* **2009**, *73* (14), 4004−4022.
(24) Larese-Casanova, P.; Scherer, M. M. Fe(II) sorption on hematite: New insights based on spectroscopic measurements. *Environ. Sci. Technol.* **2007**, *41* (2), 471−477.
(25) Larese-Casanova, P.; Scherer, M. M. Morin transition suppression in polycrystalline ^{57}hematite (α-Fe_2O_3) exposed to ^{56}Fe-(II). *Hyperfine Interact.* **2007**, *174*, 111−119.
(26) Cwiertny, D. M.; Baltrusaitis, J.; Hunter, G. J.; Laskin, A.; Scherer, M. M.; Grassian, V. H. Characterization and acid-mobilization study of iron-containing mineral dust source materials. *J. Geophys. Res.-Atmos.* **2008**, *113*, D05202.
(27) Williams, A. G. B.; Scherer, M. M. Spectroscopic evidence for Fe(II)-Fe(III) electron transfer at the Fe oxide-water interface. *Environ. Sci. Technol.* **2004**, *38* (18), 4782−4790.
(28) Schwertmann, U.; Thalmann, H. Influence of Fe(II), Si, and pH on formation of lepidocrocite and ferrihydrite during oxidation of aqueous $FeCl_2$ solutions. *Clay Miner.* **1976**, *11* (3), 189−200.
(29) Cornell, R. M.; Schwertmann, U. *The Iron Oxides: Structure, Properties, Reactions, Occurrence, and Uses*; VCH: New York, 2003.
(30) Jones, A. M.; Collins, R. N.; Rose, J.; Waite, T. D. The effect of silica and natural organic matter on the Fe(II)-catalysed transformation and reactivity of Fe(III) minerals. *Geochim. Cosmochim. Acta* **2009**, *73* (15), 4409−4422.
(31) Handler, R. M.; Beard, B. L.; Johnson, C. M.; Scherer, M. M. Atom exchange between aqueous Fe(II) and goethite: An Fe isotope tracer study. *Environ. Sci. Technol.* **2009**, *43* (4), 1102−1107.
(32) Beard, B. L.; Handler, R. M.; Scherer, M. M.; Wu, L. L.; Czaja, A. D.; Heimann, A.; Johnson, C. M. Iron isotope fractionation between aqueous ferrous iron and goethite. *Earth Planet. Sci. Lett.* **2010**, *295* (1−2), 241−250.
(33) Wu, L.; Beard, B. L.; Roden, E. E.; Johnson, C. M. Stable Iron Isotope Fractionation Between Aqueous Fe(II) and Hydrous Ferric Oxide. *Environ. Sci. Technol.* **2011**, *45* (5), 1847−1852.
(34) Yanina, S. V.; Rosso, K. M. Linked reactivity at mineral-water interfaces through bulk crystal conduction. *Science* **2008**, *320* (5873), 218−222.
(35) Catalano, J. G.; Fenter, P.; Park, C.; Zhang, Z.; Rosso, K. M. Structure and oxidation state of hematite surfaces reacted with aqueous Fe(II) at acidic and neutral pH. *Geochim. Cosmochim. Acta* **2010**, *74* (5), 1498−1512.
(36) Villa, E. M.; Ohlin, C. A.; Casey, W. H. Adding reactivity to structure 2: Oxygen-isotope-exchange rates in three isostructural oxide ions. *Am. J. Sci.* **2010**, *310* (7), 629−644.
(37) Villa, E. M.; Ohlin, C. A.; Rustad, J. R.; Casey, W. H. Isotope-Exchange Dynamics in Isostructural Decametalates with Profound Differences in Reactivity. *J. Am. Chem. Soc.* **2009**, *131* (45), 16488−16492.
(38) Eggleston, C. M. Toward new uses for hematite. *Science* **2008**, *320* (5873), 184−185.
(39) Jolivet, J. P.; Tronc, E. Interfacial electron transfer in colloidal spinel iron oxide. Conversion of Fe_3O_4-γFe_2O_3 in aqueous solution. *J. Colloid Interface Chem.* **1988**, *125* (2), 688−701.
(40) Gorski, C. A.; Scherer, M. M. Influence of magnetite stoichiometry on Fe^{II} uptake and nitrobenzene reduction. *Environ. Sci. Technol.* **2009**, *43* (10), 3675−3680.
(41) Ilton, E. S.; Boily, J. F.; Buck, E. C.; Skomurski, F. N.; Rosso, K. M.; Cahill, C. L.; Bargar, J. R.; Felmy, A. R. Influence of dynamical conditions on the reduction of U-VI at the magnetite-solution interface. *Environ. Sci. Technol.* **2010**, *44* (1), 170−176.
(42) Boland, D. D.; Collins, R. N.; Payne, T. E.; Waite, T. D. Effect of amorphous Fe(III) oxide transformation on the Fe(II)-mediated reduction of U(VI). *Environ. Sci. Technol.* **2011**, *45* (4), 1327−1333.
(43) Jolivet, J. P.; Belleville, P.; Tronc, E.; Livage, J. Influence of Fe(II) on the formation of the spinel iron oxide in alkaline medium. *Clays Clay Miner.* **1992**, *40* (5), 531−539.
(44) Tronc, E.; Jolivet, J.-P.; Lefebvre, J.; Massart, R. Ion adsorption and electron transfer in spinel-like iron oxide colloids. *J. Chem. Soc., Faraday Trans.* **1984**, *80*, 2619−2629.
(45) Gorski, C. A.; Scherer, M. M. Determination of nanoparticulate magnetite stoichiometry by Mossbauer spectroscopy, acidic dissolution, and powder X-ray diffraction: A critical review. *Am. Mineral.* **2010**, *95* (7), 1017−1026.
(46) Zahir, K. O.; Keshtkar, H. A colorimetric method for trace level determination of cobalt in natural and waste water samples. *Int. J. Environ. Anal. Chem.* **1998**, *72* (2), 151−162.
(47) Jiang, H. G.; Ruhle, M.; Lavernia, E. J. On the applicability of the x-ray diffraction line profile analysis in extracting grain size and microstrain in nanocrystalline materials. *J. Mater. Res.* **1999**, *14* (2), 549−559.
(48) Beard, B. L.; Johnson, C. M.; Cox, L.; Sun, H.; Nealson, K. H.; Aguilar, C. Iron isotope biosignatures. *Science* **1999**, *285* (5435), 1889−1892.
(49) Johnson, C. M.; Beard, B. L.; Beukes, N. J.; Klein, C.; O'Leary, J. M. Ancient geochemical cycling in the Earth as inferred from Fe isotope studies of banded iron formations from the Transvaal Craton. *Contrib. Mineral. Petrol.* **2003**, *144* (5), 523−547.
(50) Mandernack, K. W.; Bazylinski, D. A.; Shanks, W. C.; Bullen, T. D. Oxygen and iron isotope studies of magnetite produced by magnetotactic bacteria. *Science* **1999**, *285* (5435), 1892−1896.
(51) Johnson, C. M.; Roden, E. E.; Welch, S. A.; Beard, B. L. Experimental constraints on Fe isotope fractionation during magnetite and Fe carbonate formation coupled to dissimilatory hydrous ferric oxide reduction. *Geochim. Cosmochim. Acta* **2005**, *69* (4), 963−993.
(52) Verwey, E. J. G.; Haayman, P. W.; Romeijn, F. C. Physical properties and cation arrangement of oxides with spinel structures. II. Electronic conductivity. *J. Chem. Phys.* **1947**, *15*, 181−7.
(53) Gorski, C. A.; Nurmi, J. T.; Tratnyek, P. G.; Hofstetter, T. B.; Scherer, M. M. Redox behavior of magnetite: Implications for contaminant reduction. *Environ. Sci. Technol.* **2010**, *44* (1), 55−60.
(54) Itai, R.; Shibuya, M.; Matsumura, T.; Ishi, G. Electrical resistivity of magnetite anodes. *J. Electrochem. Soc.* **1971**, *118* (10), 1709−11.
(55) Tronc, E.; Belleville, P.; Jolivet, J. P.; Livage, J. Transformation of ferric hydroxide into spinel by Fe(II) adsorption. *Langmuir* **1992**, *8* (1), 313−319.
(56) Verwey, E. J. G.; Heilmann, E. L. Physical properties and cation arrangement of oxides with spinel structures. I. Cation arrangement in spinels. *J. Chem. Phys.* **1947**, *15*, 174−80.
(57) Skomurski, F. N.; Kerisit, S.; Rosso, K. M. Structure, charge distribution, and electron hopping dynamics in magnetite (Fe3O4) (100) surfaces from first principles. *Geochim. Cosmochim. Acta* **2010**, *74* (15), 4234−4248.
(58) Penn, R. L.; Erbs, J. J.; Gulliver, D. M. Controlled growth of alpha-FeOOH nanorods by exploiting-oriented aggregation. *J. Cryst. Growth* **2006**, *293* (1), 1−4.
(59) Gallagher, K. J.; Feitknecht, W.; Mannweiler, U. Mechanism of oxidation of magnetite to γ-Fe_2O_3. *Nature* **1968**, *217*, 1118−1121.
(60) Tang, J.; Myers, M.; Bosnick, K. A.; Brus, L. E. Magnetite Fe_3O_4 nanocrystals: Spectroscopic observation of aqueous oxidation kinetics. *J. Phys. Chem., B* **2003**, *107* (30), 7501−7506.

(61) Sidhu, P. S.; Gilkes, R. J.; Posner, A. M. Mechanism of the low temperature oxidation of magnetite. *J. Inorg. Nucl. Chem.* **1977**, *39* (11), 1953−1958.
(62) White, A. F.; Peterson, M. L.; Hochella, M. F. Electrochemistry and dissolution kinetics of magnetite and ilmenite. *Geochim. Cosmochim. Acta* **1994**, *58* (8), 1859−1875.
(63) Colombo, U.; Fagherazzi, G.; Gazzarrini, F.; Lanzavecchia, G.; Sironi, G. Mechanism of low-temperature oxidation of magnetites. *Nature* **1968**, *219* (5158), 1036−1037.
(64) Aggarwal, S.; Dieckmann, R. Point defects and cation tracer diffusion in (TixFe1-x)(3-delta)O-4. II. Cation tracer diffusion. *Phys. Chem. Miner.* **2002**, *29* (10), 707−718.
(65) Atkinson, A.; Odwyer, M. L.; Taylor, R. I. Fe-55 diffusion in magnetite crystals at 500° C and its relevance to the oxidation of iron. *Radiat. Eff. Defects Solids* **1983**, *75* (1−4), 169−172.
(66) Castle, J. E.; Surman, P. L. The self-diffusion of oxygen in magnetite. The effect of anion vacancy concentration and cation distribution. *J. Phys. Chem.* **1969**, *73* (3), 632−634.
(67) Abdeen, A. M.; Hemeda, O. M.; Assem, E. E.; El-Sehly, M. M. Structural, electrical and transport phenomena of Co ferrite substituted by Cd. *J. Magn. Magn. Mater.* **2002**, *238* (1), 75−83.
(68) Clementi, E.; Raimondi, D. L.; Reinhard, Wp Atomic screening constants from SCF functions 0.2. Atoms with 37 to 86 electrons. *J. Chem. Phys.* **1967**, *47* (4), 1300−1307.
(69) Coker, V. S.; Gault, A. G.; Pearce, C. I.; van der Laan, G.; Telling, N. D.; Charnock, J. M.; Polya, D. A.; Lloyd, J. R. XAS and XMCD evidence for species-dependent partitioning of arsenic during microbial reduction of ferrihydrite to magnetite. *Environ. Sci. Technol.* **2006**, *40* (24), 7745−7750.
(70) Pedersen, H. D.; Postma, D.; Jakobsen, R. Release of arsenic associated with the reduction and transformation of iron oxides. *Geochim. Cosmochim. Acta* **2006**, *70* (16), 4116−4129.
(71) Tufano, K. J.; Reyes, C.; Saltikov, C. W.; Fendorf, S. Reductive Processes Controlling Arsenic Retention: Revealing the Relative Importance of Iron and Arsenic Reduction. *Environ. Sci. Technol.* **2008**, *42* (22), 8283−8289.
(72) Islam, F. S.; Pederick, R. L.; Gault, A. G.; Adams, L. K.; Polya, D. A.; Chamock, J. M.; Lloyd, J. R. Interactions between the Fe(III)-reducing bacterium Geobacter sulfurreducens and arsenate, and capture of the metalloid by biogenic Fe(II). *Appl. Environ. Microbiol.* **2005**, *71* (12), 8642−8648.
(73) Hansel, C. M.; Wielinga, B. W.; Fendorf, S. R. Structural and compositional evolution of Cr/Fe solids after indirect chromate reduction by dissimilatory iron-reducing bacteria. *Geochim. Cosmochim. Acta* **2003**, *67* (3), 401−412.
(74) Benner, S. G.; Hansel, C. M.; Wielinga, B. W.; Fendorf, S. Reductive Dissolution and Biomineralization of Iron Hydroxide under Dynamic Flow conditions. *Environ. Sci. Technol.* **2002**, *36* (8), 1705−1711.
(75) Kocar, B. D.; Borch, T.; Fendorf, S. Arsenic repartitioning during biogenic sulfidization and transformation of ferrihydrite. *Geochim. Cosmochim. Acta* **2010**, *74* (3), 980−994.
(76) Chow, S. S.; Taillefert, M. Effect of arsenic concentration on microbial iron reduction and arsenic speciation in an iron-rich freshwater sediment. *Geochim. Cosmochim. Acta* **2009**, *73* (20), 6008−6021.
(77) Cummings, D. E.; Caccavo, F.; Fendorf, S.; Rosenzweig, R. F. Arsenic mobilization by the dissimilatory Fe(III)-reducing bacterium Shewanella alga BrY. *Environ. Sci. Technol.* **1999**, *33* (5), 723−729.

APPENDIX B: FE^{2+} CATALYZED IRON ATOM EXCHANGE IN TROPICAL SOILS

Abstract

The exchange of aqueous iron (Fe) atoms with solid phase Fe atoms has recently been demonstrated for many Fe (oxyhydr)oxide minerals. Whether this process is significant in environmentally complex systems, such as soils or sediments, however, remains unclear. Here, we demonstrate that over a month, approximately 10% of the Fe atoms in natural soil from the Bisley Site in the Luquillo Experimental Forest, Puerto Rico are exchangeable. In batch sterile and live experiments, we introduced an aqueous $^{57}Fe(II)$ spike to soil slurries under anoxic conditions and traced the isotopic composition of the aqueous phase and in 0.5 M and 7 M HCl extractions of the solid phase over 28 days. Our sterile treatments can be described as fast sorption/incorporation of $Fe^{2+}(aq)$ to the labile extractable phase (0.5 M HCl), occurring over timescales of 15 minutes, followed by exchange between the labile layer and the bulk iron (oxyhydr)oxides. The characteristic timescale for desorption is on the order of a week, whereas release from the bulk phase (7 M HCl) to the labile phase (0.5 M HCl) takes place on the order of years. Mössbauer spectroscopy results indicate that the ^{57}Fe label re-crystallizes preferentially as Fe^{III}-oxyhydroxides of very low crystallinity (i.e., short-range-order, SRO), suggesting these phases likely participate disproportionally in Fe atom exchange reactions with $Fe^{2+}(aq)$ in natural soils. Soils exposed to anoxic conditions where significant $Fe^{2+}(aq)$ is present are likely to exhibit substantial Fe-atom fluidity in SRO oxyhydroxide phases.

Introduction

The structure and composition of ferric iron minerals determines their functional roles in natural systems. Nano-scale, short-range-ordered (SRO) Fe phases are highly reactive towards chemical sorption (178-180), particle adhesion, and reductive dissolution (181) because of their high surface area to mass ratio; whereas large crystalline oxides can provide the structural framework for highly weathered substrates devoid of primary minerals. Under anoxic conditions, sorption of Fe^{2+} to the surface of

ferric-bearing minerals catalyzes the reduction of organic (e.g., chlorinated compounds (67)) and inorganic (e.g., Cr(VI) (182)) contaminants. Significant evidence has accumulated to indicate that the reaction of aqueous Fe^{2+} with Fe^{III} oxides is more complex than a simple sorption step, but instead may be comprised of sorption, electron transfer, conduction, dissolution, and, in some cases, Fe atom exchange and/or transformation to secondary minerals (183). For some Fe oxides, (e.g., goethite (21) and magnetite (184)), there is no evidence of secondary mineralization, yet results with isotopically labeled tracers have shown Fe^{2+}-catalyzed Fe atom exchange can lead to substantial Fe atom turnover in these minerals within months, suggesting that significant solid-phase Fe dynamics are occurring that go unrecognized based on aqueous phase Fe^{2+} measurements or solid-phase mineral characterization alone.

The rate and extent of Fe^{2+} catalyzed Fe atom exchange and recrystallization in natural systems is difficult to predict from the pure-mineral experimental systems studied thus far. Iron in soils and sediments resides in a range of bonding environments, including Fe^{III} minerals with the potential for a high degree of Al substitution such as goethite or ferrihydrite, mixed valence Fe^{II}-Fe^{III} minerals such as magnetite, and minerals with predominately divalent Fe such as pyrite. In addition, aluminosilicate clay minerals can contain structural Fe as well as Fe sorbed to negatively charged exchange sites (185), and in many soils and sediments appreciable Fe is strongly complexed by organic matter (186, 187). The extent to which each solid-phase Fe population can exchange with Fe^{2+}(aq) is known for only a few pure minerals (21, 188-190), and it has been shown that surface adsorption of Si and organic matter (114), and isomorphic Al-substitution can inhibit or completely block Fe atom exchange (183, 191-193). Similar retardation of Fe atom exchange is observed following phosphorus sorption (191) or when the pH is decreased below the point of net zero charge of the Fe mineral, suggesting Fe^{2+} sorption is a critical precursor modulating the extent of atom exchange in natural systems (194).

Our objective was to quantify the rate of Fe^{2+} facilitated atom exchange between aqueous Fe^{2+} and solid phase Fe in soils with active Fe redox cycling. We did this by exposing sterile soils to isotopically labeled Fe^{2+}(aq) and monitoring the migration of labeled Fe atoms into the soil solid-phase for 30 days. We then interpreted the observational data using a two-step kinetic model incorporating rapid Fe^{2+}(aq) sorption with long-term isotopic exchange. To assess the ubiquity of this process we repeated this experiment on soils across a catena that had different histories of exposure to low oxygen conditions measuring isotopic re-distribution after 56 days. Non-sterile control soils included in our experiments allow us to speculate on the role of microorganisms in modulating Fe atom exchange in soil systems.

Materials and Methods

Field Site and Soil Collection

Soil for this experiment was collected from the Bisley Research Watershed site of the Luquillo Experimental Forest (LEF) in Puerto Rico. The Bisley lower valley site soils are classified predominately as Ultisols formed from volcanic parent material with ~5% organic matter (195) and 57.9 ± 2.2 g kg^{-1} Fe residing predominately in nano-crystalline Fe^{III} oxyhydroxide phases based on ^{57}Fe Mössbauer analysis. This site is subject to periodic fluctuations in O_2 concentrations generating seasonal localized anoxic conditions (196). We collected the upper 10 cm of the soil from the location described in Peretyazhko and Sposito (195). Soils were placed in polypropylene ziplock bags, transported at field temperature to the University of Georgia and air-dried at 40ºC for 12 h prior to dry sieving and homogenizing.

Isotope Tracer Experiments

Approximately 0.75 g of soil was added to a 125 mL flask in an anoxic glovebox (Coylabs, Grasslake, MI) with a 95%:5% N_2:H_2 atmosphere and mixed with 75 mL of

incubation buffer solution with or without 6.9μM of $HgCl_2$ to create "sterile" and "live" treatment sets. The incubation solution was prepared to contain 25 mM KCl and 25 mM of 2-(N-morpholino)ethanesulfonic acid (MES) buffer and ~2.5mM Fe^{2+}(aq). The ^{57}Fe-enriched Fe^{2+}(aq) was introduced to the incubation solution by adding an aliquot of acidified $^{57}FeCl_2$ stock (113 mmol L^{-1}) and an aliquot of reagent-grade $FeCl_2$ with normal isotopic composition (Sigma-Aldrich) to obtain a final $^{57/54}$Fe ratio of 5.867, which is sufficiently distinct from the native soil $^{57/54}$Fe ratio of 0.363. After addition of the Fe^{2+} spike, the incubation solution pH was adjusted to 5.5 with KOH, allowed to equilibrate for 30 min, and filtered (0.2 μm) to remove potential Fe (oxyhydr)oxide precipitates resulting from the pH increase. All solutions were prepared from ultra-pure water (>18 MΩ-cm) that was deoxygenated by sparging with N_2 gas for 2 h and exposed to our glovebox atmosphere for 48 h. The soil slurry was then subsampled into 2 mL polypropylene centrifuge tubes for sacrificial sampling and rotated on an end-over-end shaker (7 rpm). Triplicate samples were prepared at each time point for the sterile treatment and single replicates were prepared for the "live" controls. Controls without soil and those without ^{57}Fe spikes were included to monitor the experimental integrity.

Sampling and Analysis

At 0.02, 1, 3, 7, 14, 21, and 28 days of reaction sacrificial samples were centrifuged at 21,169 relative centrifugal force (RCF) for 30 min on an Eppendorf 5430 centrifuge with a F45-30-11 rotor. The supernatant was removed, acidified and stored for analysis. To remaining pellet we added ~ 0.9 mL of 0.5M HCl (Optima grade, Fisher Scientific), reacted the resulting slurry for 2 h on an end-over-end shaker (7 rpm) then centrifuged the sample at 21,169 RCF for 30 min. and collected the supernatant for analysis. To the remaining 0.5M HCl pellet, we added ~ 0.9 mL of 7M HCl and reacted the resulting slurry for 14 d on an end-over-end shaker before centrifuging and collecting the supernatant for analysis. Samples were always opened and manipulated within our

anoxic glovebox. This procedure produced subsamples from the aqueous phase, the labile Fe layer including any surface adsorbed Fe^{II} (0.5M HCl extraction), and the bulk solid iron oxides (7M HCl extraction). Previous work has demonstrated that no isotopic fractionation takes place during Fe solubilization via HCl (197, 198), and Fe contained in silicate phases is not expected to be solubilized by any of these extractants. Following extraction all samples were analyzed for Fe^{II} and total Fe using a modified ferrozine protocol given in Thompson et al.(199) on a Shimadzu-1700 spectrophotometer at λ=562 nm.

Isotopic Analysis

Fe isotopes were measured in all subsamples by Inductively Coupled Plasma Mass Spectrometry (ICP-MS, Perkin Elmer, Elan 9000). The instrument was tuned prior to analysis on a 10 $\mu g\ l^{-1}$ solution of Ba, Be, Ce, Co, In, Mg, Pb, Rh, U (Standard ELAN & DRC-e, ISO 9001). Operating conditions were as follows: RF power of 1300 W; sample uptake rate of 24 rpm; cooling gas flow rate of 13 l min^{-1}; nebulizer gas flow rate between 0.95 and 0.99 L min^{-1}; and auxiliary gas flow rate of 0.70 min^{-1}. 65 sweeps per reading, dwell time 50 ms, 20 replicates were used. All results were referenced to iron-54 with correction of chromium concentrations by monitoring chromium-52. Mass bias of the measured isotope ratio was corrected using external standards containing a $^{57}Fe/^{54}Fe$ isotopic ratio of 0.3625, which were analyzed after every 10 samples to monitor time-dependent variation in mass-bias. The standard statistical error of $^{57/54}Fe$ ratio of was ~ 0.015 (2σ) (Figure S1), which is sufficiently precise to discern differences across our experimental variation with $^{57/54}Fe$ ratios ranging from ~ 0.3 to 5.8. To facilitate construction of our kinetic model, we used the molar abundance of ^{54}Fe, ^{57}Fe, and $^{(56+58)}Fe$ at each point in our experiment across the aqueous and two solid phase pools. ^{57}Fe and ^{54}Fe were measured on an Elan 9000 ICP-MS. Since the instrument does not have provisions to eliminate the argon-oxygen isobaric interference on mass 56, we could

not reliably measure ^{56}Fe directly. We calculated molar abundances of the other two isotopes (^{56}Fe and ^{58}Fe) assuming that the ^{54}Fe:^{56}Fe:^{58}Fe ratio remains at the native abundance ratios throughout the experiment, and only relative amount of ^{57}Fe (consisted of a mixture of isotopically normal Fe and an aliquot of 97.82% pure ^{57}Fe) changed. Consequently, ∑Fe (=^{54}Fe+^{56}Fe+^{57}Fe+^{58}Fe), where $^{57/54}$Fe and total Fe were experimentally measured, ^{57}Fe calculated as $^{57/54}$Fe*^{54}Fe, and (^{56}Fe+^{58}Fe) = ^{54}Fe /0.063508. Solving for ^{54}Fe we get ^{54}Fe = ∑Fe / ($^{57/54}$Fe+ 16.746). Other isotopes can be calculated by substituting for ^{54}Fe in the above equations. All statistical representations are given as one standard deviation of replicate measures in concise notation with the parenthetical number indicating the error in the last digit [e.g., 7.14(12) is equivalent to 7.14 ± 0.12].

Mössbauer Spectroscopy (MBS)

^{57}Fe Mössbauer spectra were collected at 13K, 77K, 140K and 295K on the unreacted soil and the sterile soil reacted with $^{57}Fe^{2+}$ for 28 days, following three rinses with an Fe-free KCl-MES buffer solution to remove Fe^{2+}(aq). Detailed explanation of the MBS methods and fitting routine are given in the supplementary information section along with spectra of the unreacted soil collected across a temperature profile of 295K, 140K, 77K and 13K.

Kinetic Modeling and Exchange Calculations

The temporal evolution of ^{54}Fe, ^{57}Fe and the sum of ^{56}Fe and ^{58}Fe concentrations in aqueous solution, the surface, and the bulk phase is described by a set of coupled ordinary differential equations. Rate constants describing the kinetics of the exchange between the three pools were optimized to match both isotope concentrations and ratios (further described in supplementary material). Percent exchange is computed as $(f(t) - f_{initial})/(f_{equilibrium} - f_{initial})$, where f = ^{54}Fe/Fe$_{tot}$ or ^{57}Fe/Fe$_{tot}$, respectively. The extent of change is calculated for both the aqueous and the 7 M HCl extractable

pools, and t = 0.02 is chosen as the initial time point to remove the large imprint of the initial sorption event. The equilibrium ratio represents the average ratio across the aqueous, 0.5M HCl and 7M HCl Fe pools . Residual Fe, not extracted by 7M HCl was excluded from the calculation.

Results and Discussion

Net Fe(II) Dynamics

Across all extracted soil pools, Fe^{II} recovery in the sterile treatment averaged 90 (4)%; in the live controls net Fe^{II} recovery was higher (101.4(5)%) by the end of the experiment, presumably due to microbial Fe reduction. Fe^{2+}(aq) concentrations in the sterile treatment decreased 13% within 1 h, further decreasing to 20% of their original values after 1 d with corresponding increases in Fe^{II}(0.5M HCl) and Fe^{III}(0.5M HCl) consistent with rapid adsorption of Fe^{2+}(aq) to the labile/surface layers of the soil (Figure B.1 and Table B.1). Following this initial sorption step, the sterilized slurries reached pseudo-equilibrium with respect to net transfer of Fe^{II} between aqueous and solid phase. However, net increases in Fe^{2+}(aq) and Fe^{II}(0.5M HCl) were observed in the live control after 14 d and 7 d of reaction, respectively, with Fe(II) production rates peaking at 2 μmol g^{-1} d^{-1} at 14 days. The Fe content of the 7M HCl extract remained constant within error throughout the experiment (Figure B.1).

Sorption of Fe^{2+} is a critical step in generating electron transfer and atom exchange events at Fe^{III}-mineral surfaces, along with the secondary effects of trace element release and mineral transformation (194). The measured decrease in Fe^{2+}(aq) reflects accumulation on Fe-(oxyhydr)oxide surfaces in addition to other competitive surfaces in the soil. Indeed, ~ 73% of the Fe^{II} mass loss from solution during the initial sorption event was recovered in the 0.5M HCl extraction, which solubilizes Fe^{2+} from outer-sphere cation exchange sites via proton competition and from inner-sphere exchange complexes with highly labile metal-(oxyhydr)oxides that are solubilized by

proton-promoted dissolution. Potential sorbents include goethite and nano-crystalline Fe phases common in these soils (195) as well as negatively charged sites on the layered silicates kaolinite and chlorite (195) and those associated with carboxylic acid functional groups on organic matter.

Since Fe^{III}-minerals are very competitive sorbents for the Fe^{2+} ion (200), it is likely all Fe^{III}-mineral surfaces have a substantial surface excess of Fe^{2+} after 1h of reaction. If we assume the initial sorption of Fe^{2+} (~35 mmol kg^{-1} soil) partitioned exclusively to goethite or nano-crystalline Fe phases in the soil we calculate a surface excess of ~ 0.47 mmol Fe^{II} g^{-1} Fe-(oxyhydr)oxides based on an Fe content of 57.9 ± 2.2 g kg^{-1} soil with 80% of this Fe present as Fe-(oxyhydr)oxides (i.e., 73.7 g FeOOH kg^{-1} soil) (Figure B.3). This is near the upper limit of Fe^{II} surface excess reported for pure Fe-(oxyhydr)oxide phases at circumneutral pH (22, 123). Our experimental pH (buffered at 5.5 by MES) is well below the point of zero net charge of goethite (PZNC ~ 8) (201), the most prominent Fe phase in our system. Fe^{2+} sorption onto Fe oxides drops substantially below pH 6.5, but can remain detectable even below pH 4, even in pure mineral systems (202).

Abiotic Evolution of Soil $^{57/54}Fe$ Ratios

The Fe^{2+} sorption in the first 30 min of the experiment coincides with a decrease in the $^{57/54}Fe$(aq) ratio from 5.88(3) to 5.77(1) and a corresponding increase in the $^{57/54}Fe$(0.5M HCl) and $^{57/54}Fe$(7M HCl) ratios from their initial natural abundance values of 0.363(4) to 4.06(4) and 0.42(0), respectively (Figure B.1). The $^{57/54}Fe$(0.5M HCl) ratio reached a peak at 4.55(5) after 3 days before declining to 4.28(4) after 28 d of reaction, whereas the $^{57/54}Fe$(aq) and $^{57/54}Fe$(7M HCl) ratios continued to slowly converge over the course of the experiment reaching values of 5.53(5) and 0.55(4), respectively after 28 d of reaction (Figure B.1).

After 28 days of incubation we calculate that ~15% (~133 mmol Fe kg^{-1} soil) of the Fe(7M HCl) exchanged with the Fe(aq) and Fe(0.5M HCl) (Table 1). This is close to the amount of Fe extractable by acid ammonium oxalate (AAO: 120 ± 10 mmol Fe kg^{-1} soil; s.d., n=3), which targets nano-crystalline Fe-(oxyhydr)oxides. Note that the % exchange estimates based on the aqueous phase measurements are lower, on the order of 4.4% (Table 1). This is attributed to that one hour is sufficient for the sorption/desorption equilibration between aqueous and solid phase pool after the addition of the tracer spike. However, it leaves the surface pool enriched compared to the bulk iron, which leads to slightly larger % exchange estimates based on the 7 M extractable solid phase measurements.

Fe-(oxyhydr)oxides are the most likely source of Fe in the 7M HCl extraction, and the most likely phase undergoing Fe atom exchange with the labeled aqueous Fe. However, Mössbauer spectroscopy also indicates that ~ 15% of the total Fe in ^{57}Fe treated soil does not magnetically order at 13K (Figure B.3) and thus is likely present in layer silicate minerals or organic complexes (203). Fe isotopic fractionation and atom exchange has been demonstrated between aqueous Fe^{2+} and Fe complexed by soluble humics (204) and several model organic compounds (205-208). The 0.5 M HCl extraction will solubilize some of this organically bound Fe, but not likely from high-affinity Fe-organic complexes common to siderophores and similar compounds. The primary silicate minerals in this soil likely to contain Fe are kaolinite and chlorite. Schaefer et al. (189) have demonstrated Fe^{2+}-facilitated electron transfer can occur with the 2:1 layer clay mineral nontronite (NAu-2), but more recent work (209) suggests only limited Fe atom exchange occurs with this clay mineral. This, together with the requirement of fluoride ions for dissolution (210) suggests aluminosilicates are unlikely to represent a significant portion of the ^{57}Fe measured in the 7M HCl pool.

The similarity in AAO extractable Fe (~120 mmol Fe kg^{-1} soil) and the calculated extent of Fe atom exchange (80 – 110 mmol Fe kg^{-1} soil) suggests Fe^{2+}-facilitated atom

exchange in soils and sediments may be limited to low crystallinity Fe solids. This is consistent with observations that Fe atom exchange is rapid for pure phase ferrihydrite and nano-scale goethite, but slow for crystalline hematite (21, 22, 183), or that exchange is limited to surface layers of larger goethite particles (190). Greater than 20% of the Fe-(oxyhydr)oxides in these soils magnetically-order below 77K, which suggests ion (e.g., Al) substitution or structural defects in the nano-crystalline Fe minerals are reducing size of the magnetic-ordering domain (Figure S2 of the supporting information). Al-substitution and even surface ion adsorption are known to decrease the rate and extent of Fe atom exchange (21, 191), particularly if Si is one of the sorbates (114, 211). However, the similarity between the calculated extent of Fe atom exchange and the concentration of SRO Fe phases suggest Al-substitution and surface passivation are not overwhelming barriers to Fe atom exchange if Fe-(oxyhydr)oxide crystallinity is sufficiently low.

Mössbauer Analysis of the Unreacted and $^{57}Fe^{2+}$ Reacted Soil

Scherer and co-workers (15, 22, 123, 183, 188, 189, 212, 213) have pioneered a technique to describe the molecular structure of recently exchanged Fe atoms. They reacted isotopically pure ^{56}Fe solid phases with $^{57}Fe^{2+}$(aq) and then examined the exchanged solid phases using Mössbauer (MB) spectroscopy. Since MB only detects ^{57}Fe atoms and the original solid phase was all ^{56}Fe, the resulting ^{57}Fe-MB spectra isolates the structural composition of the exchanged atoms, which originated as aqueous Fe^{2+}(aq). Bisley soils contain a 2.1% natural abundance of the ^{57}Fe isotope. Thus, following removal of entrained Fe^{2+}(aq), the MB spectra of our $^{57}Fe^{2+}$ reacted soil (Figure B.3a) dominantly reflect the native Fe-oxide composition (9.1 vs 23.3 mM kg^{-1} soil native ^{57}Fe from the addition and the native soil, respectively, i.e. 72% of the signal), but it is biased toward our ^{57}Fe label relative to the unreacted soil (Figure B.3b). The MBS at

the lowest collection temperature, 13K, shows an ~ 5% increase in Fe^{III}-(oxyhydr)oxides relative to the unreacted soil Fe phases (Figure B.3c and Figure S2 of the supporting information). This suggests Fe atom exchange in our experiment is accompanied by electron transfer reactions (15) and that the $^{57}Fe(aq)$ re-crystallizes predominately as Fe-oxyhydroxide phases, rather within clay minerals or organic complexes. Examining the MB spectra at 77K, where a significant portion of the Fe^{III}-oxyhydroxides in this soil are within proximity of their Néel temperatures, reveals the ^{57}Fe accumulates preferentially in lower crystallinity portions of the Fe^{III}-oxyhydroxide population. The Fe^{III}-oxyhydroxide sextets in the $^{57}Fe^{2+}$-exchanged soil exhibit broader line widths (13.9 vs. 13.2 T) and lower average hyperfine field strengths (38.5 T vs. 41.6 T) than Fe^{III}-oxyhydroxide sextets in the unreacted soil (Figure B.3). However, the Fe^{III}-oxyhydroxide peak hyperfine field strength for the $^{57}Fe^{2+}$-exchanged soil (48.3 T) remained similar to that of the unreacted soil (48.4 T), suggesting the most crystalline Fe^{III}-oxyhydroxide sites were unaffected by reaction with $^{57}Fe^{2+}(aq)$ (Figure B.3d).

Kinetic Atom Exchange Model

The observed characteristics of atom exchange can be represented by a kinetic model that takes into account sorption of Fe^{2+} onto the iron mineral, followed by exchange between the surface layer (0.5M HCl extractable Fe) and the bulk iron (oxyhydr)oxides (7M HCl extractable Fe). Sorption is well represented by fast incorporation of $Fe^{2+}(aq)$ to the labile extractable phase, occurring over time scales of 15 min. (Figure B.4). The characteristic timescale for desorption is on the order of a week, while the release from bulk to surface is on the order of years.

Alteration of Atom Exchange Rates by Fe-reducing Organisms

Our control treatments exhibited different system dynamics than the treatments receiving $HgCl_2$ as a sterilizing agent. We attribute the steady increase in $Fe^{2+}(aq)$

beginning after 14 d of reaction to iron-reduction reactions catalyzed by microorganisms. This facilitates a decrease in the $^{57/54}$Fe(aq) ratio that is twice as fast as in the sterile samples (Fig. B.1) as Fe^{2+} released during Fe reduction is enriched in ^{54}Fe relative to the original $^{57}Fe^{2+}$ spike solution. However, microbial Fe reduction also results in lower $^{57/54}$Fe(0.5M HCl) and $^{57/54}$Fe(7M HCl) ratios than the sterilized treatments (Figure B.1). By calculating ^{57}Fe concentrations from measured $^{57/54}$Fe ratios and total Fe concentrations, we find similar increases in ^{57}Fe(0.5M HCl) in the live controls and sterile treatments early in the experiments (Fig. B.2); however after 3 d, when microbial Fe reduction grows more intense, ^{57}Fe(0.5M HCl) in the live controls decreases (Fig. 2). This behavior coincides with a slower increase of ^{57}Fe(7M HCl) and higher ^{57}Fe(aq) concentration in the live controls than in the sterile treatments as the experiment progresses (Fig. B.2). Evidently, recently sorbed ^{57}Fe atoms are re-solubilized preferentially relative to indigenous solid-phase Fe. This could result from the release of sorbed $^{57}Fe^{2+}$ as the underlying indigenous Fe^{III}-hydroxide is dissolved or it could result from the reductive dissolution of $^{57}Fe^{III}$-oxides that formed from electron-transfer and atom exchange with sorbed $^{57}Fe^{2+}$ (15). The net effect is that microbial Fe reduction accelerates the calculated atom exchange between Fe(aq) and Fe(0.5M HCl), while it decreases the calculated atom exchange between Fe(aq) and Fe(7M HCl) (Table 1).

Biogeochemical Implications

Our observations document significant Fe^{2+}-facilitated atom exchange between aqueous Fe^{2+} and solid phase Fe in a natural soil. The most rapid atom exchange took place concurrently with Fe^{2+} sorption, and continued slowly, but consistently thereafter. After 28 days, Fe^{2+}-facilitated atom exchange appeared to occur predominately with the short-range-ordered (SRO) portion of solid-phase Fe that is considered the most susceptible to Fe reduction and expected to exhibit the highest available surface area for sorption reactions. Based on these results, we expect soils exposed to anoxic conditions

with significant Fe^{2+}(aq) generation to exhibit substantial Fe-atom fluidity in SRO Fe phases, even despite the presence of environmental components shown to negatively influence electron transfer and atom exchange. The possibility for these SRO Fe phases to incorporate and release trace elements remains significant, although the permanence of any sequestration is still difficult to estimate.

Table B.1. Mass balance and % recovery data.

Treatment	Day	Aqueous Fe (mmole kg^{-1} soil)				0.5M extracted Fe (mmole kg^{-1} soil)				7M extracted Fe (mmole kg^{-1} soil)				% recovery	% exchange			
															^{57}Fe exchange		^{54}Fe exchange	
		Total Fe	fFe^{2+}	f^{57}Fe	f^{54}Fe	Total Fe	fFe^{2+}	f^{57}Fe	f^{54}Fe	Total Fe	fFe^{2+}	f^{57}Fe	f^{54}Fe		Aqueous	7M HCl extract.	Aqueous	7M HCl extract.
Live treatment	0	269.9	98.09	0.2614	0.04443	17.03	0.2587	0.0213	0.05887	950.1	0.0000	0.02134	0.05887	-				
	0.02	234.3	99.26	0.2567	0.04471	34.60	0.9803	0.1508	0.05108	882.8	0.0000	0.02301	0.05877	99.0				
	1	214.4	98.79	0.2516	0.04502	57.82	0.4843	0.1871	0.04889	971.1	0.0000	0.02501	0.05865	89.1	2.77	3.90	2.78	3.84
	3	217.0	98.40	0.2509	0.04506	55.43	0.4642	0.1960	0.04836	911.4	0.0000	0.02646	0.05856	88.9	3.16	6.72	3.17	6.61
	7	214.4	95.95	0.2309	0.04626	66.61	0.6221	0.2005	0.04809	1034	0.0000	0.02780	0.05848	91.8	14.1	9.34	14.2	9.19
	14	241.3	95.33	0.2418	0.04561	52.73	0.6002	0.1854	0.04900	950.7	0.0000	0.02768	0.05849	97.2	8.14	9.10	8.18	8.95
	21	247.3	91.93	0.2383	0.04582	52.93	0.6905	0.1860	0.04896	1006	0.0000	0.02926	0.05839	98.1	10.1	12.2	10.1	12.0
	28	249.1	96.52	0.2352	0.04600	50.01	0.6533	0.1691	0.04998	926.9	0.0000	0.02756	0.05849	101.4	11.8	8.87	11.8	8.73
Sterile treatment	0	269.9	98.09	0.2614	0.04443	17.03	0.2587	0.0213	0.05887	950.1	0.0000	0.02134	0.05887	-				
	0.02	234.5	98.15	0.2576	0.04466	47.78	0.6241	0.1648	0.05024	932.3	0.0000	0.02287	0.05878	96.6				
	1	218.0	97.55	0.2545	0.04484	59.39	0.4547	0.1927	0.04856	976.5	0.0000	0.02560	0.05861	89.0	1.69	5.31	1.69	5.23
	3	213.4	99.49	0.2544	0.04485	58.32	0.4506	0.1992	0.04817	916.6	0.0000	0.02775	0.05848	88.6	1.75	9.50	1.75	9.35
	7	205.6	97.96	0.2513	0.04504	55.97	0.4931	0.1995	0.04815	1011	0.0000	0.02906	0.05840	85.1	3.42	12.1	3.44	11.9
	14	211.5	97.40	0.2516	0.04502	57.61	0.6501	0.1982	0.04823	969.5	0.0000	0.02941	0.05838	90.4	3.27	12.7	3.29	12.5
	21	201.5	95.65	0.2498	0.04513	60.00	0.6426	0.1969	0.04831	999.8	0.0000	0.03124	0.05827	85.9	4.26	16.3	4.28	16.0
	28	212.5	97.01	0.2496	0.04514	61.34	0.6872	0.1894	0.04876	955.8	0.0000	0.03060	0.05831	92.2	4.36	15.0	4.38	14.8

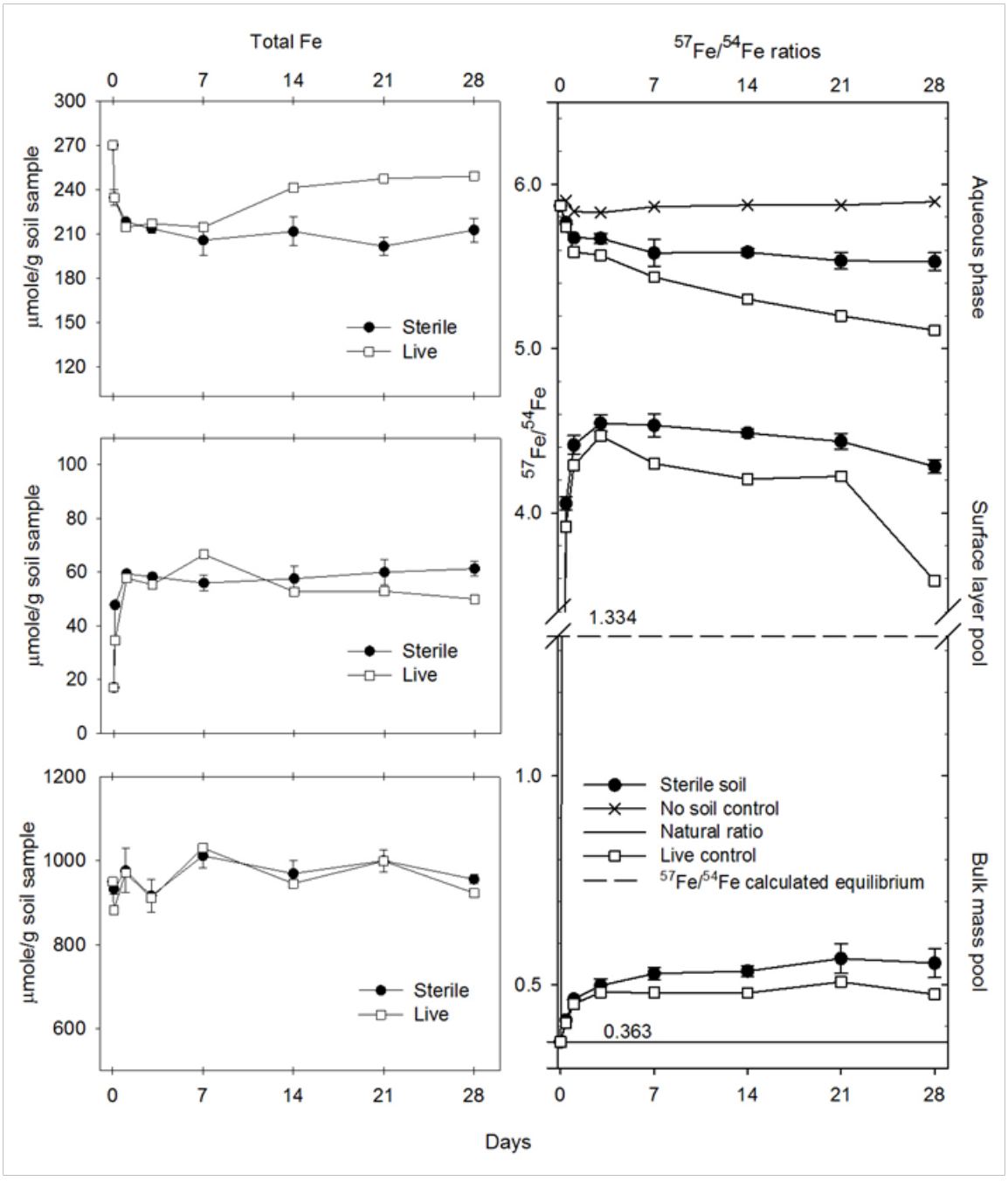

Figure B.1. Total Fe (see Table 1 for the fraction Fe^{II}) and $^{57/54}Fe$ ratios in the aqueous, surface layer (0.5M HCl extraction), and bulk (7M HCl extraction) pools in the valley soil experiment. Error bars represent ± 1σ (n=3) for the sterile treatments. Only one set of live control samples was used. An $^{57/54}Fe \sim 1.3344$ is the isotopic ratio upon complete equilibration between solution, surface and bulk oxide pools.

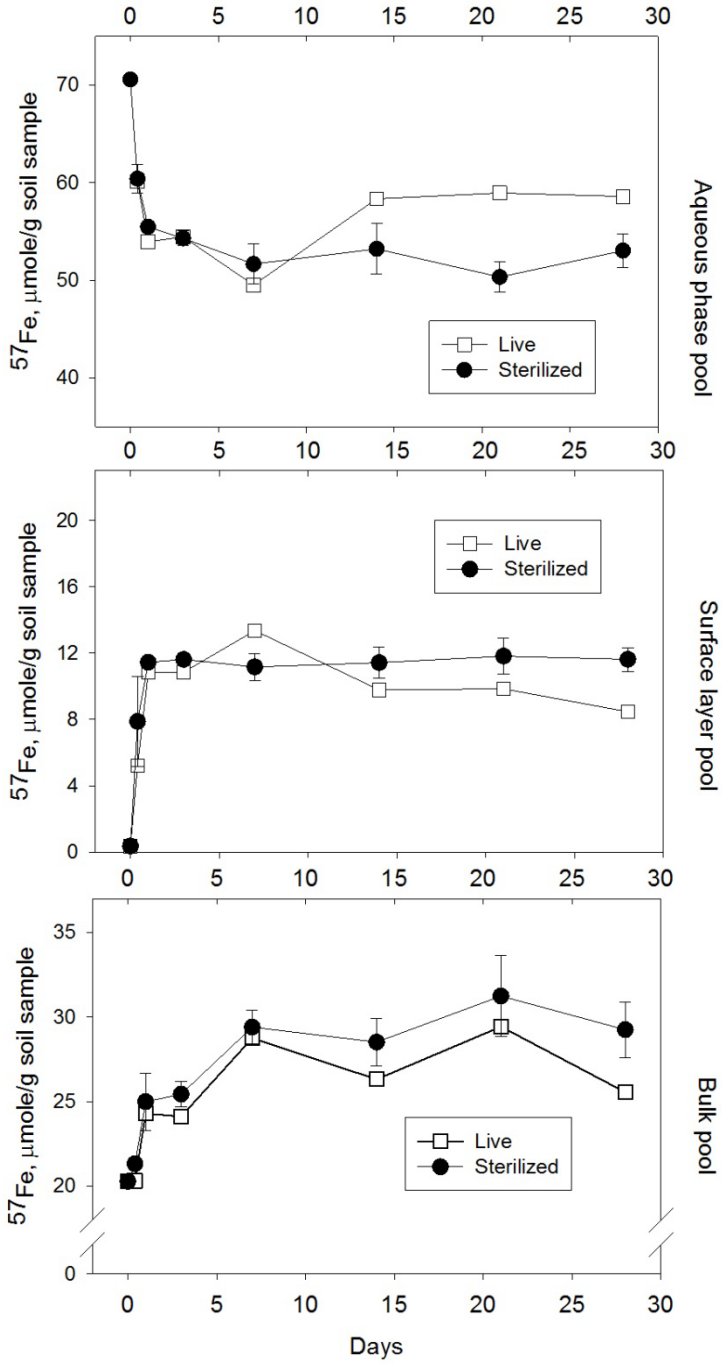

Figure B.2. ^{57}Fe in the aqueous, surface layer (0.5M HCl), and bulk (7M HCl) pools. Fe^{2+} concentrations are given in Table B.1.

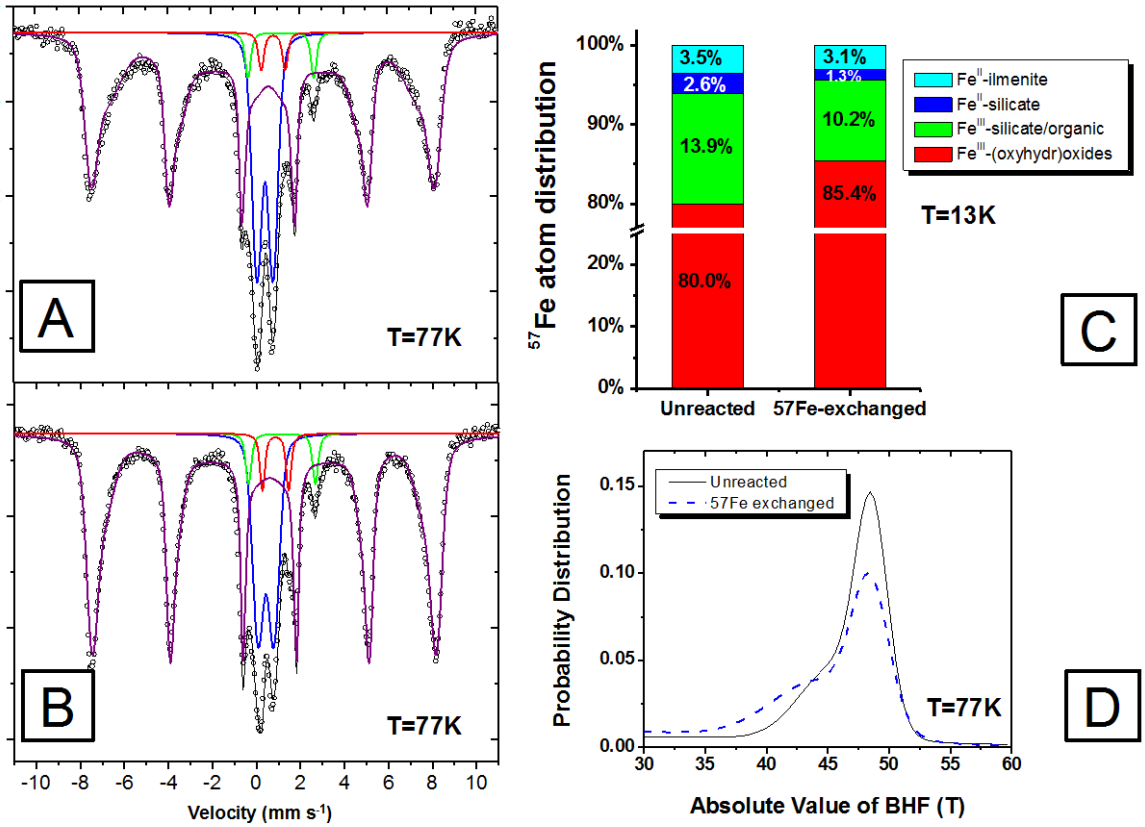

Figure B.3. Mössbauer spectra at 77K for Bisley, PR soil samples. Spectra show the $^{57}Fe^{2+}$-reacted soil following a 0.5M HCl extraction to remove surface adsorbed $^{57}Fe^{2+}$ (A) and the unreacted soil (B). In each spectrum, the black solid line is the total calculated fit, through the discrete data points. The resolved spectral components and assignments are: (1) Q-Fe^{III}-1, the deep central doublet (blue line) corresponding to Fe^{III} in aluminosilicate minerals; (2) Q-Fe^{II}-1, the narrow ferrous doublet corresponding to ilmenite (red line); (3) Q-Fe^{II}-2 the wider ferrous doublet corresponding to Fe^{II} in clays (green line); (4) HFD-OxHy, the dominant sextet (purple line) corresponding to Fe^{III}-oxyhydroxides. (C) Comparison of the spectral area of these components from Mössbauer spectra at 13K, where nearly all Fe^{III}-oxyhydroxide phases are magnetically ordered (see SI section). (D) The probability distribution of hyperfine field strengths for the HFD-OxHy sextets in the unreacted (black line) and $^{57}Fe^{2+}$-exchanged (Blue, dashed line) soils at 77K.

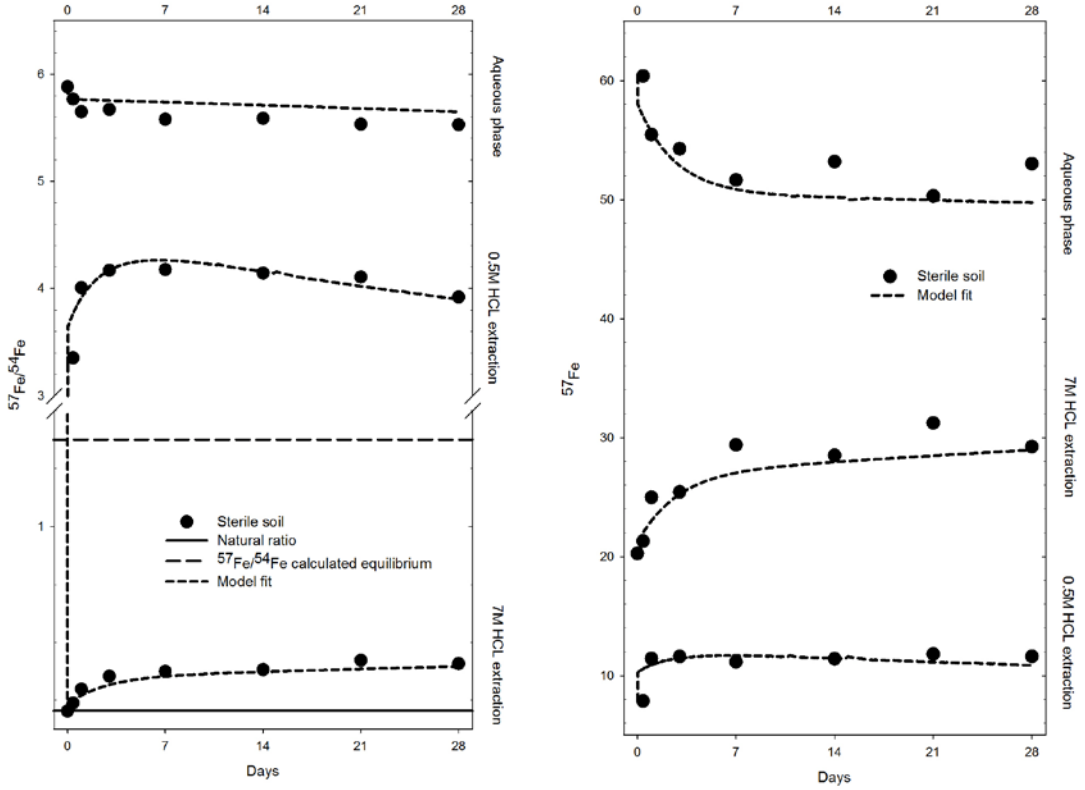

Figure B.4. $^{57/54}$Fe ratios in the aqueous, surface layer and bulk pools, and the corresponding ^{57}Fe concentrations, for the sterile treatment. Circles are the data points from Fig. 3 and the dashed lines are the model fit.

APPENDIX C: FE(III) CATALYZED FE ATOM EXCHANGE IN FE(II) OXIDES

Abstract

Recent studies into the interaction between aqueous Fe(II) and Fe(III) oxides have revealed it to be much more complex than a simple surface sorption phenomenon. Using Mössbauer spectroscopy and stable isotope measurements, interfacial electron transfer and Fe atom exchange have been observed between aqueous Fe(II) and Fe(III) oxides under geochemical conditions typical of groundwater. As the fourth most abundant element in the lithosphere, Fe is present not only in the subsurface, but in surface waters, river sediments, estuaries, marine sediments, and throughout the fresh and seawater columns. It is currently unclear whether electron transfer and atom exchange between Fe(II) and Fe(III) is restricted to anoxic, reducing environments, where concentrations of aqueous Fe(II) can be very high, or whether these processes continue in environments where Fe(II) may be bound in mineral forms, and Fe(III) may also be structurally bound, or exist complexed by organic ligands. Electron transfer and atom exchange can influence the reactivity of Fe minerals toward contaminants, and may also influence the sequestration and mobilization of trace elements and contaminants. In this study, electron transfer and atom exchange are examined by Mössbauer spectroscopy and stable isotope measurements under conditions likely to be found in marine and oceanic environments, to determine whether these processes continue to occur in environments beyond the subsurface.

Introduction

This appendix contains the results of a preliminary investigation into the possibility for aqueous Fe(III) to catalyze Fe atom exchange in minerals containing structural Fe(II). The overall objective of this work was to examine whether Fe interfacial electron transfer and atom exchange processes occur under conditions typical of marine and oceanic environments, where aqueous Fe is predominantly Fe(III) and both

Fe(II) and Fe(III) oxides exist. We used Mössbauer spectroscopy and stable isotopes to explore whether Fe electron transfer and atom exchange occurs between aqueous Fe(III) and Fe(II) or Fe(III) in Fe minerals, using model ligands such as EDTA and NTA to simulate biological ligands that complex and stabilize Fe(III) under marine conditions.

Four Fe(II) containing minerals were investigated, including mackinawite (FeS), wüstite (FeO), siderite ($FeCO_3$), and magnetite (Fe_3O_4). Mackinawite and siderite were chosen because of their roles as the dominant Fe(II) minerals controlling Fe(II) solubility in anoxic sediments, where high levels of CO_3(-II) and S(-II) present in marine waters drive their formation. Magnetite and wüstite were selected as thermodynamically predicted stable end products of the Fe-seawater system, although the low temperature of the oceanic environment kinetically limits their formation. In addition, two Fe(III) oxides (goethite (α-FeOOH) and hematite (Fe_2O_3)) were used along with magnetite to assess whether atom exchange occurs between aqueous Fe(III) and structural Fe(III).

Generally, solids are classified as one of three types based on their ability to conduct electricity. Metals easily conduct electricity, requiring little to no energy for an electron to migrate between atoms. Conversely, insulators conduct electricity very poorly, as the amount of energy required to move electrons between atoms is so large that conduction is generally not observed under normal electrical potentials. The third class, semiconductors, exhibit properties that range between those of conductors and insulators. While the Fe(III)-oxides tend to be semiconductors (e.g., lepidocrocite, goethite, hematite), mixed valent and Fe(II) minerals can range from conductors to insulators (Table C.1). The series of six minerals selected encompass a range of band gaps including conductors (mackinawite, magnetite), semiconductors (hematite, goethite, wüstite), and an insulator (siderite), to provide insight into the role of mineral conductivity in electron transfer and atom exchange.

We selected five ligands to stabilize Fe(III) in solution, including chloride, tartrate, 1,10-phenanthroline, nitrilotriacetic acid (NTA), and ethylenediaminetetraacetic

acid (EDTA). The ligands found in marine systems exhibit a wide range of physical and chemical properties, making generalizations about their behavior quite difficult. Selected ligands encompass a range of log K values ranging from 1.48 to 25.1 to examine whether Fe(III) binding affinity might influence the rate and extent of electron transfer and atom exchange (Table C.2). Further experiments could include ligands as model microbial and plant siderophores, such as desferryoxamine-B (DFO-B), aerobactin, and phytic acid.

Experimental Section

Mineral Synthesis and Characterization

Magnetite was synthesized according to the method of (214), which entails making a 1:2 Fe(II):Fe(III) under anoxic conditions, titration to alkaline pH (>11) with NaOH, and mixing overnight. Partially oxidized magnetite was synthesized by exposing this solution to varying amounts of H_2O_2, and allowing equilibration for an additional day. Wüstite was purchased from Sigma Aldrich, ground with a mortar and pestle, and sieved under anoxic conditions. Siderite was synthesized according to (215) by adding 50 mL of 0.2 M $Fe(ClO_4)_2$ dropwise to 150 mL of 0.3 M $NaHCO_3$ inside an anoxic glovebox. The precipitate formed was allowed to settle for 24 hours, after which the solution supernatant was decanted. Mackinawite was synthesized by a procedure modified from (216). Briefly, 300 mL of 1.1 M Na_2S was added to 500 mL of 0.57 M $FeCl_2$ inside an anoxic glovebox. The resulting slurry was allowed to mix for three days, at which point it was decanted into polypropylene centrifuge bottles. Centrifuge bottles were tightly sealed, centrifuged at 8000 rpm for 10 minutes, and decanted inside the glovebox. The solids were resuspended in fresh deoxygenated deionized water, shaken, and allowed to equilibrate. The process of centrifuging, decanting, and resuspending, was repeated a total of 8 times. The remaining black precipitate was freeze dried under vacuum, and sieved under anoxic conditions.

Solids were characterized by various complementary analyses. Specific surface area was measured with N_2 – Brunauer – Emmett Teller (BET) analysis (Table C.3). Powder x-ray diffraction (pXRD) patterns were obtained to verify chemical composition and crystallinity of synthesized minerals. Transmission electron microscopy (TEM) and scanning electron microscopy (SEM) were used to observe particle dimensions, morphology, and aggregation (Figure C.1). Mössbauer spectroscopy was used to verify the chemical composition and local Fe environment for synthesized materials.

Results and Discussion

Electron Transfer Between Aqueous Fe(III) and Structural Fe(II)

Working with aqueous Fe(III) as opposed to aqueous Fe(II) presents a number of experimental challenges due to the low solubility of Fe(III) (e.g., K_{sp} of $Fe(OH)_3$ = $6x10^{-38}$ at 25°C) (217). The solubility of Fe(III) at neutral pH is very low, on the order of 10^{-8} to 10^{-11} M between pH 6 and 8 (218, 219). Initially, I attempted use the high concentration of chloride typical of seawater to directly measure Fe(III) solubility, and compare to previous work looking at the solubility of Fe(III) in seawater (220). Varying amounts of Fe(III) stock were added to 15 mL of 0.7 M NaCl containing 1 mM bicarbonate buffer. Total Fe concentrations ranged from 10^{-3} to 10^{-5}, and initial pH ranged from 3 to 5. Reactors were rotated end-over-end for 7 days, after which the solution was filtered, final pH was measured, and both Fe(II) and total Fe were measured by 1,10-phenanthroline (80). There was good agreement between the concentration of Fe present and the previous results for conditions where [Fe] > 10^{-6}, which is the approximate detection limit of the phenanthroline method (Figure C.2).

Although in the presence of chloride, we can achieve Fe(III) solubility on the millimolar level below pH 3, such acidic conditions present additional problems in our experimental system. Subsequent experiments at pH 3 confirmed that up to 50 μM Fe

could be maintained in solution over 7 days, but significant dissolution of magnetite (x = 0.28, 0.48) and wüstite occurred in less than 24 hours after solids addition. Dissolution of the minerals resulted in significant aqueous Fe(II), which made accurate measurement of low levels of Fe(III) impossible (data not shown). Also, when system pH is below the point of zero charge, mineral surfaces will become positively charged, and cation sorption decreases. Lack of Fe sorption to the mineral surface could present an additional barrier to having sufficient Fe(II) oxidized in the mineral in order to detect that oxidation by Mössbauer spectroscopy.

Our group, however, has previously still observed significant Fe atom exchange when no net uptake of Fe(II) was measured (Figure C.3). Specifically, we observed 53-63% atom exchange between aqueous Fe(II) and goethite (as calculated from the goethite solids , and aqueous Fe, respectively) at pH 5.0, despite no apparent net uptake of Fe(II) from solution. The Fe atom exchange observed represents two to three times the extent predicted if only the surface of the nanogoethite participates (bottom panel dashed line, Figure C.3)

Magnetite was selected for an initial experiment to test for electron transfer because it contains both Fe(II) and Fe(III), typically in a ratio of $x = (Fe^{2+}/Fe^{3+}) = 0.5$. This ratio is referred to as stoichiometry, and it ranges from stoichiometric magnetite (x = 0.50) to maghemite (x = 0, no Fe(II) present). Small changes in magnetite stoichiometry (as little as 0.01) can be detected by Mössbauer spectroscopy, which allows us to quantitatively determine when oxidation of structural Fe(II) to Fe(III) has occurred. Approximately 30 µg of ^{57}Fe is required to obtain a useable Mössbauer spectrum, which due to the low abundance of the ^{57}Fe isotope (2.2%) translates to at least 1 mg of naturally abundant Fe. Previous analysis of magnetite by Mössbauer spectroscopy has shown that 30 mg of solids are needed to produce a high quality spectrum, for which a stoichiometry change of 0.01 represents an oxidation or reduction of approximately 0.8 nmol Fe. Reactors contained 15 mL of 0.7 M NaCl with 25 mM HEPES buffer at pH

7.2, 0.5 mM aqueous Fe(III) (phenanthroline) or 1 mM aqueous Fe(III) (EDTA, NTA), 1.5 mM dissolved ligand, and 30 mg of magnetite solids. A measurable change in magnetite stoichiometry for this system requires 5.7% (11.4% for 1,10-phenanthroline) of the aqueous Fe to participate in electron transfer with the solid. The use of ligands (1,10-phenanthroline, EDTA, NTA) to maintain aqueous Fe(III) at millimolar levels introduces a similar complication to low pH systems, in that they may prevent sorption/interaction between complexed Fe and solids.

Mössbauer spectra obtained from the electron transfer experiments with magnetite are shown in Figure C.4. Magnetite exposed to an Fe and ligand free control solution was oxidized from $x = 0.48$ to $x = 0.45$ over 7 days. Oxidation in the Fe free control reactor is likely due to the dissolution of structural Fe(II) from the magnetite solids. Magnetite exposed to 0.5 mM aqueous Fe(III) and 1.5 mM 1,10-phenanthroline was also oxidized to $x = 0.45$, which was not significantly different from the Fe and ligand free control. Magnetite exposed to 1 mM Fe(III) and 1.5 mM NTA or EDTA was oxidized to $x = 0.42$ and $x = 0.22$ respectively, which could be indicative of electron transfer from structural Fe(II) to aqueous Fe(III). It could also be indicative of a ligand-promoted oxidative leaching process, where NTA or EDTA complexes Fe(II) as it dissolves from the magnetite solids, effectively maintaining $[Fe(II)_{aq}]$ near zero, and allowing dissolution of the mineral to continue beyond the equilibrium that would be reached in a ligand free system. The dramatic increase in magnetite oxidation when EDTA is present, which forms the strongest complex with Fe(II), generally supports the possibility for oxidative leaching. Oxidation of magnetite from $x = 0.48$ to $x = 0.22$ would require the reduction of 0.027 millimoles of aqueous Fe(III), which exceeds the Fe(III) actually available in the system (186%). Although this may further point towards oxidative leaching as the mechanism responsible for the observed change in stoichiometry, the possibility for oxidation by Fe(III) still exists, since the change in stoichiometry also exceeds the EDTA available in the system by 20%.

From these results, it is apparent that a more rigorous examination of electron transfer in the presence of Fe(III)-ligand complexes is required. Additional experiments will be performed by suspending magnetite in solutions with a constant ligand concentration while varying the Fe(III) concentration. These experiments will also include Fe free controls with only the ligand present in solution. By varying the Fe(III) concentration, the concentration of free, unbound ligand will also vary inversely. Any observed correlation between oxidation of the magnetite and either the Fe(III) concentration, or the concentration of unbound ligand, should help clarify whether the oxidation observed is due to Fe(II)-Fe(III) electron transfer, or enhanced dissolution of Fe(II) from the mineral. If Fe(II)-Fe(III) electron transfer is indicated by the results of these experiments, additional studies will be performed using minerals containing solely Fe(II). Mackinawite and siderite will be synthesized using the methods described earlier with ^{56}Fe starting material (99.9%), rendering them invisible to Mössbauer spectroscopy. By reacting these minerals with isotopically labeled aqueous ^{57}Fe(III) (96%), the resulting spectrum will only reflect the oxidation state and bonding environment of the ^{57}Fe atoms. We can use this signal to observe reduction of the initially dissolved ^{57}Fe(III) to Fe(II), which may appear as a doublet characteristic of Fe(II), or as a spectrum characteristic of the underlying Fe(II) solid.

Atom Exchange Between Aqueous Fe(III) and Structural Fe(II)

The identification of atom exchange in the aqueous Fe(III) - Fe(II) and Fe(III) mineral system is complicated by the same factors as the electron transfer experiments. The use of ligands to complex Fe(III) and prevent precipitation can interfere with our colorimetric determination of aqueous Fe concentrations. In order to calculate the equilibrium "completely mixed" isotope fractionation, accurate measurements of the total Fe in the system are critical. In an attempt to work around this problem, 1,10-

phenanthroline was used to both stabilize Fe(III) in solution and to measure the aqueous Fe concentration, to avoid the ligand competition that precludes accurate measurement when EDTA or NTA are used (Figure C.5). Measurements were fairly accurate when only Fe(II) or Fe(III) were present, but at intermediate concentrations (500 μM) of each Fe species, the results were not reproducible (Figure C.6).

A reproduction of the experiment detailed in (22) was also performed, modified to fit our analytical capabilities. This experiment verified our ability to track Fe atom exchange with a single collector quadrupole ICP-MS, and to reproduce the results of (22) with a less precise instrument (ICP-MS vs. MC-ICP-MS). Results of this atom exchange experiment are shown in Figure C.7, which agree with published data. Further atom exchange experiments were conducted using the same sampling and analysis procedure. Mackinawite, wüstite, siderite, and magnetite were reacted for 7 and 14 days with 1 mM ^{57}Fe(III) complexed by 3 mM 1,10-phenanthroline in a solution of 0.7 M NaCl with 25 mM HEPES buffer at pH 7.0. Isotope measurements showed near complete Fe isotope exchange (~92%) between mackinawite solids and aqueous Fe(III) after 14 days, with similar results observed for magnetite, siderite, and wüstite (Figures C.8 to C.11). Note, however, that we suspect both mass transfer and photochemical processes complicate the interpretation of this data as shown in Figure C.12. These processes make it difficult to determine whether exchange beyond mass transfer or sorption/dissolution processes is occurring. For example, although Fe measurements indicated complete recovery of the Fe, it was nearly all Fe(II), indicating net reduction of Fe(III) to Fe(II). This is possibly due to photoreduction of the Fe(III)-phenanthroline complex; or significant mineral dissolution causing the Fe(III) signal to be swamped out by Fe(II) during measurement. Additional studies to control for mineral dissolution and Fe-ligand photochemical reduction will be required.

Summary

Recent studies have illuminated the complexity of the interaction between aqueous Fe(II) and Fe(III)-containing minerals. Revelations about electron transfer and atom exchange in these systems have raised additional questions, including whether similar processes can occur for Fe minerals under different geochemical conditions, and in more complex environments. Interaction of Fe(II)-sulfides and -carbonates with dissolved Fe(III) is prevalent throughout the marine environment, and while it seems intuitive that electron transfer and atom exchange can occur here as well, there is little evidence to either support or deny that theory. Examination of these processes in Fe(II) minerals will also contribute to our understanding of how mineral electronic properties can influence electron transfer and atom exchange. The study of electron transfer and atom exchange processes in the presence of ligands, which are ubiquitous in the environment, will provide an important bridge between laboratory studies under very simple conditions and observations at field sites and in true environmental samples.

The processes of electron transfer and atom exchange have implications for contaminant reduction, mobility of trace metals and contaminants, and isotopic fingerprinting. To determine the overall significance of these processes however, it is critical to understand under what geochemical conditions they occur. Atom exchange among Fe oxides appears to occur in natural soils, and has been shown under simulated groundwater conditions. Initial experiments show the potential for Fe atom exchange to occur between aqueous Fe(III) and structural Fe(II) in Fe minerals, possibly identifying it as a relevant process in marine environments as well. A number of experimental and analytical constraints will need to be overcome, however, to properly evaluate the potential relevance of Fe(III)-catalyzed Fe atom exchange

Table C.1. Reported band gaps for various Fe minerals (values from 109, 221-223).

Fe Mineral	Band Gap (eV)
Conductor	**≤ 0 (overlap)**
Mackinawite (FeS)	0
Magnetite (Fe_3O_4)	0.1
Semiconductor	**0.5 - 3**
Pyrite (FeS_2)	0.95
Lepidocrocite (γ-FeOOH)	2.06
Goethite (α-FeOOH)	2.10
Hematite (Fe_2O_3)	2.20
Wüstite (FeO)	2.30
Insulator	**> 3**
Siderite ($FeCO_3$)	4.4 ± 0.2

Table C.2. Stability constants for Fe-ligand complexes used in experimental systems. (Values obtained from 224, 225).

	Log k_1		Log k_2		Log k_3	
Ligand	**Fe(II)**	**Fe(III)**	**Fe(II)**	**Fe(III)**	**Fe(II)**	**Fe(III)**
Cl (-I)	-0.2	1.48		2.13		
Tartrate	2.73	7.22				
OH (-I)	4.6	11.81		23.4	13	
1,10-phenanthroline	5.85	6.50	11.15	11.40	21.00	13.80
NTA	8.9	15.93	11.98	24.0		
EDTA	14.30	25.1				

Table C.3. BET specific surface area measurements for Fe minerals in this study

Fe Mineral	BET Specific Surface Area (m^2/g)
Goethite	115.0 ± 4.6
Hematite	108.7 ± 5.4
Magnetite (x = 0.28)	77.5
Magnetite (x = 0.38)	65.4
Magnetite (x = 0.48)	60.6
Mackinawite	13.9
Siderite	53.4
Wüstite	6.7

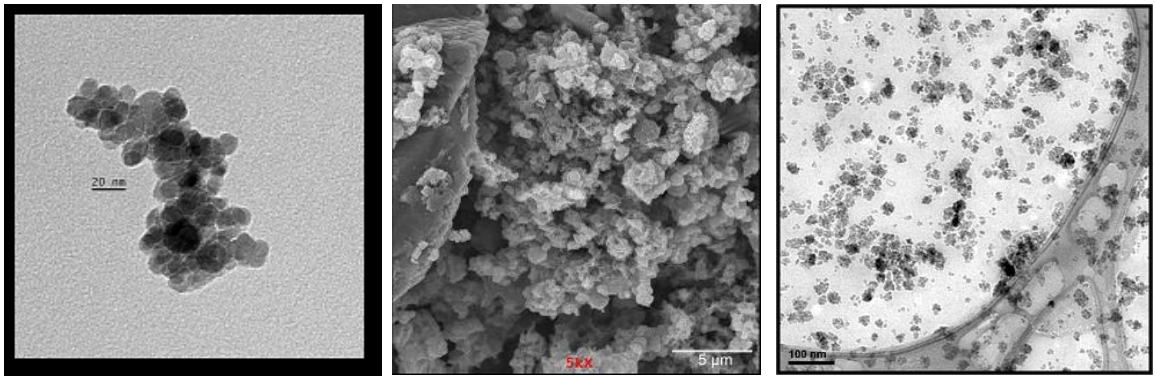

magnetite mackinawite hematite

Figure C.1. Electron micrographs of laboratory synthesized (left to right) magnetite (Fe_3O_4), mackinawite (FeS), and hematite (Fe_2O_3).

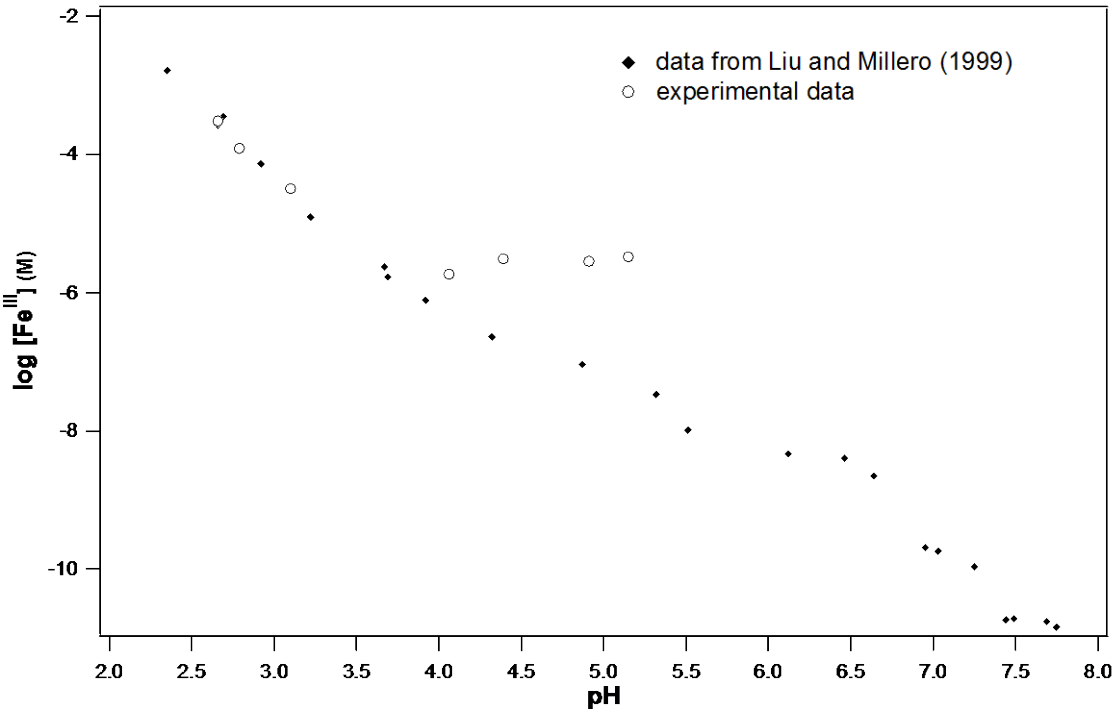

Figure C.2. Log Fe(III) solubility in 0.7 M NaCl solution as a function of pH. Fe(III) concentration was measured by 1,10-phenanthroline, which is accurate to approximately 10^{-6} M Fe.

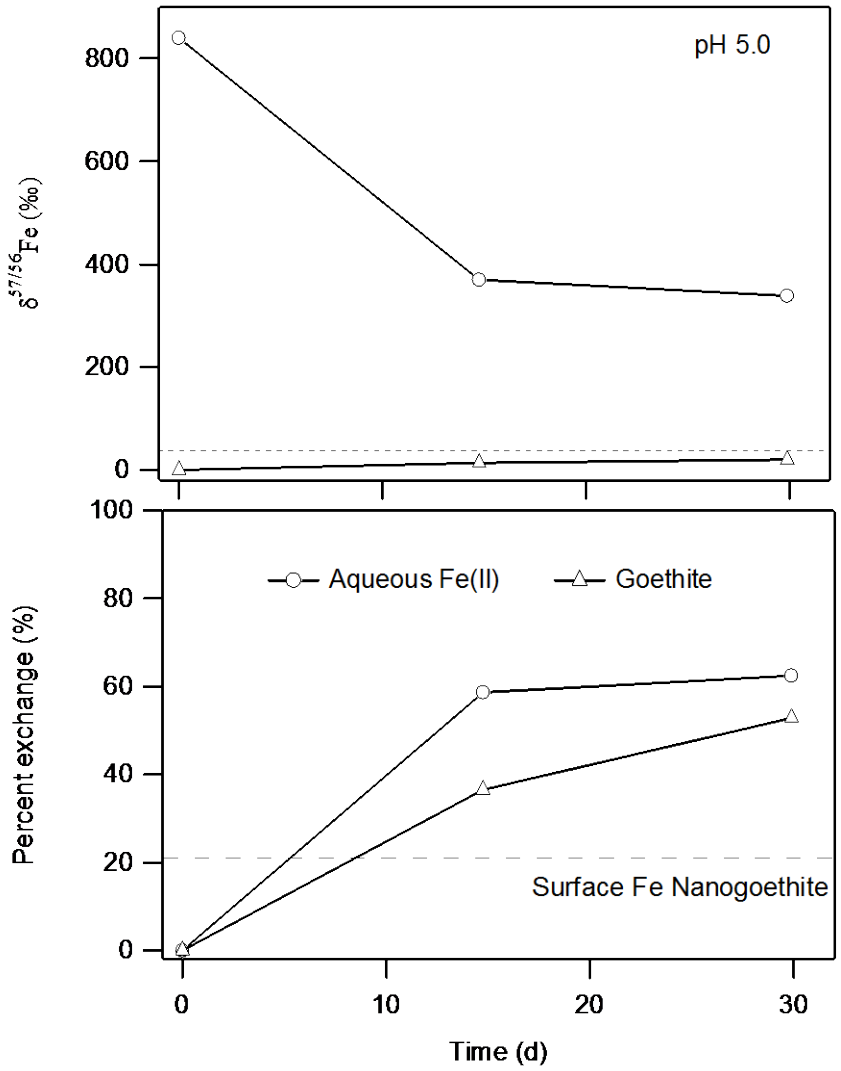

Figure C.3. Measured $\delta^{57/56}$Fe values (top panel) and corresponding percent exchange values (bottom panel) for aqueous Fe(II) and residual Fe(III) in goethite nanorods at pH 5.0. The delta value predicted by complete isotopic exchange (dashed line in top panel) is provided for reference. Percent exchange values are higher after 30 d than what would be predicted based on the available amount of Fe at the surface of goethite nanorods (- - - - , bottom panel).

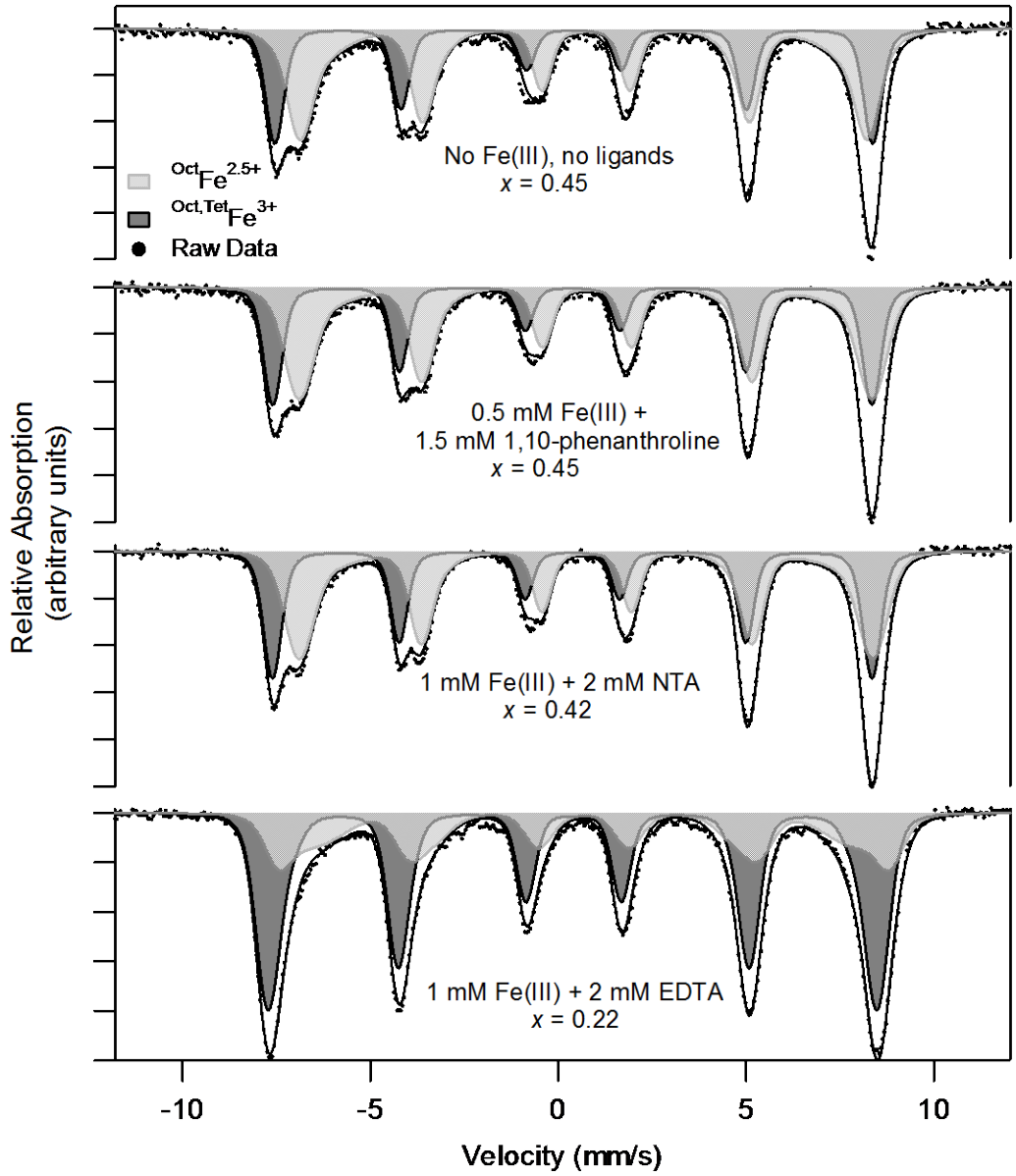

Figure C.4. Mössbauer spectra of stoichiometric magnetite in 0.7 M NaCl with 25 mM HEPES buffer, reacted with no Fe(III) or ligands (top), compared to stoichiometric magnetite reacted with aqueous Fe(III) complexed by (top to bottom) 1,10-phenanthroline, NTA, and EDTA.

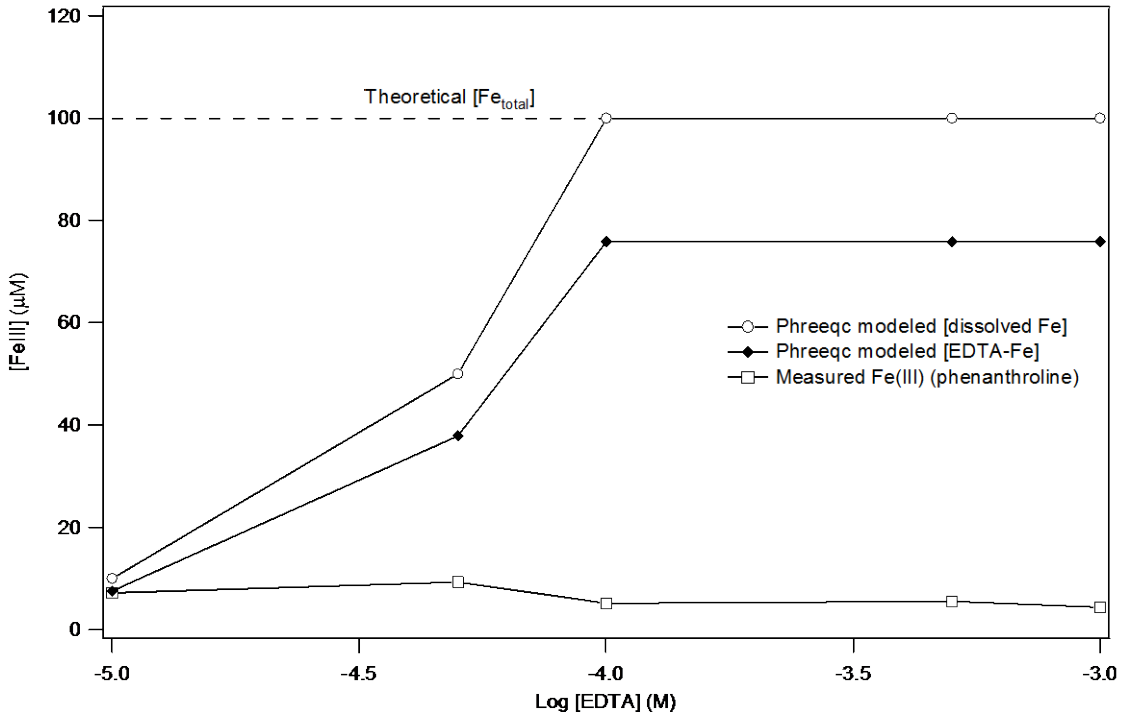

Figure C.5. Simulated Fe and Fe-EDTA complex concentrations and Fe measured by complexation with 1,10-phenanthroline. Strong Fe binding by EDTA prevents colorimetric quantification of Fe using 1,10-phenanthroline.

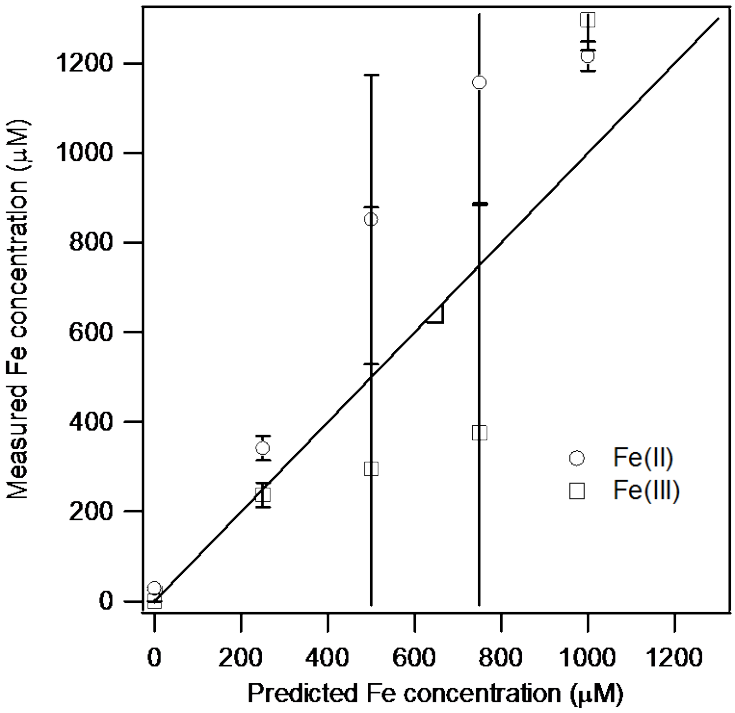

Figure C.6. Predicted and measured Fe(II) and Fe(III) concentrations in reactors containing 3 mM 1,10-phenanthroline, and 1 mM total Fe, with Fe(II) and Fe(III) ranging from 0 to 1 mM.

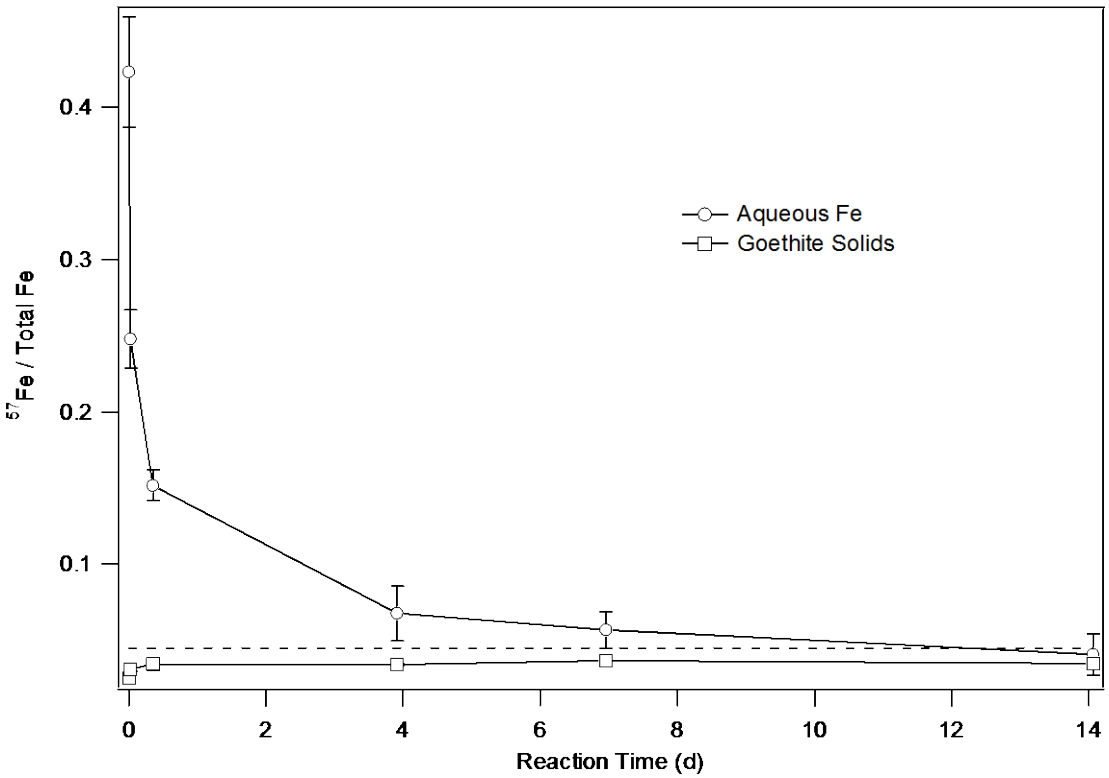

Figure C.7. Measured ^{57}Fe / Total Fe fractions for the goethite-aqueous Fe(II) system at pH 7.5. The dotted line indicates the equilibrium isotope fractionation based on a whole system mass balance

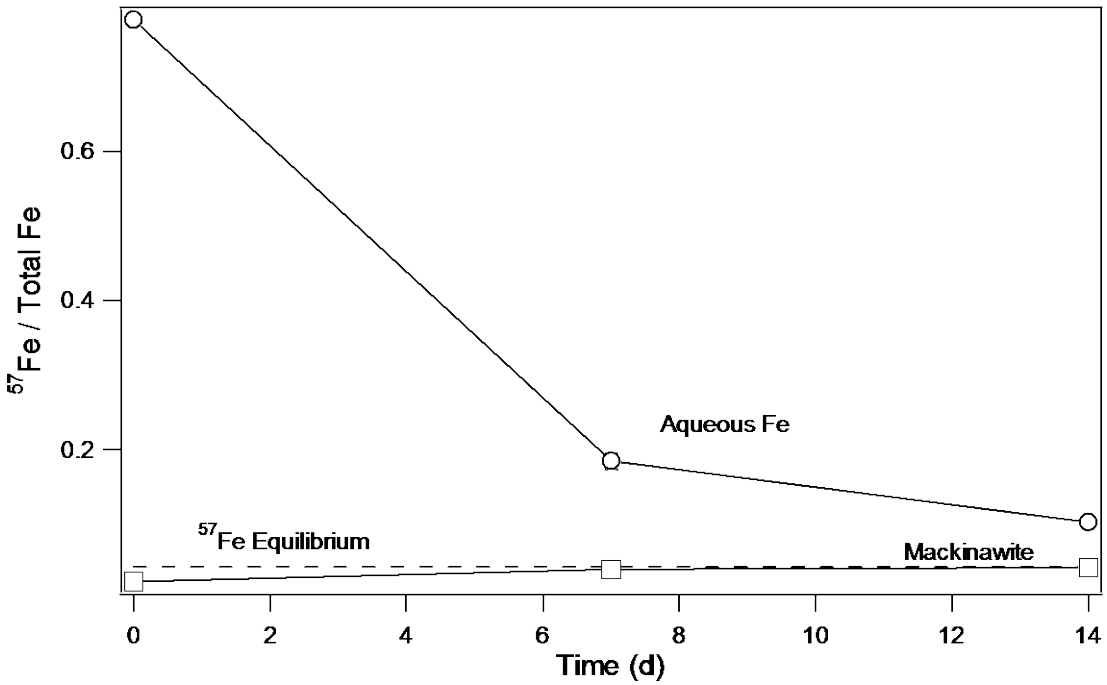

Figure C.8. Measured ^{57}Fe fraction in mackinawite solids and aqueous Fe(III) over time. Mass balance derived complete mixing isotope distribution is shown by the dotted line.

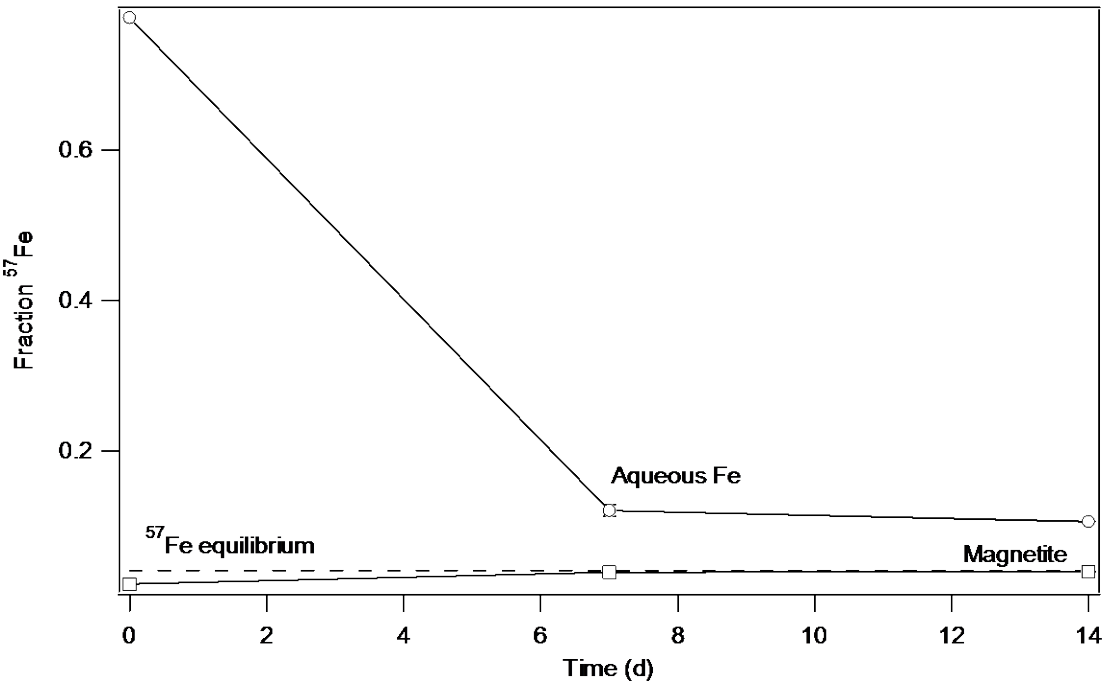

Figure C.9. Measured ^{57}Fe fraction in magnetite solids and aqueous Fe(III) over time. Mass balance derived complete mixing isotope distribution is shown by the dotted line.

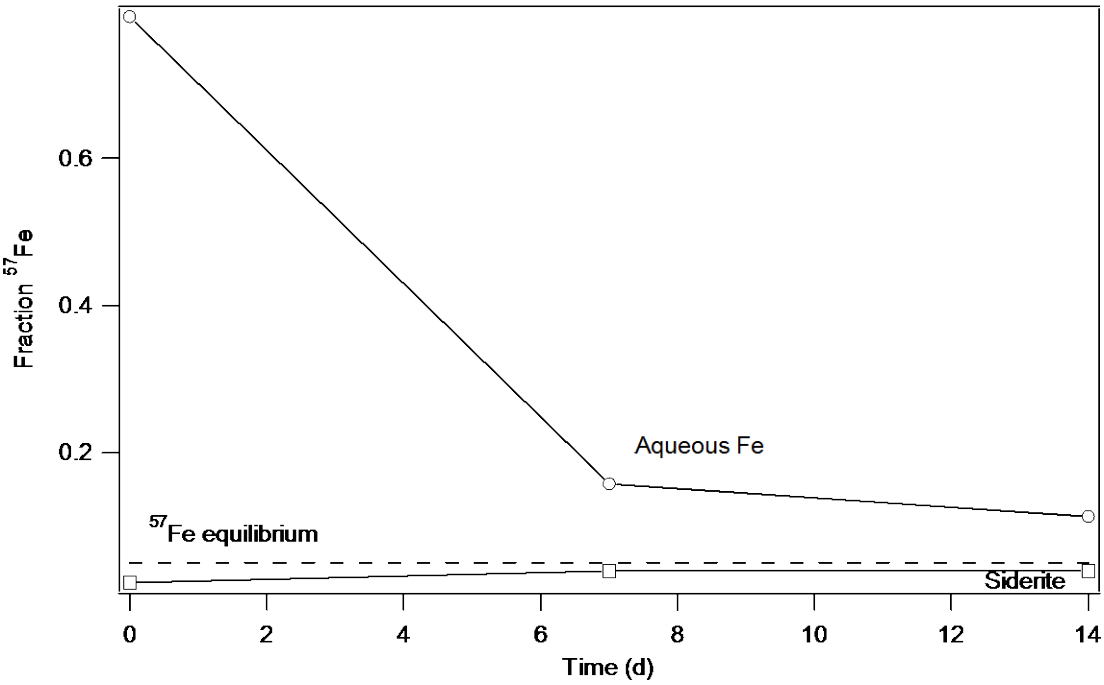

Figure C.10. Measured ^{57}Fe fraction in siderite solids and aqueous Fe(III) over time. Mass balance derived complete mixing isotope distribution is shown by the dotted line.

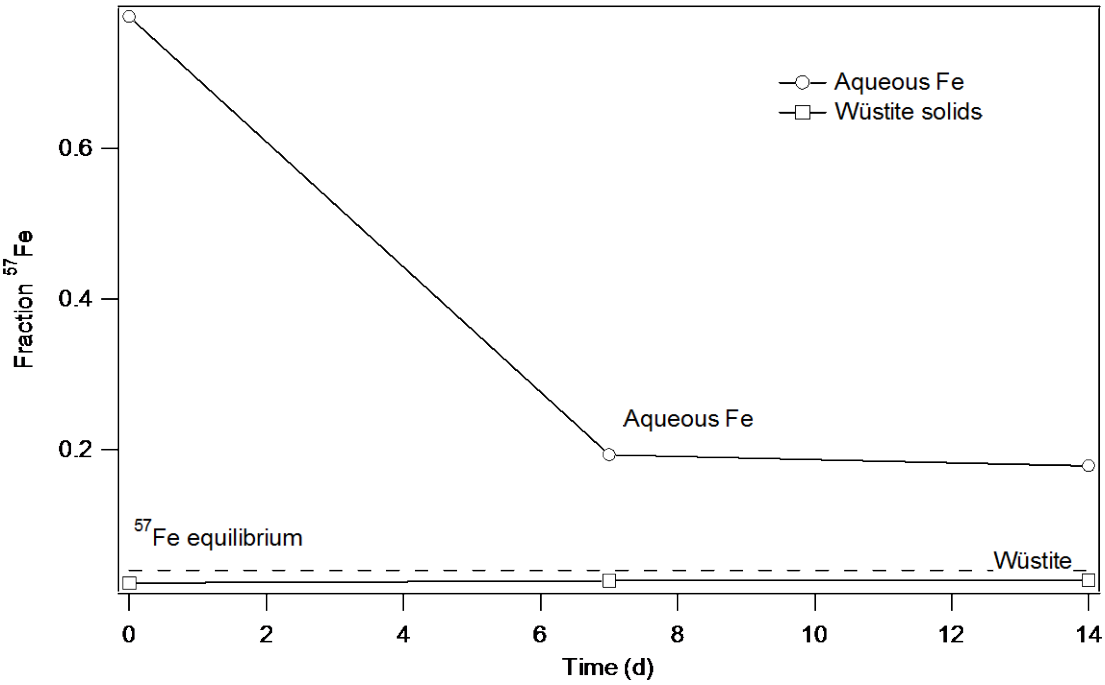

Figure C.11. Measured ^{57}Fe fraction in wüstite solids and aqueous Fe(III) over time. Mass balance derived complete mixing isotope distribution is shown by the dotted line.

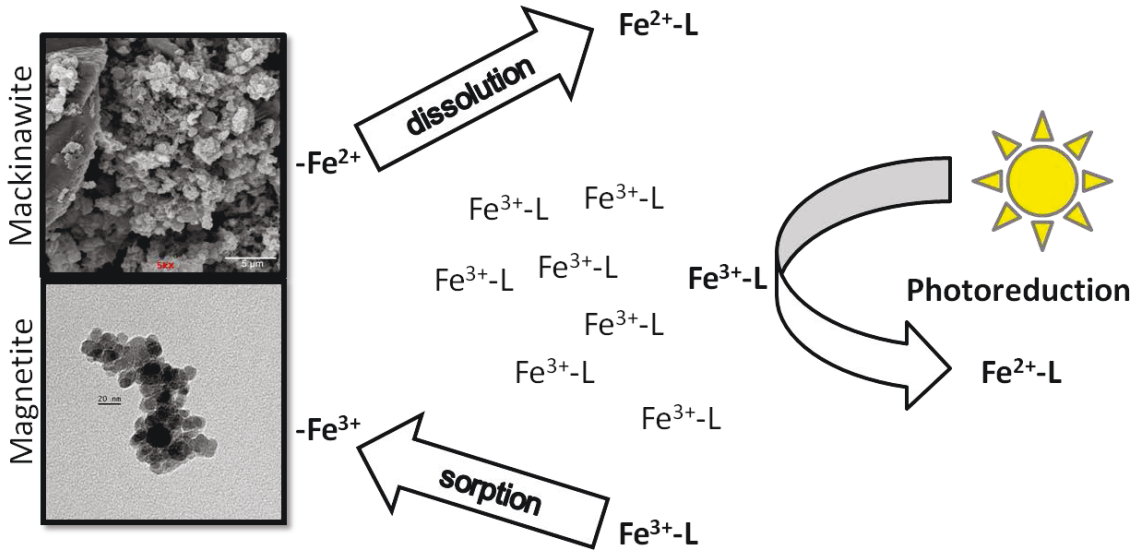

Figure C.12. Mass transfer and photochemical processes that complicate our ability to determine whether Fe(III) catalyzed Fe atom exchange occurs with Fe(II) minerals.

REFERENCES

1. Wedepohl, K.H., *The composition of the continental crust*. Geochimica et Cosmochimica Acta, 1995. **59**(7): p. 1217-1232.

2. Weber, K.A., M.M. Urrutia, P.F. Churchill, R.K. Kukkadapu, and E.E. Roden, *Anaerobic redox cycling of iron by freshwater sediment microorganisms.* Environmental Microbiology, 2006. **8**(1): p. 100-113.

3. Sunda, W., *Oceans. Iron and the carbon pump*. Science, 2010. **327**(5966): p. 654-655.

4. Moore, C.M., M.M. Mills, E.P. Achterberg, R.J. Geider, J. LaRoche, M.I. Lucas, E.L. McDonagh, X. Pan, A.J. Poulton, M.J.A. Rijkenberg, D.J. Suggett, S.J. Ussher, and E.M.S. Woodward, *Large-scale distribution of Atlantic nitrogen fixation controlled by iron availability.* Nature Geoscience, 2009. **2**(12): p. 867-871.

5. Dutkiewicz, S., M.J. Follows, and P. Parekh, *Interactions of the iron and phosphorus cycles: A three-dimensional model study*. Global Biogeochemical Cycles, 2005. **19**(1): p. GB1021.

6. Lovley, D.R. and E.J.P. Phillips, *Novel Mode of Microbial Energy-Metabolism - Organic-Carbon Oxidation Coupled to Dissimilatory Reduction of Iron or Manganese.* Applied and Environmental Microbiology, 1988. **54**(6): p. 1472-1480.

7. Schaetzl, R. and S. Anderson, *Soils: Genesis and Geomorphology*. 2005, Cambridge, UK: Cambridge University Press. 817.

8. Li, Y., H. Vali, J. Yang, T.J. Phelps, and C.L. Zhang, *Reduction of Iron Oxides Enhanced by a Sulfate-Reducing Bacterium and Biogenic H2S.* Geomicrobiology Journal, 2006. **23**: p. 103-117.

9. Charlet, L., E. Silvester, and E. Liger, *N-compound reduction and actinide immobilisation in surficial fluids by Fe(II): the surface Fe(III)OFe(II)OH degrees species, as major reductant*. Chemical Geology, 1998. **151**(1-4): p. 85-93.

10. Klausen, J., S.P. Trober, S.B. Haderlein, and R.P. Schwarzenbach, *Reduction of substituted nitrobenzenes by Fe(II) in aqueous mineral suspensions.* Environmental Science and Technology, 1995. **29**(9): p. 2396-2404.

11. Koretsky, C., *The significance of surface complexation reactions in hydrologic systems: a geochemist's perspective*. Journal of Hydrology, 2000. **230**(3-4): p. 127-171.

12. Limousin, G., J.P. Gaudet, L. Charlet, S. Szenknect, V. Barthes, and M. Krimissa, *Sorption isotherms: A review on physical bases, modeling and measurement*. Applied Geochemistry, 2007. **22**(2): p. 249-275.

13. Nano, G.V. and T.J. Strathmann, *Ferrous iron sorption by hydrous metal oxides.* Journal of Colloid and Interface Science, 2006. **297**(2): p. 443-454.

14. Hansel, C.M., S.G. Benner, and S. Fendorf, *Competing Fe(II)-induced mineralization pathways of ferrihydrite.* Environmental Science & Technology, 2005. **39**(18): p. 7147-7153.

15. Williams, A.G.B. and M.M. Scherer, *Spectroscopic evidence for Fe(II)-Fe(III) electron transfer at the iron oxide-water interface.* Environmental Science & Technology, 2004. **38**(18): p. 4782-4790.

16. Silvester, E., L. Charlet, C. Tournassat, A. Gehin, J.M. Greneche, and E. Liger, *Redox potential measurements and Mossbauer spectrometry of Fe(II) adsorbed onto Fe(III) (oxyhydr)oxides.* Geochimica Et Cosmochimica Acta, 2005. **69**(20): p. 4801-4815.

17. Larese-Casanova, P. and M.M. Scherer, *Fe(II) sorption on hematite: New insights based on spectroscopic measurements.* Environmental Science & Technology, 2007. **41**(2): p. 471-477.

18. Peretyazhko, T., J.M. Zachara, S.M. Heald, B.H. Jeon, R.K. Kukkadapu, C. Liu, D. Moore, and C.T. Resch, *Heterogeneous reduction of Tc(VII) by Fe(II) at the solid-water interface.* Geochimica Et Cosmochimica Acta, 2008. **72**(6): p. 1521-1539.

19. Gorski, C.A. and M.M. Scherer, *Influence of magnetite stoichiometry on Fe(II) uptake and nitrobenzene reduction.* Environmental Science & Technology, 2009. **43**(10): p. 3675-3680.

20. Schaefer, M.V., C.A. Gorski, and M.M. Scherer, *Spectroscopic evidence for interfacial Fe(II) Fe(III) electron transfer in a clay mineral.* Environmental Science & Technology, 2011. **45**(2): p. 540-545.

21. Pedersen, H.D., D. Postma, R. Jakobsen, and O. Larsen, *Fast transformation of iron oxyhydroxides by the catalytic action of aqueous Fe(II).* Geochimica et Cosmochimica Acta, 2005. **69**(16): p. 3967-3977.

22. Handler, R.M., B.L. Beard, C.M. Johnson, and M.M. Scherer, *Atom Exchange between Aqueous Fe(II) and Goethite: An Fe Isotope Tracer Study.* Environmental Science & Technology, 2009. **43**(4): p. 1102-1107.

23. Yanina, S.V. and K.M. Rosso, *Linked reactivity at mineral-water interfaces through bulk crystal conduction.* Science, 2008. **320**(5873): p. 218-222.

24. Gorski, C.A., R.M. Handler, B.L. Beard, T. Pasakarnis, C.M. Johnson, and M.M. Scherer, *Fe Atom Exchange between Aqueous Fe2+ and Magnetite.* Environmental Science & Technology, 2012. **46**(20): p. 12399-407.

25. Bruemmer, G.W., J. Gerth, and K.G. Tiller, *Reaction kinetics of the adsorption and desorption of nickel, zinc and cadminum by goethite. I. Adsorption and diffusion of metals.* Journal of Soil Science, 1988. **39**(1): p. 37-52.

26. Mikutta, C., F. Lang, and M. Kaupenjohann, *Citrate impairs the micropore diffusion of phosphate into pure and C-coated goethite.* Geochimica Et Cosmochimica Acta, 2006. **70**(3): p. 595-607.

27. Fischer, L., G.W. Brummer, and N.J. Barrow, *Observations and modelling of the reactions of 10 metals with goethite: adsorption and diffusion processes.* European Journal of Soil Science, 2007. **58**(6): p. 1304-1315.

28. Echigo, T., N. Monsegue, D.M. Aruguete, M. Murayama, and M.F. Hochella, Jr., *Nanopores in hematite (alpha-Fe2O3) nanocrystals observed by electron tomography*. American Mineralogist. **98**(1): p. 154-162.

29. Latta, D., C. Gorski, and M. Scherer, *Influence of Fe2+-catalysed iron oxide recrystallization on metal cycling*. Biochemical Society Transactions, 2012. **40**: p. 1191-1197.

30. Jang, J.H., B.A. Dempsey, G.L. Catchen, and W.D. Burgos, *Effects of Zn(II), Cu(II), Mn(II), Fe(II), NO3-, or SO42- at pH 6.5 and 8.5 on transformations of hydrous ferric oxide (HFO) as evidenced by Mossbauer spectroscopy*. Colloids and Surfaces a-Physicochemical and Engineering Aspects, 2003. **221**(1-3): p. 55-68.

31. Nico, P.S., B.D. Stewart, and S. Fendorf, *Incorporation of oxidized uranium into Fe (hydr)oxides during Fe(II) catalyzed remineralization*. Environmental Science & Technology, 2009. **43**(19): p. 7391-7396.

32. Pedersen, H.D., D. Postma, and R. Jakobsen, *Release of arsenic associated with the reduction and transformation of iron oxides*. Geochimica Et Cosmochimica Acta, 2006. **70**(16): p. 4116-4129.

33. Boland, D.D., R.N. Collins, T.E. Payne, and T.D. Waite, *Effect of amorphous Fe(III) oxide transformation on the Fe(II)-mediated reduction of U(VI)*. Environmental Science & Technology, 2011. **45**(4): p. 1327-1333.

34. Jeon, B.H., B.A. Dempsey, W.D. Burgos, and R.A. Royer, *Reactions of ferrous iron with hematite*. Colloids and Surfaces a-Physicochemical and Engineering Aspects, 2001. **191**(1-2): p. 41-55.

35. Frierdich, A.J., Y. Luo, and J.G. Catalano, *Trace element cycling through iron oxide minerals during redox-driven dynamic recrystallization*. Geology, 2011. **39**(11): p. 1083-1086.

36. Coughlin, B.R. and A.T. Stone, *Nonreversible adsorption of divalent metal ions (Mn-II, Co-II, Ni-II, Cu-II, and Pb-II) onto goethite: Effects of acidification, Fe-II addition, and picolinic-acid addition*. Environmental Science & Technology, 1995. **29**(9): p. 2445-2455.

37. Tiessen, H., J.W.B. Stewart, and H.W. Hunt, *Concepts of soil organic-matter transformations in relation to organo-mineral particle-size fractions*. Plant and Soil, 1984. **76**(1-3): p. 287-295.

38. Anderson, D.W., *The effect of parent material and soil development on nutrient cycling in temperate ecosystems*. Biogeochemistry, 1988. **5**(1): p. 71-97.

39. Oades, J.M., *The retention of organic-matter in soils*. Biogeochemistry, 1988. **5**(1): p. 35-70.

40. Koegel-Knabner, I., G. Guggenberger, M. Kleber, E. Kandeler, K. Kalbitz, S. Scheu, K. Eusterhues, and P. Leinweber, *Organo-mineral associations in temperate soils: Integrating biology, mineralogy, and organic matter chemistry*. Journal of Plant Nutrition and Soil Science-Zeitschrift Fur Pflanzenernahrung Und Bodenkunde, 2008. **171**(1): p. 61-82.

41. Theng, B.K.G., G.J. Churchman, and R.H. Newman, *The occurrence of interlayer clay-organic complexes in 2 New Zealand soils.* Soil Science, 1986. **142**(5): p. 262-266.

42. Eusterhues, K., C. Rumpel, M. Kleber, and I. Kogel-Knabner, *Stabilisation of soil organic matter by interactions with minerals as revealed by mineral dissolution and oxidative degradation.* Organic Geochemistry, 2003. **34**(12): p. 1591-1600.

43. Kleber, M., R. Mikutta, M.S. Torn, and R. Jahn, *Poorly crystalline mineral phases protect organic matter in acid subsoil horizons.* European Journal of Soil Science, 2005. **56**(6): p. 717-725.

44. Mikutta, R., M. Kleber, M.S. Torn, and R. Jahn, *Stabilization of soil organic matter: Association with minerals or chemical recalcitrance?* Biogeochemistry, 2006. **77**(1): p. 25-56.

45. Kaiser, K. and G. Guggenberger, *Sorptive stabilization of organic matter by microporous goethite: sorption into small pores vs. surface complexation.* European Journal of Soil Science, 2007. **58**(1): p. 45-59.

46. Henneberry, Y. and T. Kraus, *Structural stability of coprecipitated natural organic matter and ferric iron under reducing conditions.* Organic Geochemistry, 2012. **48**: p. 81-89.

47. Mikutta, C., R. Mikutta, S. Bonneville, F. Wagner, A. Voegelin, I. Christl, and R. Kretzschmar, *Synthetic coprecipitates of exopolysaccharides and ferrihydrite. Part I: Characterization.* Geochimica et Cosmochimica Acta, 2008. **72**(4): p. 1111-1127.

48. Karlsson, T. and P. Persson, *Complexes with aquatic organic matter suppress hydrolysis and precipitation of Fe(III).* Chemical Geology, 2012. **322**: p. 19-27.

49. Pedrot, M., A. Le Boudec, M. Davranche, A. Dia, and O. Henin, *How does organic matter constrain the nature, size and availability of Fe nanoparticles for biological reduction?* Journal of Colloid and Interface Science, 2011. **359**(1): p. 75-85.

50. Penner-Hahn, J.E., *Characterization of "spectroscopically quiet" metals in biology.* Coordination Chemistry Reviews, 2005. **249**(1-2): p. 161-177.

51. Koningsberger, D.C. and R. Prins, *X-Ray Absorption: Principles, Applications, Techniques of EXAFS, SEXAFS and XANES*. Chemical Analysis, ed. J.D. Winefordner. Vol. 92. 1988, New York: John Wiley & Sons. 673.

52. Long, G.J., *Mossbauer Spectroscopy Applied to Inorganic Chemistry*. Modern Inorganic Chemistry, ed. J.P.J. Fackler. Vol. 1. 1984, New York: Plenum Press.

53. Murad, E. and J. Cashion, *Mossbauer Spectroscopy of Environmental Materials and Their Industrial Utilization*. 2004: Kluwer Academic Publishers.

54. Dyar, M.D., D.G. Agresti, M.W. Schaefer, C.A. Grant, and E.C. Sklute, *Mossbauer spectroscopy of earth and planetary materials.* Annual Review of Earth and Planetary Sciences, 2006. **34**: p. 83-125.

55. Beard, B.L., C.M. Johnson, J.L. Skulan, K.H. Nealson, L. Cox, and H. Sun, *Application of Fe isotopes to tracing the geochemical and biological cycling of Fe.* Chemical Geology, 2003. **195**(1-4): p. 87-117.

56. Beard, B.L., C.M. Johnson, L. Cox, H. Sun, K.H. Nealson, and C. Aguilar, *Iron isotope biosignatures.* Science, 1999. **285**(5435): p. 1889-1892.

57. Schauble, E.A., G.R. Rossman, and H.P. Taylor Jr., *Theoretical estimates of equilibrium Fe-isotope fractionations from vibrational spectroscopy.* Geochimica et Cosmochimica Acta, 2001. **65**(15): p. 2487-2497.

58. Johnson, C.M., J.L. Skulan, B.L. Beard, H. Sun, K.H. Nealson, and P.S. Braterman, *Isotopic fractionation between Fe(III) and Fe(II) in aqueous solutions.* Earth and Planetary Science Letters, 2002. **195**(1-2): p. 141-153.

59. Mergler, D., H.A. Anderson, L.H.M. Chan, K.R. Mahaffey, M. Murray, M. Sakamoto, and A.H. Stern, *Methylmercury Exposure and Health Effects in Humans: A Worldwide Concern.* AMBIO, 2007. **36**(1): p. 3-11.

60. Selin, N., *Global Biogeochemical Cycling of Mercury: A Review*. Annual Review of Environment and Resources, 2009. **34**(1): p. 43-63.

61. Compeau, G. and R. Bartha, *Sulfate reducing bacteria: principal methylators of mercury in anoxic estuarine sediments.* Applied Environmental Microbiology, 1985. **53**: p. 261-265.

62. Kerin, E.J., C.C. Gilmour, E. Roden, M.T. Suzuki, J.D. Coates, and R.P. Mason, *Mercury methylation by dissimilatory iron-reducing bacteria.* Applied Environmental Microbiology, 2006. **72**(12): p. 7919-21.

63. U.S. Environmental Protection Agency, *Biennial National Listing of Fish Advisories*. 2010. p. 1-7.

64. Alberts, J.J., J.E. Schindler, R.W. Miller, and D.E. Nutter, Jr., *Elemental mercury evolution mediated by humic acid.* Science, 1974. **184**: p. 895-897.

65. Skogerboe, R.K. and S.A. Wilson, *Reduction of ionic species by fulvic acid.* Anal. Chem., 1981. **53**(2): p. 228-232.

66. Allard, B. and I. Arsenie, *Abiotic reduction of mercury by humic substances in aquatic system - An important process for the mercury cycle.* Water Air and Soil Pollution, 1991. **56**: p. 457-464.

67. Charlet, L., D. Bosbach, and T. Peretyashko, *Natural attenuation of TCE, As, Hg linked to the heterogeneous oxidation of Fe(II): an AFM study.* Chemical Geology, 2002. **190**(1-4): p. 303-319.

68. Jeong, H.Y., B. Klaue, J.D. Blum, and K.F. Hayes, *Sorption of mercuric ion by synthetic manocrystalline mackinawite (FeS).* Environmental Science & Technology, 2007. **41**(22): p. 7699-7705.

69. O'Loughlin, E.J., S.D. Kelly, K.M. Kemner, R. Csencsits, and R.E. Cook, *Reduction of Ag-I, Au-III, Cu-II, and Hg-II by Fe-II/Fe-III hydroxysulfate green rust.* Chemosphere, 2003. **53**(5): p. 437-446.

70. Wiatrowski, H.A., S. Das, R. Kukkadapu, E.S. Ilton, T. Barkay, and N. Yee, *Reduction of Hg(II) to Hg(O) by magnetite.* Environmental Science & Technology, 2009. **43**(14): p. 5307-5313.

71. Mishra, B., E.J. O'Loughlin, M.I. Boyanov, and K.K. Kemner, *Binding of Hg(II) to High Affinity Site on Bacteria Inhibits Reduction to Hg(0) by Mixed Fe(II/III) Phases.* Environmental Science and Technology, 2011. **45**: p. 9597-9603.

72. Schroeder, W.H. and J. Munthe, *Atmospheric Mercury - An Overview*. Atmospheric Environment, 1998. **32**(5): p. 809-822.

73. Schluter, K., *Review: evaporation of mercury from soils. An integration and synthesis of current knowledge.* Environmental Geology, 2000. **39**(3-4): p. 249-271.

74. Gorski, C.A., J.T. Nurmi, P.G. Tratnyek, T.B. Hofstetter, and M.M. Scherer, *Redox behavior of magnetite: Implications for contaminant reduction.* Environmental Science & Technology, 2010. **44**(1): p. 55-60.

75. Latta, D.E., C.A. Gorski, M.I. Boyanov, E.J. O'Loughlin, K.M. Kemner, and M.M. Scherer, *Influence of magnetite stoichiometry on U-VI reduction.* Environmental Science & Technology, 2012. **46**(2): p. 778-786.

76. Verwey, E.J.W. and P.W. Haayman, *Electronic Conductivity and Transition Point of Magnetite ("Fe3O4").* Physica, 1941. **8**(9): p. 979-987.

77. Itai, R., M. Shibuya, T. Matsumura, and G. Ishi, *Electrical resistivity of magnetite anodes.* Journal of the Electrochemical Society, 1971. **118**(10): p. 1709-11.

78. White, A.F., M.L. Peterson, and M.F. Hochella, *Electrochemistry and Dissolution Kinetics of Magnetite and Ilmenite.* Geochimica Et Cosmochimica Acta, 1994. **58**(8): p. 1859-1875.

79. Gorski, C.A. and M.M. Scherer, *Determination of nanoparticulate magnetite stoichiometry by Mossbauer spectroscopy, acidic dissolution, and powder X-ray diffraction: A critical review.* American Mineralogist, 2010. **95**(7): p. 1017-1026.

80. Tamura, H., K. Goto, Yotsuyan.T, and M. Nagayama, *Spectrophotometric determination of iron(II) with 1,10-phenanthroline in presence of large amounts of iron(III).* Talanta, 1974. **21**(4): p. 314-318.

81. Zheng, W., D. Foucher, and H. Hintelmann, *Mercury isotope fractionation during volatilization of Hg(0) from solution into the gas phase.* Journal of Analytical Atomic Spectrometry, 2007. **22**(9): p. 1097-1104.

82. U.S. Environmental Protection Agency, *Mercury Preservation Techniques*. 2003, U.S. Environmental Protection Agency.

83. Segre, C.U., N.E. Leyarovska, L.D. Chapman, W.M. Lavender, P.W. Plag, A.S. King, A.J. Kropf, B.A. Bunker, K.M. Kemner, P. Dutta, D. R.S., and J. Kaduk, *The MRCAT Insertion Device Beamline at the Advanced Photon Source*, in *Synchrotron Radiation Instrumentation: Eleventh U.S. National Conference*, P. Pianetta, Editor. 2000, American Institute of Physics. p. 419-422.

84. Harris, H.H., I.J. Pickering, and G.N. George, *The chemical form of mercury in fish.* Science, 2003. **301**(5637): p. 1203-1203.

85. Hansen, H.C.B., *Composition, stabilization, and light-absorption of Fe(II)Fe(III) hydroxy-carbonate (green rust).* Clay Minerals, 1989. **24**(4): p. 663-669.

86. Baltisberger, R.J., D.A. Hildebrand, D. Grieble, and T.A. Ballintine, *A study of the disproportionation of mercury(I) induced by gas sparging in acidic aqueous solutions for cold vapor atomic absorption spectroscopy.* Analytical Chimica Acta, 1979. **111**: p. 111-122.

87. MacNaughton, M.G. and R.O. James, *Adsorption of aqueous mercury (II) complexes on the oxide/water interface.* Journal of Colloid and Interface Science, 1974. **46**(2): p. 431-440.

88. Blinov, B.K., *Experimental evaluation of certain parameters of mercury migration from surface soil.* Sov Meteorol Hydrol, 1982. **5**: p. 43-49.

89. Rocha, J.C., E.S. Junior, L.F. Zara, A.H. Rosa, A. dos Santos, and P. Burba, *Reduction of mercury(II) by tropical river humic substances (Rio Negro) - A possible process of the mercury cycle in Brazil.* Talanta, 2000. **53**(3): p. 551-559.

90. Morse, J. and G. Luther, *Chemical influences on trace metal-sulfide interactions in anoxic sediments.* Geochimica et Cosmochimica Acta, 1999. **63**(19-20): p. 3373-3378.

91. Kim, C.S., J. Rytuba, and G.E. Brown, *EXAFS study of mercury(II) sorption to Fe- and Al-(hydr)oxides. II. Effects of chloride and sulfate.* Journal of Colloid and Interface Science, 2004. **270**(1): p. 9-20.

92. Ferrey, M.L., R.T. Wilkin, R.G. Ford, and J.T. Wilson, *Nonbiological removal of cis-dichloroethylene and 1,1-dichloroethylene in aquifer sediment containing magnetite.* Environmental Science & Technology, 2004. **38**(6): p. 1746-1752.

93. Liu, J., C.I. Pearce, O. Qafoku, E. Arenholz, S.M. Heald, and K.M. Rosso, *Tc(VII) reduction kinetics by titanomagnetite (Fe3O4-xTixO4) nanoparticles.* Geochimica et Cosmochimica Acta, 2012. **92**: p. 67-81.

94. Burnol, A. and L. Charlet, *Fe(II)-Fe(III)-Bearing Phases As a Mineralogical Control on the Heterogeneity of Arsenic in Southeast Asian Groundwater.* Environmental Science & Technology, 2010. **44**(19): p. 7541-7547.

95. Xie, Y. and D.M. Cwiertny, *Influence of Anionic Cosolutes and pH on Nanoscale Zerovalent Iron Longevity: Time Scales and Mechanisms of Reactivity Loss toward 1,1,1,2-Tetrachloroethane and Cr(VI).* Environmental Science & Technology, 2012. **46**(15): p. 8365-8373.

96. Crean, D.E., V.S. Coker, G. Van der Laan, and J.R. Lloyd, *Engineering Biogenic Magnetite for Sustained Cr(VI) Remediation in Flow-through Systems.* Environmental Science & Technology, 2012. **46**: p. 3352-3359.

97. Yavuz, C.T., J.T. Mayo, W.W. Yu, A. Prakash, J.C. Falkner, S. Yean, L.L. Cong, H.J. Shipley, A. Kan, M. Tomson, D. Natelson, and V.L. Colvin, *Low-field magnetic separation of monodisperse Fe3O4 nanocrystals.* Science, 2006. **314**(5801): p. 964-967.

98. Wang, Y.H., G. Morin, G. Ona-Nguema, F. Juillot, G. Calas, and G.E. Brown, *Distinctive Arsenic(V) Trapping Modes by Magnetite Nanoparticles Induced by Different Sorption Processes* Environmental Science & Technology, 2011. **45**(17): p. 7258-7266.

99. Kostka, J.E., J.W. Stucki, and H. Dong, *Microbial reduction of Fe(III) bound in clay minerals: Laboratory investigations of growth and mineral transformation.* Abstracts of Papers of the American Chemical Society, 2002. **223**: p. 046-GEOC.

100. Kato, S., K. Hashimoto, and K. Watanabe, *Microbial interspecies electron transfer via electron transfer through conductive minerals.* Proceedings of the National Academy of Sciences, 2012. **109**(25): p. 10042-10046.

101. Castro, P.A., E.R. Vago, and E.J. Calvo, *Surface electrochemical transformations on spinel iron oxide electrodes in aqueous solutions.* Journal of the Chemical Society-Faraday Transactions, 1996. **92**(18): p. 3371-3379.

102. Pang, S.C., S.F. Chin, and M.A. Anderson, *Redox equilibria of iron oxides in aqueous-based magnetite dispersions: Effect of pH and redox potential.* Journal of Colloid and Interface Science, 2007. **311**(1): p. 94-101.

103. Pourbaix, M., *Atlas of Electrochemical Equilibria in Aqueous Solutions*. 1966, Oxford: Pergamon. 644.

104. Straub, K.L., M. Benz, and B. Schink, *Iron metabolism in anoxic environments at near neutral pH.* Fems Microbiology Ecology, 2001. **34**(3): p. 181-186.

105. Yang, L., C.I. Steefel, M.A. Marcus, and J.R. Bargar, *Kinetics of Fe(II)-catalyzed transformation of 6-line ferrihydrite under anaerobic flow conditions.* Environmental Science & Technology, 2010. **44**(14): p. 5469-5475.

106. Villalobos, M., M.A. Trotz, and J.O. Leckie, *Variability in goethite surface site density: evidence from proton and carbonate sorption.* Journal of Colloid and Interface Science, 2003. **268**(2): p. 273-287.

107. Parfitt, R.L. and R.J. Atkinson, *Phosphate Adsorption on Goethite (Alpha-FeOOH).* Nature, 1976. **264**(5588): p. 740-742.

108. Hiemstra, T., M.O. Barnett, and W.H. van Riemsdijk, *Interaction of silicic acid with goethite.* Journal of Colloid and Interface Science, 2007. **310**(1): p. 8-17.

109. Cornell, R.M. and U. Schwertmann, *The Iron Oxides: Structure, Properties, Reactions, Occurrences and Uses* 2nd ed. 2003, Weinheim, Germany: Wiley-VCH. 664.

110. Fang, L., Y. Cao, Q. Huang, S. Walker, and P. Cai, *Reactions between bacterial exopolymers and goethite: A combined macroscopic and spectroscopic investigation.* Water Research, 2012. **46**: p. 5613-5620.

111. Omoike, A., J. Chorover, K.D. Kwon, and J.D. Kubicki, *Adhesion of bacterial exopolymers to alpha-FeOOH: Inner-sphere complexation of phosphodiester groups.* Langmuir, 2004. **20**(25): p. 11108-11114.

112. Filius, J.D., D.G. Lumsdon, J.C.L. Meeussen, T. Hiemstra, and W.H. Van Riemsdijk, *Adsorption of fulvic acid on goethite.* Geochimica Et Cosmochimica Acta, 2000. **64**(1): p. 51-60.

113. Weng, L.P., W.H. Van Riemsdijk, and T. Hiemstra, *Adsorption of humic acids onto goethite: Effects of molar mass, pH and ionic strength.* Journal of Colloid and Interface Science, 2007. **314**(1): p. 107-118.

114. Jones, A.M., R.N. Collins, J. Rose, and T.D. Waite, *The effect of silica and natural organic matter on the Fe(II)-catalysed transformation and reactivity of Fe(III) minerals.* Geochimica Et Cosmochimica Acta, 2009. **73**(15): p. 4409-4422.

115. Latta, D., J. Bachman, and M. Scherer, *Fe electron transfer and atom exchange in goethite: influence of Al-substitution and anion sorption.* Environmental Science and Technology, 2012. **46**(19): p. 10614-10623.

116. O'Loughlin, E.J., C.A. Gorski, M.M. Scherer, M.I. Boyanov, and K.M. Kemner, *Effects of oxyanions, natural organic matter, and bacterial cell numbers on the bioreduction of lepidocrocite (gamma-FeOOH) and the formation of secondary mineralization products.* Environmental Science & Technology, 2010. **44**(12): p. 4570-4576.

117. Amstaetter, K., T. Borch, and A. Kappler, *Influence of humic acid imposed changes of ferrihydrite aggregation on microbial Fe(III) reduction.* Geochimica et Cosmochimica Acta, 2012. **85**: p. 326-341.

118. Jiang, J. and A. Kappler, *Kinetics of microbial and chemical reduction of humic substances: Implications for electron shuttling.* Environmental Science and Technology, 2008. **42**: p. 3563-3569.

119. Shi, Z., J. Zachara, L. Shi, S. Wang, D. Moore, D. Kennedy, and J. Fredrickson, *Redox reactions of reduced flavin mononucleotide (FMN), riboflavin (RBF), and anthraquinone-2,6-disulfonate (AQDS) with ferrihydrite and lepidocrocite.* Environmental Science and Technology, 2012. **46**: p. 11644-11652.

120. Newman, D. and R. Kolter, *A role for excreted quinones in extracellular electron transfer.* Nature, 2000. **405**: p. 94-97.

121. Sutherland, I.W., *Microbial exopolysaccharides*, in *Polysaccharides: Structural Diversity and Functional Versatility*, S. Dumitriu, Editor. 2005, Marcel Dekker: NY.

122. Knee, E.M., F. Gong, M. Gao, M. Teplitski, J. A., A. Foxworthy, A. Mort, and W. Bauer, *Root mucilage from pea and its utilization by rhizosphere bacteria as a sole carbon source.* Molecular Plant-Microbe Interactions, 2001. **14**(775-784).

123. Cwiertny, D.M., R.M. Handler, M.V. Schaefer, V.H. Grassian, and M.M. Scherer, *Interpreting nanoscale size-effects in aggregated Fe-oxide suspensions: Reaction of Fe(II) with goethite.* Geochimica Et Cosmochimica Acta, 2008. **72**(5): p. 1365-1380.

124. Tischenko, V., C. Meile, M. Scherer, T. Pasakarnis, and A. Thompson, *Atom exchange between Fe(II) and nanocrystalline phases in tropical soils.* In preparation.

125. Gehin, A., J.M. Greneche, C. Tournassat, J. Brendle, D.G. Rancourt, and L. Charlet, *Reversible surface-sorption-induced electron-transfer oxidation of Fe(II) at reactive sites on a synthetic clay mineral.* Geochimica Et Cosmochimica Acta, 2007. **71**(4): p. 863-876.

126. Larese-Casanova, P., D.M. Cwiertny, and M.M. Scherer, *Nanogoethite formation from oxidation of Fe(II) sorbed on aluminum oxide: Implications for contaminant reduction.* Environmental Science & Technology, 2010. **44**(10): p. 3765-3771.

127. da Costa, G.M., E. De Grave, P.M.A. de Bakker, and R.E. Vandenberghe, *Influence of nonstoichiometry and the presence of maghemite on the Moessbauer spectrum of magnetite.* Clays and Clay Minerals, 1995. **43**(6): p. 656-668.

128. Xu, J., M.J. Stevens, T.A. Oleson, J.A. Last, and N. Sahai, *Role of Oxide Surface Chemistry and Phospholipid Phase on Adsorption and Self-Assembly: Isotherms and Atomic Force Microscopy.* Journal of Physical Chemistry C, 2009. **113**(6): p. 2187-2196.

129. Li, T.T. and M.J. Weaver, *Intramolecular electron transfer at metal surfaces. 4. dependence of tunneling probability upon donor-acceptor separation distance.* J. Am. Chem. Soc., 1984. **106**: p. 6107-6108.

130. Poulson, R.L., C.M. Johnson, and B.L. Beard, *Iron isotope exchange kinetics at the nanoparticulate ferrihydrite surface.* American Mineralogist, 2005. **90**(4): p. 758-763.

131. Rea, B.A., J.A. Davis, and G.A. Waychunas, *Studies of the reactivity of the ferrihydrite surface by iron isotopic exchange and mossbauer-spectroscopy.* Clays and Clay Minerals, 1994. **42**(1): p. 23-34.

132. Vermeer, A.W.P., W.H. van Riemsdijk, and L.K. Koopal, *Adsorption of Humic Acid to Mineral Particles. 1. Specific and Electrostatic Interactions.* Langmuir : the acs journal of surfaces and coll, 1998. **14**(10): p. 2810.

133. Illés, E. and E. Tombácz, *The effect of humic acid adsorption on pH-dependent surface charging and aggregation of magnetite nanoparticles.* Journal of Colloid and Interface Science, 2006. **295**: p. 115-123.

134. Chan, C., G. De Stasio, S. Welch, M. Girasole, B. Frazer, M. Nesterova, S. Fakra, and J. Banfield, *Microbial polysaccharides template assembly of nanocrystal fibers.* Science, 2004. **303**(1656-1658).

135. Oleson, T.A. and N. Sahai, *Oxide-dependent adsorption of a model membrane phospholipid, dipalmitoylphosphatidylcholine: Bulk adsorption isotherms.* Langmuir, 2008. **24**(9): p. 4865-4873.

136. Kim, J.I., G. Buckau, G.H. Li, H. Duschner, and N. Psarros, *Characterization of humic and fulvic-acids from Gorleben groundwater.* Fresenius Journal of Analytical Chemistry, 1990. **338**(3): p. 245-252.

137. International Humic Substances Society. *IHSS - Elemental Compositions and Stable Isotopic Ratios of IHSS Samples*. 2008 [cited 2013 May 1]; Available from: http://www.humicsubstances.org/elements.html.

138. Thorn, K.A., D.W. Folan, and P. MacCarthy, *Characterization of the International Humic Substances Society Standard and Reference Fulvic and Humic Acids by Solution State Carbon-13 (13C) and Hydrogen-1 (1H) Nuclear Magnetic Resonance Spectrometry*. 1989, U.S. Geological Survey. p. 93.

139. Ravichandran, M., G.R. Aiken, M.M. Reddy, and J.N. Ryan, *Enhanced dissolution of cinnabar (mercuric sulfide) by dissolved organic matter isolated from the Florida Everglades*. Environmental Science & Technology, 1998. **32**(21): p. 3305-3311.

140. Murad, E. and J.H. Johnston, *Iron oxides and oxyhydroxides*, in *Mossbauer spectroscopy applied to inorganic chemistry*, G.J. Long, Editor. 1987, Plenum Publishers: New York. p. 507-582.

141. Sundquist, E.T., *The global carbon-dioxide budget*. Science, 1993. **259**(5103): p. 934-941.

142. Schmidt, M., M. Torn, S. Abiven, T. Dittmar, G. Guggenberger, I. Jannsens, M. Kleber, I. Kögel-Knabner, J. Lehmann, D. Manning, P. Nannipieri, D. Rasse, S. Weiner, and S. Trumbore, *Persistence of soil organic matter as an ecosystem property*. Nature, 2011. **478**: p. 49-55.

143. Berner, R., *Sedimentary Pyrite Formation*. American Journal of Science, 1970. **268**: p. 1-23.

144. Schwertmann, U., F. Wagner, and H. Knicker, *Ferrihydrite-humic associations: Magnetic hyperfine interactions*. Soil Science Society of America Journal, 2005. **69**(4): p. 1009-1015.

145. Kaiser, K. and G. Guggenberger, *The role of DOM sorption to mineral surfaces in the preservation of organic matter in soils*. Organic Geochemistry, 2000. **31**(7-8): p. 711-725.

146. Schrumpf, M., K. Kaiser, G. Guggenberger, T. Persson, I. Kogel-Knabner, and E.D. Schulze, *Storage and stability of organic carbon in soils as related to depth, occlusion within aggregates, and attachment to minerals*. Biogeosciences, 2013. **10**(3): p. 1675-1691.

147. Mikutta, R. and K. Kaiser, *Organic matter bound to mineral surfaces: Resistance to chemical and biological oxidation*. Soil Biology & Biochemistry, 2011. **43**(8): p. 1738-1741.

148. Lalonde, K., A. Mucci, A. Ouellet, and Y. Gelinas, *Preservation of organic matter in sediments promoted by iron*. Nature, 2012. **483**(7388): p. 198-200.

149. Jambor, J. and J. Dutrizac, *Occurence and constitution of natural and synthetic ferrihydrite, a widespread iron oxyhydroxide*. Chemical Reviews, 1998. **98**: p. 2549-2585.

150. Lovley, D., R and E. Phillips, J, P, *Availability of Ferric Iron for Microbial Reduction in Bottom Sediments of the Freshwater Tidal Potomac River.* Applied and Environmental Microbiology, 1986. **52**(4): p. 751-757.

151. Cismasu, A., F. Michel, A. Tcaciuk, T. Tyliszczak, and G. Brown, *Composition and structural aspects of naturally occurring ferrihydrite.* Comptes Rendus Geoscience, 2011. **343**: p. 210-218.

152. Postma, D., *The Reactivity of Iron-Oxides in Sediments - a Kinetic Approach.* Geochimica Et Cosmochimica Acta, 1993. **57**(21-22): p. 5027-5034.

153. Jang, J.H. and S.L. Brantley, *Investigation of wustite (FeO) dissolution: Implications for reductive dissolution of ferric oxides.* Environmental Science & Technology, 2009. **43**(4): p. 1086-1090.

154. Eusterhues, K., F.E. Wagner, W. Haeusler, M. Hanzlik, H. Knicker, K.U. Totsche, I. Koegel-Knabner, and U. Schwertmann, *Characterization of Ferrihydrite-Soil Organic Matter Coprecipitates by X-ray Diffraction and Mossbauer Spectroscopy.* Environmental Science & Technology, 2008. **42**(21): p. 7891-7897.

155. Waychunas, G.A., B.A. Rea, C.C. Fuller, and J.A. Davis, *Surface-chemistry of ferrihydrite. 1. EXAFS studies of the geometry of coprecipitated and adsorbed arsenate.* Geochimica Et Cosmochimica Acta, 1993. **57**(10): p. 2251-2269.

156. Bancroft, G.M., *Mössbauer Spectroscopy: An Introduction for Inorganic Chemists and Geochemists*. 1973, New York: John Wiley and Sons. 1-14.

157. Murad, E. and U. Schwertmann, *The influence of aluminum substitution and crystallinity on the Mossbauer spectra of goethite.* Clay Minerals, 1983. **18**(3): p. 301-312.

158. Morup, S. and C.W. Ostenfeld, *On the use of Mossbauer spectroscopy for characterisation of iron oxides and oxyhydroxides in soils.* Hyperfine Interactions, 2001. **136**(1-2): p. 125-131.

159. Shimizu, M., J. Zhou, M. Obst, C. Schroder, A. Kappler, and T. Borch, *Dissimilatory reduction and transformation of ferrihydrite-natural organic matter co-precipitates.* In preparation.

160. Mikutta, C. and R. Kretzschmar, *Synthetic coprecipitates of exopolysaccharides and ferrihydrite. Part II: Siderophore-promoted dissolution.* Geochimica et Cosmochimica Acta, 2008. **72**(4): p. 1128-1142.

161. Morel, F.M.M. and J.G. Hering, *Principles and Applications of Aquatic Chemistry*. 1993, New York: Wiley. 588.

162. Waychunas, G.A., Y.-S. Jun, P.J. Eng, S.K. Ghose, and T. Trainor, *Anion sorption topology on hematite: comparison of arsenate and silicate*, in *Developments in Earth and Environmental Sciences*. 2001, Elsevier: Amsterdam.

163. Mayer, T.D. and W.M. Jarrell, *Formation and stability of iron(II) oxidation products under natural concentrations of dissolved silica.* Water Research, 1996. **30**(5): p. 1208-1214.

164. Schwertmann, U. and H. Thalmann, *Influence of [Fe(II)], [Si], and pH on formation of lepidocrocite and ferrihydrite during oxidation of aqueous FeCl2 solutions.* Clay Minerals, 1976. **11**(3): p. 189-200.

165. Schwertmann, U. and R.M. Cornell, *Iron Oxides in the Laboratory*. 1991, Weinheim: VCH. 137.

166. Wu, L.L., B.L. Beard, E.E. Roden, and C.M. Johnson, *Stable iron isotope fractionation between aqueous Fe(II) and hydrous ferric oxide.* Environmental Science & Technology, 2011. **45**(5): p. 1847-1852.

167. Schwertmann, U., *Inhibitory effect of soil organic matter on crystallization of amorphous ferric hydroxide.* Nature, 1966. **212**(5062): p. 645-&.

168. Tamaura, Y., K. Ito, and T. Katsura, *Transformation of γ-FeO(OH) to Fe3O4 by adsorption of iron(II) ion on γ-FeO(OH).* Journal of the Chemical Society-Dalton Transactions, 1983(2): p. 189-194.

169. Fortin, D., G.G. Leppard, and A. Tessier, *Characteristics of lacustrine diagenetic iron oxyhydroxides.* Geochimica Cosmochimica Acta, 1993. **57**: p. 4391-4404.

170. Torn, M.S., S.E. Trumbore, O.A. Chadwick, P.M. Vitousek, and D.M. Hendricks, *Mineral control of soil organic carbon storage and turnover.* Nature, 1997. **389**(6647): p. 170-173.

171. Keil, R.G., D.B. Montlucon, F.G. Prahl, and J.I. Hedges, *Sorptive preservation of labile organic-matter in marine sediments.* Nature, 1994. **370**(6490): p. 549-552.

172. Kennedy, C.B., S.D. Scott, and F.G. Ferris, *Hydrothermal phase stabilization of 2-line ferrihydrite by bacteria.* Chemical Geology, 2004. **212**(3-4): p. 269-277.

173. Chalmers, B., *How water freezes.* Scientific American, 1959. **200**(2): p. 114-122.

174. Gu, B.H., J. Schmitt, Z.H. Chen, L.Y. Liang, and J.F. McCarthy, *Adsorption and desorption of natural organic-matter on iron-oxide - mechanisms and models.* Environmental Science & Technology, 1994. **28**(1): p. 38-46.

175. Gu, B.H., J. Schmitt, Z. Chen, L.Y. Liang, and J.F. McCarthy, *Adsorption and desorption of different organic-matter fractions on iron-oxide.* Geochimica Et Cosmochimica Acta, 1995. **59**(2): p. 219-229.

176. Gu, B.H., T.L. Mehlhorn, L.Y. Liang, and J.F. McCarthy, *Competitive adsorption, displacement, and transport of organic matter on iron oxide .1. Competitive adsorption.* Geochimica Et Cosmochimica Acta, 1996. **60**(11): p. 1943-1950.

177. Elsner, M., R.P. Schwarzenbach, and S.B. Haderlein, *Reactivity of Fe(II)-bearing minerals toward reductive transformation of organic contaminants.* Environmental Science & Technology, 2004. **38**(3): p. 799-807.

178. Stumm, W., *Aquatic surface chemistry : chemical processes at the particle-water interface / edited by Werner Stumm*. Environmental science and technology. 1987: New York : Wiley, c1987.

179. Sulzberger, B., D. Suter, C. Siffert, S. Banwart, and W. Stumm, *Dissolution of fe(iii)(hydr)oxides in natural waters; laboratory assessment on the kinetics controlled by surface coordination.* Marine Chemistry, 1989. **28**(1-3): p. 127-144.

180. Deng, Y. and W. Stumm, *Reactivity of aquatic iron(III) oxyhydroxides--implications for redox cycling of iron in natural waters.* Applied Geochemistry, 1994. **9**(1): p. 23-36.

181. Lovley, D.R., D.E. Holmes, and K.P. Nevin, *Dissimilatory Fe(III) and Mn(IV) Reduction*, in *Advances in Microbial Physiology*. 2004, Academic Press. p. 219-286.

182. Wielinga, B., M.M. Mizuba, C.M. Hansel, and S. Fendorf, *Iron Promoted Reduction of Chromate by Dissimilatory Iron- Reducing Bacteria.* Environmental Science & Technology, 2001. **35**(3): p. 522-527.

183. Gorski Christopher, A. and M. Scherer Michelle, *Fe2+ Sorption at the Fe Oxide-Water Interface: A Revised Conceptual Framework*, in *Aquatic Redox Chemistry*. 2011, American Chemical Society. p. 315-343.

184. Gorski, C.A., R.M. Handler, B.L. Beard, T. Pasakarnis, C.M. Johnson, and M.M. Scherer, *Fe Atom Exchange between Aqueous Fe2+ and Magnetite.* Environmental Science & Technology, 2012.

185. Jaisi, D.P., *Fe (2+) sorption onto nontronite (NAu-2).* Geochimica et Cosmochimica Acta, 2008. **72**(22): p. 5361-5371.

186. Van Schaik, J.W.J., I. Persson, D.B. Kleja, and J.P. Gustafsson, *EXAFS Study on the Reactions between Iron and Fulvic Acid in Acid Aqueous Solutions.* Environmental Science & Technology, 2008. **42**(7): p. 2367-2373.

187. Thuróczy, C.E., L.J.A. Gerringa, M.B. Klunder, P. Laan, and H.J.W. de Baar, *Observation of consistent trends in the organic complexation of dissolved iron in the Atlantic sector of the Southern Ocean.* Deep-Sea Research Part II, Topical Studies in Oceanography, 2011. **58**(25/26): p. 2695-2706.

188. Handler, R.M., B.L. Beard, C.M. Johnson, and M.M. Scherer, *Atom Exchange between Aqueous Fe(II) and Coethite: An Fe Isotope Tracer Study.* Environmental Science & Technology, 2009. **43**(4): p. 1102-1107.

189. Schaefer, M.V., C.A. Gorski, and M.M. Scherer, *Spectroscopic evidence for interfacial Fe(II)-Fe(III) electron transfer in a clay mineral.* Environmental Science & Technology, 2011. **45**(2): p. 540-545.

190. Mikutta, C., J.G. Wiederhold, O.A. Cirpka, T.B. Hofstetter, B. Bourdon, and U. Von Gunten, *Iron isotope fractionation and atom exchange during sorption of ferrous iron to mineral surfaces.* Geochimica et Cosmochimica Acta, 2009. **73**(7): p. 1795-1812.

191. Latta, D.E., J.E. Bachman, and M.M. Scherer, *Fe Electron Transfer and Atom Exchange in Goethite: Influence of Al-Substitution and Anion Sorption.* Environmental Science & Technology, 2012. **46**(19): p. 10614-10623.

192. Frierdich, A.J., M.M. Scherer, J.E. Bachman, M.H. Engelhard, B.W. Rapponotti, and J.G. Catalano, *Inhibition of Trace Element Release During Fe(II)-Activated Recrystallization of Al-, Cr-, and Sn-Substituted Goethite and Hematite.* Environmental Science & Technology, 2012. **46**(18): p. 10031-10039.

193. Masue-Slowey, Y., R.H. Loeppert, and S. Fendorf, *Alteration of ferrihydrite reductive dissolution and transformation by adsorbed As and structural Al: Implications for As retention.* Geochimica et Cosmochimica Acta, 2011. **75**(3): p. 870-886.

194. Frierdich, A.J. and J.G. Catalano, *Controls on Fe(II)-Activated Trace Element Release from Goethite and Hematite.* Environmental Science & Technology, 2011. **46**(3): p. 1519-1526.

195. Peretyazhko, T. and G. Sposito, *Iron(III) reduction and phosphorous solubilization in humid tropical forest soils.* Geochimica et Cosmochimica Acta, 2005. **69**(14): p. 3643.

196. Silver, W.L., A.E. Lugo, and M. Keller, *Soil Oxygen Availability and Biogeochemistry Along Rainfall and Topographic Gradients in Upland Wet Tropical Forest Soils.* Biogeochemistry, 1999. **44**(3): p. 301-328.

197. Wiederhold, J.G., S.M. Kraemer, N. Teutsch, P.M. Borer, A.N. Halliday, and R. Kretzschmar, *Iron Isotope Fractionation during Proton-Promoted, Ligand-Controlled, and Reductive Dissolution of Goethite.* Environmental Science & Technology, 2006. **40**(12): p. 3787-3793.

198. Skulan, J.L., B.L. Beard, and C.M. Johnson, *Kinetic and equilibrium Fe isotope fractionation between aqueous Fe(III) and hematite.* Geochimica et Cosmochimica Acta, 2002. **66**(17): p. 2995-3015.

199. Thompson, A., O.A. Chadwick, D.G. Rancourt, and J. Chorover, *Iron-oxide crystallinity increases during soil redox oscillations.* Geochimica Et Cosmochimica Acta, 2006. **70**(7): p. 1710-1727.

200. Jeon, B.H., B.A. Dempsey, W.D. Burgoes, and R. Royer, *Adsorption of ferrous ion onto ferric oxide.* 2000.

201. Cornell, R.M. and U. Schwertmann, *The Iron Oxides: Structure, Properties, Reactions, Occurrence and Uses.* The Iron Oxides, ed. R.M. Cornell and U. Schwertmann. 1996, New York, NY: VCH.

202. Jeon, B.-H., B.A. Dempsey, W.D. Burgos, and R.A. Royer, *Reactions of ferrous iron with hematite.* Colloids and Surfaces A: Physicochemical and Engineering Aspects, 2001. **191**(1-2): p. 41-55.

203. Thompson, A., D.G. Rancourt, O.A. Chadwick, and J. Chorover, *Iron solid-phase differentiation along a redox gradient in basaltic soils.* Geochimica et Cosmochimica Acta, 2011. **75**(1): p. 119-133.

204. Sedlácek, J., E. Gjessing, and J.P. Rambaek, *Isotope exchange between inorganic iron and iron naturally complexed by aquatic humus.* Science of The Total Environment, 1987. **62**: p. 275-279.

205. Morgan, J.L.L., L.E. Wasylenki, J. Nuester, and A.D. Anbar, *Fe Isotope Fractionation during Equilibration of Fe-Organic Complexes*. Environmental Science & Technology, 2010. **44**(16): p. 6095-6101.

206. Dideriksen, K., J.A. Baker, and S.L.S. Stipp, *Equilibrium Fe isotope fractionation between inorganic aqueous Fe(III) and the siderophore complex, Fe(III)-desferrioxamine B*. Earth and Planetary Science Letters, 2008. **269**(1-2): p. 280.

207. Brantley, S.L., L. Liermann, and T.D. Bullen, *Fractionation of Fe Isotopes by Soil Microbes and Organic Acids*. Geology, 2001. **29**(6): p. 535-538.

208. Matthews, A., X.-K. Zhu, and K. O'Nions, *Kinetic iron stable isotope fractionation between iron (-II) and (-III) complexes in solution*. Earth and Planetary Science Letters, 2001. **192**: p. 81-92.

209. Neumann, A. and M.M. Scherer, *Interfacial Fe(II)-Fe(III) Electron Transfer and Atom Exchange in Smectites: Effect of Smectite Properties*. Mineralogical Magazine, 2012. **76**(6): p. 2164.

210. Hossner, L.R., *Dissolution for total elemental analysis.*, in *Methods of Soil Analysis: Part 3-Chemical Methods* D.L. Sparks, Editor. 1996, Soil Science Society of America: Madison, WI. p. 49-64.

211. Lingling, W., B.L. Beard, E.E. Roden, and C.M. Johnson, *Stable Iron Isotope Fractionation Between Aqueous Fe(II) and Hydrous Ferric Oxide*. Environmental Science & Technology, 2011. **45**(5): p. 1847-1852.

212. Beard, B.L., R.M. Handler, M.M. Scherer, L.L. Wu, A.D. Czaja, A. Heimann, and C.M. Johnson, *Iron isotope fractionation between aqueous ferrous iron and goethite*. Earth and Planetary Science Letters, 2010. **295**(1-2): p. 241-250.

213. Larese-Casanova, P. and M.M. Scherer, *Fe(II) Sorption on Hematite: New Insights Based on Spectroscopic Measurements*. Environ. Sci. Technol., 2007. **41**(2): p. 471-477.

214. Regazzoni, A.E., G.A. Urrutia, M.A. Blesa, and A.J.G. Maroto, *Some observations on the composition and morphology of synthetic magnetites obtained by different routes*. Journal of Inorganic & Nuclear Chemistry, 1981. **43**(7): p. 1489-1493.

215. Jonsson, J. and D.M. Sherman, *Sorption of As(III) and As(V) to siderite, green rust (fougerite) and magnetite: Implications for arsenic release in anoxic groundwaters*. Chemical Geology, 2008. **255**(1-2): p. 173-181.

216. Butler, E.C. and K.F. Hayes, *Effects of Solution Composition and pH on the Reductive Dechlorination of Hexachloroethane by Iron Sulfide*. Environmental Science and Technology, 1998. **32**(9): p. 1276-1284.

217. Sawyer, C.N., P.L. McCarty, and G.F. Parkin, *Chemistry for Environmental Engineering*. 4th ed. 1994, New York: McGraw-Hill, Inc.

218. Byrne, R.H. and D. Kester, *Solubility of hydrous ferric oxide and iron speciation in seawater*. Marine Chemistry, 1976. **4**(3): p. 255-274.

219. Kuma, K., J. Nishioka, and K. Matsunaga, *Controls on Iron(III) Hydroxide Solubility in Seawater: The Influence of pH and Natural Organic Chelators.* Limnology and Oceanography, 1996. **41**(3): p. 396-407.

220. Liu, X. and F. Millero, *The solubility of iron hydroxide in sodium chloride solutions.* Geochimica et Cosmochimica Acta, 1999. **63**(19-20): p. 3487-3497.

221. Sherman, D.M., *Electronic structures of siderite (FeCO3) and rhodocrosite (MnCO3): Oxygen K-edge spectroscopy and hybrid density functional theory.* American Mineralogist, 2009. **94**(1): p. 166-171.

222. Puthussery, J., S. Seefeld, N. Berry, M. Gibbs, and M. Law, *Colloidal iron pyrite (FeS2) nanocrystal inks for thin-film photovoltaics.* Journal of the American Chemical Societry, 2011. **133**(4): p. 716-719.

223. Kirsch, R., D. Fellhauer, M. Altmaier, V. Neck, A. Rossberg, T. Fanghanel, L. Charlet, and A.C. Scheinost, *Oxidation state and local structure of plutonium reacted with magnetite, mackinawite, and chukanovite.* Environmental Science & Technology, 2011. **45**(17): p. 7267-7274.

224. Buerge, I.J. and S.J. Hug, *Influence of organic ligands on chromium(VI) reduction by iron(II).* Environmental Science & Technology, 1998. **32**(14): p. 2092-2099.

225. Jensen, J.N., *A problem solving approach to aquatic chemistry*. 2003: Wiley.